Evaluation of residual stress distribution in laser welding process including the effect of phase transformation kinetics

Bikash Kumar

Department of Mechanical Engineering

Indian Institute of Technology Guwahati

March 2021

Evaluation of residual stress distribution in laser welding process including the effect of phase transformation kinetics

submitted in partial fulfillment of the requirements
for the degree of

Doctor of Philosophy

by

Bikash Kumar

(156103023)

Supervisor:

Swarup Bag

Department of Mechanical Engineering

Indian Institute of Technology Guwahati

March 2021

Dedicated to

Lord Shayam-Shyama, parents, sister, teacher,

and my bestie *Bittu*

THESIS APPROVAL SHEET

The thesis titled

Evaluation of residual stress distribution in laser welding process including the effect of phase transformation kinetics

by

Bikash Kumar

is approved for the degree of Doctor of Philosophy.

Examiners

_____

_____

_____

Supervisor

_____

Chairman

_____

Date: 24th March, 2021

Place: IIT Guwahati

Department of Mechanical Engineering
Indian Institute of Technology Guwahati
Guwahati-781039
INDIA

CERTIFICATE

It is certified that the work contained in the thesis entitled **"Evaluation of residual stress distribution in laser welding process including the effect of phase transformation kinetics"** submitted by **Mr. Bikash Kumar** to the Indian Institute of Technology Guwahati for the award of the degree of doctor of Philosophy has been carried out under my supervision in the Department of Mechanical Engineering, Indian Institute of Technology Guwahati. This work has not been submitted elsewhere for the award of any other degree or diploma.

The thesis, in my opinion, has reached the standard fulfilling the requirements for the award of degree of Doctor of Philosophy in accordance with the regulations of the Institute.

Date: 24th March, 2021

Swarup Bag

Department of Mechanical Engineering, Indian Institute of Technology Guwahati, Guwahati, Assam 781039, India

Declaration

I declare that the present written submission is my thoughts in my own words. I have adequately been cited and referenced the original sources, where others' ideas have been involved. I also declare that I have followed to all principles of academic morality and honesty and have neither fabricated nor falsified any idea/data in the present thesis. I realize that any defilement of the above will be cause for disciplinary action by the Institute and can also induce disciplinary action from the sources which have thus not been properly cited.

(Bikash Kumar)

Date: 24th March, 2021

Roll No: 156103023

Abstract

The accurate assessment of welding induced residual stress are pivotal due to its detrimental effect on structural stability and mechanical performance of welded structure that can reduce the fatigue life and premature failure of the welded joints. Especially, the thin structure is susceptible towards the severe distortion and locked-in (residual) stress development due to relatively low stiffness and high heat input during fusion welding process. In the current research, this takes as a window of opportunity to address all the challenges aiming at the amendment of tensile residual stress in laser welded thin structure of Ti6Al4V and SS304 stainless steel, as well as in shielded metal arc welding of thick 9Cr ferritic-martensitic steel. The volumetric dilation and thermodynamic property variation at fusion zone and heat-affected zone is associated with phase change. The development of residual stresses is substantially governed by the diffusional and non-diffusional phase transformation kinetics and resulting microstructural morphologies. Coarse grain morphology, i.e., thick α′-lath within coarse prior β-grain boundary or lathy δ-ferrite within austenite matrix, promotes tensile residual stress due to deformation incompatibility around the lamellae interface or due to highly localized stress field caused by heterogeneous microstructure. The present thesis is mainly oriented towards the directions that address the thermal-metallurgical-mechanical interaction to characterize the residual stress in autogenous laser welding process. Fine δ-ferrite or acicular α′-martensitic lath accomplished at optimum heat input or sufficiently high cooling rate attributes less heterogeneity at weld zone microstructure. Hence, it finds a way not only to mitigate residual stress, even changes its nature from tensile to compressive. It is evident that the quantification of transient temperature growth and resulting metallurgical change is exceptionally complicated, and there is an ambiguity to precisely estimate the residual stresses. Hence, the computational model provides flexibility to simulate physical phenomena such as non-uniform temperature distribution, phase fraction and mechanical response during modeling of the welding process. Thus, a finite element based thermal-metallurgical-mechanical (TMM) model for fusion welding process is attempted to develop in the present research work.

The laser beam welding process in both pulse and continuous mode is used for the welding of Ti6Al4V alloy and SS304 stainless steel, whereas shielded metal arc welding and electron beam welding technique is employed for the fabrication of 9Cr steel. A reliable database of weld dimensions, residual stress distribution, and microstructural morphology is created by laser welding process. The model for phase transformation kinetics utilizes the characteristic of microstructural morphology. The measurement of weld dimensions and residual stress serves to validate the results from numerical model. The development of TMM models for aforementioned alloy systems serves to aid the accurate prediction of

residual stress by incorporating the solid-state phase transformation kinetics. Overall, high lattice expansion accompanied with martensitic transformation mainly reduces the overall tensile residual stresses of weldments. First, the interaction of microstructural morphology with residual stress for Ti6Al4V alloy is established where solid state phase transformation kinetics is accounted for material model. Secondly, it is attempted to understand the solidification behavior of SS304 stainless steel weld metal as well as its interaction with δ-ferrite formation and residual stress distribution. Finally, the significance of change in weld chemistry by playing with alloying compositions on the development of residual stress in fabricated 9Cr steel weld is attempted. Overall, the microstructural morphology is more sensitive to residual stress pattern for Ti-alloy and P91 steels whereas the influence of solid state phase transformation is minimum for stainless steel weldment. Thus, the developed computational framework not only act as reliable method for residual stress calculation, but also acts as a directive to reduce tensile residual stress in a weldment which are sensitive to the choice of materials.

Keywords: Current pulsation, 9Cr steel, distortion, electron beam welding, finite element model, heat input, heat source model, Laser welding, microstructure, phase transformation, residual stress, shielded metal arc welding, stainless steel, titanium alloy, thermo-metallurgical-mechanical model, topography, volumetric dilation.

CONTENTS

List of Figures

List of Tables

Acknowledgement

Over the journey of five and half years at IIT Guwahati, I have been accompanied and supported by many people that helped me to accomplish the research work. Foremost, I would like to express my deep appreciation and sincere gratitude to my supervisor, Dr. Swarup Bag. He has been a tremendous mentor for me. His untiring guidance in the form of research effort, demand for excellence and encouragement, professional expertise brought the best from all involved. I owe him lots of gratitude for his guidance.

I would like to acknowledge, Prof. S. Senthilvelan, Head, Department of Mechanical Engineering, for providing environs for higher learning. I would also like to acknowledge my doctoral committee members Prof. S. Pal, Prof. P. Biswas and Prof. K. D. Singh for their insightful comments and encouragement which incented me to widen my research from various perspectives.

I would like to convey my deep regards to Dr. C. P. Paul and Laser Material Processing Division team at Raja Ramanna Centre for Advanced Technology, Indore, India for their support and helpful technical discussions regarding my research work. I would also like to acknowledge Dr. Chitta Ranjan Das and Dr. S. Mahadevan at Indira Gandhi Centre for Atomic Research, Kalpakkam, India, and Dr. P. Ganesh, Dr. R. Kaul at Raja Ramanna Centre for Advanced Technology, Indore, India for their kind support and assistance to conduct experiments for my research progress.

I would like to thanks Mr. S. Ahmed, Mr. J. Basumatary, Mr. N.K. Das, Mr. C. Banikya and Central Instrument Facility team for their support to perform the research work in the laboratories and Central Workshop.

I am extremely grateful to my Parents and Family members for his love, prayers, care and support for educating and preparing me for my future. Also, I express my thanks to my sister, for her support and valuable prayers. My special thanks go to my friends, for their mental support and keen interest shown to complete this thesis successfully.

And finally, I would thank the Almighty God for his showers of blessings throughout my life and during period of research work to complete the research successfully.

March 2021

Bikash Kumar

IIT Guwahati

Nomenclature

Symbol	Description	Unit
(T_i)	Initial temperature	K
(ε_{ij}^{t})	Total strain	-
$f_{\beta\rightarrow\alpha'}$	Phase fraction for β to α′-phase transformation	-
σ_{ij}	Cauchy stress tensor	-
$[C^{thrml}]$	Thermal stiffness matrix	-
$[D^{el}]$	Elastic matrix	-
$[D^{ep}]$	Elasto-plastic matrix	-
$[D^{pl}]$	Plastic matrix	-
$f_{\gamma}^{eqb.}$	Phase fraction of γ-phase at equilibrium stage	-
b_i	Sum of the body force vector	-
C_{pc}	Specific heat capacity	J kg $^{-1}$K^{-1}
E_{hkl}	Elastic modulus for hkl plane	N mm^{-2}
f_i	Phase fraction of individual phase	-
h_c	Convective heat transfer coefficient	W m^{-2}K^{-1}
h_g	Rate of internal heat generation	J s^{-1}
H_i	Heat input	J mm^{-1}
$K_{\alpha\rightarrow\beta}$	Rate constant for α → β transformation	-
P_{av}	Average power	W
q_*	Maximum heat flux at centre of heat source	W mm^{-2}
R_a	surface roughness parameters	μm
$T_{\alpha\rightarrow\beta}$	α-dissolution temperature	K
T_β	β-transus temperature	K
Z_o	Variable depth of hourglass heat source model	mm
H	Shear modulus	K mm^{-2}
σ_B	Stefan-Boltzman coefficient	J K^{-1}

Symbol	Description	Unit
α_i	Coefficient of thermal expansion for i-phase	K^{-1}
α_t	Coefficient of thermal expansion	K^{-1}
$\gamma_{\alpha\rightarrow\beta}$	Avrami exponent for $\alpha \rightarrow \beta$ transformation	-
δ_{ij}	Kronecker delta	-
ε_{ij}^{cp}	Creep strain	-
ε_{ij}^{el}	Elastic strain	-
ε_{ij}^{pl}	Plastic strain	-
ε_{ij}^{ptr}	Strain due to phase transformation	-
ε_{ij}^{thrml}	Thermal strain	-
ε_{ij}^{trp}	Transformation induced plasticity	-
ε_{ij}^{vp}	Visco-plastic strain	-
ε_{kk}	Strain component	-
ν_{hkl}	Poisson's ratio for hkl plane	-
ρ_j	Density of weldment	Kg m^{-3}
σ_{11}	Longitudinal stress	N mm^{-2}
σ_{22}	Transverse stress	N mm^{-2}
σ_{av}	Average stress	N mm^{-2}
σ_B	Stefan-Boltzman coefficient	J K^{-1}
σ_o^{rs}	Initial residual stress	N mm^{-2}
$\sigma^{rs}(T,t)$	Residual stress value at temperature T and time t	N mm^{-2}
σ_y	Yield strength	N mm^{-2}
ΔH	Activation enthalpy	J
ΔT	Temperature change	K
C	Stiffness tensor	-
d	Inter-planar spacing	Å
k	Thermal conductivity	W $m^{-1}K^{-1}$

Symbol	Description	Unit
r_t, r_b, r_m	Radial distance of hourglass heat source model	mm
T	Temperature	K
t	Time	s
V	Welding speed	mm s^{-1}
E_T	Elastic modulus	N mm^{-2}
Z_t, Z_b, Z_m	Depth of hourglass heat source model	mm
$\Delta\theta$	Bragg scattering angle	degree
ε	Elastic strain	-
ε_{ij}	Element of the strain tensor	-
λ	Incident wavelength	nm
ν	Poisson ratio	-
Ψ	Polar angles to the tensor coordinate system	-
C_S	Solid state specific heat capacity	J kg^{-1} K^{-1}
Δf_i	Change in phase fraction of phase i	-
a_f	extent of heat source from its center in the front ellipsoid	-
a_r	extent of heat source from its center in the rear ellipsoid	-
f_f	heat distribution in front part of ellipsoid	-
f_i	Attained phase fraction of i-phase	-
f_r	heat distribution in rear part of ellipsoid	-
f_β^c	Equilibrium β-phase fraction	-
q_f	heat flux in front part of ellipsoid	W m^{-2}
q_r	heat flux in rear part of ellipsoid	W m^{-2}
r_{eff}	Effective radius	mm
$[Cr_{eq.}]$	Chromium equivalent	-
$[Ni_{eq.}]$	Nickel equivalent	-
$u_{i,j}$	Displacement gradient	-
M_{st}	Martensitic start temperature	K
M_{ft}	Martensitic finish temperature	K

Symbol	Description	Unit
f_γ	Volume fraction of γ-austenitic phase	-
$k_{\delta\rightarrow\gamma}$	Rate constant for $\delta \rightarrow \gamma$ transformation	-
$N_{\delta\rightarrow\gamma}$	Avrami exponent for $\delta \rightarrow \gamma$ transformation	-
$\dot{Q}(Z, r)$	Heat flux in hourglass model function of Z and r	W m^{-2}
b	bead width	mm
c	depth of penetration	mm
α_{ptr}	Expansion coefficient resulting from phase transformation	K^{-1}
$\varepsilon_i^{\Delta vc}$	Strain induced due to volume change	-
$T_{\alpha'}$	α' finish temperature	K
V_α	Unit cell volume of α-phase	$Å^3$
V_β	Unit cell volume of β-phase	$Å^3$
$\alpha_{PTC}(T)$	Expansion coefficient in cooling cycle	K^{-1}
$\alpha_{PTH}(T)$	Expansion coefficient at heating stage	K^{-1}
P_d	Pulse duration	Hz

Chapter 1

1.0 Introduction

1.1 General background

Joining of metals using fusion welding process is ever demanding in the manufacturing sector for a variety of engineering components, extending from quite large structure to very complex structure or miniature components for micro-electronics and biomedical applications (Norrish, 2006). However, fusion welding involves several interactive physical phenomena such as thermal, metallurgical and mechanical that occurs simultaneously. It is also regarded as one of the complex manufacturing processes in the context of number of parameters engaged and factors contribute to the reliable joint. Application of intense heat during welding exhibits mismatch between different parts, different phases and different locations within same structure. However, welding induces strain due to non-uniform temperature gradients as well as volumetric dilation in weld metal leads to the development of residual stresses (Dar et al., 2009). Even, welding of thin structure becomes challenging with rising miniaturization of components in biomedical industry. Specially, thin weld structure is highly sensitive towards tensile residual stress and severe distortion owing to relatively low stiffness and high heat input. It is also associated with solid-state phase transformation strain, which unavoidably contribute to residual stress generation. However, phase transformation induced stresses can be of tensile or compressive nature accordingly they can affect overall magnitude and behavior of residual stress profile in a welded structure (Payares-Asprino et al., 2008). These retained stresses are critical

for the life-assessment of weldments. The mitigation of tensile residual stress and even changing its behavior to compressive enhances the scope of the present research to include the effect of metallurgical aspects. The experimental measurement of metastable phase transformation effect is restricted due to complexity of the process. Hence, the major thrust in the current work is vested to develop thermal-metallurgical-mechanical (TMM) model for reliable prediction of residual stress profile in a laser-welded structure. The present work emphasizes on micro scale or Type II residual stress that includes stress generation due to the formation of daughter phase, microstructural evolution, variation in inter and intra-granular features. Various materials act differently with the application of heat in terms of volumetric dilation and microscopic changes in the weld zone and heat affected zone (HAZ) due to the variation in thermo-physical and thermo-mechanical properties. This volumetric dilation exhibits solid state phase transformation that plays significant role in the alteration of residual stress distribution. Therefore, in order to determine robustness of the developed model, metals belong to three different alloy system i.e., Ti6Al4V ($\alpha + \beta$)-alloy, SS 304 (austenitic stainless steel) and P91 (ferritic-martensitic steel) are taken into account for the current research, which probably a suitable choice to study thermal, metallurgical and mechanical interaction featured through experimental and computational frameworks.

Conventional welding techniques involve large heat input and produces relatively wider weld bead that adversely affects the joints quality. Regulated heat input controls the metallurgical and microstructural inhomogeneity in welded structures that helps to improve the mechanical performance of the weldments. In order to minimize heat input, fusion zone and HAZ, highly localized intense heat source, laser-welding technique is found to be promising substitute to conventional processes. Besides, the pulse mode laser welding keeps more option to regulate heat input in a small-scale welding process and capable to weld highly heat-sensitive components with the modulation of pulse. Application of high pulse frequency increases the weld depth-to-width ratio and minimizes HAZ, which leads to the reduction in residual stress magnitude by virtue of localization of energy input (Tseng and Chou, 2002). Therefore, the preliminary focus is vested on to thin sheet welding of Ti-alloy and SS304 steel alloy using both pulse and continuous mode laser welding processes.

1.2 The problem statement

Lightweight characteristics and excellent strength of dual phase Ti-alloy attracts the fabrication of the intricate components for aerospace applications. Dual phase alloy renders good combination of mechanical properties, which can be accomplished by thermo-mechanical processing and heat treatment processes (Geetha et al., 2001; Semiatin and Bieler, 2001). Nevertheless, Ti6Al4V alloy attributes lower ductility and reduced strain-hardening effect as compared to steel in post-weld condition. Several advanced welding techniques are employed in order to produce successful weld of Ti6Al4V alloy. Due to high chemical activity at elevated temperature, this alloy easily absorbs gases such as oxygen, hydrogen and nitrogen, which severely deteriorates its mechanical performance. Therefore, special attention towards the proper shielding has taken into account in order to get defect free weld. Surface discoloration technique has implemented to determine the oxidation level or degree of contamination. Topographical analysis of the weld surface is performed under various process conditions for the assessment of surface appearance. Even the microstructural morphologies are highly sensitive towards the cooling rate for Ti6Al4V alloy (Ahmed and Rack, 1998). The interaction of microstructural morphologies with weld joint performance in terms of residual stress distribution is significant which is assessed with the aid of a FE based TMM model.

Austenitic stainless steel (SS304) is primarily known for its strength at elevated temperature, cost-effectiveness, fracture toughness at low temperature and corrosion-resistant properties. However, considerably high thermal expansion coefficient and low specific heat capacity facilitate higher distortion, shrinkage and residual stress generation in a welded structure (Lin and Chou, 1995). The distribution and amount of δ-ferrite at weld metal controls the properties and on-site behavior relating to thermal stability, mechanical characteristics and residual stress generation (Balmforth and Lippold, 2000; Fukumoto et al., 2008). The variation in properties among austenite and ferrite phase may affects the stress distribution at grain scale. Nevertheless, the lattice constant, which depends on interstitial atom content, plays a vital role in interpretation of Type II residual stress in austenite matrix (Hummelshøj et al., 2010). Enriched δ-ferrite content and its grain size promotes the tensile residual stresses (Unnikrishnan et al., 2014). The variation in thermal expansion coefficient in δ-ferrite and γ-austenite attributes compressive strain in ferrite core for ferrite-austenite alloy (Harjo et al., 1998). Thus, the residual

stress in austenitic steel is highly complicated where the participation of solidification behaviour and morphology are predominant. The mitigation of residual stress by controlling microstructural morphologies can elude the failures of a welded joint. Therefore, the present work attempts to understand the solidification behavior of weld metal as well as its correlation with δ-ferrite formation and residual stress distribution.

In contrast, 9Cr-1%Mo steel (P91) belongs to the family of steel, which is extensively used in thermal power plants and steam generators of fast breeder reactors that usually operates at high temperature (i.e. 873 K), because of its appreciable mechanical properties and enhanced oxidation resistant ability at elevated temperature (Klueh, 2005). These steels exhibit superior thermal conductivity and lower thermal expansion rather than austenitic stainless steels. Nevertheless, premature failure is the major drawback of P91 steel weldment which limits its utility (Das et al., 2008). Type IV cracking is the main culprit that promotes high rate of void formation in inter-critical HAZ of welded structure (Kundu et al., 2013). Additionally, welding of P91 steel structure using conventional technique significantly induces residual stress at type IV region. Moat et al. (2011) used filler wires of ferrite alloy having alloy compositions 12% Ni, 0.5% Mn and 0.65% Si, with martensitic start temperature of 250 °C that evolved compressive residual stress in weld metal. Weld consumable with enriched austenitic stabilizing elements improves the quality of weld joint by reducing tensile residual stress because of low transformation temperature (Payares-Asprino et al., 2008). Austenitic stabilizing elements present in weld metal strongly influence the transformation kinetics and the transformation induced strain (Mašek et al., 2010). Lowering of martensitic transformation temperatures put the weld surface in compression state cause compressive residual stress evolution in the welded joint (Payares-Asprino et al., 2008). Adaptation in weld chemistry by playing with alloying compositions may help to overcome the issue of residual stress. Therefore, the residual stress development in thick 9Cr weld metals fabricated using shielded metal arc welding process are critically examined and the influence of weld metal compositions on residual stress evolution is extensively explored.

Adequate knowledge of the evolved time-temperature field at fusion zone and HAZ is a prerequisite for the determination of weld bead geometry, phase fraction, residual stress and distortion. However, due to simultaneous occurrence of various phenomena at extremely high

temperature, the experimentation is not only complex, even time consuming, expensive and needs dedicated set-up. Finite element based tool provides an effective route to model the thermal behavior, metallurgical variation and mechanical response of the welded structure. Mathematical model also provides a better understanding and realistic representations of physical phenomenon involves during welding process. Therefore, the thermo-metallurgical models are developed for the incorporation of diffusional and non-diffusional solid-state phase transformation kinetics to aid the precise estimation of residual stress distribution for different types of materials. In the general frame of FE based commercial software, the metallurgical model is incorporated through user subroutines in a thermo-mechanical model. The model results are also validated with the experimental value to establish the FE model for parametric analysis.

1.3 Research objectives and scope of the thesis

The primary objective of the current research work is to develop computational methodologies to predict laser welding induced residual stress including the effect of solid-state phase transformation. To achieve the same, the experimental investigation is performed to create a reliable database of weld dimensions, residual stress distribution, and microstructural morphologies for Ti6Al4V, austenitic stainless steel (SS304) and ferritic-martensitic steel (9Cr-Mo). To fulfill research objectives and proposed scope, following modules are carried out either parallel or sequentially over the entire span of research work.

- The rate of temperature change generated due to localized heating and cooling governs the metallurgical-mechanical performance of weldments. The critical assessment of thermal, metallurgical and mechanical characteristics of thin laser-welded Ti-alloy using both pulse and continuous mode of operation is the primary objective.

- Development of 3D sequential coupled thermal-metallurgical-mechanical (TMM) model using finite element method for accurate prediction of residual stress and distortion in a butt-welded structure.

- To examine the role of diffusional or diffusionless transformation on residual stress distribution for all three different alloy systems by developing appropriate transformation kinetics as a function of temperature and rate of change of temperature.

- To investigate the mode of laser welding on microstructural morphology of Ti-alloy.

- To understand the interaction of microstructural morphology with residual stress distribution and resulting mechanical properties in all three different alloy systems. The intuitive objective is to find a way to promote compressive residual stress in a welded structure.

- To investigate the influence of weld metal composition on residual stress evolution in fusion welded 9Cr steels through experimentation and finite element based computational model.

In the context of research objectives, scope of present work are summarized as:

The primary objective of the present work is to address several issues related to experimental investigation of various fusion-welding processes (laser beam welding, shielded metal arc welding and electron beam welding) to bring out an envelope of suitable combination of process variables needed to produce successful weld. There is a scope to analyze the effect of process variables on the quality and mechanical performance of the joint to bring out the optimum set of parameters. In lieu of that, thin sheet welding of Ti6Al4V and austenitic stainless steel, and thick plate welding of ferritic-martensitic steel is attempted here. There is a scope for the development of FE based heat transfer model. The Fourier heat conduction model with an appropriate selection of volumetric heat source is enough to obtain temperature distribution in both continuous and pulse mode of laser welding. The sole objective of the present work is to predict accurate residual stress field by incorporating solid-state phase transformation kinetics. Therefore, there is a scope for the development of phase transformation kinetics model with the help of microstructural morphology where solid-state phase transformation produce significant transformation strain in case of Ti-alloy and ferritic-martensitic steel. The transformation strain for austenitic steel is not that much significant like Ti-alloy or ferritic-martensitic steel, however, still it affect the residual stress distribution to some extent. A sequentially coupled thermal-metallurgical-mechanical model is very much needed to investigate the influence of

microstructural morphology and the impact on residual stress distribution. There is a scope to find the way of mitigation of residual stress from the analysis. It is indeed important to investigate the interaction of microstructural morphology with residual stress distribution. Therefore, the characterization of welded microstructures and mechanical properties are very much needed to furnish fundamental insight into the kinetics. The interaction between the pattern of thermal history and the metallurgical finding has to be critically assessed with the aid of FE based model. Moreover, the dependency of mechanical properties on the microstructural morphology is aimed to explore extensively. It is evident that the micro strain induced due to solid-state phase transformation and heterogeneous microstructure morphologies contributes to residual stress alteration. Therefore, the changing the mode from continuous to pulse can also trigger the residual stress pattern by modifying the solidification kinetics and solid state phase transformation for Ti6Al4V and SS304 weld. An attempt is to be made to carry out the necessary experiments and numerical simulation to explore the importance of kinetics and to establish the relation with microstructure formation. It is necessary to optimize weld metal chemistry for the improved reliability of engineering components by considering the strong influence of austenitic stabilizers. Hence, one of the objectives of the current work is to understand their influence on martensitic transformation temperature of weld metal and its impact on residual stress distribution in the 9Cr-Mo weld joints. Nevertheless, it is of significant interest to develop the thermo-metallurgical-mechanical model by incorporating the effect of austenitic stabilizers and to validate the predicted residual stress pattern with the experimental value.

1.4 Motivation for research

With growing interest of aforementioned alloys for the crucial components of aero engine, airframe, gas turbine (Boeing 777), low-pressure compressor in aerospace industry and, high temperature boiler and turbine of ultra-supercritical power plant, motivated the current research to investigate the thermal, metallurgical and mechanical interaction featured through experimental and computational frameworks. A bit of thermo-mechanical modelling techniques is established by the University of Nottingham to model industrial welding processes for a range of activities comprising welding simulation, residual stress and associated distortion distribution over the thin and thick welded components fabricated from steel alloy (Yaghi et al., (2005),

Yaghi et al., (2007)) and nickel-based superalloy (Bennett et al., (2007), Rauer et al., (2014)) for power plant and aero-engine application. It is realized that the development of process window for the investigated materials is significant for practical application, which requires a lot of trials. There is a lack of establishment for proper TMM model by incorporating solid-state phase transformation effect. In this aspect, the validation of the FE model with experimentally measured residual stress is also significant. The interaction of microstructural morphology with welding induced residual stress helps to incorporate the metallurgical aspect in the TMM modelling approach. This opens up the possibility of controlling the nature and magnitude of residual stress with proper design of welding process parameters. Even, interplay of weld composition and residual stress distribution is also a promising direction to find the way of modifying the residual stress behavior for 9Cr-Mo steel weldments. It is also realized that integration of the transformation kinetics not only improves in-depth understanding of residual stress generation but also enhance the reliability of the modeling calculations.

1.5 Significance of study and hypothesis statement

In the current research work, the major thrust is given to the development of computational methodologies to predict laser welding induced residual stress including the effect of solid-state phase transformation. Investigation of residual stress in a welded joint is vital from the perspective of component fabrication and working life of a weldment. A clear understanding and accurate measurement of residual stress and associated distortions are critical for the performance of intricate components so that service failure can be hindered. Hence, the development of reliable model for the prediction of residual stress by incorporating phase change as well as microstructural morphology would be beneficial to the system designer. With this objective, a TMM model is developed to predict residual stress by considering metallurgical effect. The model results are also validated with experimental results. Nevertheless, the accuracy of the model can be improved by incorporating other induced strains due to heterogenous microstructural morphologies and transformation induced plasticity.

Therefore, it is obvious that if accurate predictive models which accounts majority of interactive physical phenomena that come into existence in the course of welding process such as thermal, mechanical as well as metallurgical aspects, are established and endorsed by the aero

engine, aerospace industries and ultra-supercritical power plant, then trial-error based approaches can be avoided which may allow for improved material performance whilst minimizing production costs. The proposed investigation which is an amalgamation of experimental and computational frameworks, can also provide a better understanding and comprehensive knowledge about methodologies of thermo-metallurgical-mechanical behavior and their role in the holistic process of the life assessment and design improvement of engineered components being worked on in the academic and several other industrial sector.

1.6 Layout of report

The thesis comprises of six chapters to outline all the prospects aimed at research objectives. A brief introduction to the subject and the overall layout of the report is presented in C**hapter 1**.

Chapter 2 includes the comprehensive literature survey on existing work which is focused on laser welding of thin structure, difficulty in experimental measurements, the interaction of laser with different materials, effect of pulse and continuous mode in welding, factors affecting phase transformation and effect of solid-state phase transformation on microstructural morphology as well as mechanical properties in the context of welding induced residual stress. Further, an extensive part of chapter is devoted to review of finite element based numerical model and issues related to the implementation of the model.

Chapter 3 presents the detailed experimental methodologies in order to create a reliable database for the validation of the simulated results using TMM model. For the fulfillment of present aim, various measurement techniques such as optical microscopy, field emission scanning electron microscopy (FESEM), surface profilometry, dilatometry, energy dispersive analysis (EDS), X-ray diffractometer (XRD), transmission electron microscopy (TEM), optical emission spectroscopy (OES) are utilized for the characterization of the samples. X-ray diffractometric analysis is carried out to measure residual stress distribution for Ti-alloy, stainless steel and 9Cr-Mo welded samples. High resolution-based scanning electron microscopy is utilized for better understanding of microstructural morphology at the weld zone and HAZ.

Overall, the mechanism for the interaction of microstructural morphology with residual stress is investigated with the aid of different experimental measurements.

Chapter 4 is extensively present the theoretical formulation of TMM model based on FE method. The thermal model is developed by using appropriate volumetric heat source model. The metallurgical model is established using constitutive relation guided by temperature flag where solid-state phase transformation is accounted by separate strain component. Finally, the mechanical analysis is performed in incremental mode using temperature distribution as an input.

Chapter 5 provide a detailed analysis pertaining to thermal-metallurgical-mechanical characterization of continuous and pulse laser welded thin sheet Ti6Al4V and stainless steel alloy, and SMA welded 9Cr-Mo steel alloy. Primarily, the first section is comprised of three sub-sections among which the initial sub-section is fully devoted to the development of sequentially coupled TMM model for pulse laser welding condition. Different phases at weld metal are qualitatively estimated as a function of transient temperature change. The influence of non-isothermal diffusional transformation and non-diffusional transformation on residual stress and deformation profile is also studied. In the second sub-section, the significance of the pulse parameter over continuous mode in Yb-fiber laser welding of 800 μm thin Ti6Al4V alloy is investigated. It also includes the fundamental insight into the simultaneous interaction of thermal-metallurgical-mechanical characterization at both pulse and continuous mode of operation through cooling rate calculation and targeted experimental analysis. Additionally, the integration between temperature field and the metallurgical phenomena is decisively evaluated. The dependency of mechanical properties on the geometrical dimension of acicular α'-phase is briefly explained through FESEM analysis. The third sub-section includes the study associated with the amendment of the residual stress distribution by employing the effect of solid-state phase transformation for Ti6Al4V alloy through pulsation effect. The second section outlines the understating of the microstructural interaction with the thermo-mechanical performance of Yb-Fiber laser-welded austenitic stainless steel (SS304) at different heat inputs and varying defocus distances. The implication of dual-phase microstructure and morphology distribution on the residual stress generation mechanism is critically accessed. Further, the FE-based, sequentially coupled TMM model is developed to predict the instantaneous phase fractions of constituent phases and corresponding residual stress distributions. The third section describes the detailed

analysis of residual stress development in 9Cr steel welded joints as a function of weld metal composition. The experimentally evaluated RS profiles are validated using a computational model established to predict RS evolution in 9Cr steel weldments. The model considers the volumetric dilation effect accompanied with martensitic transformation using state dependent variables (SDVs) approach.

The important conclusions that are drawn from the current studies executed using various experimentations and numerical tools as a part of the thesis work is summarized in the **Chapter 6**. Additionally, the scope of future works in terms of the theme of current research work are also highlighted in this chapter. Lastly, list of references is presented at the end.

Chapter 2

2.0 Literature Survey

2.1 Introduction

In the current chapter, a comprehensive literature review on difficulty in experimental measurements, the interaction of laser with different materials, effect of pulse and continuous power in welding as well as influence of solid-state phase transformation on microstructural development and mechanical properties are carried out from the perspective of the residual stress generation in a welded structure. There is considerable variation of residual stress pattern in line with the choice of welded materials as well as process parameters. The difficulty in experimentation enhances many folds with the reduction in geometric dimension of the materials to be welded. Overall, the residual stress generation is a direct consequence of non-uniform heat transport, material flow within small weld pool, metallurgical transformation during solidification and solid-state phase transformation, and mechanical boundary constraints during heating and cooling stages of welding process. The simultaneous effect of transient thermal cycles, metallurgical changes, and resulting stress field in the fusion welding process makes it difficult to evaluate experimentally. The finite element (FE) based numerical simulation is an effective tool to simulate the thermal and corresponding mechanical behavior. Therefore, the literature review is mainly focused on the interaction of microstructural morphology with residual stress that directs to the development of thermo-mechanical model including the effect of solid-state phase transformation. In another way, the directives to the mitigation of residual stress for different welded structure with different materials are an effective output from the present investigation.

2.2 General background

Residual stress is defined as internally locked stress existing within the structure even after removal of external loads to withstand equilibrium condition. A broad range of residual stress states originates from several manufacturing processes and material processing technologies that may substantially affect the performance and structural integrity of the engineered structure. Thus, it is of specific interest for engineers to pay attention towards its origin, measurement techniques, and assessment and mitigation of the detrimental impact in a welded structure. The fusion welding process is complicated in nature due to simultaneous interaction of thermal, metallurgical and mechanical variation that involves microstructural change due to heating and cooling cycles. The mechanical variation includes changes in mechanical properties due to metallurgical transformation. The application of heat to perform welding causes non-uniform thermal expansion, and uneven rapid contraction in a localized position. The non-linear temperature distribution leads to plastic deformation influenced by solid-state phase transformation. All these variations are responsible for the generation of residual stress in a welded structure. Residual stress induced by shrinkage of the molten region is usually tensile. Transformation induced residual stress occurs at the part of HAZ and FZ decided by the critical value of phase transformation. When phase transformation is predominant, the evolution of compressive residual stresses takes place in the transformed region. Distortion in the weldment results from unbalanced thermally induced stress in non-restrained parts.

Real-time measurement of the transient growth of weld pool is a challenging task and there is uncertainty to accurately measure the residual stress of the weld joint. Alternately, the computational model of increasing complexity based on scientific principle alone is an effective route to analyse the differential influence of process parameters during the fusion welding process. Solid-state phase transformation also plays a vital role in residual stress generation. Hence, it is essential to track microstructural modification in pre- and post-weld conditions. The differential cooling rate and large temperature gradients can effectively inhibit grain growth. The rate of temperature change can influence the rate of dissolution and coarsening of the precipitate, grain growth and effectively influence on grain size and thermal histories. Therefore, literature review mainly aims to understand the prediction accuracy of residual stress and the role of several factors on residual stress generation in a welded structure.

2.3 Laser welding technology

Foremost, Theodore Maimann developed first laser machine in 1960. Since, commercial laser is firstly launched in the mid of 1970s, revolutionary advancements in laser welding technology have facilitated latest and innovative joining application (Cao et al., 2006). In the early stage, it was applied for heavy or exotic application and welding of thick material due to its high energy beam density. However, advancement in technology made it possible to control laser beam and hence, broadened its domain to micro-joining industries as well. Thereafter, a variety of laser systems are developed for micro-joining applications in electrical & electronics-based components, fabrication of internal vacuum tubes and biomedical implants and, for other special devices where conventional techniques are not successfully applied. In the early 1990s, pulsed Nd:YAG laser system arrived and, furnished means of welding thin and reflective metal such as aluminium and copper (Watkins K. G., 2003). Capability to generate high power density and modulation of pulses are the prime factors to enable its application for welding. Enhancement of its capacity up to multi-Kilowatt ensured its entrance into high production-based welding and cutting industries in the late 1990s (Haferkamp et al., 1997). And now laser welding system equipped with different laser source is a full-grown part of metal working industry for commercial and industrial use.

Laser welding is non-contact and high energy beam process where the incident laser beam subjected on metal surface to attain temperature beyond its melting point for the generation of weld pool and, permitted it to flow through the interface of weldment that has to be welded. Although it is easier to regulate the continuous based laser welding technique due to involvement of less number of input variables, it is disadvantageous for the processing of thin material. Pulse assisted laser welding approach is well suited for a micro joining application because of controlled heat input and capability to weld highly heat-sensitive components (Blackburn, 2012). Pulse welding is expressed as a sequence of overlapping spot welds for the formation of weld zone. It is noteworthy that pulsed Nd:YAG laser can provide enriched depth of penetration than continuous mode for the same average power (Gao et al., 2013). It involves impingement of energy to the localized area comes not only from single pulse but also from overlapped pulse on same beam spot. The pulse modulation is characterized by high peak power that could be 10-50

times larger than the average power of beam, allows remelting and solidification of weld pool within fraction of second.

For the same average power, pulsed Nd:YAG lasers provide much higher penetration levels than continuous Nd:YAG laser. Pulsed systems are modulated to output a series of pulses with an off time and between those pulses. Theses lasers also have the ability of pulse shaping at pulse repetition rates of up to several kHz and with the durations varying from 0.5 to 20 ms (Tzeng, Y. F., 2000). This flexibility gives control of thermal input with a precision not previously available. It also allows the controls of penetration, melt pool shape and size, the onset of boiling, and keyhole formation (Sabbaghzadeh et al., 2008). Pulse laser welding is characterized by high peak powers that may be 10-50 times larger than average power of beam, allowing melting and solidification to take place in fraction of second (Zhou and Tsai, 2007). The pulsed process is differentiated from continuous wave laser welding by both its high peaks and by the types of fusion zone that are created. With increase in pulse duration, the peak load is also increased, which may involve increasing the melted area. In order to control the pulsed laser welding process, the average laser power, peak laser power, laser pulse duration, pulse repetition rate, beam diameter and travel speed must be optimized for desired shape of weld (Blackburn, 2012). Therefore, selection of welding process is critical that can change the thermal, temperature assisted microstructural and mechanical attributes of welded structure to acquire desired engineering properties and improve service life of welded structure. In order to minimize heat input and generate highly localized intense heat source, laser-based welding technique is promising approach as a substitute to conventional arc welding process, hence adopted herein.

2.4 Welding induced residual stress and distortion

Residual stresses in a body are those that are not essential to maintain equilibrium between the body and the surrounding (Withers and Bhadeshia, 2001). Non-uniform heating and cooling (ordinary quenching), structural deformation from metal working (heat treatment), heterogeneity of a chemical crystallographic order (case hardening), various surface treatments (coating) are responsible for the generation of residual stresses in a welded structures. It can be considerably detrimental to the performance of the components. Alternatively, beneficial effect of residual stress can be introduced by shot peening and toughening of glass to improve

mechanical properties or fatigue life. However, under the influence of the alloying composition in the weld zone, HAZ and base metal, the cooling rate mainly decides the different residual stress pattern (Pilipenko, 2001). Even, the selective positions with reference to the heat source location on the weldment bring the variation in residual stress and distortion (Fig. 2.1). Consider different sequence of Fig. 2.1 where welding is carried out along the X-axis, and the heat source is located somewhere in the weld line (point O). Presence of a molten pool at cross-section B-B ensures almost zero stress adjacent to the heat source. The non-uniform temperature distribution produced during welding gives rise to incompatible strains, resulting in the generation of self-equilibrating residual stresses and their distribution, which remain in the structure even after cooling down to ambient temperature. The evolved residual stress in the welding direction is usually tensile in nature, while balancing compressive residual stress is developed adjacent to the weld region upon cooling, as indicated at cross-section C-C. Eventually, along section D-D, the molten metal and the nearby region have contracted more upon cooling, therefore produces high tensile residual stresses near the weld line and compressive stress at a further location.

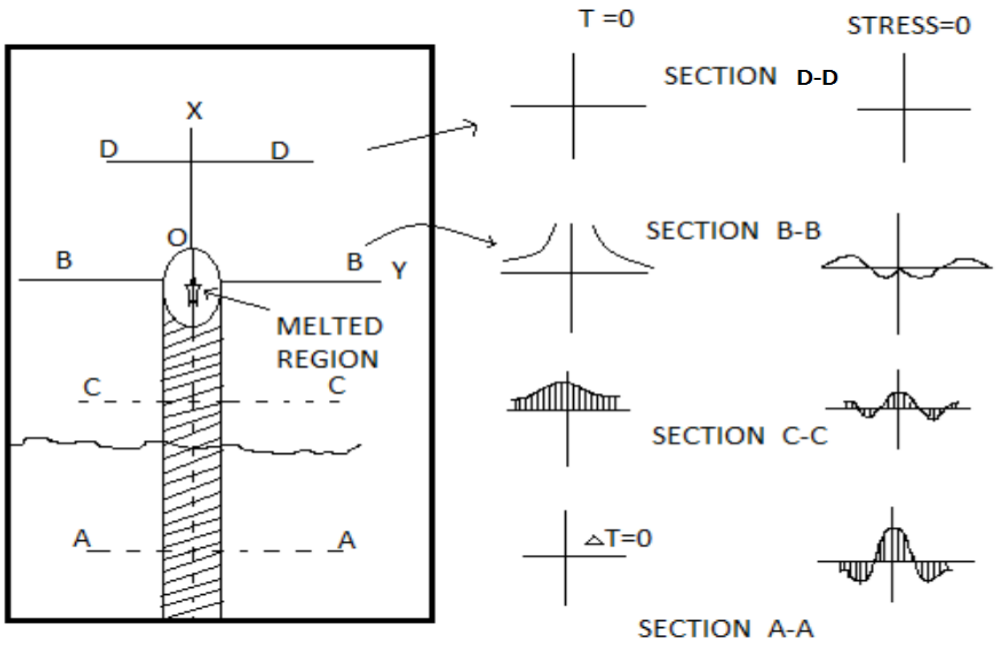

Fig. 2.1 Schematic representation of variation of stress and temperature during welding (Sluzalec, 2005)

Metal in the weld zone expands due to localized heating during the welding process, resulting in a sharp thermal gradient and heterogeneous thermal expansion in a molten zone. Nevertheless, the nearby cold zone, i.e., the base metal region, inhibits thermal expansion, which leads to the generation of thermal stresses. Since yield strength is a function of temperature and decreases at elevated temperature, when thermal stress surpasses yield value, inhomogeneous plastic deformation takes place. As a result of heating and subsequent cooling, tensile residual stresses come into existence in the weld zone. In contrast, compressive stress arises at nearby region in order to satisfy structural equilibrium condition. On the contrary, if volumetric expansion accompanied by solid-state phase transformation is prevalent at weld region, compressive residual stress forms in weld region and tensile stress state exists in the adjacent area (Radaj, 2012). If the weldment is in constrained condition, the transverse residual stresses are generated in the plane of a welded plate in accordance with the transverse contraction mechanism. Furthermore, the compressive state of stress develops near the edge to compensate the tensile stress that emerges in the center of the weld zone (Hansen, 2003). The schematic description of the longitudinal and transverse component of residual stresses over the substrate material is illustrated in Fig. 2.2.

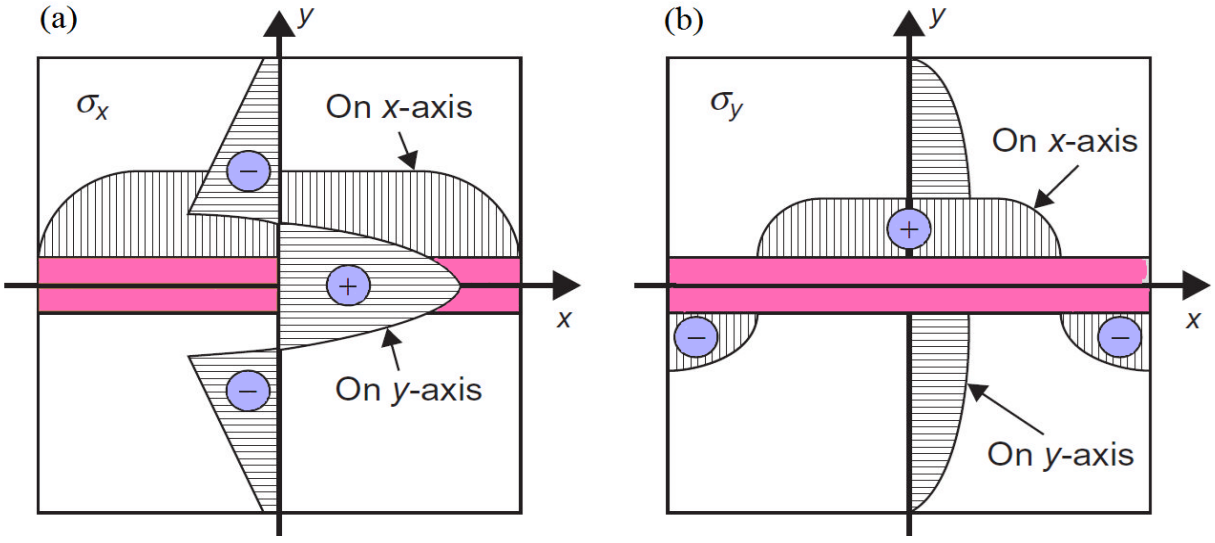

Fig. 2.2 Representation of paradigm of (a) longitudinal, (b) transverse residual stress distribution (Ueda et al., 2012)

The path followed by the weldments for stress generation in the fusion welding process is displayed in Fig. 2.3. Initially, heat input interacts with weld surface, due to which thermal agitation occurs in the localized area, and subsequently, the temperature rises beyond its melting point. As the heat source moves ahead, the trailing part experiences cooling cycle and exhibits solid-state phase transformation (SSPT) accompanied with volumetric dilation. After reaching room temperature, heterogeneous microstructural evolution occurs in the weld zone and nearby region, which induces microstrain in the weld region. This microstrain contributes to the alteration in the residual stress pattern.

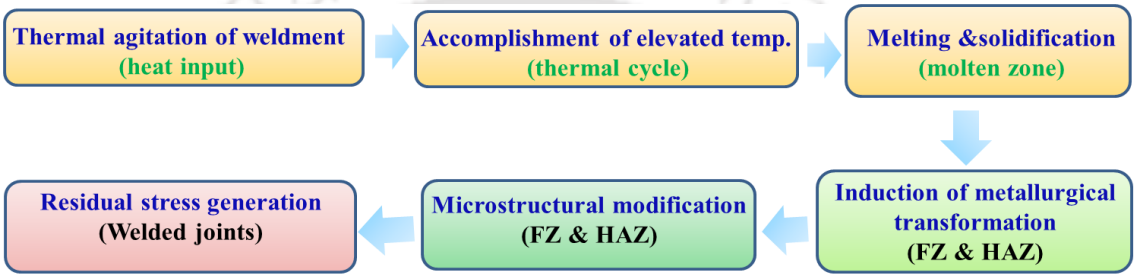

Fig. 2.3 Flowchart of residual stress generation process

Residual stress may be categorized by cause, by the scale over which they self-equilibrate, or according to the method by which they are measured. Based on the length scale approach, residual stresses are categorized into three groups, i.e., Type I, Type II and Type III. Type I is known as macro residual stress that develops in the body of component on a larger than the grain size of a material, as shown in Fig. 2.4. Generally, a thermally or mechanically induced residual stress comes under this category. Type II residual stress involves micro-stresses that vary on the scale of individual grain. It arises due to the variation in elastic and thermal properties of differently oriented neighboring grains (Withers and Bhadeshia, 2001; Withers and Bhadeshia, 2001). Moreover, Type III residual stresses involve micro-stresses within a grain, essentially due to the presence of dislocations and other crystalline defects.

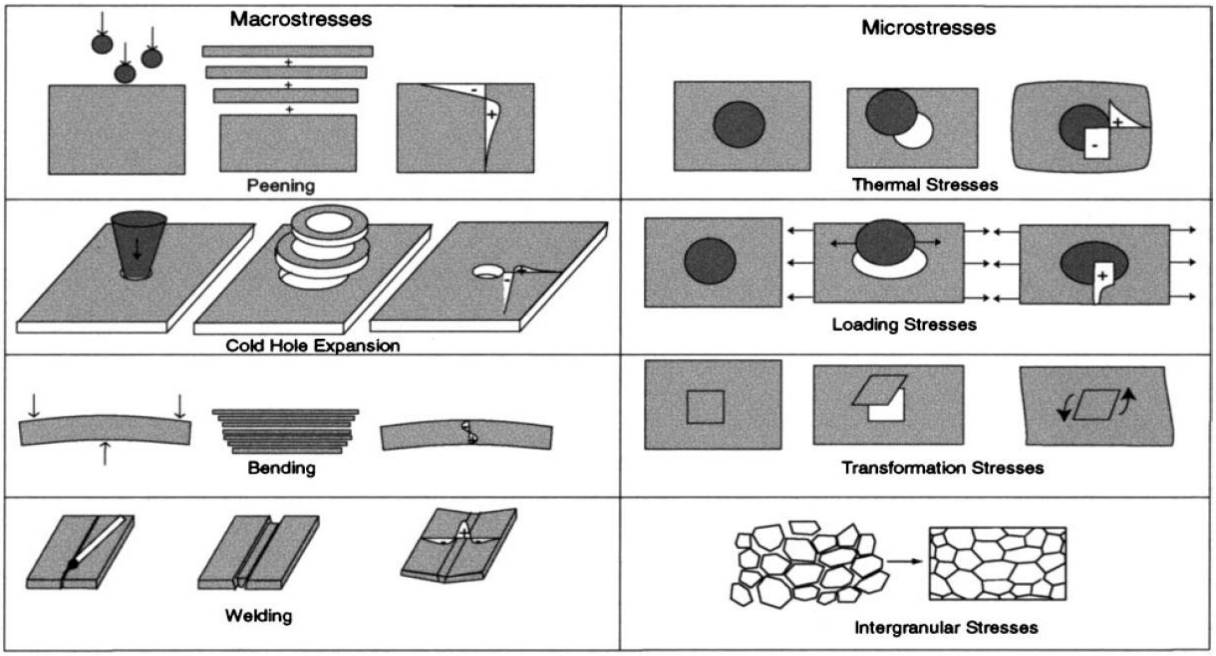

Fig. 2.4 Different types of macro- and micro- stress (Withers and Bhadeshia, 2001)

Welding induced residual stresses and distortions are always interrelated with each other (Li and Shi, 2011). Both are the two facets results from non-uniform transient strain caused by welding. When the value of residual stress exceeds the elastic limit of metal leads to permanent deformation, and post-elastic deformation is accommodated in the form of distortion (Deng et al., 2002; Radaj, 2003). Because of solidification shrinkage and thermal contraction of the weld metal, the substrate tends to deform. The change in dimensions and shape of the weldments resulting from the interaction of solidifying molten metal with the parent metal of the same structure is referred to as distortion. Welding induced distortion may severely impair the fabrication and pertinence of the manufactured components. It primarily imparts adverse effects on the physical appearance, fabrication accuracies and strength properties of the welded structure; hence, studies associated with its accurate measurements and remedies are of significant interest in the present work.

2.4.1 Measurement methods

Techniques to measure residual stresses may be classified as either destructive or semi destructive or non-destructive (Ivetic et al., 2009). The destructive and semi-destructive

measurement methods are also known as mechanical methods. It involves approximating the original stress from the displacement incurred by fully or partially relieved stress by peeled off the material. The destructive technique includes slitting method, contouring method, sach's boring. In contrast, semi-destructive encompasses deep hole-drilling, central-hole drilling, ring core method, while non-destructive method comprises X-ray diffraction, neutron diffraction, synchrotron X-ray, ultrasonic and magnetic method.

The hole-drilling method is a relatively simple and most popularly used semi-destructive residual stress evaluation technique that can provide stress distribution across the thickness. In principle, a small hole is progressively formed (of about 1.8 mm dia and up to 2.0 mm deep) at the location where residual stresses are to be measured. Due to hole drilling, the locked-up residual stresses are relieved. The corresponding strains on the surface are measured using suitable strain gauges bonded around the hole on the surface (Olabi and Hashmi, 1996). The ring-core method is an "inside-out" variant of the hole-drilling method (Keil, 1992). This method involves measuring the deformation in a central area caused by cutting an annular slot in the surrounding material. The deep-hole method (DeWald and Hill, 2003) is a further variant, comprises of both, i.e., the hole-drilling and ring-core methods. In this technique, a hole is first drilled throughout the thickness. Subsequently, the hole diameter is measured, and then a core of material around the hole is trepanned out to release the retained stresses in the core. The diameter of the hole is re-measured, allowing finally, the residual stresses to be calculated from the change in diameter of the hole. Zhadanov and Gonchar (Zhdanov et al., 1978) used the deep-hole method to measure residual stresses in steel welds. Sectioning technique is another destructive method that also relies on the release of residual stress upon removal of material from the specimen (Tebedge et al., 1973). The sectioning method consists of making a cut on an instrumented plate in order to release the retained stresses present on the cutting line. In this method, the cutting process should not introduce plastic deformation or heat so that the original residual stress can be measured without the influence of plasticity effects on the cutting planes. The contour method, firstly proposed in 2000, is a newly established method that enables mapping of 2D residual stress on a plane of interest (Cowley, 1992). Moreover, the splitting and curvature method is alternatively used to access the residual stress in a thin-walled tube.

On the other hand, the non-destructive method usually measures some parameters that are associated with the stress component. The X-ray diffraction (XRD) technique is a non-destructive surface residual stress measurement method (Noyan and Cohen, 2013). This method is applicable for crystalline, relatively fine-grained materials and produces diffraction for any orientation of the sample surface. Since metals are composed of atoms arranged in a regular three-dimensional array to form a crystal, XRD method can directly measure atomic inter-planar spacing. The diffraction methods follow the principle of changing interplanar spacing from their stress-free value. Thereafter, the strain could be calculated using Bragg's law, where it is essential to have an accurate measurement of stress-free interplanar spacing. Change in interplanar spacing is used in Bragg's equation to detect elastic strain ε through knowledge of the incident wavelength λ and the change in the Bragg scattering angle Δθ. Using the diffraction principle, it is only possible to determine the lattice strain for a given (hkl) plane spacing in the direction of the bisector of the incident and diffracted beam. For the calculation of stress (or strain) tensor at a sampling gauge location, independent measurements of strain in different directions, i.e., $\varepsilon\{\phi,\psi\}$ are estimated as

$$\varepsilon\{\phi,\psi\} = \varepsilon_{11}\cos^2\phi\sin^2\psi + \varepsilon_{12}\sin^2\phi\sin^2\psi + \varepsilon_{22}\sin^2\phi\sin^2\psi + \varepsilon_{33}\cos^2\psi + \varepsilon_{13}\cos\phi\sin2\psi + \varepsilon_{23}\sin\phi\sin2\psi \quad (2.1)$$

$$\sigma_{ij} = C_{ijkl}\varepsilon_{kl} = \frac{E_{hkl}}{1+\nu_{hkl}}\left(\varepsilon_{ij} + \frac{\nu_{hkl}}{1-2\nu_{hkl}}\varepsilon_{kk}\delta_{ij}\right) \quad (2.2)$$

where C is the stiffness tensor and ψ, ϕ are the polar angles to the tensor coordinate system. E_{hkl} and ν_{hkl} represents elastic modulus and poisson's ratio in direction of hkl, respectively. δ_{ij}, ε_{kk} and σ_{ij} denotes Kronecker delta, strain and stress component. In many cases, the principal stress directions can be deduced by symmetry arguments, and thus only three strain values are required to calculate the principal stresses. The principal stress is expressed as

$$\sigma_{11} = \frac{E_{hkl}}{(1-\nu_{hkl})(1-2\nu_{hkl})} \times [(1-\nu_{hkl})\varepsilon_{11} + \nu_{hkl}(\varepsilon_{22}+\varepsilon_{33}) \quad (2.3)$$

In certain cases, to determine an in-plane bi-axial plane stress ($\sigma_{11} = \sigma_{22}, \sigma_{33} = 0$) only the in-plane strain ε_{11}or the out-of-plane strain ε_{33} is required where

$$\sigma_{11} = \frac{E_{hkl}\,\varepsilon_{11}}{(1-\nu_{hkl})} \text{ or } -\frac{E_{hkl}\,\varepsilon_{33}}{(2\nu_{hkl})} \quad (2.4)$$

Electron diffraction measurement follows the same principle for measuring the residual stresses (Norton and Rosenthal, 1944). Very high lateral spatial resolution can be achieved using electron beams that can readily be focused to diameters as small as 10 nm. This method provides a way of measuring the type II and type III stresses generated by misfit strains between α/α' phases in Ti6Al4V alloy. The Neutron diffraction method is considered more advantageous than the XRD technique due to its higher penetration depth. Thus, it can be applied to calculate the internal residual stresses of the substrate. The major limitations of the technique are the complexity, size, and weight of the component, as well as the cost of using a neutron facility. Martinson et al. (Martinson et al., 2009) have implemented the neutron diffraction technique to characterize laser and resistance spot welds to gain an understanding of residual stresses of different joint geometries. One of the promising directions in developing a non-destructive technique for residual stress measurement is the application of ultrasound. It is capable of mapping residual stress of thick components as well (Belahcene and Lu, 1999). Some of the researchers (Uzun and Bilge, 2011) investigated the welding induced residual stress using ultrasonic wave velocity variations. Another non-invasive technique, i.e., Positron annihilation spectroscopy (PAS) has been used to estimate residual stresses and internal defects in austenitic and martensitic stainless steels, which involves the application of high energy, deep penetrating gamma-ray to the thick sections of the welded structure (Asoka-Kumar et al., 1994). Therefore, it is very often to use non-destructive methods since they are free from material demolition, widely applicable and highly reliable technique of residual stress measurements.

Accurate and reliable measurements of distortions are also a challenging task. Bajpei et al. (Bajpei et al., 2017) observed that the unbalanced thermal stress plays a vital role to induce distortion in a non-restrained welded structure. Degree of constraints or clamp is highly influential on welding distortion and an appropriate selection of clamping condition can significantly mitigate this aberration (Desai and Bag, 2014). An interrelation between elastic limit, degree of constraint and spot welding induced residual stress or permanent deformation is established (Desai and Bag, 2014). It is explained that a higher degree of constraints can exhibits relatively more deformed structure. Theoretically, welding distortion is significantly influenced by three major factors (McDill et al., 1990). The initial class is referred to as material related

factor that includes thermo-physical and mechanical properties of the materials. The second group is associated with design-related factor, involves type of joints, dimension of structure, etc. The final class is process related factor that comprises welding technique, weld sequence, degree of constraints, etc. Wang et al. (Wang et al., 2006) described that the metal with higher thermal expansion and low thermal conductivity is susceptible to distortion. A various form of distortion evolved during welding of thin structure is depicted in Fig. 2.5. Longitudinal shortening in the weld direction is referred as longitudinal shrinkage, whereas the contraction that occurs perpendicular to weld direction is transverse shrinkage. On the other hand, angular shrinkage is out of the plane distortion appears due to a non-uniform temperature field throughout the thickness of the structure. Twisting or rotational distortion is also an out of plane distortion caused by thermal expansion or contraction. Besides, buckling is another form of distortion, usually arises by due to compressive stresses.

Kihara and Masubuchi (Kihara and Masubuchi, 1954) and Watahnabe and Satoh (Watanabe and Satoh, 1958) studied the effect of welding process parameters on distortion and obtained relatively high distortion for the weld fabricated at elevated heat input. A thin weldment has tendency to buckle during and after welding due to thermal and residual stresses (Pattee, 1975). If the compressive longitudinal residual stress away from the weld zone exceeds the buckling stress of weldments then buckling occurs (Deo and Michaleris, 2003). By investigating the micro-welded structure of titanium alloy, it is concluded that the final distortion consists of angular distortion and longitudinal contraction due to the difference in the final shrinkage forces at above and below of the neutral axis as shown in Fig. 2.6 (Baruah and Bag, 2016). Masubuchi (Masubuchi, 1953) reported the critical buckling wavelength parameter as a function of plate size and welding state by which buckling type distortion can be evaluated. Practically, the presence of initial gap and misalignment has remarkable effect on distortion (Deng et al., 2007). Welding distortion often occurs in thin structure due to its relatively low stiffness. Therefore, geometrical non-linearity must be considered during modeling of welding deformation in order to produce error-free measurement (Deng and Murakawa, 2008).

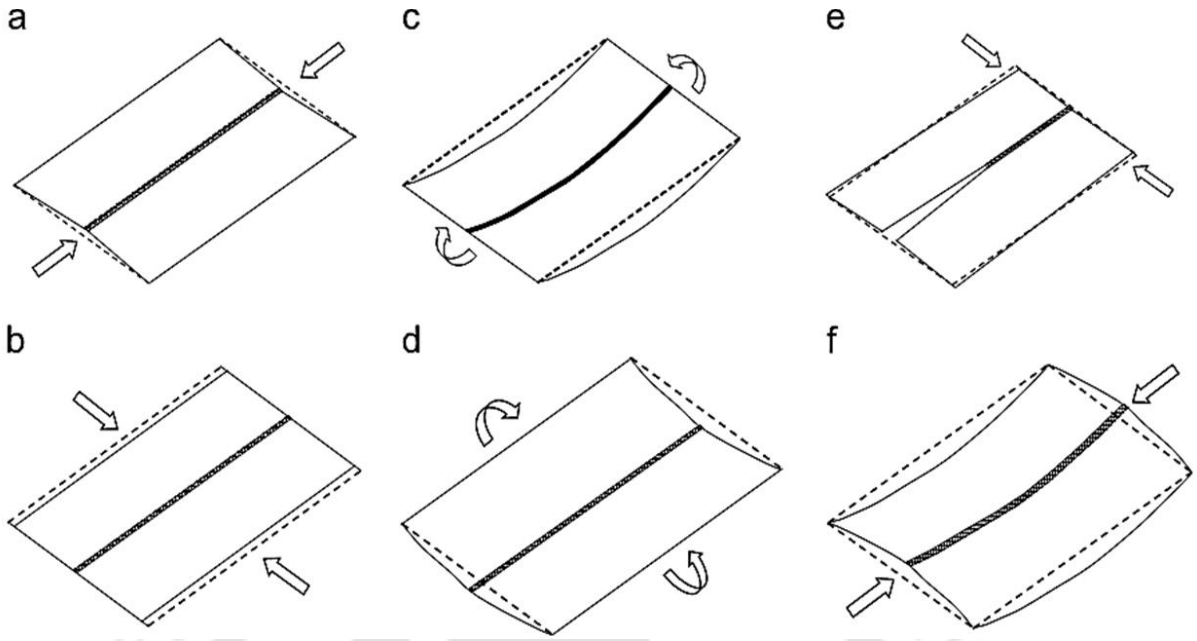

Fig. 2.5 Different types of welding distortion in thin plate butt welded joint (a) longitudinal distortion, (b) transverse distortion, (c) longitudinal bending, (d) transverse bending, (e) rotational deformation and (f) buckling deformation (Wang et al., 2016)

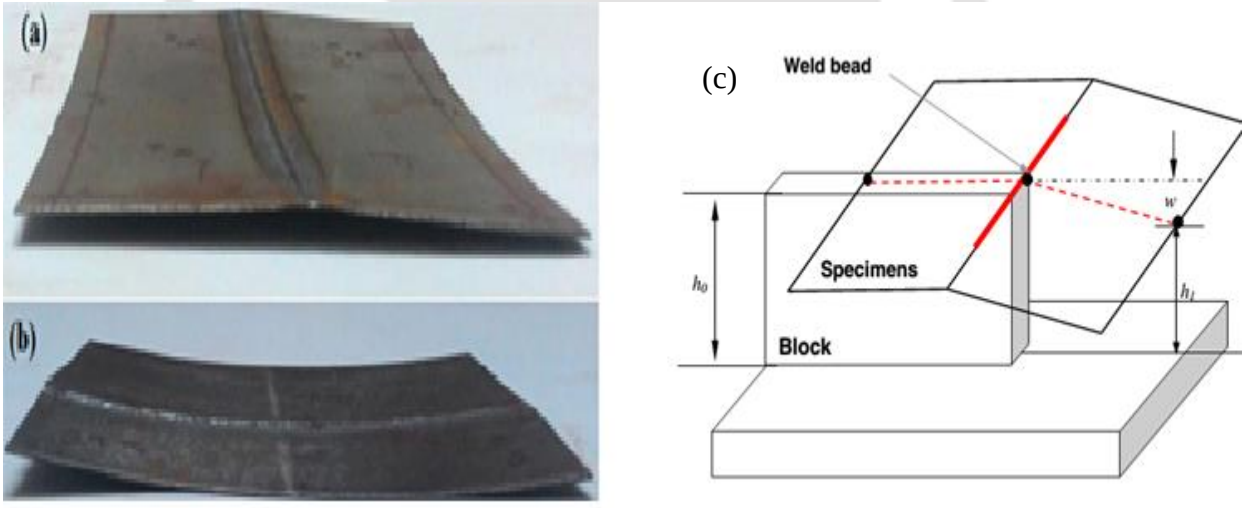

Fig. 2.6 Distortion pattern (a) transverse direction (Baruah and Bag, 2016), (b) longitudnal direction and (c) schematic diagram of distortion of butt welded specimen (Deng and Murakawa, 2008)

It is obvious that the non-destructive residual stress measurement methods have the advantages of specimen preservation. They are particularly helpful for the production quality

control of valuable specimens. Nevertheless, these techniques normally need detailed calibrations on representing substrate material to give required computational data. In fact, the X-ray diffraction technique has limits in measuring residual stresses along the thickness of welded structure. However, it can be employed for thin structural components. There are various methods for the characterization of residual stresses and distortion. Before selecting one method over another, it is important to consider the sampling volume characteristics of the techniques and the types of stresses (I, II, III). Distortion minimization is also a challenging task. The experimental technique is expensive and time consuming for the large and complex structure. Hence, finite element based analysis can reduce the cost and time efficiently.

2.4.2 Mitigation methods

In shipbuilding, railroad, automotive, and aerospace industries, thin plate parts are frequently used. Minimization of welding distortion is most important because it is not only affecting assembling process but also degrading final product quality. Distortion mitigation process is categorized into three groups, i.e., pre-weld mitigation method, in-process weld mitigation technique, and post weld mitigation technique. The pre-weld mitigation technique includes pre-tensioning, pre-deformation process. Whereas, in-process technique involves parallel heating, vibration control, weld sequencing, etc. Post weld technique comprises post weld heat treatment, shot peening method, press straightening, laser shock processing, hammer peening, etc. In some cases, the pre-tensioning technique is applied as an active in-process control method to avoid buckling distortions in the shell along longitudinal welds or in plates with web stiffeners. Before welding, the edges of shells and panels to be welded are tension-loaded by a specially designed installation. As a result, the incompatible plastic strains in the weld zone are reduced effectively (Brown and Song, 1992).

Pre-deformation (counter-deformation) technique for mitigation and avoiding buckling in shell elements was successfully adopted in manufacturing jet engine cases (Ueda et al., 1979). The incompatible plastic strains of the circular weld in different directions are adequately compensated by the pre-deformations, either in the elastic state or in the elastic-plastic state. The residual stresses also need to be controlled to much lower than the critical compressive stress at which buckling occurs. Burak et al. (Burak et al., 1979) suggested the implementing a steady

state thermal tensioning method that involves generating tensile stress in weld line before and after welding, by applying a preset temperature gradient. However, the major drawback of this technique is in using intricate and complicated welded structure. Michaleris et al. (Michaleris et al., 1999) proposed a transient thermal tensioning technique that can be implemented in any intricate shape or long weld. In the case of fabrication of T-joint stiffener, weld bowing or camber distortion is most significant. Terai et al. (Terai et al., 1978), Michaleris et al. (Michaleris and DeBiccari, 1996) concluded that modification of structural configuration and reduction of heat input plays an vital role in decreasing bowing distortion. Guan et al. (Guan, 1994) suggested a productive in-process trailing heat sinking technique to resolve the buckling distortion of the thin section. It involves stretching effects on weld metal on cooling. This method is most predominant for titanium thin plate distortion mitigation (Li et al., 2004).

Chou and Lin (Chou and Lin, 1992) conducted experiments on 304 steel and successfully decreased residual stress and deformation using the parallel heating welding technique. This method involves the moving a parallel heating gun attached to the welding gun on both sides as a movable heat source during welding. Experiments have been carried out on SS304 steel alloy, and it is observed that PHW reduces residual stress and distortion up to 21-32%. Preheating technique can remarkably reduce the angular distortion (Ohata et al., 1999). Residual stress patterns can be modified by material properties of base and weld material (Bru, 1997). Application of consumables with a low-temperature martensitic phase transformation to carbon steel weldments can change the state of stress from tensile to compressive. Pre-strain technique (Jung and Tsai, 2004) plays a significant role in minimizing residual stress and distortion.

Hurrell et al. (Hurrell et al., 2006) revealed that post-weld heat treatment (PWHT) is routinely applied to welds in safety-critical plant. Ideally, the whole body is uniformly exposed under slow heat-up/cool-down rates. Under this technique, at least two stress relief mechanism are possible i.e. plasticity caused by the reduced yield stress at elevated temperature which occurs instantaneously as the temperature increases, and creep mechanisms which occur over a longer period of time. Holzapfel (Holzapfel et al., 1998) took a simple empirical approach based on the Avrami relation to obtain an approximate measure of the stress relaxation at a peened surface.

$$\frac{\sigma^{rs}(T,t)}{\sigma_o^{rs}} = \exp\left(-\left[D\exp\left(-\frac{\Delta H}{KT}\right)t\right]^n\right) \quad (2.5)$$

where $\sigma^{rs}(T,t)$ the residual stress value after annealing at temperature T (in K) for time t (min), σ_o^{rs} the initial residual stress, ΔH is activation enthalpy for actual residual stress relaxation, $n \sim 0.122$, D (1.22×10^{21} min^{-1}) a rate constant and K is Boltzmann constant.

Many researchers have suggested various distortion control method. In summary, the general philosophy was applied such as controlling heat input (Greene, 1946), current pulsation, maximizing constraint during operation, improving fitting practices, reduction of applied weld load (Teng and Lin, 1998), plasticity distortion analysis (Colegrove et al., 2009), weld sequencing (Teng and Lin, 1998), combining vibration with welding method (Munsi et al., 2001) to get rid of this detrimental factor.

2.5 Experimental investigation

2.5.1 Welding of Titanium alloy

Due to miniaturization of fabricated components, the techniques for welding of thin sheets of Ti6Al4V alloy are highly commendable. Ti6Al4V alloy is comprised of Al (~ 6 wt. %) as α-stabilizer and V (~ 4 wt. %) as β-stabilizer, and is considered as dual-phase (α + β) alloy. Reversible transformation of crystal structure from hexagonal close-packed (HCP) to body-centered cubic (BCC) during heating is an essential attribute possessed by (α + β) alloy. Ti-alloy, particularly Ti6Al4V attributes lower ductility, lower strain-hardening effect and minimum anisotropy behavior as compared to steel. Several advanced welding process has been performed successfully for joining of Ti-alloy. The fusion welding such as Gas tungsten arc welding (GTAW) (Short, 2009), solid state welding (Mironov et al., 2008), and high energy beam process (Cao and Jahazi, 2009) are commonly employed for welding of Ti6Al4V alloy. However, this alloy is highly susceptible to the nitrogen and oxygen affinity at an elevated temperature (>500℃) that primarily deteriorates mechanical property of welded joints (Baruah and Bag, 2017). Pre weld surface condition is one of decisive factors that affect the weld quality. It essentially alters the absorptivity of laser light on the surface and enhances the weld penetration.

Besides, the shielding environment of the laser welding system greatly influences the reliability and quality of weld joint. Hence, isolated chamber sometimes is used to conduct the welding that essentially reduces the chances of porosity formation (Reed et al., 2000). Thus, it is necessary to pay special attention towards the monitoring of contamination level in the weld pool by proper shielding system.

The researchers studied various aspects including phase transformation during solidification (Poondla et al., 2009), high temperature solid-state phase transformation (Fan et al., 2005), causes and remedies pertaining to defects during welding of Ti6A4V alloy (Gursel, 2017). Poondla et al. (Poondla et al., 2009) showed that duplex microstructure of $\alpha + \beta$ alloy shows extraordinary mechanical properties. Rapid solidification assists the formation of martensitic phase and gives rise to the formation of intermetallic Ti_3Al, due to segregation of α-stabilizer. Malinov et al. (Malinov et al., 2001) defined 900℃ as threshold temperature beyond which nucleation and growth of α-grain boundary takes place. Fan et al. (Fan et al., 2005) concluded that HAZ of laser assisted Ti-alloy structure is composed of α′-martensite, primary-α, secondary α and retained β. Tsay et al. (Tsay et al., 2006) indicated that randomly oriented α′-martensite alters the crack growth direction. It is thus obvious that tensile strength, fatigue strength, and corrosion-resistance of fusion zone and heat affected zone (HAZ) of Ti-alloy weldment are highly influenced by morphology of evolved microstructure (Poorhaydari et al., 2005). The microstructures are characterized by basket-weaved, equiaxed, Widemanstatten, and needle-shaped acicular α′-martensite according to the size and distribution of α-phase within β-matrix (Lin et al., 2016). Specific morphology can be achieved by controlled thermal cycle, which is primarily determined by the mode of thermo-mechanical processing. Senkov et al. (Senkov et al., 2002) investigated the effect of controlled cooling rate on morphology of microstructure and they reported combination of elongated and finer α-lamellae along with residual prior β-phase at a cooling rate of 20 - 490 K/min. Diffusionless acicular α′-martensite is characterized by nucleation and movement of perfect and partial dislocations at high cooling rate. Microstructural morphology in the weldment varies with different welding processes, which accounts mainly the temperature gradient and cooling rate. Yunlain and co-worker (Yunlian et al., 2000) reported serrate and plate-shaped microstructure for electron beam welding (EBW) whereas fine acicular α′ structure is reported for CO_2 laser welding process due to the variation in cooling rate and welding process conditions. However, a mixture of coarse serrate and acicular

α structure appears for GTAW process. More substantial heat input favours the coarsening of prior β-grain size, whereas low heat input helps in the reduction of prior β-grain size. Not only morphologies, but even variation in geometrical dimensions of α-lamellae also affects mechanical properties significantly (Cheng et al., 2009). It was observed that the width of α-lamellae plate and size of α-colony decreases with increase in cooling rate, which results in a relatively higher yield strength of a welded join.

The laser welding of Ti-alloy is often associated with the formation of porosity, where the amount of hydrogen and other gases entrapped within a molten pool and solubility of a gas in the molten pool decides the nature of pore (Matsunawa et al., 1998). Proper choice of pulse parameters diminishes the overall porosity level in laser-welded Ti6Al4V alloy (Gao et al., 2013). The risk of undercut also reduces with the appropriate choice of pulse parameters and laser beam focal plane (Blackburn, 2012). Pulse welding involves impingement of energy to the localized area comes not only from single pulse but also from overlapped pulse on same beam spot. The pulse modulation is characterized by high peak power that could be 10-50 times larger than the average power of beam, allows remelting and solidification of weld pool within fraction of second. Hence, pulse laser is much suitable for a thin structure welding application. The current pulsation is also useful for the grain refinement, reduction of HAZ width, and control chemical segregation. Keyhole formation resulting from pulse laser welding favours high melting ratio with respect to continuous mode welding (Sabbaghzadeh et al., 2008). Elevation of overlapping factor from 40% → 80% renders the formation of fully transformed HAZ. Increasing overlapping factor give rise to preheat region temperature for upcoming pulse and diminishes cooling rate, which results in formation of fully transformed HAZ.

Becker and his college predicted that low frequency pulse GTAW neither affects tensile properties nor influences grain size remarkably from that obtained in constant current mode (Becker and Adams, 1979). Several researchers (Mehdi et al., 2016; Sundaresan et al., 1999) explained that pulse phenomena favour grain refinement of prior β-phase in the solidified structure of fusion zone that leads to an appreciable increase in hardness, elongation and tensile strength. However, an increase of pulse frequency attributes a relatively higher amount of residual β-phase content, which in turn decreases hardness. It is inferred that proper selection and

optimum interaction of pulse and continuous parameters can be suitably implemented for thin sheet welding of Ti6Al4V alloy as compared to continuous mode or GTAW process.

2.5.2 Welding of Austenitic stainless steel

The fusion welded austenitic stainless steel (SS304) is commonly used material employed for the bellow fabrication and other commercial purposes. Attribute such as excellent strength at elevated temperature, good fracture toughness at low temperature and corrosion-resistant properties make it suitable candidates for wide application in various industries. A temperature driven metallurgical aspect alters the microstructural development at the fusion zone and HAZ. Several authors studied the microstructural development through alteration of heat input by using different welding techniques and under various process conditions (Kumar and Shahi, 2011; Yan et al., 2010). It is observed that dendrite size and inter-dendritic spacing increases upon increasing heat input at the fusion zone whereas grain coarsening takes place at HAZ in gas tungsten arc (GTA) welding of SS304 (Kumar and Shahi, 2011). Laser and hybrid-laser assisted welding processes generally produce smaller dendrite of δ-ferrite that attributes relatively better mechanical properties as compared to conventional techniques (Yan et al., 2010). A comparative study between solid state friction stir welding and GTA welded joints demonstrated that arc-based welded samples exhibits the microstructure composed of austenitic matrix embedded with skeletal and lath shaped δ-ferrite whereas FSW produces almost equiaxed crystallized austenite grain with small content of elongated δ-ferrite (Sabooni et al., 2015). Several factors such as primary mode of solidification, cooling rate, solute distribution during cooling, nucleation and growth performance of $\delta \rightarrow \gamma$ transformation during solidification decides the microstructural morphologies in the weld zone. Most of the literature opined that it is utmost important to pay attention towards the distribution and amount of δ-ferrite formed in welding of stainless steel since it controls the properties and on-site behavior of weld joint in terms of thermal stability, mechanical characteristics and residual stress generation (Balmforth and Lippold, 2000; Fukumoto et al., 2008). Growth of δ-ferrite primarily depends on the chemical composition, cooling rate and primary mode of solidification manifested during welding (Pordilha and Rios, 2002). Martorano et al., (Martorano et al., 2012) implemented magnetic method to measure the ferrite content and perceived insignificant influence of cooling rate on samples with 0.5 probability. Few samples show decreasing trend of ferrite content, upon

increasing cooling rate from 0.78 to 2.7 K/s. The ratio of chromium [$Cr_{eq.}$] and nickel equivalent [$Ni_{eq.}$] that predominantly controls the primary mode of solidification in favour of δ-ferrite formation, recommended within the range of 1.5-1.9 for SS 304L (Korinko and Malene, 2001). However, austenite/ferrite interface is a susceptible site for corrosion attack and can be minimized through preheating that is essentially reduces δ-ferrite by virtue of decreasing cooling rate (Rajani et al., 2012). Moreover, sensitization of steel alloy results in degradation of engineering properties as well as corrosion behavior.

Many researchers have studied the impact of various process parameters, including laser power, effective beam radius, shielding gas, laser-material interaction, scanning speed, and stand-off distance for different laser sources (Kawahito et al., 2008). It is observed that Nd: YAG and CO_2 lasers are widely used for the fabrication of the welded structure. However, the usefulness of fiber laser has increased nowadays due to enhanced power utility, high stable beam quality, very small focal spot diameter, and high efficiency for deep penetration at lower wavelength relative to other laser sources (Matsumoto et al., 2017). Higher melting efficiency of fiber laser relative to CO_2 favours producing near I-shaped weld bead geometry as compared to Y-shape at low heat input (Ren et al., 2015). Recent studies show that relatively good quality welds with minimum tensile residual stress and improved mechanical properties for stainless steel was possible to achieve using fiber laser under the specified condition as compared to Nd: YAG and CO_2 lasers (Ahn et al., 2017). Therefore, the process variables, such as welding speed, feed rate, defocusing distance, and pulse shaping, have a significant impact on weld joint characteristics. Investigation on the optimization of process variables and the influence of laser process parameters on the welding of austenitic stainless steel is well explained by earlier work (Ragavendran and Vasudevan, 2020; Zhang et al., 2014). Ma et al. (Ma et al., 2007) demonstrated that directional solidification is efficacious technique to study microstructural evolution during solidification. It allows independent monitoring of interface velocity and temperature gradients within wide range. The ferrite ratio and austenitic grain size in the weld region is a function of heat input where ferrite ratio increases and the austenite grain size decreases with heat input. Ragavendran and Vasudevan (Ragavendran and Vasudevan, 2020) demonstrated that the cooling rate is a function of laser power and weld speed, which in turn influence the ferrite to austenite transformation in the weld zone. Coarser microstructure and

austenite-ferrite mode of solidification is perceived for hybrid laser tungsten arc welded stainless steel (316L(N)) joints by virtue of high heat input. In addition, one of the researchers (Zhang et al., 2014) critically examined the performance of defocusing distance on weld characteristics. The positive defocusing exhibits partial penetration with less porosity, whereas negative defocusing resembles keyhole based full penetration with possible weld defects (Getto et al., 2015). In effect, all parameters have a significant influence on residual stress evolution in the weld joint.

2.5.3 Welding of 9Cr-Mo steel

9-12%Cr martensitic-ferritic steels are considered as prominent candidate material for the fabrication of various components in advanced fusion and fission reactor (Klueh, 2005). These steels are characterized by relatively higher thermal conductivity, lower thermal expansion constant as compared to austenitic stainless steel, which lead to higher demanding application for high temperature power application. In this family of steel, 9Cr-1%Mo ferritic steel has extensive applicability in power plant components fabrication which usually operates at high temperature (i.e., 873 K), because of its appreciable mechanical performance and better oxidation resistance properties at elevated temperature. Furthermore, 9Cr-1%Mo steel achieves improved properties when crossed through normalization at 1323-1343 K and tempered at 1013-1053 K due to generation of tempered martensitic morphology which results in fine precipitates and moderately high dislocation density (Das et al., 2008). Although advantages of martensitic steel are well acknowledged, however some drawbacks are also existed which limits it's utility. Pre-mature failure at the heat affected zone (HAZ) of welded joints is one of the most prominent examples for P91 steel. The failure exists due to type IV cracking (Kundu et al., 2013). Type IV cracking is characterized by high rate of void formation in inter-critically annealed HAZ in the welded structure. Whenever P91 steel structure girth is welded by conventional process significant residual stresses produced in type IV region which usually cannot be released even during post weld heat treatment. Therefore, assessment of residual stress generation has to be taken care during weld fabrication of 9Cr-Mo steel plate.

2.5.4 Influence of phase transformation on residual stress

Interactions of inhomogeneous thermal strain caused by temperature gradients and volumetric change by virtue of phase transformation results in residual stress generation. The strain induced by phase transformation can change the state of residual stress (Payares-Asprino et al., (2008)). The state of residual stress is determined through expansion possessed during martensitic transformation and thermal shrinkage accompanied by cooling cycle (Ahn et al., 2017). In addition, martensitic start and finish temperature are also stated as critical parameters to control residual stress in welded structure (Payares-Asprino et al., n.d.). Induced tensile transformation strain amplifies the overall magnitude of tensile residual stress. On the contrary, if transformation strain is of compressive nature and it is algebraically added to the overall tensile stress causes minimization of overall tensile magnitude of residual stresses. Hence, it is essential to understand the physics behind the stress variation during the weld cooling cycle to optimize the interrelation between thermal contraction and transformation strain. Volumetric dilation during diffusional or diffusionless transformation at cooling stage is found to be advantageous in minimizing the thermal contraction. Tensile residual stress can be easily reduced at some extent by the minimizing martensitic transformation temperature in such a way that phase transformation can continue to counteract for the accumulation of compressive strain down to ambient temperature (Stone et al., 2008). Besides, volumetric dilation accompanied by martensitic transformation permits the molten metal to expand however surrounding metal tries to be in equilibrium, hence obstruct the expansion which evolves compressive transformation strain in molten pool. Therefore, compressive transformation stress decreases the overall tensile stress in welded structure (Deng and Murakawa, 2008).

On the contrary, evolution of residual stress is crucial aspect during welding of SS304 as well. In order to control residual stress for stainless steel weldments, it is essential to understand the theory of its origination and the interaction with the microstructural morphology (Khurshid et al., 2017). Stress variation attributed to the scale of grain size may occur due to the variation in properties among austenite and ferrite phase, which includes elastic strain, thermal, and plastic misfit for austenitic stainless steel. However, the lattice parameter, which is the function of interstitial atom content, is a crucial factor for the interpretation of desired residual stress in expanded austenite (Hummelshøj et al., 2010). On the other hand, it is justified that solid-state

phase transformation has an insignificant effect on residual stress distribution in stainless steel due to δ-ferrite ↔ γ-austenite transformation at very high temperature and minimal changes in volumetric strain owing to transformation (Lin and Chou, 1995). The residual stress in austenitic steel is more complex where solidification mode and morphology may play an important role. Hence, a clear understanding and accurate measurement of residual stresses distribution are vital to ensure the quality of stainless steel welded joints. There are very few studies, which deals with the relation between microstructural evolution and residual stress (Chen et al., 2019; Harjo et al., 1998). In general, relatively high tensile residual stress is evolved due to increasing δ-ferrite content and its grain size (Unnikrishnan et al., 2014). In ferrite-austenite Fe-Cr-Ni alloy, the compressive elastic strain is generated in ferrite phase whereas tensile elastic strain emerges within γ-austenite matrix due to variation in their thermal expansion coefficients (Harjo et al., 1998). Thibault et al. (Thibault et al., 2010) reported that the residual stress in 13%Cr-4%Ni steel was triaxial state and the compressive residual stress in the welded structure was observed due to low martensitic transformation temperature. Hsieh et al. (Hsieh et al., 2013) showed that the specimen which owns enriched δ-ferrite content accompanied by extremely high resonant frequency elevate tensile residual stress. Hence, a clear understanding and accurate prediction of residual stresses distribution by virtue of solute distribution (i.e., γ-austenite, δ-ferrite) during solidification are vital to ensure the quality of stainless steel welded joints.

Only a few literatures are found which focuses on the relationship between variations of elemental composition and associated residual stresses for the welded structures (Mašek et al., 2010). Taking advantage of solid state $\gamma \rightarrow \alpha'$ transformation, low alloy HSLA steel consumable has been developed to achieve compressive residual stress in the weld metal (Alipooramirabad et al., 2016). This development improved the fatigue life of components. Moat et al. studied the effect of austenitic and ferritic weld filler wires on residual stress development and suggested that a ferritic alloy with 12% Ni, 0.5% Mn and 0.65% Si had an Ms temperature of 250 °C and showed compressive stresses in the weld metal (Moat et al., 2011). Austenite stabilizing elements like Si, Cu, Cr, C, Ni and Mn have been reduced in 9-12Cr steels over a period of time to improve high temperature microstructural stability of ferritic-martensitic steels (Payares-Asprino et al., (2008)). However, weld consumables used for joining of these steels have higher content of these elements. Because these elements reduces A1 temperature of the steel that favours easy post weld heat treatment at lower temperature to achieve adequate toughness.

Nickels (Ni), Manganese (Mn) are austenitic stabilizing elements whereas Silicon (Si) is ferrite stabilizer. These alloying elements (i.e. Mn+Ni) play significant role to control phase transformation kinetics and retained austenite stabilization. These elements restrict carbide precipitation during martensitic tempering and stabilize retained austenite at ambient environment (Mašek et al., 2010; Payares-Asprino et al., (2008)). Additionally, Manganese (Mn) and Nickel (Ni) are also austenitic stabilizing alloying element which enhances carbon solubility in austenite and opens cooling region by arresting pearlite formation. Thus, it is evident that solid state phase transformation is another key factor that contributes to change the behavior of retained stress state. Modification in weld chemistry can also control the state and magnitude of residual stress.

2.5.5 Factors affecting phase transformation

2.5.5.1 Heating rate

For Ti-alloy, if the attained heating rate is sufficiently low, then $\alpha + \beta \rightarrow \beta$ transformation follows the thermodynamic equilibrium curve, and the volume fraction of α-phase decreases up to a negligible amount at or before β-transus temperature (1000 ℃). Nevertheless, if the heating rate is sufficiently high, then the complete dissolution of α-phase requires high temperature; as a result equilibrium curve shifts towards the right side, as illustrated in Fig. 2.7. The diffusional $\alpha + \beta \rightarrow \beta$ transformation is linearly related to heating rate (Szkliniarz and Grosman, 1988). For the particular conditions of welding and metal deposition, high heating rates entail maximum transformation rate. The progress of β and α-phase fraction is studied at varied heating rate, i.e., 5, 20 and 100 K/min for Ti6Al6V-2Sn alloy as shown in Fig. 2.8 (Barriobero-Vila et al., 2015). Within the temperature range of 450-550 ℃, the highest increment of ∼3 vol. % of α-phase fraction is noticed for 5 K/min, while an insignificant elevation in phase fraction is observed at 20 and 100 K/min. Lattice expansion is controlled by the thermal expansion coefficient at the onset of the heating cycle, resembling little variation in a volume fraction. Several researchers considered solidus, liquidus and β transus temperature within the range of 1605-1693 ℃, 1655-1701 ℃ and 956-975 ℃, for Ti6Al4V alloy (Elmer et al., 2004). A significant difference between liquidus and β-transus temperature implies that molten

pool in the weld might be surrounded by relatively large area of β matrix that differs in size in response to variation in temperature gradient around the molten pool.

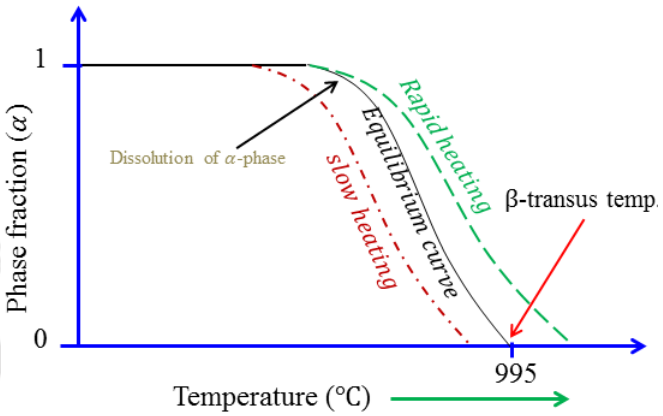

Fig. 2.7 Representation of shifting of equilibrium curve due to variation in cooling rates

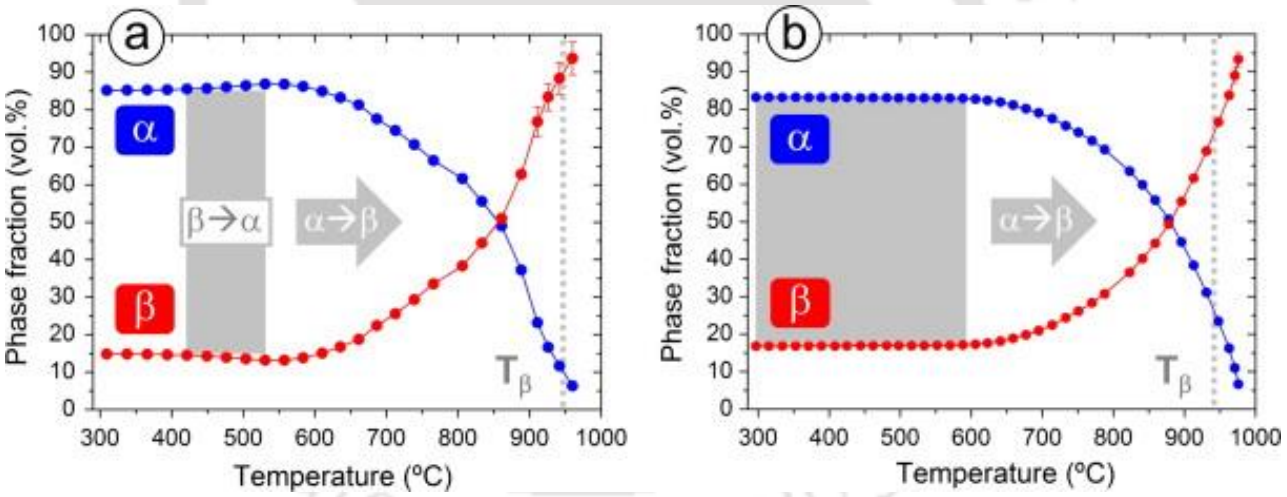

Fig. 2.8 Evolution of the volume fractions of α and β obtained by Rietveld refinement analysis: Heating at (a) 5 K/min, (b) 100 K/min (Barriobero-Vila et al., 2015)

2.5.5.2 Cooling rate

The cooling rate determines the characteristic features of the evolved microstructure and associated morphologies, such as the size of the α lamellae, the α colony size, and the thickness of α layer at prior β grain boundaries (Homporova et al., 2011). In general, the width of α-

lamellae or plate and the size of α coloines, decreases with increasing cooling rate. The solid state phase transformation and corresponding microstructural evolution in the FZ and HAZ are severely controlled by the heating and cooling rate which in turn depends on several welding parameters (El-Batahgy and DebRoy, 2014). If the diffusionless transformation takes place athermally and attained cooling rate is 2×10^5 K/s, martensitic transformation temperature will not be the function of cooling rate. Nevertheless, transformation temperature decreases in the vicinity of 5×10^4 K/s which indicates that the transformation is thermally activated (Jepson et al., 1970). It is interesting fact that the α-lath and prior β-grain size produced upon long exposure at elevated temperature, are significantly affected by cooling rate (Broderick et al., 1985). A lenticular shaped α morphology is obtained in the order of less than 10^5 K/s, whereas beyond 10^5 K/s, the α morphology transformed into globular form at weld zone of the Ti6Al4V alloy. Furthermore, Ahmed and Rack described that hexagonal α′-martensite can be obtained if the cooling rate exceeds 525 K/s. Fig. 2.9a signifies the processed heat flow profile against the temperature attained at different cooling rates (Kherrouba et al., 2016). It indicates that the transformation temperature associated with diffusional β → α transformation during the cooling stage can be estimated in accordance with the deviation in curve from baseline (Sieniawski et al., 2013). The transformation finish temperature noticed from the present DSC curves shows inverse relation with cooling rates (Malinov et al., 2001). Fig. 2.9b illustrates the variation of widemanstatten α-lath thickness with cooling rate. It reveals that the thickness of α-lath decreases upon increasing cooling rate. This is because the undercooling is predominant as cooling gets relatively faster.

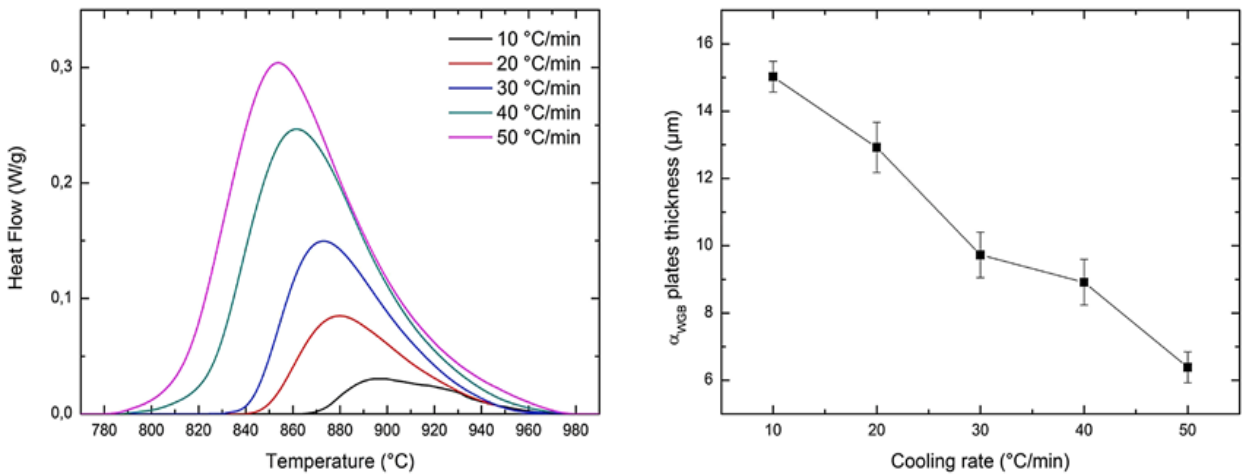

Fig. 2.9 (a) DSC curve for cooling stage at different cooling rates, kept at isothermal holding at 1373 K upto 20 min, (b) variation of Widmanstatten α-lath thickness with cooling rates (Kherrouba et al., 2016)

2.5.5.3 Effect of pulsation

High current density (10^2-10^3A cm^{-2}) pulses and low continuous current (~0.1 A cm^{-2}) during solidification refines the microstructure of metal alloy. The pulse current offers an additional mechanism of microstructural refinement from columnar to equiaxed grain growth during solidification of molten pool (Suresh et al., 2004). The pulsation on the resulting microstructure of cast iron (~2% Cr and ~0.9% C) revealed that the pulsation in the melt lowered the length of columnar grains and modified the pearlitic structure during casting (Yong et al., 1999). Application of high pulse frequency increases the depth-to-width ratio and minimizes HAZ, which leads to the reduction in residual stress magnitude by localization of energy density (Tseng and Chou, 2002). Larger pulse spacing or greater amplitude ratio (function of base and pulse current) induces a relatively less heat input. A high amplitude ratio minimizes the temperature gradient between the fusion zone and the base metal region. Therefore, the magnitude of shrinkage stress is diminishes due to a smaller temperature gradient.

In dual-phase Ti-alloy welding, current pulsation is one of the techniques due to which refinement of FZ grain structure occurs that improves the mechanical properties [Babu et al., (2007)]. Welding of Ti-alloy is characterized by a very narrow solidification range than other metals like aluminium and austenitic steel (Hallum and Baeslack, 1990). Grain refinement due to pulsation at an optimized frequency (6 Hz for Ti6A-4V and Ti6Al-2Sn-4Zr-2Mo) is depicted in Fig. 2.10 and 2.11. The pulsation effect minimizes the temperature gradients, intensifies the fluid flow and continuous variation in weld pool shape and size that helps the growth of new grains (Grill, 1981). Pulse parameters regulate the cooling rate and peak temperature which are predominant factor to determine the solidification behavior and phase distribution of the weld microstructure (Pal and Pal, 2011). Application of current pulsation enhances the convective force in the weld pool that has a beneficial effect on refinement of β-grain structure in Ti6Al4V alloy; this improves tensile strength, but, minimizes the ductility (Balasubramanian et al., 2011). TEM analysis confirms that the volume fraction of diffusional transformation is prevalent at

current pulsation due to enhanced fluid flow which leads to more shallow thermal gradients and therefore, a relatively low cooling rate. However, the effect of succeeding pulse on solidification of the weld pool is very less at sufficiently low frequency (Balasubramanian et al., 2008).

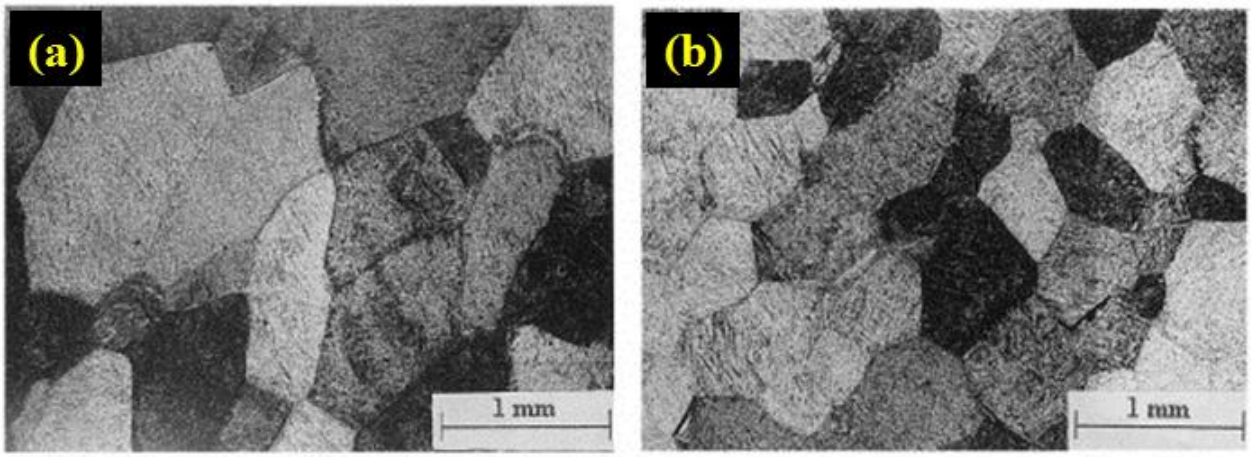

Fig. 2.10 Macrostrutural depiction of Ti6Al4V alloy fusion zone (FZ) at a frequency of 6 Hz in: (a) Continuous, (b) pulsed condition (Sundaresan et al., 1999)

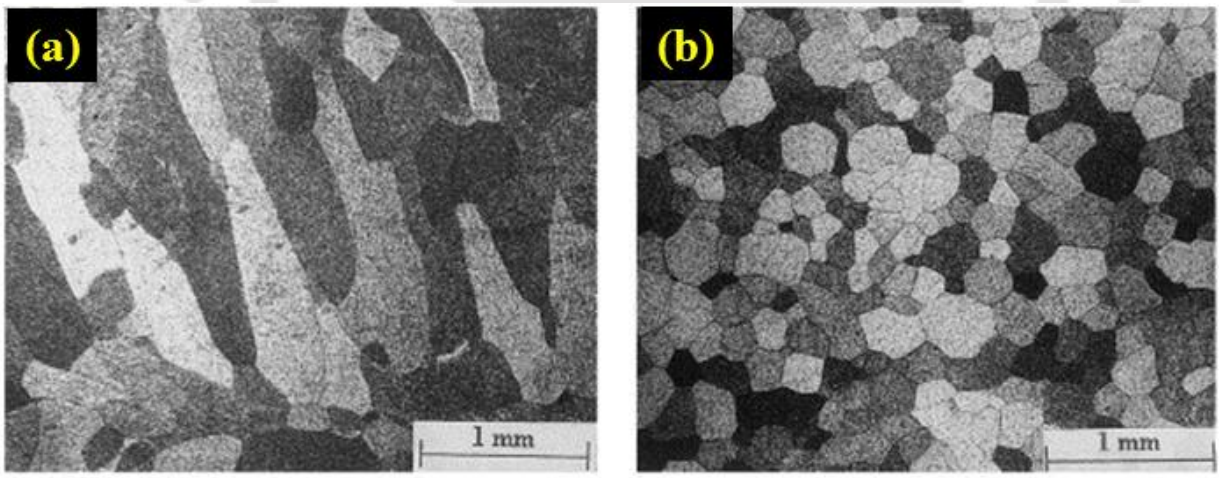

Fig. 2.11 Macrostrutural depiction of Ti-6Al-2Sn-4Zr-2Mo fusion zone (FZ) at a frequency of 6 Hz in: (a) continuous, (b) pulsed condition (Sundaresan et al., 1999)

2.6 Numerical model

Several interactive physical phenomena that come into existence during the welding process can be modelled mathematically, and the robustness of the model can be verified by comparing it with the experimental result. The aero engine and aerospace industry accounts for the majority of worldwide titanium consumption about ~80%; of which Ti6Al4V alloy is the most widespread variant. The primary application of this alloy includes the airframe (Boeing 777), low-pressure compressor components, fastener to fan blades in a gas turbine engine, landing gear parts and large wing beam (Rae, W. (2019)). Whereas, 9Cr-Mo steel weldment is chosen as a structural material for test blanket modules in ITER and tritium breeding blanket application in DEMO reactor (Das et al., (2012)). This alloy is also recommended for high temperature (~873 K) application in boiler and turbine of ultra-supercritical power plant (Abe, F. (2001)). The aforementioned components are often subjected to a prescribed set of thermal and thermo-mechanical cycle to accomplish a final microstructure that produces favourable mechanical properties, yet residual stress must be considered adequately in order to ensure optimal performance. The knowledge about the origin and evolution of residual stress throughout the manufacturing process is a key challenge faced by those industries as it cannot be accessed through the experimental techniques. FE based numerical modelling approach can be successfully used to gain knowledge about a wide range of outputs including geometrical dimension, material properties, thermal output, microstructural evolution, metallurgical changes and mechanical behavior of the welded structures. Hence, there has been a continued interest to develop model and simulation tools that exhibit proper guidance for microstructure and engineering properties optimization (Glavicic et al., (2006)). Even, esteemed industry, i.e., Rolls-Royce corporation is interested to develop and utilize computer-based simulation tools in order to produce next-generation components fabricated from Ti-alloy with enhanced capability (Glavicic et al., (2010)). On the other hand, European Commission funded Framework Programme (FP6), i.e., COMPACT which stands for a COncurrent approach to Manufacturing induced Part distortion in Aerospace ComponenTs (BoeingB787, AirbusXWB), intends to develop a thorough, rigorous and deterministic approach to understand the source of residual stress and management of part distortion using material processing and multi-functional FE modelling technique (Sim, W. M. (2010)). In addition to this, European Union funded research

agency namely, “Virtual Engineering for Robust manufacturing with Design Integration” (VERDI) includes the development of manufacturing design methodologies with an objective to reduce and complement exhaustive pre-study experiments and costs employing modelling approach (Lindgren, L. E. (2001), Charles, C. (2016)). It is opined that the material model is observed to be a crucial factor for accurate simulation and it is essential to account for the influence of undergoing microstructural changes on a material model. International Thermonuclear Experimental Reactor (ITER) test blanket module steadily trying to develop an improved axisymmetric model to predict accurate residual stress and its relaxation upon heat treatment for P91 steel alloy (Serizawa et al., (2013)). So, it is worthwhile to explore the accurate predictive model which account for the majority of interactive physical phenomena such as thermal, mechanical as well as metallurgical aspects. If it is developed and adopted by the aforementioned industries, then trial-and-error based approaches can be avoided which may allow for improved material performance whilst minimizing production costs (Turner et al., (2014), Rae W. (2019)).

Heat source model is considered as an essential part of thermal analysis. Various numerical methods such as finite element and finite difference are extensively used to simulate the welding process. The majority of the work is restricted by the assumption of conductive heat transfer. Temperature-dependent material properties are adopted as they are important to consider in the transient thermo-mechanical analysis. The essential data that has to be calculated during metal welding is the temperature field for describing the extent of phase transformation, cooling rate that would affect the evolution of non-diffusional martensite, welding induced stresses, and deformation.

2.6.1 Heat source model

Several analytical models related to welding phenomena exists from early date backs, with a lot of clarification, deduction, and prediction (Nguyen et al., 1999; Rosenthal, 1941). However, the analytical approaches are limited to various simplified assumptions and tend to neglect several factors such as fluid flow, temperature dependency of physical properties, latent heat, actual heat flux distribution, etc. Despite, these served as key elements for the calculation of the temperature field. Rosenthal (Rosenthal, 1941) attempted to calculate the temperature field

analytically, for the stationary and linear arc welding processes. However, calculation failed to estimate the temperature at the centre of heat source, and temperature dependency has also not been considered (Eagar and Tsai, 1983). Friedman implemented Gaussian assisted disc model using finite element technique and achieved remarkably better thermal history rather than Rosenthal model (Friedman, 1975). Mazumdar and Steen (Mazumder and Steen, 1980) are the foremost who have modeled the thermal analysis considering Gaussian based surface heat flux using finite difference method. However, they also incorporated energy absorption coefficient within the depth of molten pool by following Beer-Lambert's principle. Further, Chande and his college (Chande and Mazumder, 1984) improved the aforesaid model via including temperature dependency of material properties and latent heat of fusion by artificially increasing specific heat capacity between solidus and liquidus temperature ranges. Implementation of surface heat flux may not help much in order to get sufficient depth of penetration during thermal modeling.

Goldak et al. (Goldak et al., 1984) proposed a semi-ellipsoid model to incorporate the effect of arc stiffness for the arc welding process where the momentum effect of arc is predominant. The arc stiffness is a property which is mainly determined by the electromagnetic force and current magnitude (Chen et al., 2014). The numerical output from this model produced a less steep temperature gradient at the front and a gentler gradient at the trailing edge of the heat source relative to the measured one. The development of a double ellipsoidal model (Fig. 2.12) by combining two semi-ellipsoids resolved this issue to a certain extent (Goldak, 1985). The aforementioned model yielded reliable temperature field output for deep penetration welds like GMAW (Goldak and Akhlaghi, 2005). The ratio of front and rear length of present model has significant effect on weld geometry as well as mechanical features. The proposition for the selection of the length of a front and rear ellipsoid over the range of welding current and velocity is suggested by Yadaiah and Bag (Yadaiah and Bag, 2012). However, the double-ellipsoidal distribution of heat intensity is still not applicable for the high-density welding processes (LBW, EBW, PAW) with a high aspect ratio (d/w). Several mathematical representations of heat sources have been developed where the geometric shape is mainly mapped with the weld pool shape and size (Baruah and Bag, 2016; Zhan et al., 2017).

Chang and Na (Chang and Na, 2002) studied various heat source equations to model laser spot welding for thin stainless steel plates. The results suggested that the thermal profiles and

weld distortion vary in accordance with the heat source equation of the laser beam. Cho et al. (Cho and Kim, 2002) used the finite difference method to simulate micro-joining of thin A3003 Al sheets by a pulsed Nd:YAG laser beam. The authors depicted that the welding stability and evaporation are greatly affected by the modulation of laser pulse shape for the same laser energy and welding parameters.

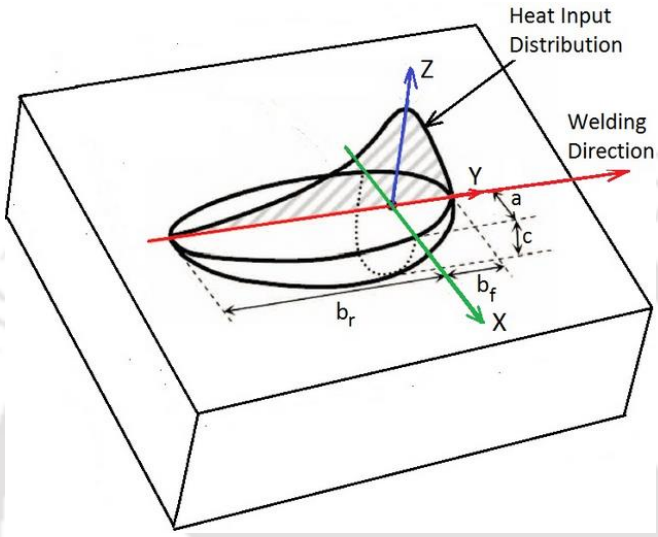

Fig. 2.12 Double ellipsoidal heat source model (Reddy et al., 2009)

The quasi-steady state heat transfer model is developed to determine temperature distribution in GTA welding by considering temperature dependent material properties and latent heat of melting and solidification (Bag and De, 2008). An adaptive heat source model based on the transient mapping of weld pool geometry is established to represent the laser beam source that overcomes a-priori definition of heat source parameters (Bag et al., 2008). Baruah and Bag (Baruah and Bag, 2017) investigated the influence of pulsation in Nd:YAG laser microwelding of Ti6Al4V alloy. It assumed Gaussian distributed heat flux over the volume so that flux density decreases along the thickness direction. A pulse characteristic has also been included over time domain in their heat flux model. Furthermore, the basic shape of the ellipsoid is modified and transformed into egg-shaped heat source model by Yadaiah and Bag (Yadaiah and Bag, 2014) through flattening of symmetric shape. It is advantageous for moving heat source conditions because egg-shaped model is non-symmetrical as compared to an ellipse. Hence, it can be implemented for asymmetric heat distribution for both, i.e., shallow as well as deep penetration

laser welding process (Yadaiah and Bag, 2014). The Three-dimensional egg-shape in terms of Cartesian coordinate system by modifying ellipsoidal is expressed as:

$$\frac{y^2}{b^2} + \left\{\frac{x^2}{a^2} + \frac{z^2}{c^2}\right\} \times \{f(y)\} = 1 \quad (2.6)$$

If velocity vector is along 'y' direction, then f(y) function decides degree of asymmetry and shape of egg-curve.

Primarily, researchers have incorporated different heat source models according to the welding process and thickness of the materials to be welded (Bag et al., 2012; Baruah and Bag, 2017; Trivedi et al., 2006). The temperature distribution and melt depth for laser-based additive manufacturing of Ti6Al4V powder is predicted by solving the conduction-diffusion equation. For this purpose, a single pulse static point heat source is used (Criales and Özel, 2017). Various other heat source geometry such as conical, cylindrical, and hourglass, have been adopted to accurately measure the temperature field during laser welding (Churiaque et al., 2016; Goldak and Akhlaghi, 2005; Zhan et al., 2017). For the representation of full depth of penetration, an hourglass-like heat source with Gaussian power density distribution is developed by combining two frustums. A material flow phenomenon is the leading cause for the generation of "hourglass" shaped bead profile.

It is obvious that the estimation of temperature field in conduction-based heat transfer model with enhanced accuracy depends on the choice of an appropriate heat source model. However, an accurate and suitable heat source to incorporate heat transfer phenomena in thermal modeling of thin sheet welding is not well documented. Still, it is required to examine appropriate selection of heat source model for laser welding of thin sheet.

2.6.2 Thermo-mechanical model

It is vital to develop a realistic and reliable model that can effectively predict residual stress and distortion under various process conditions. Nowadays, with the help of commercial software, these thermal, metallurgical and thermo-mechanical analyses can be done easily and efficiently. The Finite Element (FE) based numerical tool facilitates the adequate measurement of thermal and mechanical characteristics such as temperature, cooling rate, residual stress and

distortion in difficult-to-reach location and also capture other intricate physical phenomena like phase transformation, volumetric dilation, and microstructural development, etc., which are otherwise difficult to achieve by simple experimental set-up (Trivedi et al., 2006). However, establishing the reliable heat transfer model by the appropriate representation of laser-material interaction is essential.

Contemporary process designers are strongly assisted by the numerical model, which contributes to simulating complex phenomena like fusion welding process where thermal, mechanical and metallurgical attributes are simultaneously involved. The development of the FE-based thermo-mechanical model started with 2D form using temperature dependent physical properties (Argyris et al., 1982). Michaleris et al. (Michaleris et al., 1999) implemented decoupled 2D and 3D approaches to estimate longitudinal plastic strain components, particularly for large ship panel. Carmignani and his workers (Carmignani et al., 1999) developed a 3D-sequentially coupled model to analyze the stress-strain field for laser-welded thick stainless steel by considering the elastic-viscoplastic material model through fully implicit time-integration technique in order to surmount uncertain behavior of the rate-independent constitutive model. Researchers also presented a non-linear finite element technique to model the welding induced residual stress distribution (Munsi et al., 2001; Teng and Lin, 1998). Muránsky et al. (Muránsky et al., 2012) investigated the influence of different hardening rules, i.e., isotropic, kinematic, and mixed kinematic-isotropic hardening on thermo-mechanical behavior of stainless steel weld. It is observed that the isotropic hardening model exhibit over-prediction, whereas the kinematic hardening model reveals under-prediction for calculated residual stress field. However, the mixed model predicted the accurate stress field. Liu et al. (Liu et al., 2017) developed thermo-mechanical model by assuming an elasto-plastic material model for the prediction of residual stress in laser welding process by incorporating Ludwik-Voce hardening law and classical Johnson-Cook term for temperature sensitivity function. The material anisotropy under the elasto-plastic response of the substrate had great influence on internal stress generation within the welded structure.

Canas et al. (Canas et al., 1996) studied the effect of strain hardening and temperature-dependent properties on the residual stresses and used hypothetical time-temperature relation (Eq. 2.7) for numerical analysis of residual stresses in weldments of aluminium alloy Al-5083-O.

$$T - T_0 = \frac{Q}{2\pi\lambda} e^{\frac{v}{2k}w} K_0 \left[\frac{v}{2K}[w^2 + x^2]^{\frac{1}{2}}\right] \quad (2.7)$$

where $w = y - vt$ which is time dependent relation.

A few authors often used cut-off temperature above which no changes in the mechanical properties are accounted to minimize computational time. Tekriwal and Mazumder (Tekriwal and Mazumder, 1991) explained that when the cut-off temperature varied from 873K to 1173 K, a small residual stress variation is observed for carbon steel weldments. However, the computational time is significantly reduced. Zhu and chao (Zhu and Chao, 2002) systematically investigated the influence of each temperature-dependent material property on the transient temperature, residual stress, and deformation. They concluded that the yield stress is highly sensitive to thermo-mechanical modeling of welding processes. Its value significantly affects the residual stress as well as associated distortion. Teng et al. (Teng and Lin, 1998) inferred that more restrained joints promote higher residual stress generation than unrestrained conditions.

Furthermore, Yang et al. (Yang et al., 2000) developed a model by considering the initial deformity of the plate for estimating buckling type deformation in the MIG welded structure. Depradeux and Jullien (Depradeux and Jullien, 2004) conducted a thermo-mechanical analysis for the TIG welding process. They used temperature fields as input for sequentially coupled structural analysis in order to examine the mechanical response of a welded structure. Lee et al. (Lee et al., 2012) presented a sequentially coupled-thermal stress model for static stress analysis of butt-joint. The interrelation between average cooling rate and transverse residual stress at different welding speed is shown in Fig. 2.13. The element death-birth analysis and lumped technique is implemented for the addition of filler metal in welding simulation.

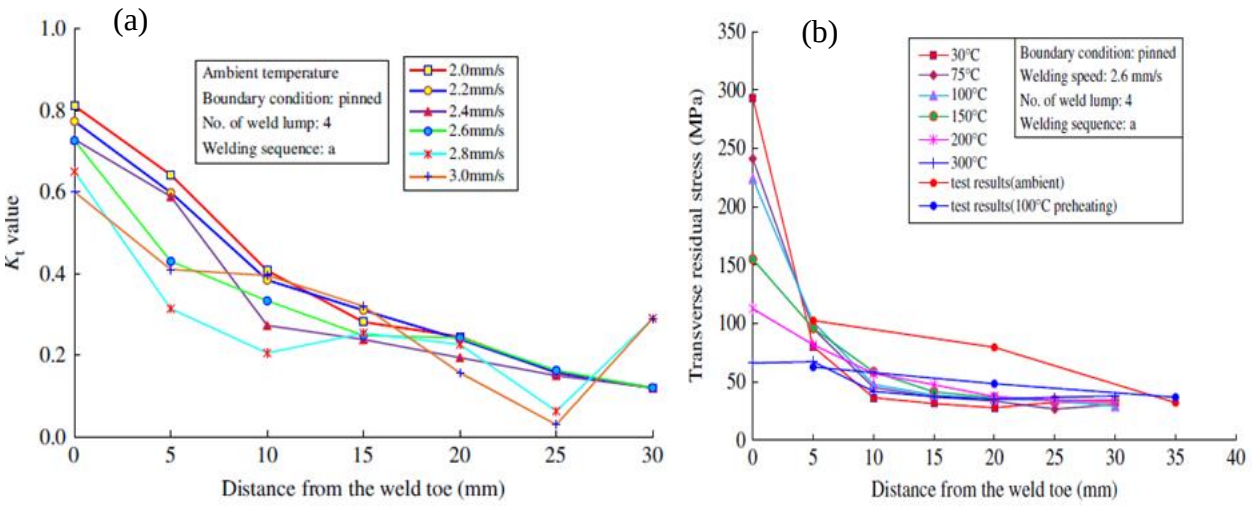

Fig. 2.13 (a) Average cooling rate for different welding speed, (b) Comparison of transverse residual stress with different welding speed (Lee et al., 2012)

Michaleris and Debiccari (Michaleris and DeBiccari, 1996) followed a two-step numerical analysis procedure for evaluating welding induced deformation. Firstly, 2D thermo-mechanical simulation is established, then output is employed as an input during elastic analysis of the 3D structure. Ueda and other researchers (Ueda et al., 2012) critically examined the characteristics distributions of inherent strains over the different configurations of butt weld joints, namely T and I shape, and estimated residual stress and distortion pattern. Ha et al. (Ha et al., 2007) developed an analytical method, i.e., modified equivalent loading method based on the inherent strain that adapted hardening effect, to suppress post-weld distortion at heat affected zone (HAZ). It is assumed that external force resulting from inherent strain (plastic strain) is responsible for post-weld deformation. Deng and Murakawa (Deng and Murakawa, 2008) employed inherent strain theory and revealed that apart from the thermo-elastic-plastic model, application of the inherent strain as initial strain is advantageous to minimize the computational time in the course of modeling of complex welding structure. The deformation and residual stress dispersion on gas arc welded thin sheet (1 mm) is simulated by considering elastic–plastic material behavior and temperature dependent material properties without using any external constraint (Deng and Murakawa, 2013). During analysis, it is assumed that the total strain is comprised of three basic strain components:

$$\varepsilon_T = \varepsilon_{th} + \varepsilon_{pl} + \varepsilon_{el} \quad (2.8)$$

where ε_T is overall strain component, whereas ε_{th}, ε_{pl} and ε_{el} represents thermal, plastic and elastic strain component, respectively.

2.6.3 Thermo-metallurgical-mechanical model

Even though considerable progress has been made in computational welding mechanics, but there are many key problems, i.e., development of an advanced material model to roundly consider the influence of metallurgical transformation on welding induced residual stress and deformation, modeling of transformation induced volumetric change, etc., are still exist in the present era. It has been found that most of the thermo-mechanical models discussed above consider sequentially coupled thermal and mechanical characteristics only. In contrast, when a metallic substrate is welded through a fusion welding technique, solid-to-solid and liquid-to-solid state phase transformation effects need to be incorporated during modeling. Accurate temperature dependent data, as well as different algorithms, are required to precisely simulate the phase transformation phenomena. In order to enhance the robustness of the thermo-mechanical model, few researchers (Ahn et al., 2017; Cho and Kim, 2002) incorporated phase transformation kinetics to predict reliable residual stress and distortion pattern. A few literatures have come up which deals with mathematical modeling of phase transformation for titanium alloy (Ahmed and Rack, 1998; Malinov and Sha, 2005). Katzarov et al. (Katzarov et al., (2002)) established a mathematical model by considering nucleation and growth phenomena of diffusional transformation for dual phase Ti-alloy during the continuous cooling cycle. The modeling assumed diffusional transformation as a function of volume covered by a β-phase field in a time-space domain. Fachinotti et al. have given some effort to establish a relation between thermal behavior and complex microstructural attributes of shape metal deposited wall of Ti6Al4V alloy (Fachinotti et al., 2012). This model predicted the geometrical features of the top cupola with distinct morphology and insignificant martensitic structure during cooling of shape metal deposited component. The coupling of a thermo-metallurgical-mechanical field served as a basic requirement of prediction of model, and the associated state of stress evolution is schematically represented in Fig. 2.14. Leblond et al. (Leblond et al., 1986) propounded a model to investigate anomalous plastic characteristics during phase transformation of steel by using the Hill-Mandel

homogenization technique. The differentiated transformation plasticity behavior is perceived might be caused by the distinguished response of components due to the variation in phase fraction. It is reported that the total macroscopic strain does not only consist of elastic and plastic parts, even thermo-metallurgical components, which emphasize the volumetric change and thermal dilatations due to phase transformation, also contributes to overall strain generation. Zubairuddin et al. (Zubairuddin et al., 2014) performed a FE based analysis for steel plate welding by considering with and without phase transformation effect. The model performed well by including the phase transformation effect. However, a large discrepancy is found when the phase transformation effect is neglected. It indicates that volumetric changes during phase transformation are the predominant factor for the altering residual stress distribution that may significantly minimize the accumulated longitudinal stress. During phase transformation, the volumetric expansion in molten zone and heat affected zone (HAZ) takes place due to change in crystallographic orientation from face centred cubic (FCC) to body centred tetragonal (BCT) structure (Deng and Murakawa, 2013). Further, a FE based thermo-metallurgical model for ferritic steel welding has been developed considering transformation induced plasticity (Hamelin et al., 2014). The influence of transformation plasticity is remarkable when the martensitic transformation effect is taken into account. The accuracy of the model is improved when both solid state phase transformation (SSPT) and transformation induced plasticity (TRIP) are explicitly captured. Yaghi et al. (Yaghi et al., 2008) estimated the residual stress in a multi-pass weld of P91 steel pipe by considering SSPT and post-weld heat treatment effect. The superimposed hoop and axial stress were tensile on the upper surface of the weldments. When the SSPT effect is accounted, retained stress field is found to be reduced significantly at different locations. Furthermore, at a half depth of the weld zone, both stresses (axial and hoop) are suppressed remarkably and changed into compressive in the vicinity of last weld pass. Deng and Murakawa (Deng and Murakawa, 2013) have developed thermo-mechanical model to predict residual stress of thin plate by undertaking volumetric dilation, transformation induced plasticity, and mechanical properties variation. The incorporation of TRIP effect released both longitudinal and transverse stress in the welded and nearby area, whereas the distinct effect of volumetric dilation is found to be ambiguous. Siwek et al. (Siwek et al., 2013) presented the modeling of the TIG process for thin plate (0.5 mm) components and compared with the measured one for different power (0.6, 1.2, 2.4kW). During modeling, the factors such as variation in pressure

gradient and momentum effect are also considered, which is related to two-phase region, i.e., mushy zone for the prediction of structural characteristics with enhanced accuracy.

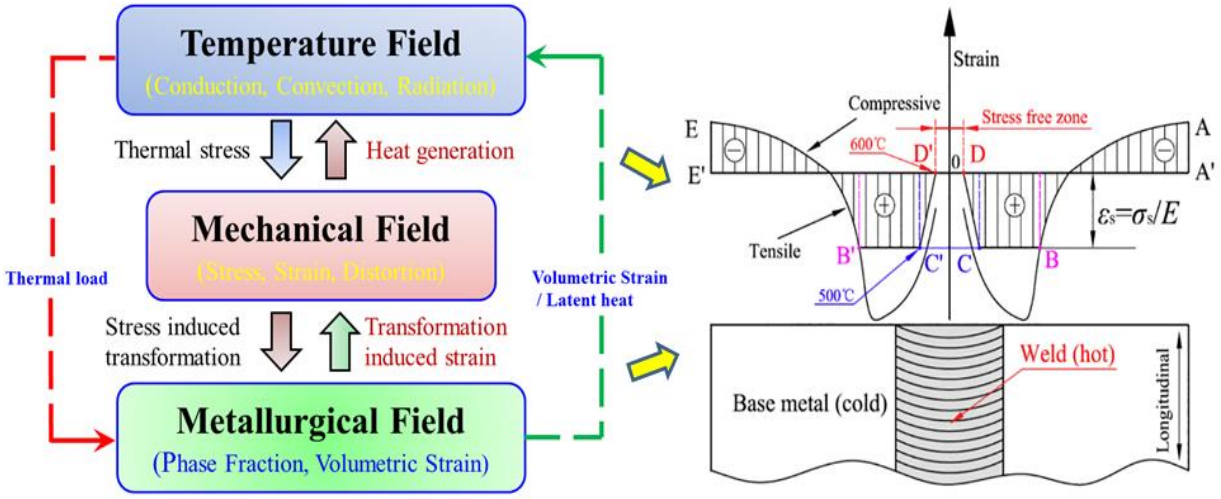

Fig. 2.14 Illustration of evolution of longitudinal residual stress and strain due to SSPT (Jiang et al., 2018)

Deng (Deng, 2009) established FE based sequentially coupled thermal-metallurgical-mechanical model for low carbon and medium carbon steel alloy. A very small change in residual stress result is revealed due to lower volumetric dilation in low carbon steel, whereas, the distinguishable difference is obtained for medium carbon steel owing to significant martensitic transformation. Lei et al (Lei et al., 2016) introduced a non-isothermal Johnson-Mehl-Avrami-Kolmogorov (JMAK) equation to predict $\gamma \rightarrow \alpha$ transformation for low carbon (~0.002 wt%) steel alloy using weld thermal cycles. This equation is accurately applicable under linear cooling conditions where phase transformation is emphasized by random site saturated nucleation and growth. Ahn et. al. (Ahn et al., 2017) demonstrated an insignificant influence of phase transformation on residual stress distribution by virtue of less change in a specific volume of several phases of Ti-alloy.

The FE based numerical model has increasing demand to precisely predict the residual stress field and associated deformation in a large structure. Therefore, establishing a time-effective numerical modeling technique by undertaking complex material models for titanium alloy and austenitic stainless steel associated with phase constituent and corresponding stress

generation is crucial. In addition, a direct correlation between microstructural stability and residual stress evolution during welding by optimizing weld metal chemistry through the numerical framework increases the reliability of engineered components with strong influence of austenitic stabilizers on ferritic-martensitic steel weldments.

2.7 Summary

This chapter describes various aspects of residual stress and distortion analysis from the perspective of material models for Ti-alloy, stainless steel and ferritic-martensitic steels. A comprehensive review on residual stress and distortion measurement techniques are also performed. Various mitigation techniques of residual stress are followed in the light of the impact of microstructural morphology on residual stress. An extensive part of this chapter is devoted to address the issues on welding of Ti6Al4V alloy and stainless steel by using laser welding process. Secondly, several modeling approaches on the estimation of residual stress and distortion with and without phase transformation effect are discussed. In a nutshell, this chapter provides an overview on the influence of metallurgical transformation and microstructural development on residual stress and distortion in a welded structure. The difficulties faced during welding of 9Cr-Mo steel plate using conventional processes are also briefly explained. Further, the techniques used by the researchers to minimize the detrimental effect of residual stress through changing the weld chemistry are addressed. The key findings from this chapter are summarized as:

- Few researchers have come up in the field of thin plate welding to find out an envelope of the process parameters for successful joints. The combined effect of various welding parameters on the weld joint shape and size, and microstructural morphology has been investigated. It is established that a low heat input with high energy density maintaining conduction mode welding is preferable for thin sheets. Thus, researchers apply laser welding to minimize HAZ and increased concentrated monochromatic beam effect on weldment. Very few literatures have come up with an optimized set of pulse parameters for laser welding of thin sheets and the impact on the solid state phase transformation kinetics.

- The literature indicates that the selection of welding process, amount of heat input, cooling rate, peak temperature and welding process parameter have a definite effect on the shape and dimension of weld joint, which in turn affects the mechanical properties of the joint. Thus, the researchers have targeted to find an optimum combination of the welding parameters which ensures the required quality of the final joint with minimum defects.
- Experimental measurement of temperature and flow conditions in the micro-scale welding process is extremely difficult. The construction of a reliable numerical model is an utmost important to investigate thermo-mechanical parameters and metallurgical parameters for thin sheet weldment. Such model will help to understand and relate the physical phenomenon to reduce the cost and cumbersome experimental effort.
- Thin sheets with low stiffness are more susceptible to distortion. Quite a few literatures have found which can signify the influence of metallurgical change on the generation of residual stress and deformation in the weld metal. Most of the researchers neglected the effect of phase transformation during residual stresses and distortion analysis owing to its complexity. There is insufficient literature that comes up to predict distortion of thin sheets including the effect of solid state phase transformation.
- There is a lack of a complex thermo-metallurgical-mechanical model in thin sheet joining processes, specifically for Ti-alloy and austenitic stainless, which incorporate predominant physical phenomena to simulate distortion and residual stress in a solidified structure. The correlation between microstructure of the weld and laser process parameters for thin plates are still to be looked into.
- Various mitigation techniques are adopted to reduce residual stresses and distortion of thin sheet structures. Temporal variation of laser energy supply is one of them. However, there is a scarcity of literature that focuses on alteration in residual stress and distortion by changing the mode from laser welding from continuous to pulse. Further, understanding the role of solid state phase transformation on stress and distortion filed is still unclear for pulse welding.
- Few literatures dealt with mechanism of phase transformation in 9Cr-Mo steel weldments. The interaction of austenitic stabilizer and ferritic stabilizing elements remarkably control the transformation behavior and thermodynamic properties. Moreover, there is an insufficient

literature that signifies the influence on volumetric dilation and associated locked-in stress state by playing with alloying element compositions or weld chemistry.

- The literature indicates that the integration of the transformation kinetics not only enhances the in-depth understanding of residual stress generation, but also enhances the reliability of the modeling calculations.

Chapter 3

3.0 Experimental Methodology

3.1 Introduction

The weldability of different biocompatible materials through proper choice of process parameters as well as analysis of the welded joints requires extensive focus on various experimental techniques. Hence, the present chapter is oriented to discuss about conventional and nonconventional experimental methodologies on fulfilling the objectives of the present work. Several measurement techniques such as optical microscopy, field emission scanning electron microscopy (FESEM), surface profilometry, dilatometry, energy dispersive analysis (EDS), X-ray diffractometer (XRD), transmission electron microscopy (TEM), optical emission spectroscopy (OES) are employed for the analysis of laser welded samples. In addition, X-ray diffractometric analysis is performed to measure residual stress distribution for Ti-alloy, stainless steel and 9Cr-Mo welded samples. High resolution-based scanning electron microscopy is utilized to study the microstructural morphology at the weld zone and HAZ. Overall, the mechanism for the interaction of microstructural morphology with residual stress is investigated with the assistance of several experimental measurements.

3.2 General background

The experimental investigations are carried out in order to fundamentally create a reliable database for intricate and comprehensive validations of the computed results using thermal-metallurgical-mechanical model. The welding experiments are performed to scrutinize the effect of pulsation on the evolved microstructure and associated morphologies compared to continuous mode laser welding for Ti6Al4V alloy weldments. Furthermore, some of the experimental data such as macrograph and laser welding induced distortions are extracted from the independent literature. These data are mainly used to validate the computed results from FE-model of pulse laser welding. On the other hand, continuous mode laser welding is performed over the austenitic stainless steel weldment by varying focusing and defocusing distances. Pulse parameters have significant impact on solidification mode, which is the promising factor in deciding the metallurgical and mechanical behavior of the welded structure. Since enriched δ-ferrite phase fraction, i.e., >15 % due to incomplete δ -ferrite → γ-austenite transformation may detrimentally affect weld joint property, it is significant to pay attention towards the identification of the daughter phase and accomplished morphology at room temperature under various process conditions. Further, welding experiments are carried out on 9Cr-Mo thick steel plate using shielded metal arc (SMA) welding and electron beam (EB) welding technique to investigate the influence of weld composition on transformation temperature and martensitic lath size leading to the alteration in stress state. In the present work, heat input (or heat input per unit length) is considered as a significant process parameter, which combines the effect of laser or arc power and welding velocity. Heat input governs the cooling rates in weld interface and nearby region and thereby affects the microstructure and their morphology at the molten zone and HAZ. A variation in microstructure is correlated with the mechanical properties of the weld joint as well as the residual stress level. Thus, it is essential to control the heat input by regulating its constituent parameters. The continuous mode laser welding experiments are performed at Laser Material Processing Division, Raja Ramanna Centre for Advanced Technologies (RRCAT), Indore, India. The pulsed laser welding is conducted at Reactor Design and Technology Group, Indira Gandhi Center for Atomic Research (IGCAR), Kalpakkam, India. Additionally, residual stress measurements for stainless steel are assessed from Non-Destructive Evaluation Division, IGCAR whereas PROTO iXRD setup available at Laser Material Processing Division, RRCAT

is used for residual stress measurements of Ti-alloy weldments. In the present chapter, a brief outline of all the experimental techniques used for the fulfillment of the present dissertation is discussed.

3.3 Laser welding of Ti6Al4V alloy

As-received Ti6Al4V alloy of dimension 120 × 65 × 0.8 mm^3 are butt-welded using both pulse Nd: YAG laser and continuous Yb-Fiber laser system. Fig. 3.1 depicts the welding set-up used for autogenous welding of 800 µm thin sheet in pulse (Fig. 3.1a) and continuous (Fig. 3.1b) mode of operation. Pulse laser system (TRUMPF 556, 10 kW) consists of three main components, including a laser processing system, beam delivery head, and (computer numerical control) CNC workstation. The laser beam is delivered to the workstation through a fiber optic beam delivery system. In addition, a closed-circuit television-viewing system is attached to monitor the laser-substrate interaction in order to ensure focused laser beam accurately positioned over the place of joining. Apart, Yb-Fiber laser set-up (YLS 2000, 2 kW) equipped with CNC workstation in glove box, CNC controller, processing head and evacuating system, is used to perform continuous welding experiments. The laser processing head is inclined by 5° angle with vertical axis in order to avoid impairment of lens due to back reflection of laser beam. The glove box controls the atmospheric condition during laser processing. Welding experiments are carried out under open self-protective atmosphere of argon.

The faying surface of the material is cleaned using acetone to remove any contamination prior to welding. Since Ti-alloy is highly susceptible with surrounding elements (especially oxygen) at elevated temperatures, adequate measure was considered to shield the HAZ and FZ until they are cooled below the critical temperature (Donachie, 2000). It is essential to perform superficial surface preparation in pre-weld condition to obtain enhanced laser absorption potential(Howard et al., 2006; Sánchez-Amaya et al., 2014). Hence, in order to pull out the contaminated layer of oxide, oil grease or external unwanted solid particles, the surface of weldments is grounded with grit paper (G80) followed by acetone cleaning prior to welding. Furthermore, to prevent reaction between external environment and molten pool, the weld bead is sincerely shielded by providing inert argon gas supply through coaxially fitted three pipes

around the nozzle (Fig. 3.1b) in such a way that the molten pool will be protected from all sides during welding. Material of welding fixture is a very important tool in case of welding of thin plates in various categories of welding processes. A custom made fixture is designed and constructed for the operation of welding procedure in open air. The backing and top plate of the fixture is made of pure copper. Since the thermal conductivity of copper is remarkably high, due to which it allow rapid heat transfer and hence, the chances of oxidation and entrapment of other gases within weld pool get reduced. Since, stable welding conditions exist over a narrow domain, heat input per unit length is considered as controlling parameter for thin sheet welding to identify optimum condition in order to get stable weld. The process variable at which weld found to be spatter free, without porosity and continuous uniform bead with full depth of penetration is assumed as stable weld condition in the present work. A lot of trial runs have been performed to identify the favourable conditions for good quality weld joints. The experimental condition used for weld fabrication is presented in Table 3.1.

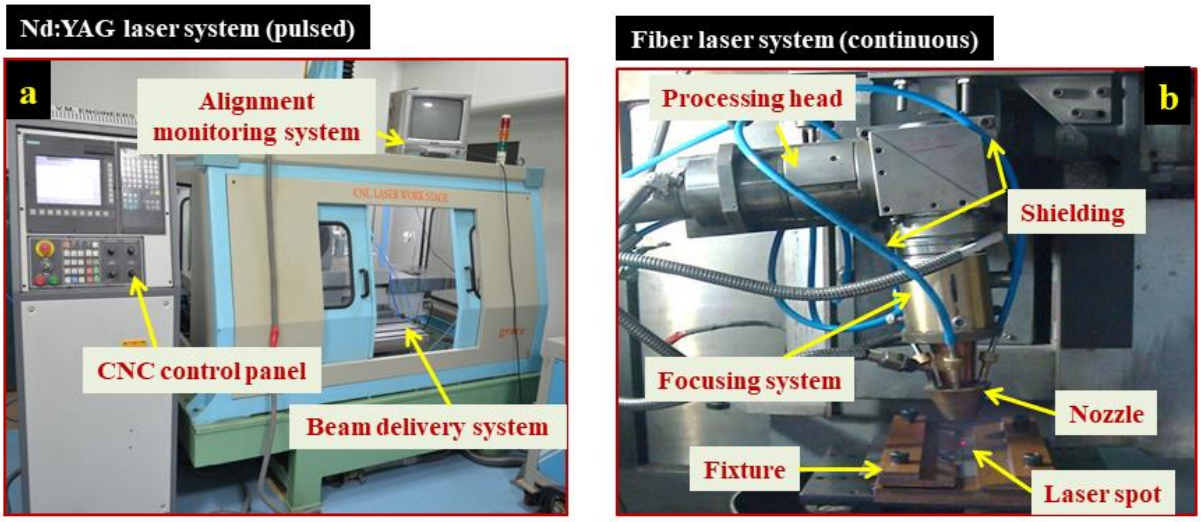

Fig. 3.1 Laser welding set up: (a) pulse mode (Nd: YAG), (b) continuous mode (Yb-Fiber)

Pulse welding resembles periodic heating of the workpiece by collimated high power density laser beam which allows melting and solidification phenomena consecutively. Pulse energy involves series of overlapping spots. The quality of the welded joint depends upon optimal amalgamation of various pulse parameters like pulse energy, pulse duration and pulse repetition rate (Tzeng, 2000). In the present work, the experiments are conducted by varying the laser scanning speed and pulse duration at constant pulse frequency. A lot of trials are required

for careful selection of optimum parameters for successful weld joints due to involvement of several process parameters. A spot overlap of 60 – 80% corresponding to welding speed 600-1000 mm/min is used. The average power during welding is evaluated using empirical relation, expressed as

$$P_{av} = E_{pl} \times f\,; \qquad P_{av} = \frac{E_{pl}}{t_{on}} \tag{3.1}$$

Heat input per unit length (H_i) based on average power is calculated as

$$H_i = \frac{P_{av}}{U} \tag{3.2}$$

where P_{av} is average power (W) and U is welding speed (mm/s).

The substrates are rigidly clamped by using the copper backing plate and clamping strip to acquire minimum distortion in the welded plate. A front and back argon shielding system is used at a flow rate of 6.5 l/min for continuous mode and 5 l/min for pulse mode of laser welding. The process parameters such as average power (P_{avg}) ranges from 48-143 W, pulse energy (P_e) of 6-13 J, pulse duration (P_d) of 6-10 ms at a constant scanning speed of 240 mm/min are chosen for pulse laser experiment. However, the constant power ranges from 750-800 W at a scanning speed of 600-1000 mm/min is considered for a continuous mode of laser welding. Table 3.2 depicts the primary process variables that are employed for the present set of experiments.

Table 3.1 Experimental condition employed for laser welding

Laser Parameters	**Values**	**Values**
Mode of laser welding	Continuous	Pulsed
Fiber core diameter (F_d)	50 µm	600 µm
Wavelength (λ)	1080 nm	1064 nm
Beam angle (B^o)	90°	90°
Flow rate (f_r)	6.5 l/min	5 l/min
Defocused distance (f_d)	0 mm, -0.4 mm, -0.8 mm	0 mm
Beam mode (B_d)	Multi-mode	Multi-mode
Laser spot diameter (D)	200 µm	800 µm

Table 3.2 Major process parameters used for welding

Sample	Peak power (W)	Pulse frequency (Hz)	Pulse energy (J)	Pulse width (ms)	Scanning speed (mm/min)	Average power (W)	Defocus (mm)	Heat input (J/mm)
Continuous mode								
C1	750	--	--	--	1000	750	0	45
C2	750	--	--	--	700	750	0	65
C3	800	--	--	--	600	800	-0.4	80
C4	800	--	--	--	600	800	-0.8	80
Pulse mode								
P1	1000	8	6.0	6	240	48.0	--	12
P2	1200	8	9.6	8	240	76.8	--	20
P3	1200	11	9.6	11	240	105.6	--	26
P4	1300	11	13.0	11	240	143.0	--	36

Under post processing of welded specimen, the welded specimens are cross-sectioned normal to the welding line. Wire-electrical discharge machine (EDM) is used to cut the sample since it prevents the alteration of residual stress and microstructure. Then samples are hot mounted within resin powder followed by polishing with different grade of abrasive papers for metallographic analysis. Final polishing is completed by using velvet cloth with suspension of alumina powder. Thereafter, polished samples are etched in Kroll's reagent solution by following ASTM E407 standard containing distilled water, nitric acid and hydrofluoric acid in the ratio 46:3:1 (ASTM In. 2014). The micrograph of etched samples is investigated under optical microscope. The phase analysis at the weld region is investigated by diffraction analysis using an

X-ray diffractometer with Cu K_α radiation ($\lambda = 154.06$ μm) according to ASTM E975 standard (ASTM In., 2013). The high-resolution microstructure is obtained using a field emission scanning electron microscope (FESEM) in accordance with ASTM E2142-01 standard, to investigate the variation of α'-martensite lath at different welding conditions (ASTM St., 2008). The tensile properties of the welded joints are examined with a universal testing machine (capacity 250 kN) at a crosshead speed of 1 mm/s by following ASTM E8M standard (ASTM St., 2008).

In order to evaluate the oxidation rate, energy dispersive X-ray (EDX) analysis is employed to figure out the elemental distribution in pre (i.e. base metal) and post-weld samples. The sample of size 3×3 mm^2 is prepared and carbon tape is used for holding the sample inside the Energy Dispersive X-ray system chamber which is equipped with silicon drift detector. Using the variable pressure scanning electron microscope, a clear optical image of the sample is selected and different spectrum places are selected on the image to start the analysis. The chemical composition of Ti6Al4V alloy (wt. %) is depicted in Table 3.3.

Table 3.3 The chemical composition of as-received Ti6Al4V alloy (wt. %)

Element	**Al**	**V**	**Fe**	**Si**	**O**	**H**	**Ti**
Wt. %	6.2	3.9	0.2	0.2	0.1	0.015	Balanced

Fig. 3.2 depicts the constituent elements of base material and welded samples from EDX analysis. The oxygen concentration is found as ~ 3.8 % in welded condition whereas it is only ~ 0.1 % in pre-weld condition. The interaction of laser beam with substrate creates high temperature and the weld region is consistent with the formation of TiO_2 during laser welding. A layer of TiO_2 and Al_2O_3 provides improved wear-resistant property to the weld surface (Wang et al., 2014). It is found that the maximum oxygen percentage is ~3.8 % for the selected range of process parameters which can be considered as in acceptable range for a good weld joint. This resembles the feasible choice of process parameter range for laser welding of Ti6Al4V alloy in the present system. It can also be concluded that for the protection of welded zone and exhibited

mechanical properties, proper shielding as well as control on cooling condition viz. the microstructural morphology is also required.

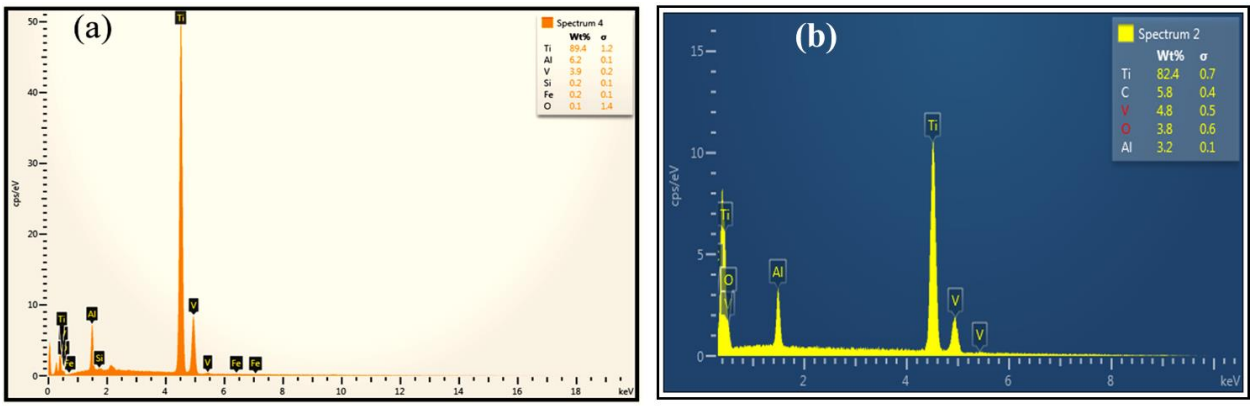

Fig. 3.2 Percentage of alloying elements of (a) base metal, (b) welded sample (45 J/mm) based on EDX analysis

3.3.1 Measurement of surface topography

Surface topography predominantly influences the deformation and stiffness of contacting surface, stress concentration, fatigue behavior and stress corrosion resistant properties in engineered product. It also affects the stress generation on the surface and sub-surfaces, structural integrity and wear performance of the welded joints. Thus, it is obvious that the surface topological behavior of fabricated joints and other mechanical components are crucial parameter in order to determine the performance of adopted mechanical process and its quality check, whether the joints are fit for desirable working condition or not. In present section, surface roughness parameters, i.e., R_a, is estimated to ensure the efficacy of surface finish under different weld conditions for Ti6Al4V alloy. Furthermore, the variation in topological behavior upon changing the mode of welding is also taken into account.

The surface roughness or finish is estimated by longitudinal deviation of an original surface from its ideal form. If the diversion is large, the surface is assumed to be rough or having low surface finish. Arithmetic roughness i.e. R_a is characterized by scanning of particular length i.e. L of surface. It is average value of the ordinates (δ_1, δ_2, δ_3…..δ_n) with respect to central line. Empirically, R_a (μm) can be written as (Rogante, 2009):

$$R_a = \frac{1}{L}\int_0^L |\delta|\, dx\ (\mu m) \qquad (3.3)$$

where L is scanned length of analyzed surface and δ represents the amplitude of crest and trough obtained on the surface during scanning.

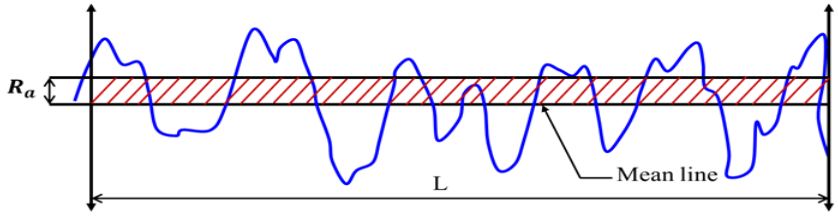

Fig. 3.3 Representation surface roughness parameter, i.e., R_a

Surface topographical measurements are performed according to ASTM B946 standard on top surface of molten zone using a non-contact type 3D optical profilometer (TALYSURF CCI MP) as depicted in Fig. 3.4 (ASTM In. 2011). Twenty times magnified lens are used to ensure the measurement of surface with dimensions 825 × 825 μm. The implemented lateral resolution is of 0.88 μm whereas precision of vertical resolution of optical profilometer is set as 1MP (mega pixel) primarily, and gradually increased up to 5 MP (mega pixel). The top surface of weld zone is analyzed under the measuring head using associated measurement control software with ~2 times repeatability. Finally, different surface roughness parameters are calculated as its averaged value corresponding to ISO 25178 and applied for the further analysis.

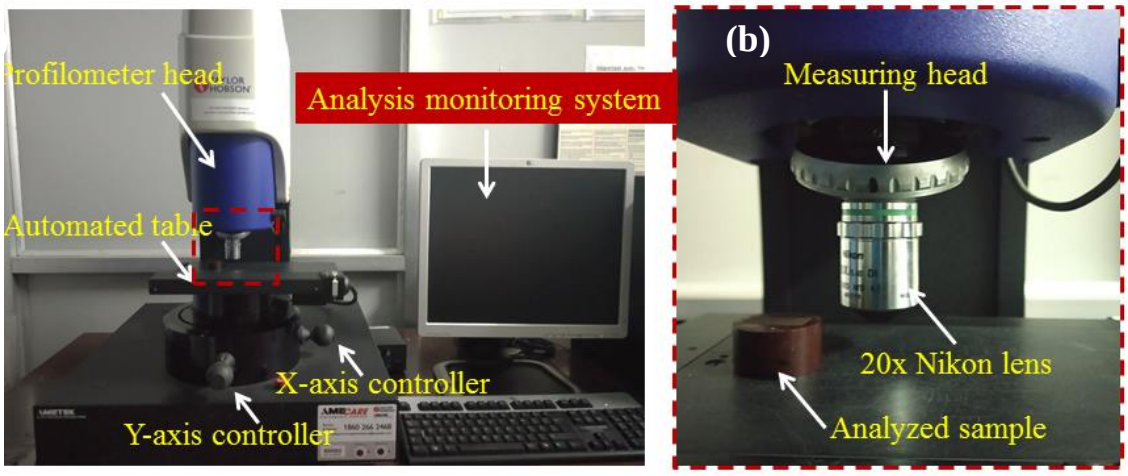

Fig. 3.4 (a) Illustration of surface topography measurement system, (b) magnified view (lens & mounted sample)

Sufficient penetration depth during welding is not only criteria to decide whether the weld quality is good or poor, however, favourable surface finish condition has to be maintained even after welding. Fig. 3.5 illustrates the topological characteristics of the weld surface (Top) observed under various weld conditions. It is obvious that a lot of disparities, micro scaled uneven surface or wear scar is available in the fusion zone for both the mode i.e. continuous (CM2) and pulsed (PM2) sample, owing to thermal agitation and higher thermal gradient. However contour plot reveals that the distribution of uneven scars is severe for the case of elevated heat input rather than pulsed one. Furthermore, it is also clarified that the agglomeration of uneven surface is higher at semi-circular overlapping region in current pulsation mode due to remelting and resolidification phenomena within very less fraction of time (μs).

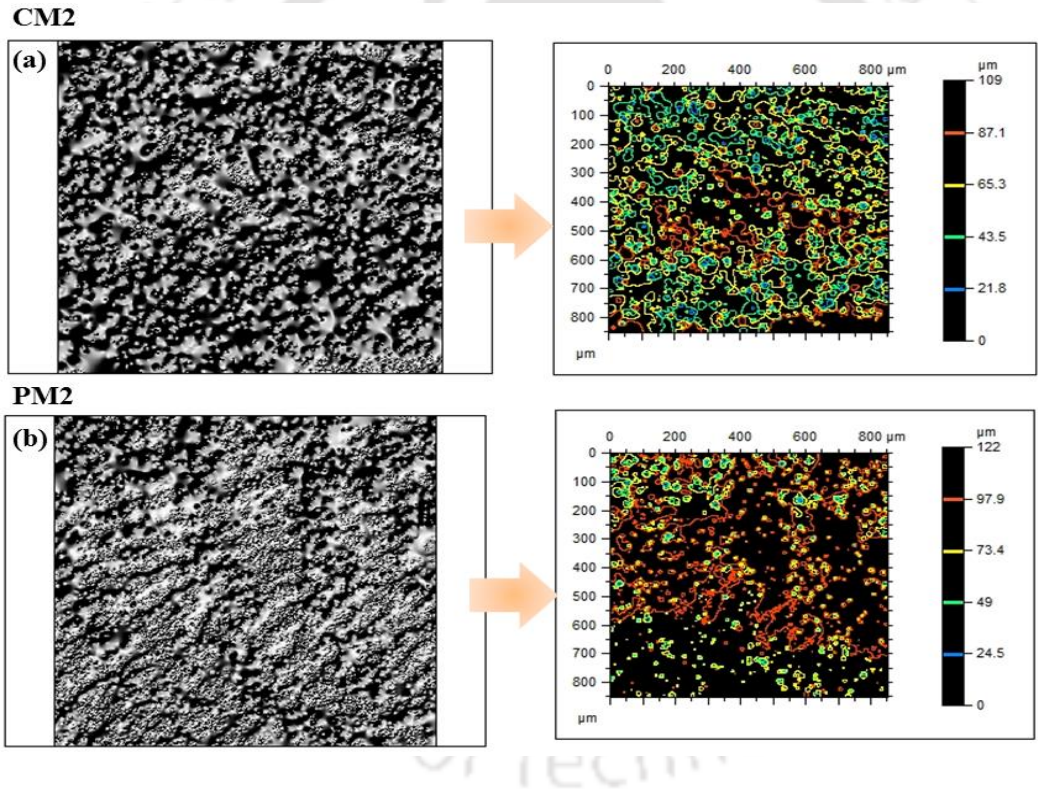

Fig. 3.5 Representation of 2D contour plot of surface topological behavior at 70 and 16.5 J/mm

Appearance of peak-valley characteristics resulting from irregular or uneven surface morphology is a prefect indication of presence of surface roughness. Fig. 3.6 shows the graphical representation of longitudinal deformity i.e. deviation of actual scanned surface in linear direction from its idea or mean surface that arises due to the existence of peak-valley

characteristics. Corresponding arithmetic mean is also depicted in the graphical spectrum. It confirms that as the heat input increases from 56 → 70 J/mm for CM1 → CM2, the magnitude of R_a is also reaches from 6.5 → 8.7 µm. A similar trend of output is observed for pulsed mode as well. Nevertheless, value is significantly dampens upon changing the mode from continuous to pulse. Presence of higher magnitude of surface roughness accompanied by high peak/valley characteristics indicates inferior quality of surface finish. This is attributed to the fact that the formation of oxides with alloying elements of parent metal i.e. TiO_2 and Al_2O_3 renders better wear resistance properties to the substrate surface. It automatically spall off by rise in oxidation temperature owing to long exposure of weld pool at sufficiently high temperature i.e. beyond melting temperature.

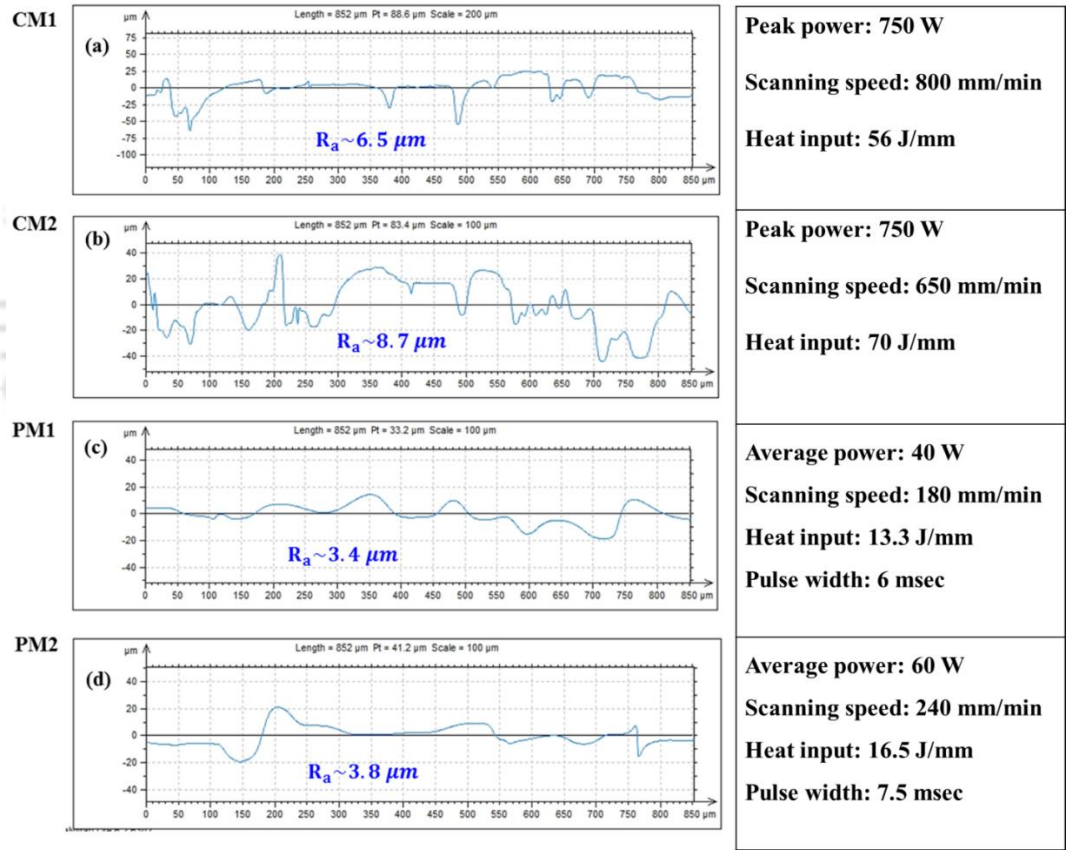

Fig. 3.6 Graphical representation of surface finish over different weld conditions

3.4 Welding of austenitic stainless steel (SS304)

A continuous wave Yb-Fiber laser (~ 2 kW) is used for welding purpose. Schematic representation of the experimental set-up is demonstrated in Fig. 3.7. The entire welding system is composed of five major subsystems i.e., Fiber laser (YLS 2000), CNC controller, laser processing head (Fig. 3.7c), five axes manipulator and workstation in a glove box. The laser scanning speed is along X-axis and the movable laser head is mounted vertically (i.e., Z-axis). However, rotation of a workstation (which is positioned stationary) is controlled by CNC. The optic has a focal length of 200 mm. Argon shielding gas is used in welding. A mixed mode laser beam comprised of TEM00 (40%) and TEM01 (60%) is implemented to assign a near-flat top beam profile. The geometrical dimension of each 304 Stainless steel plate is 120 × 65 × 1 mm^3 as depicted in Fig. 3.7b. The custom made fixture made up of pure copper metal (consists of 2 clamping and 1 backing plate) is utilized to perform the welding experiment (Fig. 3.7d). The process conditions used in experiment is depicted in Table 3.4.

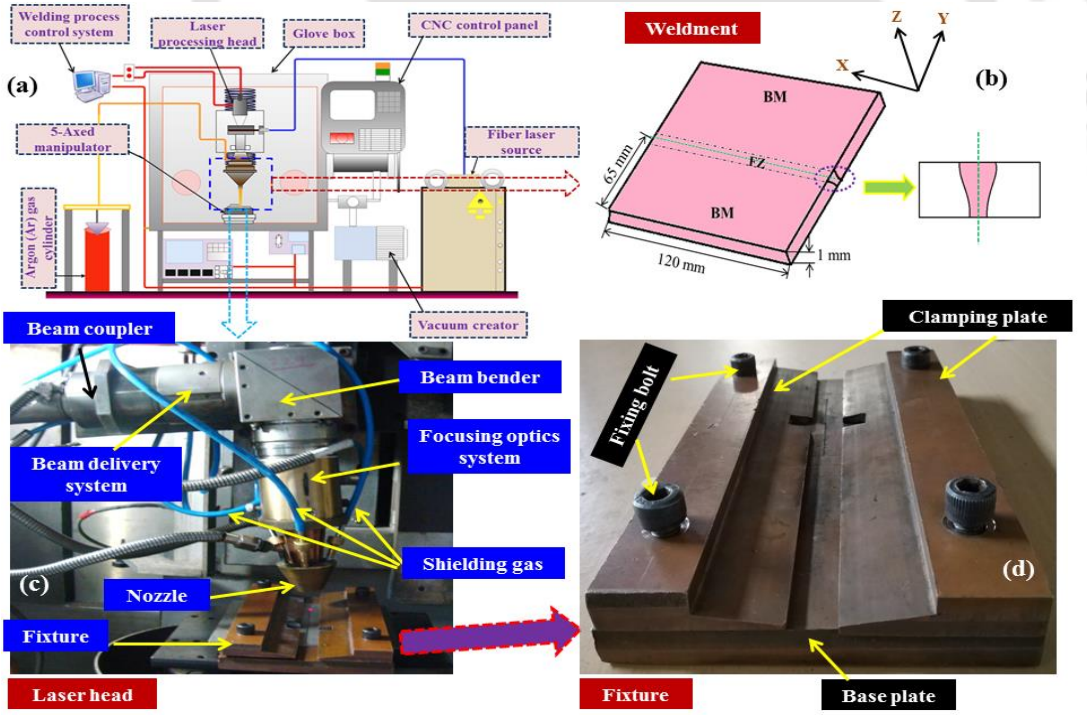

Fig. 3.7 Schematic representation of Yb Fiber laser welding setup, (a) welding system, (b) weldment specification, (c) laser processing head and (d) fixture

Table 3.4 Experimental conditions involved in laser welding

Process characteristics	**values**
Mode of laser welding	Continuous
Fiber core diameter (F_d)	50 µm
Wavelength (λ)	1080 nm
Beam angle (B^o)	90°
Flow rate (f_r)	10 L/min
Defocused distance (f_d)	0 mm, - 0.5 mm, - 1 mm
Beam mode (B_d)	Multi-mode
Laser spot diameter (D)	200 µm, , 294 µm, 388 µm

The power density on the workpiece surface varies with defocused distances for fixed laser power. Hence, three different cases of defocusing i.e., focused on top surface ($f_d = 0$), defocused on the mid thickness ($f_d = -0.5$ mm) and bottom surface ($f_d = -1$ mm) are chosen to conduct welding experiments (Fig. 3.8). The chemical composition of the base metal perceived by EDX analysis is depicted in Table 3.5.

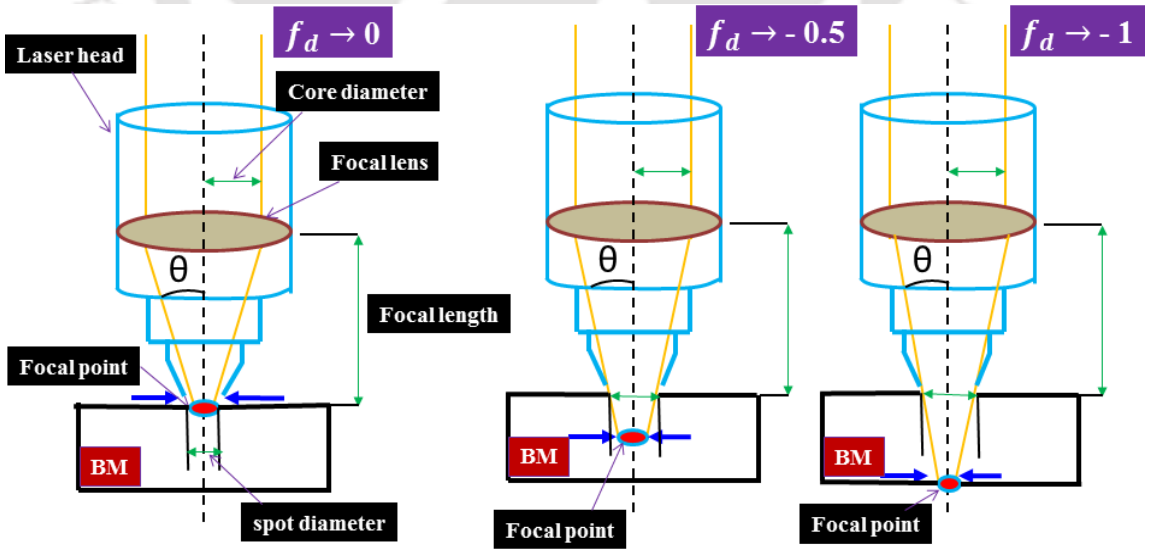

Fig. 3.8 Schematic depiction of weld phenomena for different defocusing distance

Table 3.5 Chemical composition of stainless steel used in present investigation (wt. %)

Elements	**Cr**	**Ni**	**Mo**	**Si**	**Pb**	**Mn**	**Al**	**Fe**
wt. %	18.5	8.5	0.2	0.6	0.1	1.8	0.1	Balanced

Bead-on-plate trial experiments are performed at a laser power of 600 W, 750 W and 800 W to ensure full depth of penetration. Lack of penetration has been observed at 600 W, whereas over penetration with burn-out a rim characteristic is perceived for 800 W. The intermediate laser power (~ 750 W) that furnishes full depth of penetration is considered as an optimized power for further welding experiments. The welding parameters employed in the present work and the weld bead profile (top view) is listed in Table 3.6. The nomenclature of the samples is performed by indicating the heat input and defocus distances. It is noteworthy that the weldment $S_{56}D_3$ is accidentally broken during handling; hence, it is not analyzed in the present study. The specimens are cut across the weld central line and are polished by standard metallography process. The samples are dipped into a chemical solution (Glyceregia) for etching purpose. Macro- and micro-structural images are captured under an optical microscope. Moreover, highly magnified microstructural spectrums are apprehended under a field emission scanning electron microscope (FESEM) to study the morphological characteristics. The composition analysis is performed through an energy dispersive spectrometer (EDS), and different phases possessed in the weld zone are analyzed under an X-ray diffractometer (XRD). To examine the tensile strength and elongation of the welded sample, Universal testing machine (UTM) of load capacity 250 kN is used.

Table 3.6 Weld parameters and longitudinal bead profile of laser welded samples

Weld condition	Power (W)	Travel speed (mm/min)	Defocus (mm)	Heat input (J/mm)	Weld dimension (top view)
$S_{45}D_1$	750	1000	0	45	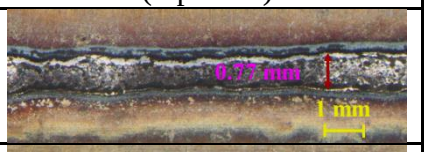
$S_{45}D_2$	750	1000	-0.5	45	
$S_{45}D_3$	750	1000	-1.0	45	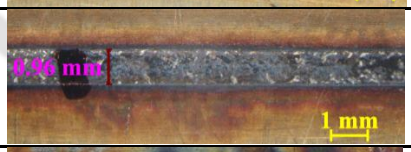
$S_{56}D_1$	750	800	0	56	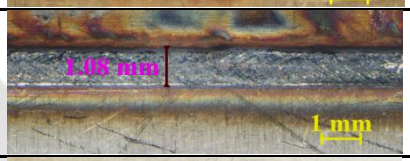
$S_{56}D_2$	750	800	-1.0	56	
$S_{75}D_1$	750	600	0	75	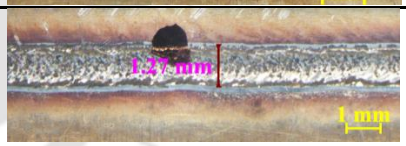
$S_{75}D_2$	750	600	-0.5	75	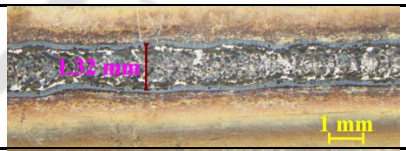
$S_{75}D_3$	750	600	-1.0	75	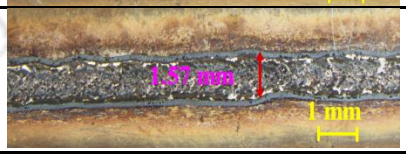

3.5 Welding of ferritic-martensitic steel

Four weld joints of 12 mm thickness with different weld metal compositions are prepared from 9Cr based steels. Among these, one is prepared with RAFM steel using electron beam

welding (EBW) to achieve lowest austenite stabilizing element in the weld metal and is defined as W1. Three weld joints (W2, W3, W4) of modified 9Cr-1Mo steel (P91 steel) are fabricated using shielded metal arc welding (SMAW) process. The process parameters corresponding to fabrication of these weld joints are presented in Table 3.7. The designations (i.e. 1 to 4) are chosen based on the increasing content of austenite stabilizing elements in the weld metal. The weld joint configuration for SMAW process had a groove angle of 70° with a land and root gap of 2 and 2.5 mm, respectively. A total of 9 passes are used to complete each of the weld joints. Stringer bead technique is used for fabrication of weld pads. The weld joints are subjected to post weld heating at 250 – 300 °C to remove any residual hydrogen to avoid hydrogen cracking. All the weld joints are fabricated under similar restraint condition nonetheless a W1 weld joint is prepared under vacuum environment with clamping.

Table 3.7 Process parameter applied for fabrication of welded joints

Process	**Voltage** (V)	**Current** (A)	**Velocity** (mm min^{-1})	**Heat input** (J mm^{-1})
EBW	55,000	0.135	1000	445
SMAW	30	130	200	1170

The compositions of various weld metals are presented in Table 3.8. The elements such as C, N, Ni, and Mn are austenitic stabilizer that reduces Ac1 and Ms temperature of steel (Mašek et al., 2010; Payares-Asprino et al., 2008). Among the four austenite stabilizing elements, C and N remain almost the same in all weld metals, whereas Ni and Mn vary.

Table 3.8 Composition (Wt. %) of various weld metals

	Elemental Compositions in wt. %									
Weld	**C**	**Cr**	**Mo**	**Mn**	**Ni**	**Si**	**Nb**	**V**	**N**	**Ni+Mn +C+N**
W1	0.093	9.07	0.002 W-1.01	0.56	0.005	0.09	0.001	0.22	0.02	**0.68**
W2	0.1	9.0	1.0	0.75	0.52	0.32	0.065	0.21	0.06	**1.43**
W3	0.11	8.81	0.96	0.7	0.67	0.22	0.05	0.23	0.038	**1.52**
W4	0.062	9.0	1.1	1.50	0.9	0.3	0.03	0.012	0.03	**2.49**

Fig. 3.9 shows the weld bead profile obtained using SMA and EB welding process. It indicates a significant variation in geometrical dimension as well as shape of the weld seam. The shape of weld bead profile transformed from conical cup to frustum by changing the welding technique from SMAW to EBW process, respectively. Minimum heat input as well as highly localized beam emission is the extraordinary feature of electron beam process. Nevertheless, a very large amount of heat input increases the volume of molten metal that leads to the formation of significantly wider weld bead in SMA welding process rather than electron beam welded specimen.

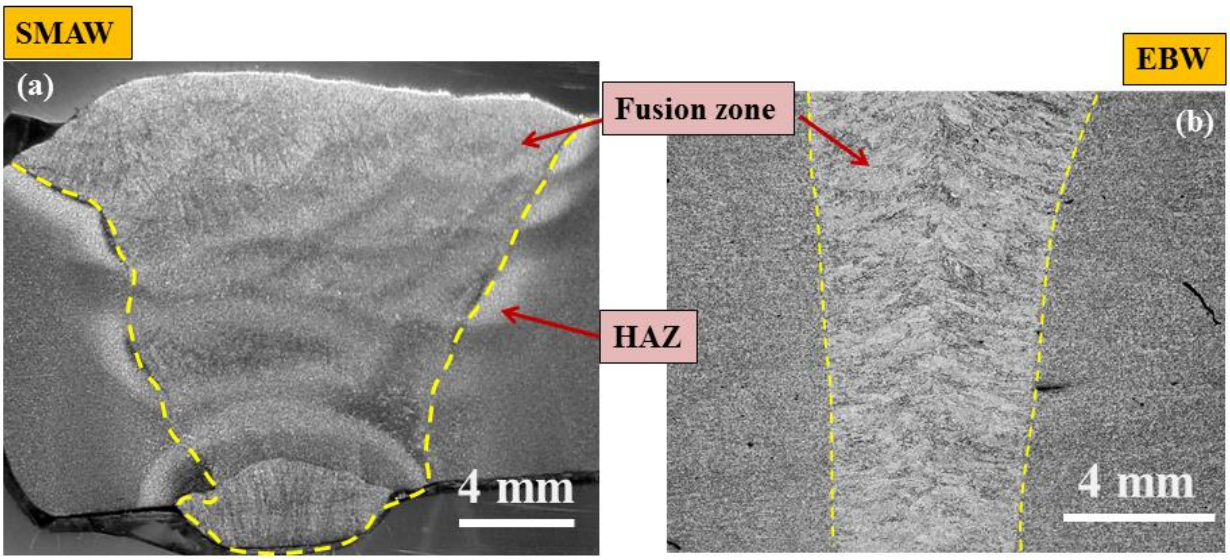

Fig. 3.9 Weld bead profile of 9Cr-Mo welded joints (a) SMA welding process, (b) EB welding process.

Dilatometric analysis

The composition of the weld metal is measured using optical emission spectroscopy (OES) analysis. Critical transformation temperatures, i.e., Ac1 and Ac3 for different weld metals are calculated in THERMOCALC software. The actual characteristic transformation temperatures associated with dilation in length or volume during welding thermal cycle is measured by dilatometric analysis. In accordance with ASTM A1033 standard, cylindrical samples are used for dilatometric analysis (ASTM, 2010). Further, volumetric change strain during heating and cooling cycle is measured using thermo-mechanical simulator. Samples are heated using alternating-current (AC) resistance system that utilizes heat equally throughout the cylindrical cross-section. The evolved temperature of the samples during course of test is continuously evaluated by a K-type thermo-couple which deliver signal so that feedback control of samples can be precisely achieved. In addition to that, samples are quenched in a vacuum chamber. Thereafter, a dilatometer is used to estimate the changes in diameter of the sample during heating and cooling cycle. The thermal cycle of the samples comprises heating the specimens with heating rate of 45 K/s to peak temperature of 1300 ℃ in order to enable full austenization before cooling cycle begins. Martensite start (Ms) and finish (Mf) temperatures are extracted from the cooling cycle of dilatation plot. Moreover, microstructure of weld metals and

alteration in martensitic lath due to welding phenomena is analyzed under transmission electron microscope (TEM). Specimens for TEM observation were prepared from 150 μm thick slices of weld metals. These specimens were mechanically polished to 80 μm and then 3.0 mm diameter disks were cut from these polished specimens. 3.0 mm diameter specimens were subjected to jet thinning. Hardness measurements were also performed according to the ASTM E384 standard, through Vickers's hardness tester by applying 500 g load on weld interface for dwell time of 15 - 20 second (ASTM int., 2012).

Dilatation experiments are carried out at a heating rate of 45 °C/min to understand the phase transformation behavior and determine the volumetric strain for defining transformation kinetics during modeling. Fig. 3.10 shows the dilatation plots for all the specimens. During heating, the temperature at which the relative change in length, i.e., $\Delta L/L_O = f(T)$ deviates from its linearity, is expressed as Ac1. On subsequent heating, thermal contraction begins and gives rise to volumetric strain by virtue of diffusional $\alpha \rightarrow \gamma$ transformation and terminates at Ac3 temperature. Beyond Ac3, the constant rising slope of the curve $\Delta L/L_O = f(T)$ is attributed to the expansion of the austenite phase. After complete transformation, the metal is allowed to expand till 1050 °C and cooled continuously at a cooling rate of - 50 °C/min. As the weld metal attains Ms temperature, thermal expansion occurs, resulting in volumetric strain because of diffusionless $\gamma \rightarrow \alpha'$ transformation and finishes at M_f temperature. Furthermore, after the completion of martensitic transformation, the specimens are allowed to cool up to ambient temperature.

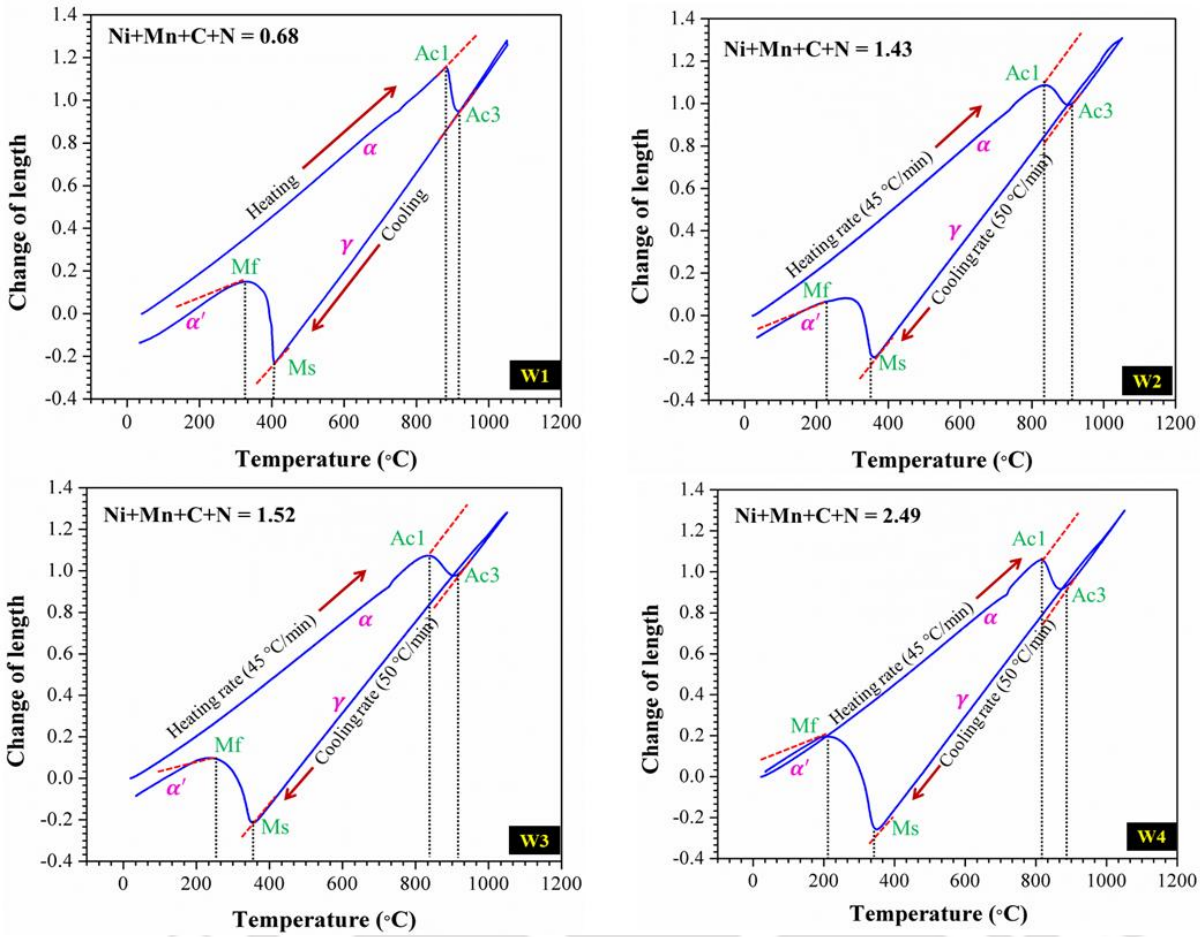

Fig. 3.10 Dilatation plots for weld metals: (a) W1 (b) W2, (c) W3 and (d) W4 under high heating and cooling rate

3.6 Measurement of residual stress

Any micro- or macro- mechanism that exhibits misfit between different parts, different phases and different zones within same structure, arises non-uniform thermal strain as well as phase transformation strain that inevitably generate residual stresses. It is an undesirable characteristic that remains within welded structure even after removal of its original causes such as external force, thermal gradients. Residual stress is classified into three categories, i.e., Type I (σ^{I}), Type II (σ^{II}) and Type III (σ^{III}) as schematically represented in Fig. 3.11(De and DebRoy, 2011; Dong, 2005; Withers and Bhadeshia, 2001).Macroscopic stress comprises of inelastic deformation comes under Type I (σ^{I}), while stress evolution as a result of intergranular

interaction by virtue of phase transformation and precipitation accounted as Type II (σ^{II}). Further, stress generated due to intragranular aberration owing to twinning and dislocation density variation comprises Type III (σ^{III}) stress. Nonetheless, the residual stress generated due to phase transformation and associated microstructural modification is taken into consideration herein. Most likely, micros stress induced due to austenite, martensite phase in carbon steel, γ-phase and δ-ferrite for stainless steel, α′-martensite, α and β-phase for Ti-alloy along with varied microstructural morphology distribution. Hence, it can be concluded that in the present work Type II (σ^{II}) stress investigation has been carried out carefully.

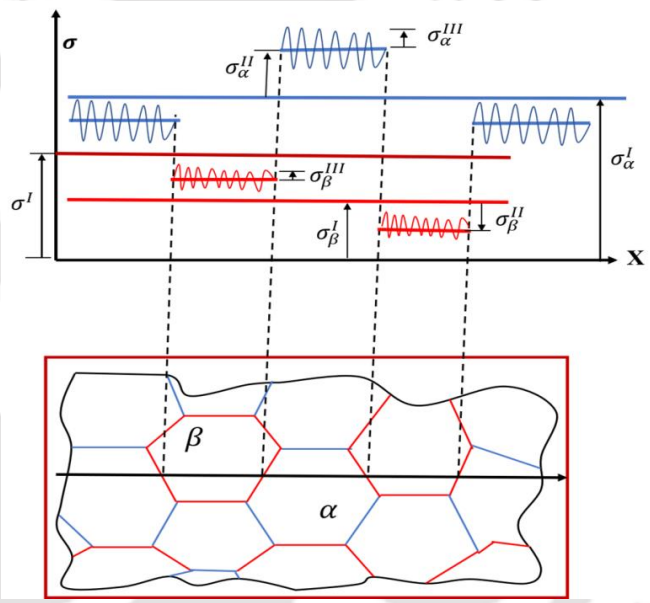

Fig. 3.11 Illustration of residual stress of Type I, II and III within solidified weld metal

3.6.1 XRD measurement

During quantifying residual stress using XRD measurement technique, the strain possessed in the crystal lattice is estimated and the corresponding residual stress is evaluated from the elastic constants considering a linear elastic deformation of the suitable crystal lattice plane. This is because, X-ray subjected over the surface area of the specimen, numerous grains and crystal which contributes to the measurements. An estimation of residual stress using X-ray diffraction technique rests on the principle interaction between the wavefront of the X-ray beam and crystal lattice which can be extensively described by the Bragg's law.

In present work, residual stress measurements are carried out by X-ray diffraction technique using the newly installed Proto iXRD, a portable residual stress measurement system. The Proto iXRD system consists of two wide 2θ position sensitive scintillation detectors on each side for simultaneous collection of the diffracted beams. The goniometer is of 40 mm focal distance and is capable of stress measurement along the required direction of the sample. It's fully integrated system along with the windows based software XRDWIN for data acquisition and stress analysis.

Bragg's law clearly defines the interrelation between the diffraction pattern that is obtained when X-ray is diffracted through crystal lattice and the inter-planar spacing within the specimen. Different diffraction pattern can be obtained by changing the interplanar spacing. The inter-planar spacing of a strain free material exhibits a characteristics diffraction pattern as compared with strained or elongated specimen within a crystal lattice, which changes the inter-planar spacing of {hkl} plane. This induced change in inter-planar spacing reflects the shifting of diffraction pattern. Therefore, change in inter-planar spacing can be estimated through accurate measurement of this shift, and thus, strain induced within material can be deduced. The presence of residual stresses in the material results in shift in the angular position of X-ray diffraction peak, which is estimated by detector. The diffraction peak is determined after suitable background subtraction, Lorentz-polarization absorption (LPA) corrections followed by peak fitting algorithms. For a known X-ray wavelength λ and n equal to unity, the diffraction angle 2θ is measured experimentally and d-spacing in then estimated using Bragg's law:

$$2d \sin\theta = n\lambda \tag{3.4}$$

Once the inter-planar spacing (d) is measured in unstressed (d_o) and stressed (d_n) conditions, the strain, i.e., ε is calculated using

$$\varepsilon = \left(\frac{d_n - d_o}{d_o}\right) \tag{3.5}$$

The stress analysis is performed by the $\sin^2\psi$ method, which is calculated based on a change in the diffraction peak position for more than two orientations of the specimen defined by tilt angle (Mousavi and Miresmaeili, 2008). The stress calculation based on the $\sin^2\psi$ method is expressed as

$$\sigma = \frac{Y}{(1+\nu)\sin^2\psi}\left(\frac{d_\psi - d_o}{d_o}\right) \quad (3.6)$$

where Y, ν represents elastic modulus and Poisson's ratio of parent metal, respectively. ψ is the angle subtended by the bisector of the incident and diffracted beam, keeping the surface as normal position. Besides, d_o represents the interplanar spacing for stress-free surface. The experimental conditions employed for the measurement of residual stress for Ti6Al4V alloy and austenitic stainless steel weldments are indicated in Table 3.9. A circular aperture is used for the stress distribution measurement of stainless steel, while rectangular aperture is utilized for the Ti-alloy. Similar measurement technique and methodology has been used for measurement of the residual stress distribution in the 9Cr-Mo steel weld pad. Fig. 3.12 illustrates the method of measurement of residual stress distribution across the weld interface at the middle of the welded structure. The visualization of intermediate stage during experimental investigation of residual stress for pulsed and continuous weld condition is displayed in Fig. 3.13-14, respectively, for Ti6Al4V alloy weldment.

Table 3.9 Parametric value applied during stress measurement using XRD technique

Sample	**Plane**	**Target**	**Wavelength** (Å)	**Voltage** (kV)	**Current** (mA)	**ψ Tilt**	**Bragg Angle**	**d-spacing** (Å)
SS304	{311}	Mn	2.103	25	5	3°	152.8°	1.0819
Ti-alloy	{302}	Cu	1.542	25	5	3°	148.7°	0.0819

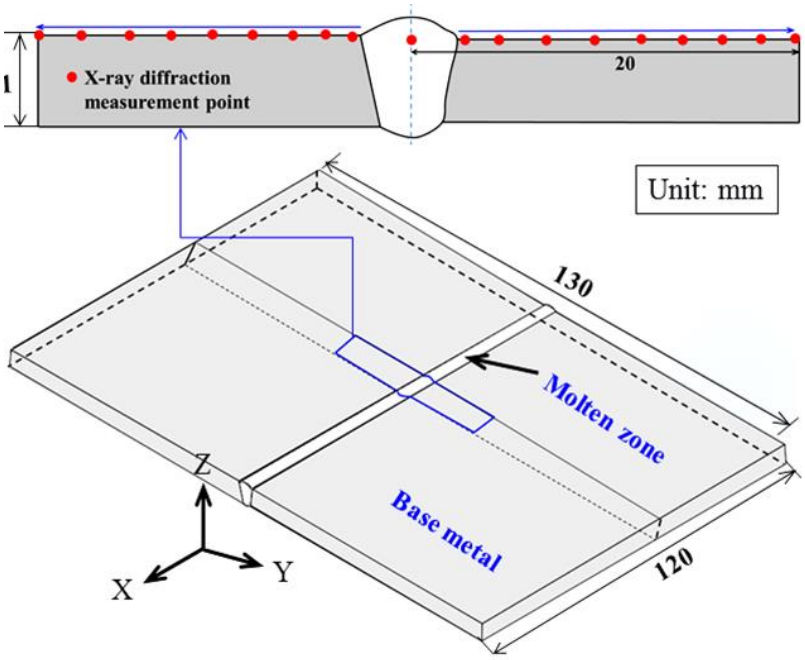

Fig. 3.12 (a) Schematic view of the measurement points of residual stress indicated by red dots for stainless steel welded structure

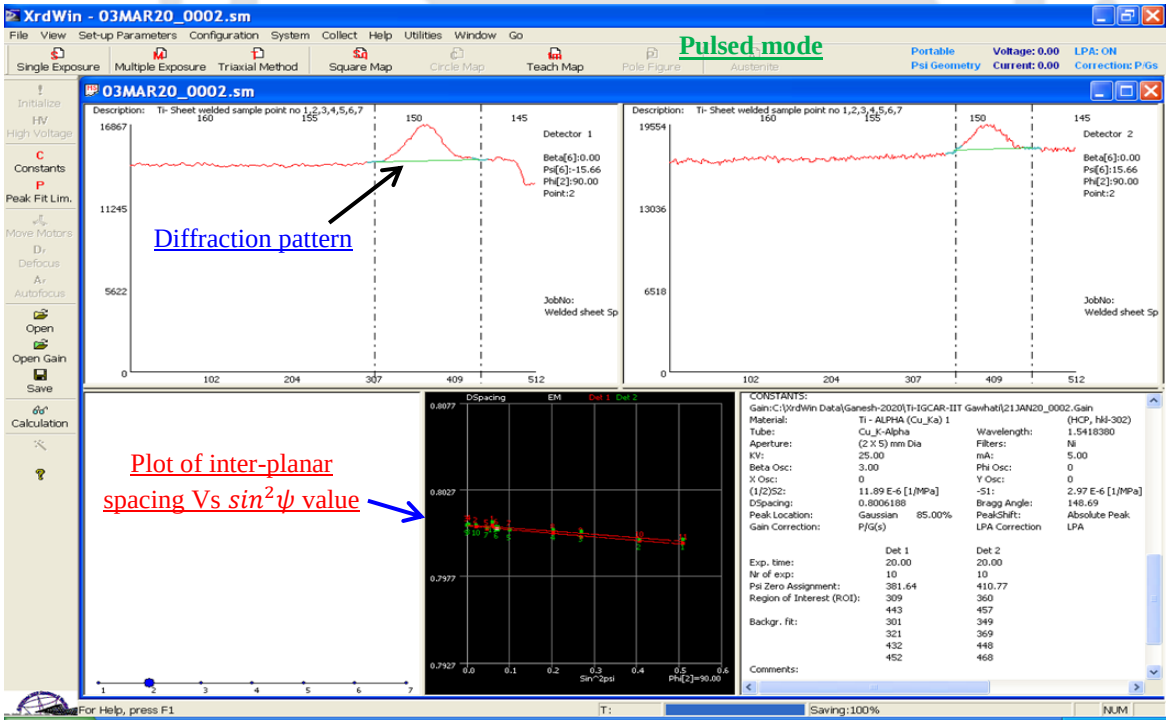

Fig. 3.13 Methodology used for the estimation of residual stress pattern for pulsed welding condition

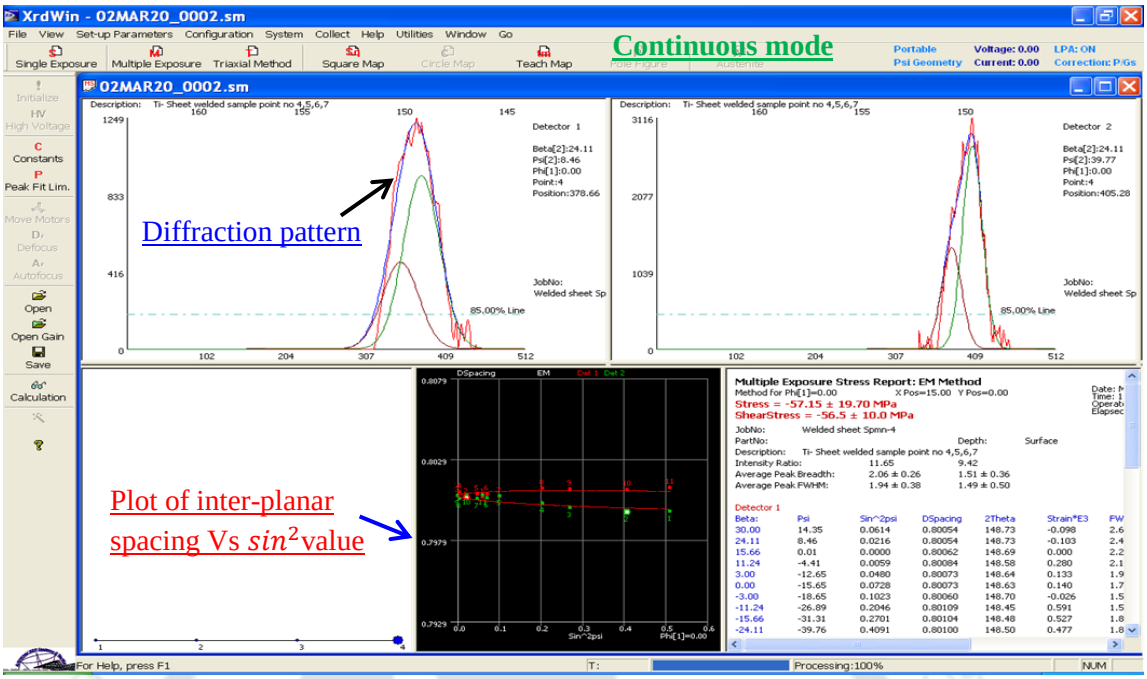

Fig. 3.14 Methodology used for the estimation of residual stress pattern for continuous welding condition

3.6.2 Residual stress measurement of Ti6Al4V alloy

Fig. 3.15 illustrates the surface residual stress measurements across the Ti6Al4V alloy weld metals fabricated using pulsed and continuous current under various process conditions. It is identified that the significant variation in residual stress value is obtained upon changing the mode of welding from continuous to pulse. It is also evident that distinguishable variation in magnitude of residual stress is perceived even at the weld line as well. The utmost compressive stress of magnitude -190 $\pm$ 60 is observed for lowest heat input of 12 J/mm for pulsed mode of operation, while maximum tensile stress of magnitude 116 $\pm$ 19 is perceived for highest heat input of 80 J/mm for continuous mode. Furthermore, upon increasing distance towards base metal residual stress distribution for most of the weld metals converge towards datum line indicates insignificant stress generation at distant location. Our aim of present investigation is to analyze the residual stress distribution accurately and try to diversify its behavior from destructive direction to constructive application. The metallurgical transformation and assisted solidification behavior that come into existence during changing the mode from continuous to pulse is responsible for this alteration is extensively discussed in Chapter 7. However, it can be

conclude here that the heat input is deterministic parameter along with mode change of welding that influences intermediate phenomena during and instantly after the welding process, can alters residual stress pattern for laser welded thin structure of Ti-alloy sheet.

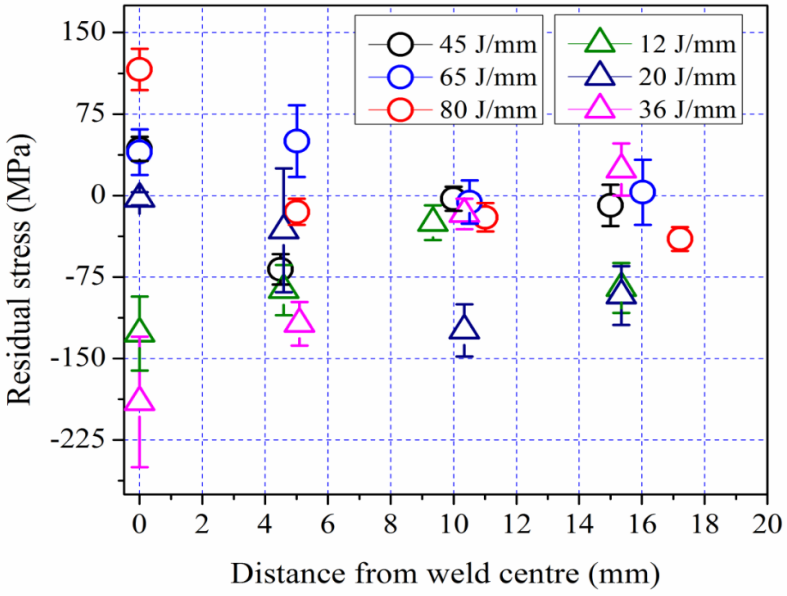

Fig. 3.15 Longitudinal residual stress distribution across the weld interface for Ti-alloy

3.6.3 Residual stress measurement of SS304

Fig. 3.16a represents the distribution of longitudinal (S11) residual stress across the weld bead at different measurement points for austenitic stainless steel (SS 304) weldments. The M-shape longitudinal residual stress distribution on the surface changes its nature from tensile to compressive at a distance of ~ 8 mm from the weld center for the specimens $S_{56}D_2$ and $S_{75}D_1$. In contrast, it is ~ 10 mm for $S_{75}D_3$. Upon cooling, the contraction of the weld region tries to hold the initial length and may result in the plastic deformation of the weld region. Hence, tensile stress is generated at the weld region. Accordingly, longitudinal compressive stress evolves in the base metal to satisfy the strain compatibility condition. The maximum tensile residual stress is 303 ± 11 MPa at 1 mm from the weld center for $S_{56}D_2$, 328 ± 10 MPa at 2 mm distance for $S_{75}D_1$, and 347 ± 47 MPa at 1.5 mm distance for $S_{75}D_3$. A remarkable difference in residual stress of 44 ± 36 MPa is apparent between weldments $S_{56}D_2$ and $S_{75}D_3$. When the area undergoes a high-temperature difference and experiences excessive contraction, it results in high misfit strain. High heat input (~ 75 J/mm) usually promotes a broader region (up to

~3.5 mm from weld center) of outraged residual stress (average ~ 330 MPa). However, low heat input diminishes the probability of a high tensile residual stress region by lowering the temperature gradient. Upon increasing spot diameter (for -1 mm defocus distance of $S_{75}D_3$), the average tensile residual stress (~ 330 MPa) at region up to ~ 3.5 mm from the weld center increases due to the involvement of a wider HAZ as compared to zero focal distance ($S_{75}D_1$). A small discrepancy in residual stress distribution is observed from one side to another in every case is probably due to misalignment in backing and non-uniform clamping force. Fig. 3.16b shows the distribution of transverse (S22) residual stress across the central weld line. Overall, transverse stress is found to be much smaller than longitudinal stress. When heat input increases from ~ 56 J/mm ($S_{56}D_2$) to ~ 75 J/mm ($S_{75}D_3$), transverse stress also significantly increases from 63 ± 14 MPa to 77 ± 24 MPa. In general, the fusion zone width is the deciding factor for transverse stress distribution (Ishigami et al., 2017). Narrow weld profile at lower heat input remarkably reduces its magnitude even changes its nature from tensile to compressive. At high heat input ($S_{75}D_1$and $S_{75}D_3$), the magnitude of stress at the weld-center line is lower, increasing away from the weld center. At low heat input (~56 J/mm), a high magnitude of residuals stress (63 ± 14 MPa) is observed at the weld line. It gradually reduces to compressive and finally to zero at the outer rim of the weld plate. Fig. 3.16b also shows that the overall transverse residual stress shift towards the compressive in nature upon decreasing heat input.

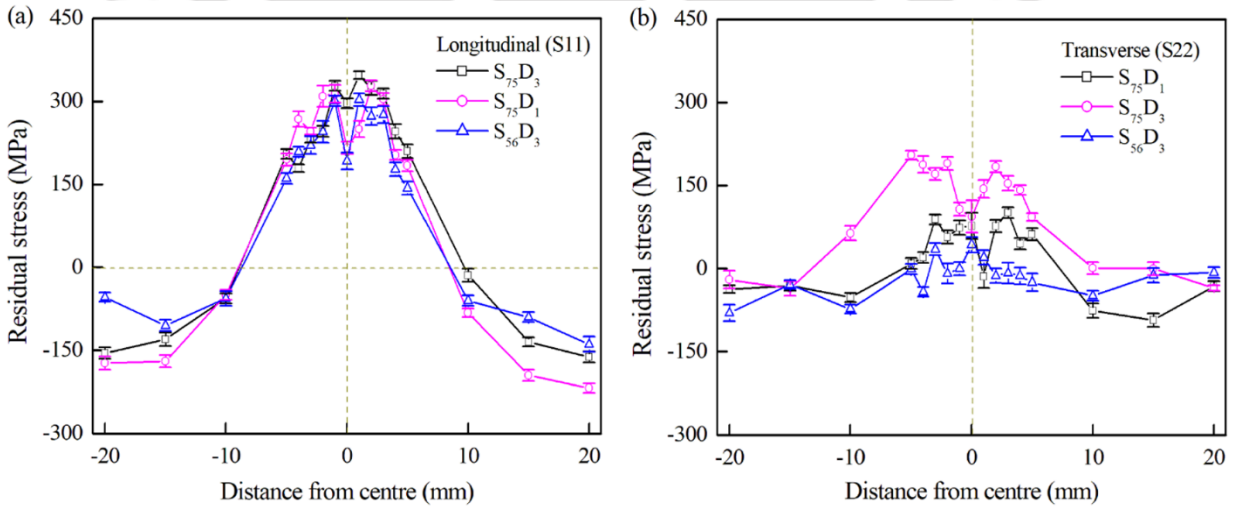

Fig. 3.16 Experimentally measured residual stress distribution for $S_{56}D_2$, $S_{75}D_1$ and $S_{75}D_3$: (a) longitudinal (S11), (b) transverse components (S22)

3.7 Summary

In the current chapter, extensive discussions have been made pertaining to the experimental methodologies employed in order to address the objectives considered in the present dissertation. A wide range as well as combination of process parameters is available for the welding using pulse and continuous modes. However, the domain for the procurement of sound weld is very narrow for thin sheet welding mainly because of low stiffness. The optimization of process parameters are performed through the hit and trial technique. Finally, the sets of parameters are selected to obtain the full depth of penetration for Ti-alloy and austenitic stainless steel joining. Proper shielding and adequate clamping is another essential criterion that has to be fulfilled to produce sound weld, especially for the very thin structure and the metal that is having high affinity for oxidation at elevated temperature (Ti-6Al4V alloy). Hence, the custom-made copper fixture with three coaxially channels for shielding gas systems is adopted to protect the weld pool.

The experimental measurement of residual stress distribution using the X-ray diffraction technique is only limited to the surface since X-ray is unable to penetrate beyond 10 μm. A dilatometry test for varying alloying compositions of 9Cr-Mo steel is systematically explored. However, the purpose of dilatometry analysis may not suitable for thin sheet Ti-alloy and stainless steel. Proper selection of etchant for a specific material is crucial in order to track metallographic analysis. Standard metallography has been followed for the preparation of the samples in case of EDX, FESEM and optical microscopy. The topological analysis helps to measure the surface irregularity in the order of microscale due to the narrow size of the indenter. Therefore, this technique is restricted to the small domain and not applicable for welding of thick plates. The experimentally measured weld bead dimensions are employed for the validation of developed numerical model. Analysis of the microstructure is utilised to develop thermal-metallurgical-mechanical model to understand the influence phase transformation on residual stress distribution in a welded structure.

Chapter 4

4.0 Theoretical Models

4.1 Introduction

The present chapter addresses the theoretical background that has been followed during the development of a sequentially coupled thermal-metallurgical-mechanical (TMM) model for the investigated weld metals using finite element method. The results of numerical model are executed in two different stages. First, the thermal analysis is performed in order to estimate time-temperature history for the entire solution domain through the application of appropriate volumetric heat source. The metallurgical model is developed using constitutive relation guided by temperature flag where solid-state phase transformation is accounted by separate strain component. Finally, the mechanical model is executed in incremental mode using temperature distribution as an input. The material behavior is assumed as elastic-plastic with isotropic hardening and von-Mises yield criteria.

4.2 General background

Fusion welding process is a complex phenomenon due to the involvement of thermal, mechanical and metallurgical variations simultaneously within a small solution domain. The complexity and rapidness of the process make it impossible to capture each phenomenon independently. Thus, finite element (FE) based numerical tool plays a vital role to model such complex physical phenomena in an approximate way. The mathematical model offers better insight into the underlying physics involved in the fusion welding process. In the current work, a FE-based numerical model is established to analyse laser welding, shielded metal arc welding (SMAW), and electron beam welding (EBW) processes. Further, the material models are also improved by defining the solid-state phase transformation kinetics. The thermal analysis is carried out using Fourier conduction model. A sequentially coupled thermo-elasto-plastic model is also developed to simulate the mechanical response of the welded structure using commercial software ABAQUS. The FE model estimates the temperature field, cooling rate, phase fraction, volumetric strain, and weld induced distortion and residual stresses. However, the fluid flow of the molten pool is not considered in the present analysis because it has insignificant impact on the residual stress pattern and associated distortion. The phase transformation kinetics and resulting volumetric strain is incorporated through USDFLD and UEXPAN subroutines for three different materials, i.e., Ti6Al4V alloy, austenitic stainless steel and 9Cr-Mo steel. Overall, the metallurgical model is developed by utilizing the microstructural morphologies and dilation curve for different alloying compositions of P91 steel weldments. The coupled analysis is executed in two different stages. In former stage, a transient non-linear heat transfer analysis is carried out to estimate time-temperature field for entire welding process. The prediction of fusion zone (FZ) and heat-affected zone (HAZ) are performed using isotherm contours. The metallurgical-mechanical analysis incorporates thermal history as input within predefined field for the accomplishment of phase transformation and associated residual stress in a welded structure.

4.3 Conduction mode heat transfer analysis

It is well-known fact that only heat conduction model is sufficient for a thin and thick weld structure. Also, the assumption of only conduction for a stationary liquid with adjustment of effective thermo-physical properties makes a substitute for computationally expensive fluid flow model. To compensate the convective flow of liquid, the volumetric heat source is often preferred by replacing actual heat source (Ghafouri, 2018). The formulation of thermal model follows several assumptions, which are pointed out as follows:

- The specimen is assumed to be solid deformable body without any mass diffusion during welding and totally stress free. The top surface of molten zone is assumed to be flat, neglecting the influence of shielding gas pressure.
- Only half of the solution domain is accounted due to symmetry with respect to weld velocity vector. This minimizes the computational time.
- A homogenous and isotropic material property along with phase transformation is considered.
- The thermo-physical properties of the substrate materials are considered as temperature dependent.
- The initial temperature of weldment is assumed as 300 K.

The transient temperature field is estimated based on 3D Fourier heat conduction equation which is expressed as

$$\frac{\partial}{\partial x}\left(k\frac{\partial T}{\partial x}\right)+\frac{\partial}{\partial y}\left(k\frac{\partial T}{\partial y}\right)+\frac{\partial}{\partial z}\left(k\frac{\partial T}{\partial z}\right)+h_g=\rho_j C_{pc}\left(\frac{\partial T}{\partial t}-V\frac{\partial T}{\partial x}\right) \quad (4.1)$$

where ρ_j is density of weldment (i.e. j could be Ti6Al4V, SS304, 9Cr-Mo steel in kg/m^3), k denotes the thermal conductivity (W/m K), h_g is rate of internal heat generation in the solution domain, C_{pc} is specific heat (J/kg K), T denotes temperature (K), V is the welding speed along x-axis (m/s), t is time (s), and x, y, z are coordinate axis. The term on the left side represents conductive heat transfer within solution domain. The first term of right side refers to the transient nature of the heat transfer and the second term accounts the weld velocity.

The thermal boundary conditions imposed over the all surfaces of solution domain is depicted in Fig. 4.1. At the contact surface with fixture, the effective boundary condition is in the form of convective heat transfer. The different nature of boundary conditions is imposed as follows.

a. Dirichlet boundary condition, where the initial temperature of full geometry is assumed as ambient (T_i) i.e. at time $t = 0$

$$T(x, y, z, 0) = T_i = 300\ K \tag{4.2}$$

b. Temperature gradient normal to the symmetric surface is zero

i.e., $\frac{\partial T}{\partial y} = 0$ (4.3)

c. Natural or Neumann boundary condition; heat transfer at all the surfaces is given by

$$k\frac{\partial T}{\partial n} - q_f + \varepsilon_j \sigma_B (T^4 - T_i^4) + h_c (T - T_i) = 0 \tag{4.4}$$

where k denotes isotropic thermal conductivity, q_f is heat flux applied on weldments, ε_j is the emissivity for investigated material, σ_B denotes Stefan-Boltzman coefficient (5.67×10^{-8} $Jm^{-2}s^{-1}K^{-4}$), h_c is the convective heat transfer coefficient between welded surface and outer environment. The convection coefficients of 25 $Wm^{-2}K^{-1}$ for Ti-alloy, 17 $Wm^{-2}K^{-1}$ for 9Cr-Mo alloy and 100 $Wm^{-2}K^{-1}$ for SS304 is assigned to the surface which are in contact with air (Baruah and Bag, 2017, 2016; Yaghi et al., 2008). Nevertheless, the bottom surface and the section of top surface which are in close contact with copper fixture (accelerates rate of heat transfer) and clamping plate respectively, are allocated relatively higher (1000 $Wm^{-2}K^{-1}$) heat transfer coefficient value for all materials (Baruah and Bag, 2017).

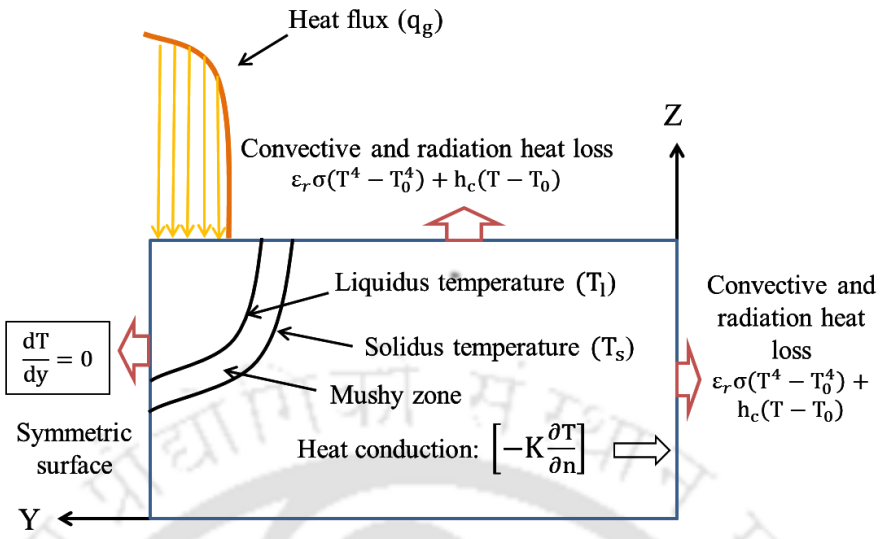

Fig. 4.1 Boundary interaction associated with thermal simulation

The whole solution geometry is discretized using eight nodded brick elements and further, the governing equation and boundary conditions are discretized using Galerkin's weighted residue technique. Different types of volumetric heat sources are implemented in different welding processes.

4.4 Heat source model

The correct estimation of temperature field is important to precisely calculate residual stress distribution. Hence, the role of heat source model is significant in conduction mode heat transfer analysis where the interaction of laser and material is represented by a volumetric heat. It is well-known fact that surface heat source is unable to produce adequate depth of penetration, until a well-structured heat source model is described to account the penetration depth by a high energy density laser beam. Depending upon the shape and size of weld zone, the suitable heat source model is adopted here. A double ellipsoidal heat source model (Soylemez, 2018; Yadaiah and Bag, 2012) is considered for laser welding of Ti6Al4V alloy. When, full depth of penetration is achieved, an hourglass-type heat source model is more suitable to define the unique weld pool shape. Even hourglass heat source is flexible enough to accommodate different weld pool shape

associated with laser welding process. However, the experimentally measured weld dimensions are generally mapped with heat source parameters. In all the cases, the heat source parameters are needed to define before start of the simulation.

4.4.1 Double ellipsoidal model

Well-established double-ellipsoid type heat source model has been applied for arc and laser welding processes to perform thermal simulation (Yadaiah and Bag, 2012). This model is considered as a most versatile and based on the fusion of two ellipsoids, i.e., rear and front having semi-axis a_r and a_f, respectively as shown in Fig. 4.2a. These ellipsoids are geometrically different but maintain C^1 continuity. Selection of parameters for double ellipsoidal model is a challenging task. Most of the researchers use trial and error method for optimization of the parameters. The width and depth of ellipsoid is mapped from experimental measurement as demonstrated in Fig. 4.2a. However, the length of front and rear ellipse is estimated by trial and error method. Besides, the pulse phenomena is incorporated through a time varying function, $h(t_p)$. The power density distribution inside the front quadrant is defined as

$$q_f(x,y,z) = h(t_p)\frac{6\sqrt{3}(f_f Q)}{cba_f\pi\sqrt{\pi}}\exp\left(\frac{-3(x-vt)^2}{a_f{}^2} - \frac{3y^2}{b^2} - \frac{3z^2}{c^2}\right) \quad (4.5)$$

whereas, the power density at rear ellipsoid of heat source is expressed as

$$q_r(x,y,z) = h(t_p)\frac{6\sqrt{3}(f_r Q)}{cba_r\pi\sqrt{\pi}}\exp\left(-\frac{3(x-vt)^2}{a_r{}^2} - \frac{3y^2}{b^2} - \frac{3z^2}{c^2}\right) \qquad x < 0 \quad (4.6)$$

where a_f, a_r signifies the extent of heat source from its center in the front and rear ellipsoid respectively, b is bead width, and c is depth of penetration parallel to the x, y, z axes respectively. Moreover, weighting fraction of heat deposition corresponding to rear and front ellipse are designated as f_r and f_f, respectively such that f_r+f_f = 2. Since, the temperature gradient in front part is steeper than rear part so f_f, f_r are assumed as 1.33 and 0.67, respectively (Deng and Murakawa, 2008). Further, $h(t_p)$ signifies the temporal variation of power density, i.e., at pulse on-time, the value of $h(t_p)$ is 1 and at pulse off time, the value of $h(t_p)$ is 0. The optimized heat source parameters used in the present analysis is depicted in Table 4.1.

Table 4.1 Parameters used in double ellipsoidal heat source model

Parameter	a_f	a_r	b	c	$f_f = \frac{2a_f}{a_f + a_r}$	$f_r = \frac{2a_r}{a_f + a_r}$
Value (mm)	1.5	3.0	0.12	0.8	0.67	1.33

The highly predominating characteristics of the double ellipsoid geometry is that it can be easily changed to model both the shallow penetration in arc welding as well as the deeper penetration in high energy beam density welding processes (De et al., 2003). The Gaussian distribution of heat flux density is more realistic representation of laser beam welding. However, this heat source may not suitable to represent welding where full depth of penetration is achieved. Therefore, the author investigated an alternate heat source model, which follows an hourglass type profile.

4.4.2 Hourglass heat source model

When heat input is more, an equivalent heat source assortment with a specific volumetric shape is of significant interest. However, finding a satisfactory spatial distribution is not easy since power density is approximately remains constant in upper half and lower half of the thickness in a full-penetrated laser welding system. The simplest method is to identify the energy distribution from the weld bead shape. It is indicated from the macrograph that the shape of the full-penetrated welds cannot be precisely represented by the double ellipsoidal heat source. Therefore, an hourglass-like heat source model is developed that can attain unique shape of weld bead profile in case of austenitic steel and 9Cr-Mo steel weld (Zhan et al., 2017). The schematic diagram of the hourglass heat source is demonstrated in Fig. 4.2b. The mathematical expression of hourglass heat source is briefly explained in Appendix A. The power distributions in upper and lower cone acquired in such a way that the weighting fraction of heat deposition at top and bottom would be higher than the mid surface. The heat flux distribution is represented as

$$\dot{Q}(Z, r) = \frac{3d\eta P}{\pi.[1-\exp(-d)].(Z_t - Z_m)[{r_m}^2 + r_m.r_t + {r_t}^2]} \exp\left[-d\frac{r^2}{{r_{eff}}^2}\right]; \qquad \text{for upper cone } (Z_o \geq Zm) \tag{4.7}$$

$$\dot{Q}(Z,r) = \frac{3d\eta P}{\pi.[1-\exp(-d)].(Z_m - Z_b)[r_m{}^2 + r_m.r_t + r_t{}^2]} \exp\left[-d\frac{r^2}{r_{eff}{}^2}\right]; \qquad \text{for lower cone } (Z_o < Zm)$$

(4.8)

where d is a power distribution function, Z_t is the total height, Z_m is the mean height, Z_b is bottom height and Z_o is variable, whereas r_m, r_t and r_b are radius corresponding to mid, top and bottom surface of hourglass, respectively. The effective radius of the upper half cone and the lower cone is extracted from experimental measurement and is expressed as

Upper truncated cone: $r_{eff} = \frac{Z_o - Z_m}{Z_t - Z_m}(r_t - r_m) + r_m \qquad Z_o \geq Zm$ (4.9)

Lower truncated cone: $r_{eff} = \frac{Z_o - Z_b}{Z_m - Z_b}(r_b - r_m) + r_m \qquad Z_o < Zm$ (4.10)

The radial distance is at any depth is defined as

$r^2 = (x - vt)^2 + y^2$ (4.11)

where x and y are Cartesian coordinate system and ‘vt’ indicates the distance moved by the heat source at time t.

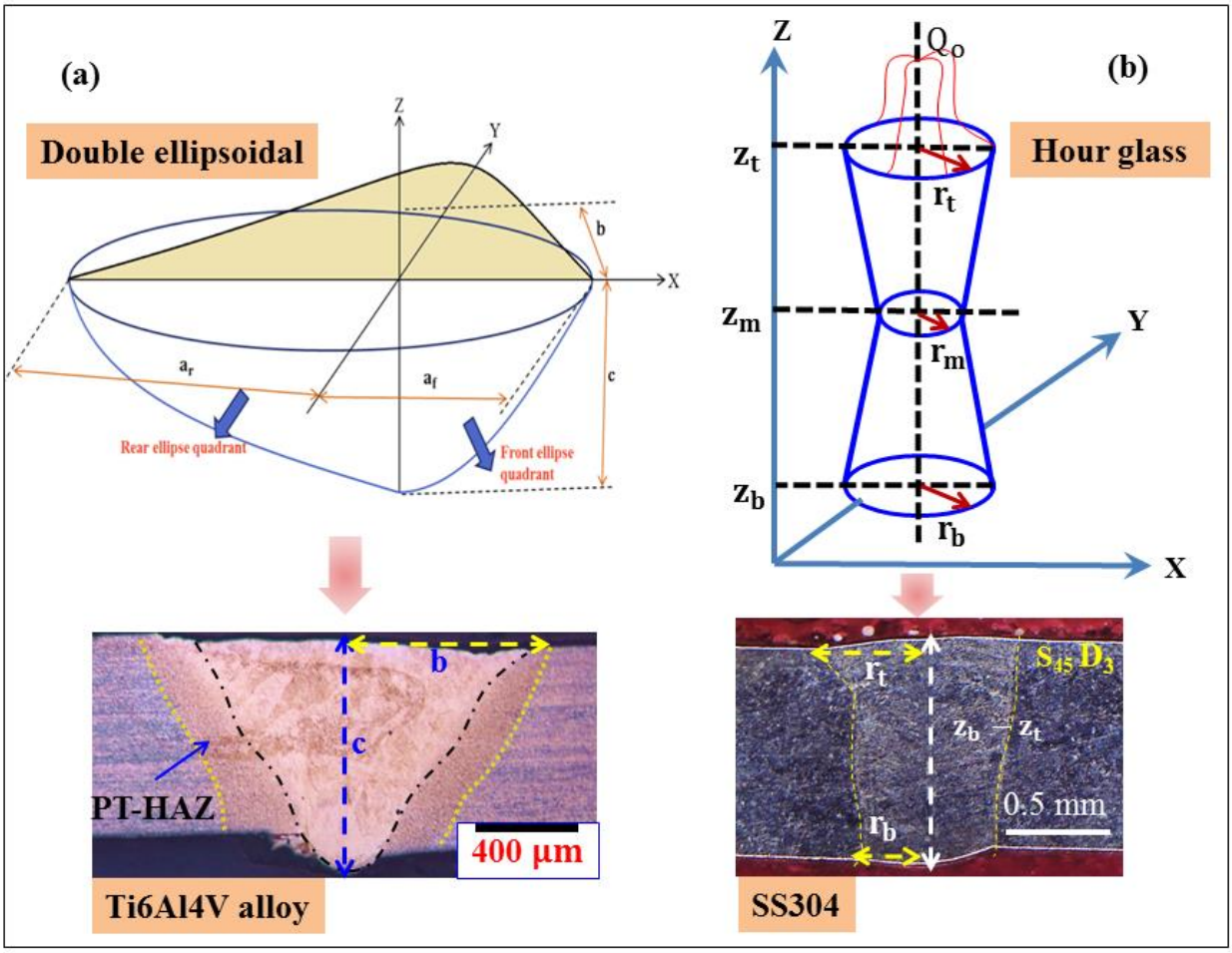

Fig. 4.2 Schematic diagram of heat source model (a) Double-ellipsoidal, (b) Hourglass

4.5 Mechanical analysis

The mechanical analysis is executed by the application of nodal temperature data, which is obtained from thermal analysis and implemented as a predefined field for each incremental time step. As inertia does not have an impact on mechanical response of the weldments, hence static stress mechanism is undertaken for the present investigation. The static equilibrium equation based on Lagrangian reference frame is expressed as

$$\frac{\partial \sigma_{ij}}{\partial x_j} + b_i = 0 \qquad (4.12)$$

The stress tensor is symmetric in nature, i.e. $\sigma_{ij} = \sigma_{ji}$ (4.13)

where σ_{ij} denotes Cauchy stress tensor and b_i is sum of the body force vector. The total strain (ε_{ij}^{t}) is represented as the sum of the discrete components of the elemental strain as

$$\varepsilon_{ij}^{t} = \varepsilon_{ij}^{el} + \varepsilon_{ij}^{thrml} + \varepsilon_{ij}^{cp} + \varepsilon_{ij}^{pl} + \varepsilon_{ij}^{trp} + \varepsilon_{ij}^{vp} + \varepsilon_{ij}^{ptr} \quad (4.14)$$

where ε_{ij}^{el} is elastic stain, ε_{ij}^{thrml} is thermal strain, ε_{ij}^{cp} is creep strain, ε_{ij}^{pl} is plastic strain component, ε_{ij}^{trp} is transformation induced plasticity, ε_{ij}^{vp} is visco-plastic strain and ε_{ij}^{ptr} is strain due to phase transformation. The mechanical behavior of the material is determined by using infinitesimal (small) strain theory. Considering thermo-elasto-plastic behavior, the thermal strain is expressed as

$$\varepsilon_{t+\Delta t}^{thrml} = \Delta t \sum_{i=1}^{n} \alpha_i [T(t)] f_i(t+\Delta t) + \sum_{i=1}^{n} \varepsilon_i^{vc} [T(t)] \Delta f_i(t+\Delta t) \quad (4.15)$$

where α_i is thermal expansion coefficient, f_i is the phase fraction of individual phase i and n is the number of existing phases within phase mixture. In the present investigation, the strain component caused by transformation-induced plasticity, creep effect, and visco-plasticity is not considered for the calculation because of their insignificant influence on the residual stress distribution (Ahn et al., 2017). The elastic strain component is estimated using the isotropic Hook's law with temperature dependent modulus of elasticity and Poisson's ratio. As the present study neglected the visco-plastic effect, yield stress is considered independent of strain rate, and depends upon plastic strain and temperature. The weld metals are supposed to follow Von-Mises yield criterion and associated isotropic hardening rule for incorporating rate independent plasticity. It is noted that welding thermal cycle is non-isothermal phenomena, so implementation of isothermal elasto-plastic input data for strain hardening will not help during cooling cycle. To overcome this aberration, annealing step is considered during mechanical simulation by setting up equivalent strain as zero above annealing temperature such that the impact of prior hardening is lost. Incorporation of strain component due to solid-state phase

transformation is thoroughly discussed in Section 4.4. The thermal strain component is calculated using the coefficient of thermal expansion and is expressed as

$$d\varepsilon^{Thrml} = \alpha_t * \Delta T \quad (4.16)$$

where α_t is the thermal expansion coefficient and ΔT is the change in temperature. The constitutive relationship between stress and strains based on Von-Mises yield criterion for thermo-elasto-plastic component is described by

$$\varepsilon_{ij} = \frac{1+\upsilon}{E}\sigma_{ij} - \frac{\upsilon}{E}\sigma_{ij}\delta_{ij} + \lambda S_{ij} + \left[\alpha_t(T - T_i)\delta_{ij}\right] \quad (4.17)$$

where E, α_t, λ, S_{ij} and δ_{ij} are modulus of elasticity, coefficient of thermal expansion, plastic flow factor, deviatoric stress component and kronecker delta notation respectively. For the elastic deformation, λ is zero otherwise it is greater than zero. The Von-Mises stress is represented in terms of deviatoric stress component given by

$$S_{ij} = \sigma_{ij} - \frac{1}{3}\sigma_{kk}\delta_{ij} \quad (4.18)$$

The infinitesimal strain theory or small deformation theory where strains can be expressed as a linear function of displacement is adopted herein for the prediction of distortion in the welded structure. The strain tensor as a function of the displacement gradients is written as

$$\epsilon_{ij} = \frac{1}{2}\left(u_{i,j} + u_{j,i}\right), \; i,j = 1,2,3 \quad (4.19)$$

where ϵ_{ij} is the element of the strain tensor ϵ and $u_{i,j} = \delta u_i / \delta x_j$ is the displacement gradient.

In thermal model, the non-linear heat conduction equation is discretized in the spatial region followed by the temporal (time) domain. The temperature dependent material properties are taken into account where the governing equations and boundary conditions are implemented in element wise. Further, the elemental contributions are assembled to form a global set of equations, which are then solved in order to obtain the state variables for each node point or in an element. The stress model considers the thermal load from time-temperature database and solves for the displacement field by assuming the incremental mode of strain. Except phase

transformation strain, the overall strain increment can therefore be decomposed into three different components as follows

$$\{d\varepsilon^{Total}\} = \{d\varepsilon^{el}\} + \{d\varepsilon^{pl}\} + \{d\varepsilon^{Thrml}\} \quad (4.20)$$

Assuming Prandtl-Reuss rule and Von-Mises Yield criteria, the incremental stress is represented as (Singh et al., 2014)

$$\{d\sigma\} = [D^{ep}]\{d\varepsilon\} - [C^{thrml}]\{dT\} \quad (4.21)$$

$$\text{where } [D^{ep}] = [D^{el}] - [D^{pl}]; [C^{th}] = \{\alpha\}[D^{el}] \quad (4.22)$$

$[D^{ep}]$ is elasto-plastic matrix whereas $[D^{el}], [D^{pl}]$ and $[C^{thrml}]$ represents elastic, plastic and thermal stiffness matrix. $\{dT\}$ is the temperature increment. The elasto-plastic matrix is expressed as

$$[D^{ep}] = \left([D^{el}] - [D^{el}]\left\{\frac{\partial f}{\partial \sigma}\right\}\left\{\frac{\partial f}{\partial \sigma}\right\}^{T}[D^{el}]\frac{1}{3H+E_T}\right) \quad (4.23)$$

where $[D^{el}]$ depicts the elasticity matrix which consists of mechanical properties like Young's modulus and Poisson's ratio, H is shear modulus and E^T is local slope between stress and plastic strain. The elasto-plastic matrix is due to restoration of elastic response when the metal is in plastic deformation zone. The second term on the right hand side of Eq. 22 turns into zero when the metal is in elastic zone only. The function "f" predicts the yield surface and the formation of the yield surface are controlled by the hardening rule. The equivalent stress following von-Mises yield function is expressed as

$$\sigma_{av} = \sqrt{\frac{1}{2}[(\sigma_1 - \sigma_2)^2 + (\sigma_2 - \sigma_3)^2 + (\sigma_3 - \sigma_1)^2]} \quad (4.24)$$

where σ_1, σ_2 and σ_3 are principal stresses and σ_{av} is average one-dimensional stress.

4.6 Solid state phase transformation (SSPT)

The kinetics of solid-state phase transformation is governed by inhomogeneous distribution of alloying element. It exhibits strong influence on the residual stress pattern within the weld pool, which determines the overall mechanical performance of the welded structure (Homporova et al., 2011). Several factors play crucial role for the alteration of residual stress pattern. Melting and solidification, and interaction between recrystallization and solid state phase transformation leads to residual stress modification within the structure during welding process. Effectively, the strain induced during phase transformation can amend the state of retained stress. Usually, phase transformation accounted during cooling cycle, and associated volumetric change can have remarkable effect on retained stress and deformation of the structure. To attain martensitic transformation, it is essential that the thermo-mechanically processed material to be cooled instantaneously and quick enough to surmount the elevated temperature. The diffusion-controlled lamellar structure as well as intermediate secondary phases may occur at relatively slow cooling process. The work hardening of different phases due to variation in specific volume, thermal expansion and crystallographic reorientation of unit cell, is responsible for the generation of transformation induced volumetric strain in carbon steel (Deng et al., 2009). However, in case of pure Titanium, α and β phases are having similar specific volume, leads to insignificant variation in crystallographic arrangement during α to β transformation. In this circumstances, effect of phase transformation on work hardening is negligible and hence, little amount of internal stress generation is desirable during α to β transformation. Nevertheless, diffusionless or martensitic transformation exhibits significant volumetric dilation, which results in modification in residual stress pattern. The variation of temperature during welding alters the lattice parameter through thermal expansion or contraction, which results in volumetric change, hence phase transformation occurs at fusion zone (FZ), and heat affected zone (HAZ). In general, two different modes of phase transformation is accounted during thermo-mechanical processing of materials; one is diffusional and other one is diffusionless transformation. Transformation kinetics associated with these phase change, implementation methodologies, calculation of corresponding volumetric strain and attributed response in stress generation is discussed in this section.

4.6.1 Diffusional transformation

Diffusional transformation is characterized by chemical composition variation from parent phase to daughter phase and requires long-distance diffusion. On the other hand, diffusional growth might proceed in another fashion, i.e., parent phase decomposes into one or more daughter phases with similar composition, however, different crystalline structure. Primarily, it comprises of nucleation and growth mechanism (Elmer et al., 2004). Nucleation can be continuous and site saturation based on the size and number of nucleated particles at the interface of parent and daughter phase (Kempen et al., 2002). Diffusional phase transformation can be attained at both, i.e., heating and cooling cycle during welding for Ti6Al4V alloy and 9Cr-Mo steel alloy. Heating stage renders phase change from α (HCP) + β (BCC) → β(BCC) i.e. diffusional growth of β on α/β matrix. Whereas cooling stage accomplishes $\beta \rightarrow \beta + \alpha/\alpha'$ transformation for Ti-alloy in accordance with attained cooling rate beyond β-transus temperature (Yang et al., 2019). Besides, austenitic stainless steel (SS304) follows diffusional mechanism for transformation from δ-ferrite (BCC) → γ-austenite (FCC) within narrow range of temperature during cooling cycle because phase transformation is insignificant at heating stage.

4.6.1.1 Transformation kinetics in heating cycle

During heating cycle, dual phase Ti-alloy exhibits rapid diffusional transformation from α-phase to β-phase, which implies nucleation and growth of β-phase and dissolution of α -phase in prior α/β interface. β-phase is intergranular phase due to which it is difficult to recognize and estimate its amount in mixed condition. Hence, it is assumed that beta phase fraction increases by equivalent amount of alpha dissolution. Once transformed β-phase fraction attains equilibrium amount, it follows beta equilibrium curve as shown in Eq. 4.25. For the sake of convenience, it is assumed that initially Ti-alloy consists of only α-phase and consequently α → β transformation occurs during heating cycle. Eq. 4.26 depicts the estimation of α -phase fraction by subtracting it from current β-phase fraction from equilibrium β-phase fraction as (Ahn et al., 2017)

$$f_{\alpha\rightarrow\beta}(t_1, T_1) = f_{\beta}^{eqb.}(T_1) \tag{4.25}$$

$$\Delta f_{\alpha\rightarrow\beta}(t_1, T_1) = -\Delta f_{\alpha} = f_{\beta}^{eqb.}(T_1) - f_{\beta}(t_o, T_o) \tag{4.26}$$

It is presumed that α to β transformation follows Modified Avrami-Function equation based Weibull probability distribution function of temperature (Buffa et al., 2013, 2012). $\alpha \rightarrow \beta$ transformation during heating cycle is expressed as

$$f_{\alpha\rightarrow\beta}(t_1, T_1) = 1 - \exp\left[K_{\alpha\rightarrow\beta} \left(\frac{T - T_{\alpha\rightarrow\beta}}{T_\beta - T_{\alpha\rightarrow\beta}} \right)^{\gamma_{\alpha\rightarrow\beta}} \right] \qquad (T_\beta \geq T \geq T_{\alpha\rightarrow\beta}) \tag{4.27}$$

$$f_{\alpha\rightarrow\beta}(t_1, T_1) = f_\beta^c(T_\beta) = 1 \qquad (T > T_\beta) \tag{4.28}$$

where $f_{\alpha\rightarrow\beta}$ is growth of phase fraction β that get transformed from prior α-phase at temperature T_1 during heating. The parameter $K_{\alpha\rightarrow\beta}$ is rate constant and $\gamma_{\alpha\rightarrow\beta}$ is Avrami exponent, are considered as – 1.86 and 4.35 respectively, accessed from TTT diagram for Ti6Al4V alloy (Buffa et al., 2013). $T_{\alpha\rightarrow\beta}$ is α-dissolution temperature (i.e. 940 K) and T_β is β-transus temperature (1275 K). The term f_β^c represents the equilibrium β-phase fraction at β transus temperature. Likewise, modified John-Mehl-Avrami-Kolmogorov (JMAK) based transformation kinetics for Ti-alloy is followed for the prediction of decomposition of α-ferrite phase into γ-austenite during modeling of austenitic transformation in case of 9Cr-Mo steel. Initially it is presumed that 9Cr-Mo steel completely comprises of ferrite phase. As the temperature increases beyond Ac1, the austenite phase fraction (γ) progressed by an amount equivalent to that of reduction in ferrite phase fraction. Critical temperature, i.e., Ac1 and Ac3 corresponding to austenitic transformation for different weld metal compositions are taken from the THERMOCALC software to model $\alpha \rightarrow \gamma$ transformation for four different weldments. Additionally, $K_{\alpha\rightarrow\gamma}$ and $\delta_{\alpha\rightarrow\gamma}$ are material constants corresponding to $\alpha \rightarrow \gamma$ transformation employed from the literature as -4.9 and 2 respectively for Cr-Mo steel corresponding to 98% phase transformation (Bennett et al., 2013; Iracheta et al., 2015).

4.6.1.2 Transformation kinetics in cooling cycle

Solid-state phase transformation (SSPT) during cooling cycle whether it is diffusional or diffusionless, plays decisive role in determining the final state of residual stress and corresponding mechanical behavior of welded structure. Austenitic stainless steel possesses

diffusional transformation in a narrow range of temperature during cooling cycle. However, significantly high cooling rate is attained by Ti-alloy weldment and air-hardenable 9Cr-Mo steel with the current range of process parameters. Therefore, diffusional SSPT is not considered for these alloys in the present work. However, diffusional SSPT is investigated only for SS304 steel weldment. The phase transformation behavior of SS304 is well described by a pseudo-binary diagram of the Fe-Cr-Ni ternary system (depicted in Fig. 4.5). Additionally, the transformation kinetics is predominantly determined by its solidification behavior which is a function of Chromium equivalent [$Cr_{eq.}$] and Nickel equivalent [$Ni_{eq.}$]. In order to determine the solidification mode of laser welding, [$Cr_{eq.}$] and [$Ni_{eq.}$] are calculated. The value of [$Cr_{eq.}$] and [$Ni_{eq.}$] is estimated as 20.9 and 12.4, respectively, and fitted on the isopleth of ternary diagram of Fe-Ni-Cr system (with 70 wt.% Fe-content).

SS304 follows eutectic reaction comprises of a liquid, γ-austenite, and δ-ferrite phases within solidus (1673 K) and liquidus (1723 K) range of temperature as shown in Fig. 4.5 (Lippold and Kotecki, 2005). The kinetics for the transformation from a liquid phase to some other solid phases is not considered since present investigation is fully focused on solid-state phase transformation. On the verge of SSPT, austenitic steel is composed of γ-austenite and δ-ferrite at solidus temperature. The solubility of austenite (Ni) is relatively high at elevated temperature and δ-ferrite is highly stable at elevated temperature. For the current study, the initial phase fraction of γ-austenite and δ-ferrite is arbitrarily assumed as 5-6% and 94-95% respectively, at solidus temperature (Lippold and Kotecki, 2005). It is assumed that δ-ferrite → γ-austenite transformation follows JMAK equation, which is expressed as (Avrami, 1940)

$$f_\gamma(T(t)) = \left[1 - \exp\left(-k_{\delta\to\gamma}(\tau)^{N_{\delta\to\gamma}}\right] . f_\gamma^{\,eqb.} \qquad (4.29)$$

where f_γ is volume fraction of austenitic phase at a particular temperature T and time t; $k_{\delta\to\gamma}$ defines the nucleation and growth rate, and explicitly depends on temperature. $N_{\delta\to\gamma}$ is Avrami coefficient taking care of nucleation and growth mechanism whereas $f_\gamma^{\,eqb.}$ represents the maximum phase fraction of γ-phase at equilibrium stage. Based on TTT diagram, the maximum transformation is considered as 98% and accordingly $N_{\delta\to\gamma}$ and $k_{\delta\to\gamma}$ is calculated as 2.65 and 0.01, respectively (Kemda et al., 2019).

To employ JMAK theory for the assessment of non-isothermal transformation kinetics, continuous cooling curve is discretized into several isothermal steps as depicted in Fig. 4.3. If t_j is time required to attain phase fraction (f_i) during isothermal holding at T_j and Δt_j is incremental step time considered at temperature T_i during continuous cooling, then

$$\sum_{j=1}^{i} \frac{\Delta t_j}{t_j} = 1 \tag{4.30}$$

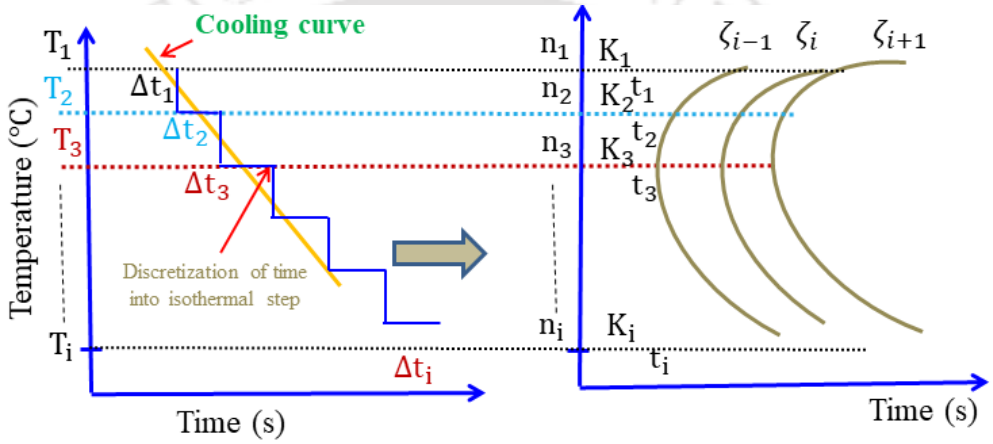

Fig. 4.3 Schematic diagram representing discretization of cooling curve and corresponding phase fraction in TTT-curve

From the basic formulation of JMAK equation, degree of transformation can be obtained as

$$f_i = 1 - \exp[-(K_1.t_1)^{n_1}] = 1 - \exp[-(K_2.t_2)^{n_2}] = .. = 1 - \exp[-(K_i.t_i)^{n_i}] \tag{4.31}$$

4.6.1.3 Conversion into non-isothermal domains

Eq. 4.29 is applied to predict phase fraction growth of isothermal transformation, although the welding process is associated with non-isothermal behavior. Several successful attempts are made to utilize the isothermal kinetics for non-isothermal processes using different approaches (Elmer et al., 2004; Farjas and Roura, 2006; Kherrouba et al., 2016; Martin, 2010). Although Eq. 28 is derived for isothermal process, it forms the basis for non-isothermal process as well. The conversion mechanism of isothermal into non-isothermal transformation using

Scheil's and Steinberg's (Verdi and Visintin, 1987) additive rule is explained in Fig. 4.4. It is most widely used technique to define non-isothermal phase transformation kinetics (Elmer et al., 2003; Kelly et al., 2005). It states that the total time required to achieve a certain phase fraction under continuous cooling can be attained by adding the fraction of time to reach same phase fraction in an isothermal increment until the sum approaches unity (Kemda et al., 2019). Continuous cooling transformation (CCT) curve is discretized into addition of consecutive isothermal steps at temperatures T_1,T_2 and T_3. The continuous variation of temperature with time is estimated by succeeding isothermal steps of incremental time Δt_1, Δt_2 and Δt_3. The metallurgical transformation kinetics is approximated from TTT-diagram for each and every isothermal step. Hence, phase fraction is known corresponding to particular time and isothermal step. Furthermore, this time is relocated as fictitious time during next isothermal step arrival. Finally, evaluation of daughter phase fraction is transferred into actual (or real) time scale. Black, blue and brown dotted line represents isothermal temperature T_1,T_2 and T_3 followed by incremental time Δt_1, Δt_2 and Δt_3. Scheil's additivity principle is written as

$$\int_0^{t_o} \frac{dt}{t(f_o,T)} = 1 \qquad (4.32)$$

where $t(f_o, T)$ is the time needed to achieve fraction f_o isothermally at temperature T.

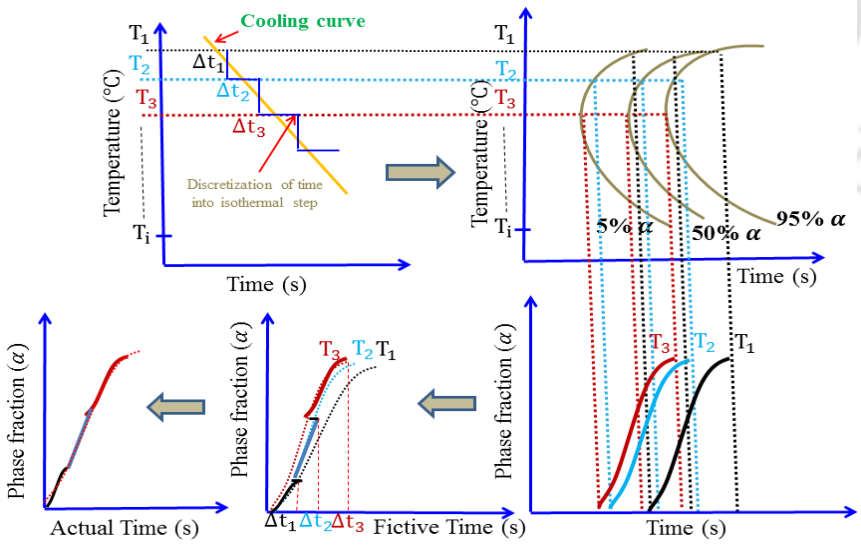

Fig. 4.4 Representation of additive principle for the conversion of isothermal approach into non-isothermal kinetics (Charles, 2016; Grong and Shercliff, 2002; Kelly et al., 2005; Malinov et al., 2001)

For the incorporation of non-isothermal behavior of phase transformation, the term fictious time t^* is introduced. It is the time required for the transformation to arbitrary volume fraction k, i.e., $f_{\delta\to k}$ at temperature T_o, considering an isothermal transformation at temperature $T_o + \Delta T$. The fictious time is estimated as (Kemda et al., 2019; Kumar and Dixit, 2018)

$$\tau^* = \left\{\frac{1}{-k_{\delta\to k}}.\ln\left(1-\frac{f_{\delta\to k}^{eqb.}(T_o)}{f_{\delta\to k}^{eqb.}(T_o+\Delta T)}\right)\right\}^{1/N_{\delta\to k}} \tag{4.33}$$

To estimate the equilibrium phase fraction of γ-phase at a particular temperature T_t and $T_{t+\Delta t}$, equilibrium phase fraction for $\delta \to \gamma$ transformation is plotted against temperature using the Avrami model (Ahn et al., 2017; Avrami, 1940). Hence, by incorporating fictitious time, Eq. 4.29 is modified as

$$f_\gamma(t+\Delta t, T+\Delta T) = \begin{cases} \left[1-\exp\left(-k_{\delta\to\gamma}(\tau_0^* + \Delta\tau)^{N_{\delta\to\gamma}}\right)\right].f_\gamma^{eqb.} & (1273\ K \le T < 1673\ K) \\ 0.05 & (T > 1673\ K) \end{cases} \tag{4.34}$$

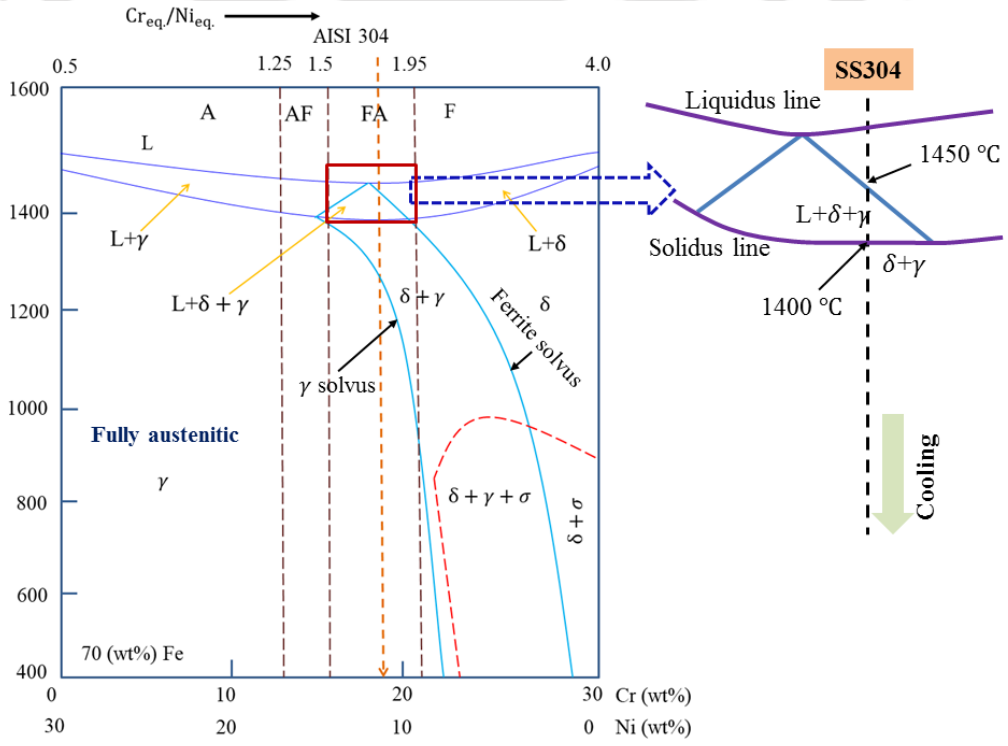

Fig. 4.5 Isopleth of ternary Fe-Ni-Cr system with 70 wt.% Fe-content

4.6.2 Diffusionless transformation

The transformation in which the chemical composition of the nascent phase, which is thermodynamically metastable, remains identical to parent phase, however, the crystallographic arrangement changes is termed as diffusionless transformation (James and Moon, 1970). Diffusionless transformation is associated with high cooling rate. Higher is the solidification rate, the chances of getting diffusionless transformation would be more. Martensitic transformation is diffusionless or displacive transformation which is accompanied by change in crystallographic arrangement from BCC (β-phase) → HCP (α′-phase) for Ti6Al4V alloy (Fig. 4.6), and from FCC (γ-austenite) → BCT (α′-phase) for 9Cr-Mo steel, whereas chemical composition remains same as parent phase (Xia and Jin, 2018).

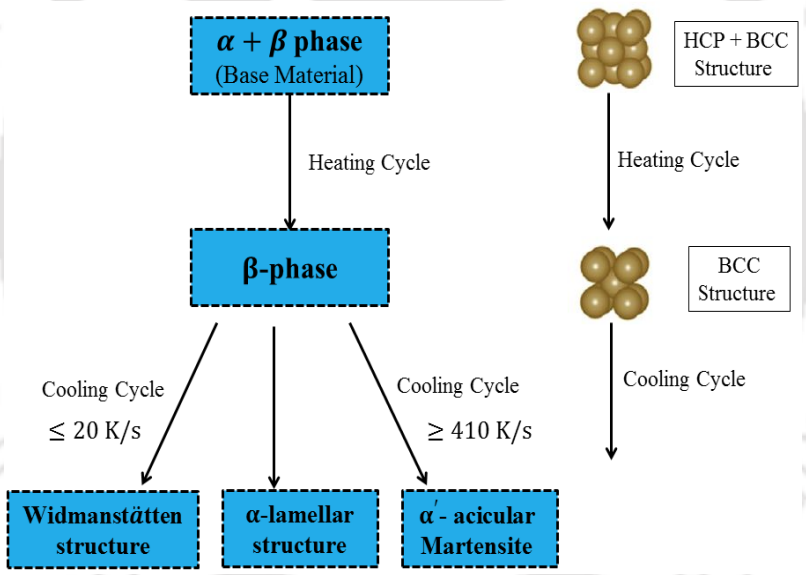

Fig. 4.6 Transformation diagram associated with welding of Ti6Al4V alloy

The cooling rate determines the nascent daughter phase and associated microstructure evolution in case of dual phase Ti-alloy weldment. Beyond critical cooling rate (>410 K/s), hexagonal α′-acicular type martensitic structure is predominant (Ahmed and Rack, 1998). Due to the involvement of rapid cooling in laser welding process, only martensitic transformation is expected in the present study. It is assumed that martensitic transformation follows Koistenen-Marburger (KM) formulation and is expressed as

$$f_{\beta\rightarrow\alpha'}(t,T) = 1 - \exp\left[-K_{\beta\rightarrow\alpha'}\left(T_{\beta\rightarrow\alpha'} - T\right)\right].\ f_{\beta}(t,T) \qquad (T_{\alpha'} \leq T \leq T_{\beta\rightarrow\alpha'}) \tag{4.35}$$

where $f_{\beta\rightarrow\alpha'}$ is phase fraction of α'-aiccular martensitic structure at current temperature T during cooling stage and $K_{\beta\rightarrow\alpha'}$ is material constant taken as 0.015 for Ti6Al4V alloy. $T_{\beta\rightarrow\alpha'}$ is martensitic start temperature (1053 K) whereas $T_{\alpha'}$ is martensitic finish temperature (i.e. 923 K). $f_{\beta\rightarrow\alpha'}$ is updated as martensitic phase fraction at every incremental step and is depicted as

$$f_{\beta\rightarrow\alpha'}(t_1,\ T_1) = f_{\beta\rightarrow\alpha'}(t_0,\ T_0) + \Delta f_{\alpha'} \tag{4.36}$$

Furthermore, similar transformation kinetics is adopted for 9Cr-Mo steel weldments in order to trace the fractional growth of martensitic phase at different alloying compositions (Table 3.8). The non-diffusional or shear-type martensitic transformation needs sufficiently high driving force rather than diffusion-controlled growth of ferrite from austenite because mechanical shearing of the austenite lattice requires more energy to be transformed into martensite. The critical temperature, i.e., Ms and Mf corresponding to martensitic transformation is approximated from volumetric dilation curve at varied weld compositions. $K_{\gamma\rightarrow\alpha'}$ represents the overall rate constant and the value is 0.02 K^{-1} which is extracted from CCT diagram corresponding to cooling rate of 50 K/s (Heinze et al., 2013). In addition, it is stated that the rate constant depends on alloy composition, especially on the carbon content and a value of 0.02 K^{-1} is reported for low carbon steel (Van Bohemen, 2012).

4.6.3 Volumetric strain

Volumetric contraction or expansion during heating or cooling stage and corresponding volumetric strain accompanied by phase transformation is algebraically added to thermal strain component. Hence, the overall strain comprises of

$$d\varepsilon^{th} + d\varepsilon^{ptr} = \alpha(T)\ .\Delta T + \alpha_{ptr}(T)\ .\ \Delta T \tag{4.37}$$

$$= \Delta T\left[\sum_{i=1}^{n}\alpha_i\left(T(t)\right)\right] + \left[\sum_{i=1}^{n}\varepsilon_i^{\Delta vc}\left(T(t)\right)\Delta f_i(t,T)\right] \tag{4.38}$$

where Δf_i is change in phase fraction of phase i, n signifies the different phase exist in phase mixture and $\varepsilon_i^{\Delta vc}$ is strain induced due to volume change associated with phase transformation. Further, α_{ptr} denotes expansion coefficient resulting from phase transformation. On the contrary, if attained temperature lies beyond phase transformation range then simply it would follow temperature dependent thermal expansion and calculated thermal strain is expressed as

$$d\varepsilon^{th} = \alpha\big(T(t)\big) . \Delta T \tag{4.39}$$

The volumetric strain ($\varepsilon^{\Delta vc}$) is estimated through the interpretation of lattice constant of α and β-phase as

$$\varepsilon^{\Delta vc}(T) = \frac{1}{3}\frac{dV}{V} = \frac{\sqrt[3]{V_\beta} - \sqrt[3]{V_\alpha}}{\sqrt[3]{V_\alpha}} \tag{4.40}$$

where V_β and V_α are unit cell volume of β and α-phases, respectively. Variation of unit cell volume of both phases along with estimated $\varepsilon^{\Delta vc}(T)$ with temperature are detailed in Section 4.5.3.3. Therefore, strain increment due to thermal and phase transformation components are expressed as

$$d\varepsilon^{th} + d\varepsilon^{ptr} = \begin{cases} (\alpha_T(T) + \alpha_{PTH}(T))\,\Delta T & \text{Heating cycle} \\ (\alpha_T(T) + \alpha_{PTC}(T))\,\Delta T & \text{Cooling cycle} \end{cases} \tag{4.41}$$

where $\alpha_{PTH}(T)$ is expansion coefficient during phase transformation at heating stage, while $\alpha_{PTC}(T)$ indicates the expansion coefficient during phase transformation in cooling cycle.

4.7 Model geometry and material properties

The accuracy of the estimated results relies on the proper selection of mesh size, time step and type of element. The current section discusses the properties of Ti6Al4V alloy, austenitic stainless steel and 9Cr-Mo steel alloy that have been employed for the thermal-metallurgical-mechanical model in the current study. The model geometry and optimization of mesh are also demonstrated in this section.

4.7.1 Model geometry and mesh optimization

The geometrical configuration of solution domain in Cartesian coordinate system is shown in Fig. 4.7. It is noteworthy that the dimension of geometrical model that has been created for the numerical analysis is same as actual weldment. The solution domain is partitioned in three parts along the transverse direction in order to allocate varied heat transfer coefficients as thermal boundary condition.

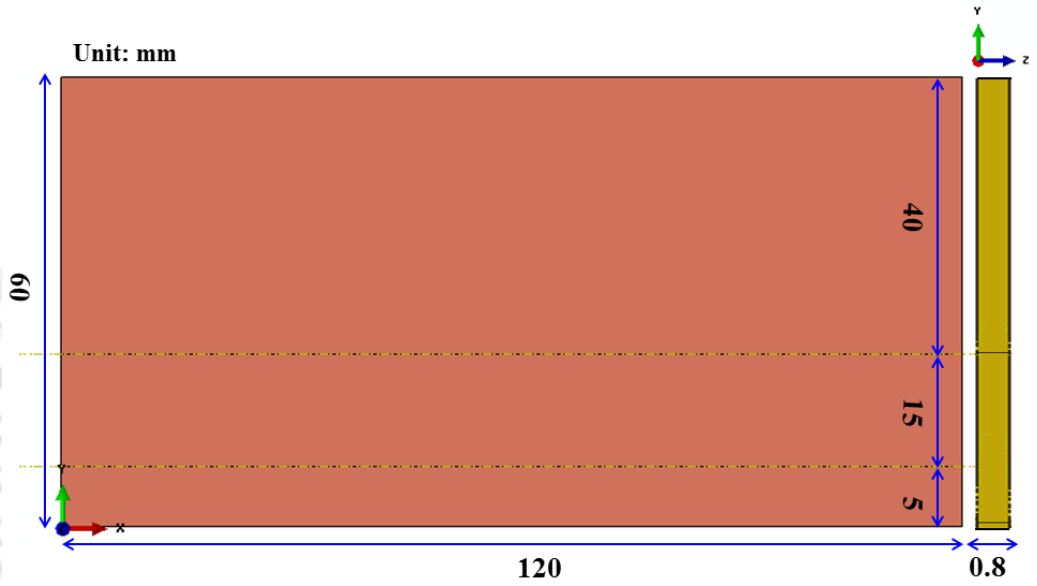

Fig. 4.7 Geometrical representation of solution domain

The time discretization is one of the most important factors that determines the stability and efficiency of the numerical analysis. The coupling of thermal, metallurgical and mechanical modules is complex and requires large memory and high CPU time, resulting in high computational cost. Convergence issues may arise to such an extent that very small time increment and more iteration per increment are required. In order to overcome this aberration, mesh sensitivity analysis need to be performed to find optimum time-step without compromising the quality of the computed results. Very fine mesh is required near the weld line to track steep temperature gradient. The influence of localized heat concentration dampens out the far end of solution geometry. Hence, fine mesh is adopted for location upto 5 mm from weld line and is indicated in Fig. 4.8. Five different mesh size, i.e., fine (0.1 mm) to coarse (1 mm) mesh are

allocated to this region. The mesh size along with simulation time and corresponding computed temperature is presented in Fig. 4.8.

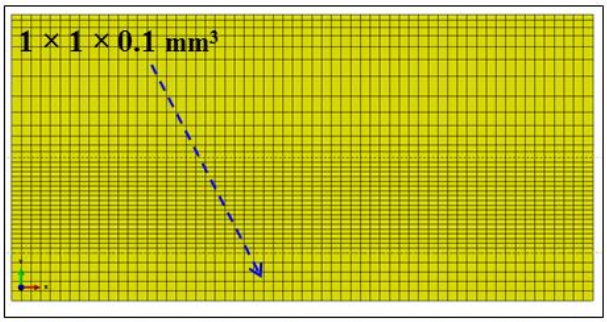

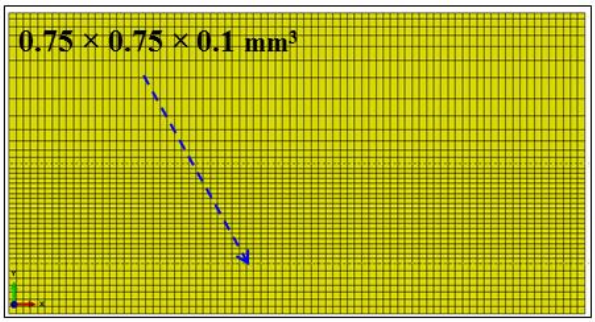

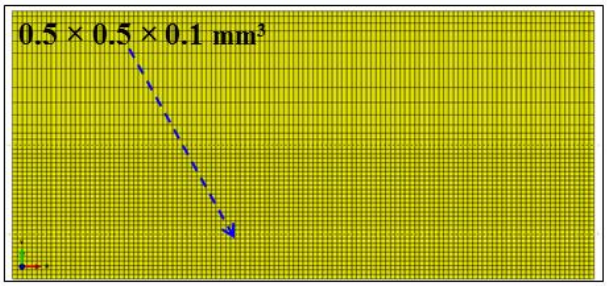

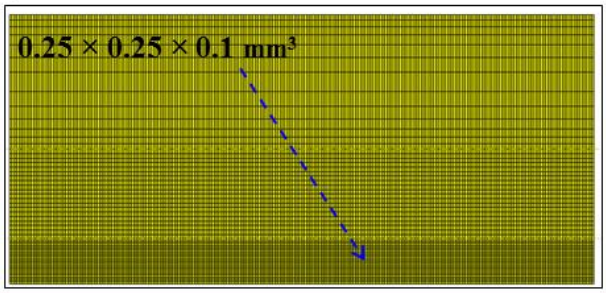

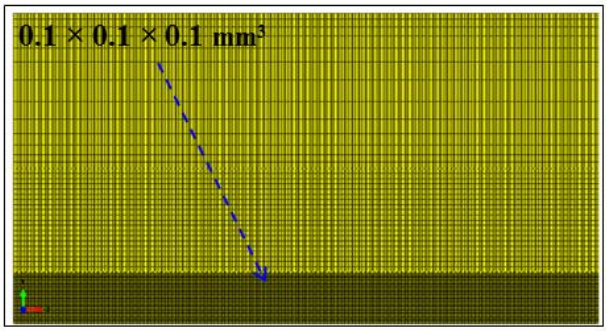

Element size (mm^3)	Number of elements	Simulation time	Peak temperature
1 × 1 × 0.1	18,240	2:50 Hrs	3544 K
0.75 × 0.75 × 0.1	25,600	3:30 Hrs	3443 K
0.5 × 0.5 × 0.1	41,280	4:05 Hrs	3308 K
0.25 × 0.25 × 0.1	**95,760**	**5:30 Hrs**	**3080 K**
0.1 × 0.1 × 0.1	2,98,400	7 Hrs	3027 K

Fig. 4.8 Mesh sensitivity analysis and corresponding temperature data (Table)

It is obvious that number of elements and simulation time increases with decreasing mesh size. It is obvious that as mesh size decreases from 0.25×0.25×0.1 mm^3 to 0.1×0.1×0.1 mm^3, the number of elements dramatically increases from 95,760 to 2,98,400. The variation in peak temperature is observed to be very less, i.e., 53 K unlike other mesh size. Hence, 0.25×0.25×0.1 mm^3 set of mesh size is considered as optimized size with optimum computational time. This particular mesh specification is adopted for thermo-metallurgical-mechanical model. Figure 4.9 indicates the solution geometry of thermos-mechanical analysis. 3D eight nodded diffusive heat transfer elements, i.e., CD3D8 are considered for thermal simulation. However, 3D eight nodded elements with reduced integration, i.e., C3D8R are applied for mechanical analysis. A reduced

integration characteristic reduces gauss integration point in order to minimize computational time without compromising the convergence of computed result. It is noteworthy that similar mesh configuration is adopted for thermal as well as structural analysis.

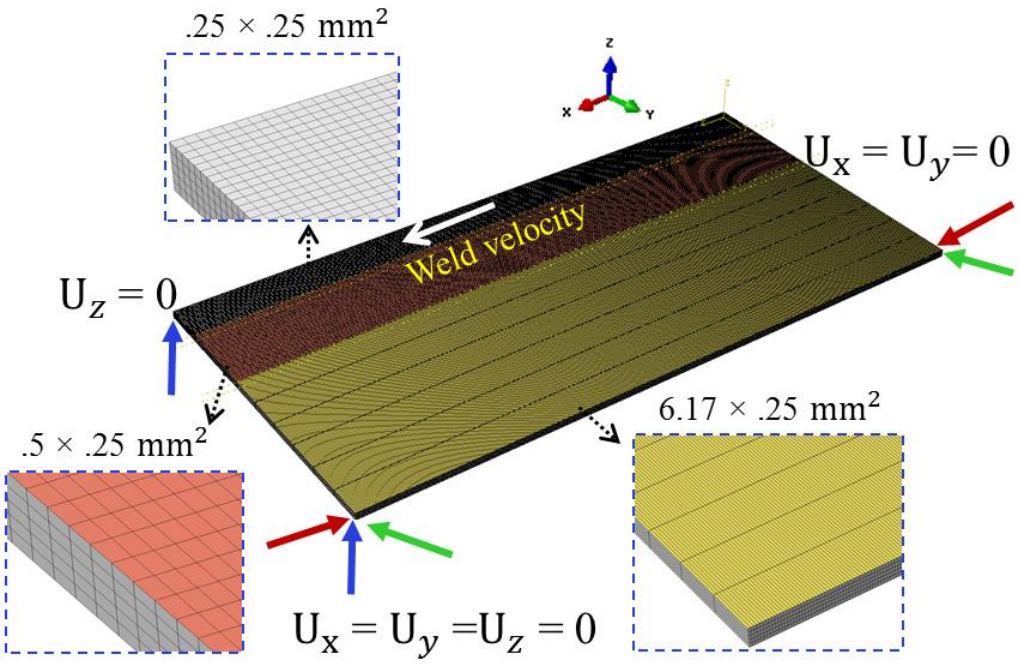

Fig. 4.9 Set of adopted mesh characteristics along with mechanical constraints used for metallurgical-mechanical modeling

4.7.2 Selection of time-step

The computational time and the rate of convergence are highly influenced by the selection of the time step in transient analysis. The transient analysis is performed by dividing the overall simulation time into a huge number of time increments. The convergence of the temperature solution is henceforth attempted in each of these small time steps in thermal simulation. The time increments can be controlled based on a user-prescribed highest allowable nodal temperature change in an increment, $\Delta\theta_{max}$. On the other hand, if $\Delta\theta_{max}$ is not applied, fixed time increments equal to user-defined time increment, $\Delta t_{0,}$ will be used throughout the analysis. In transient analysis with second-order elements, there is a relationship between the minimum usable time increment as a function of element size and material properties (Hughes, 1977)

$$\Delta t_{cr} \leq \frac{(\Delta d_{nd})^2 \rho C_p}{k} \quad (4.42)$$

Accordingly, the critical time step for minimum nodal distance, i.e., Δd_{nd}= 0.25 mm is evaluated as 0.022 for Ti-alloy and 0.015 for SS304 alloy. Moreover, for minimum nodal distance of 0.5 mm, critical time step is calculating as 0.033 on the account of 9Cr-Mo steel. Nevertheless, in the present work, the time step of 0.01 s is considered for Ti6Al4V and SS304 alloy, whereas 0.015 s for ferritic-martensitic steel that lies well below the critical time step value.

4.7.3 Material properties

The present section describes thermo-physical, mechanical and metallurgical properties of investigated materials used in numerical model. During welding simulation, properties are often adopted as function of temperature (Zhu and Chao, 2004). To evaluate the phenomena correctly and enhance the accuracy of developed model, sufficient knowledge of material properties as well as parameters that may highly influential such as cooling rate, seems to be essential. In present study, several material properties involved during TMM modeling are considered from independent literature.

4.7.3.1 Thermo-physical properties

Usually the specific heat, thermal conductivity, and density vary with temperature. Bhatti et al., (2015) indicated that among all thermal properties, specific heat capacity is most sensitive to change in temperature and therefore assuming a constant value may lead to severe errors in calculation (Watt et al., 1988). On the other hand, incorporation of temperature dependent density has insignificant influence on result due to negligence of mass diffusion. Hence, constant value of density is considered in the present analysis. Moreover, the latent heat of fusion and solidification is often encountered with specific heat. The mushy zone of Ti6Al4V alloy is highly sensitive towards specific heat parameter, therefore in present work, change in specific heat is considered as a function of solid and liquid state specific heat capacity, expressed as follows (Piekarska et al., 2012)

$$C_{pc} = \begin{cases} C_S & \text{for} \quad T < T_S \\ \frac{C_L + C_S}{2} + \frac{L_f}{(T_M + T_S)} & \text{for} \quad T_S \leq T \leq T_{M_l} \\ C_L & \text{for} \quad T > T_M \end{cases} \tag{4.43}$$

d

where C_S and C_L is solid and liquid state specific heat capacity respectively, taken as 570 J/kg K and 830 J/kg K for Ti6Al4V alloy. Thermal conductivity, k, predominantly depends on temperature. Hence, temperature dependent conductivity is considered for the thermal analysis. The temperature dependent thermo-physical characteristics are displayed in Fig.4.10, whereas, the constant thermo-physical properties used in simulation for all investigated materials are presented in Table 4.2.

Table 4.2 Constant thermo-physical properties of material employed for thermal simulation

Property	**Ti6Al4V**	**SS304**	**9Cr-Mo steel**
ρ	4430	8000 kg m^{-3}	7765 (RAFM) kg m^{-3} 7770 (P91) kg m^{-3}
T_b	3563	3090 K	3090 K
T_M	1933	1723 K	1773 K
T_S	1877	1673 K	1693 K
L_{fs}	360	360 kJ kg^{-1}	260 kJ kg^{-1}
ε_s	0.6	0.44	0.30
T_o	300 K	300 K	300 K

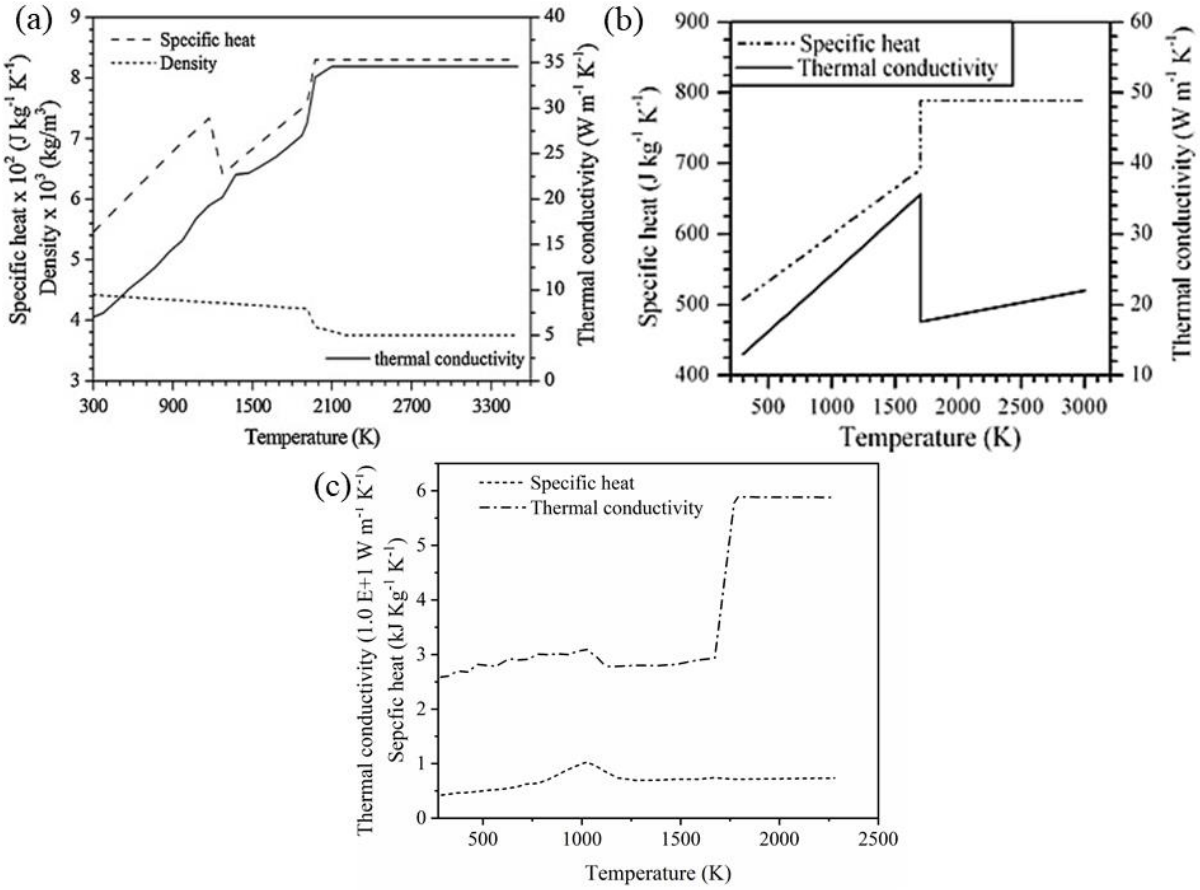

Fig. 4.10 Representation of temperature dependent thermo-physical properties: (a) Ti6Al4V, (b) SS304 alloy and (c) 9Cr-Mo steel

4.7.3.2 Thermo-mechanical properties

The mechanical properties include yield strength, modulus of elasticity, thermal expansion coefficient and Poisson's ratio that contributes to thermo-mechanical response of material. Modulus of elasticity as well as Poisson's ratio characterizes the elastic behavior of material. Due to its insignificant variation with temperature, constant value is considered (Bhatti et al., 2015). Besides, yield strength and thermal expansion coefficient is assumed as a function of temperature. The temperature dependent mechanical properties adopted from the literatures is depicted in Fig. 4.11 (Albert et al., 2016; Baruah and Bag, 2016; Deng and Murakawa, 2006; Mills, 2002; Yaghi et al., 2008; Zhang et al., 2014; Zhu and Chao, 2004; Zubairuddin et al., 2017).

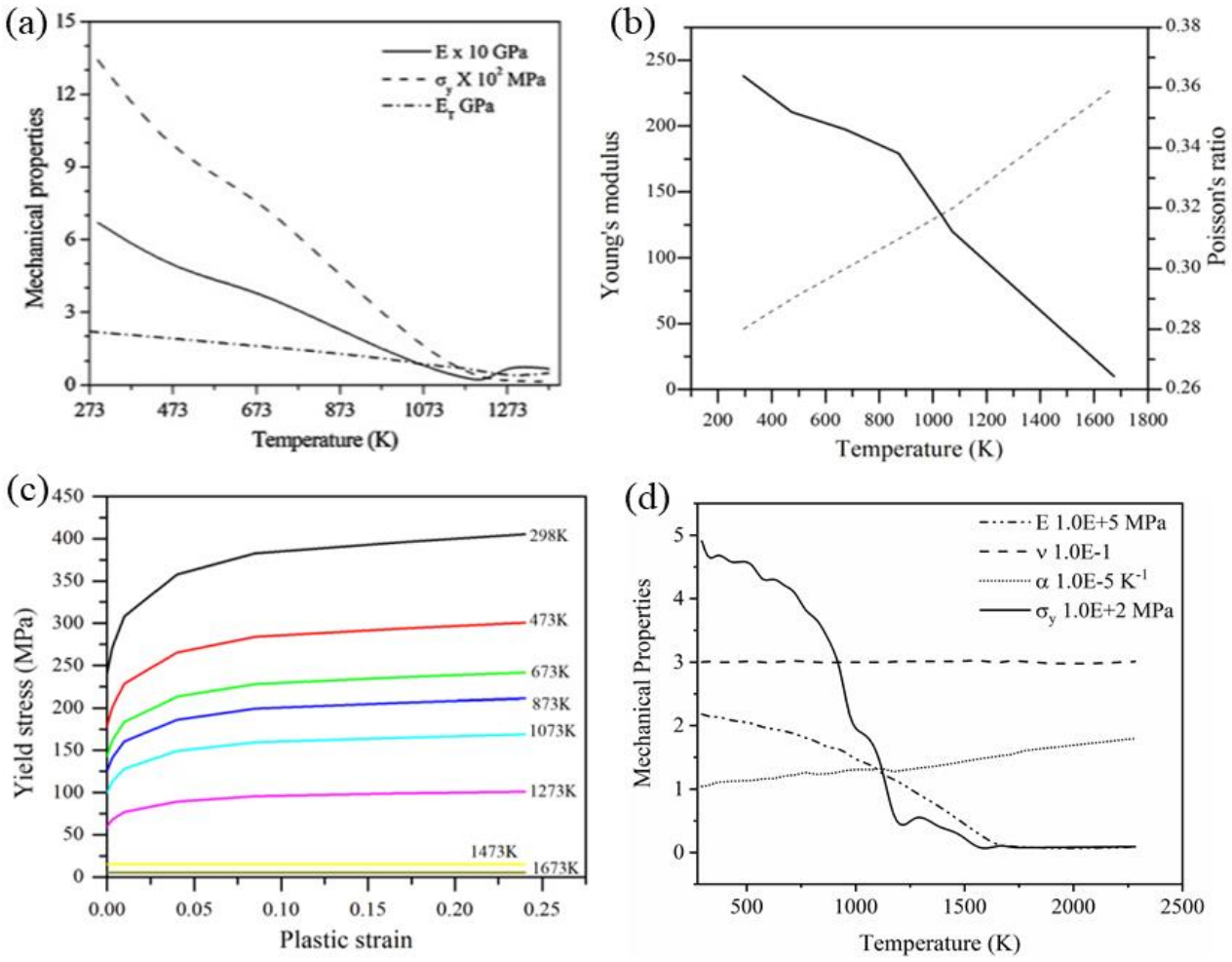

Fig. 4.11 Representation of temperature dependent mechanical properties: (a) Ti6Al4V, (b-c) SS304 and (d) 9Cr-Mo steel

4.7.3.3 Properties for metallurgical model

Volumetric dilation involves during phase transformation phenomena plays a deterministic role in the alteration of residual stress behavior. The volumetric change strain $\varepsilon^{\Delta vc}(T)$ can be estimated through the interpretation of lattice constant of constituent phases, i.e., α and β-phase for Ti6Al4V alloy, whereas δ and γ-phase for SS304 alloy. Variation of unit cell volume of both phases for Ti-alloy along with estimated $\varepsilon^{\Delta vc}(T)$ with temperature are illustrated in Fig. 4.12 (Tan et al., 2019). The lattice parameters of ferrite and austenite phase for austenitic stainless steel is estimated by

$$A_\gamma(T) = \{0.36308 + (0.00075 \times C\%)\}.\left[1 + \{24.92 - (0.61 \times C\%)\} \times 10^{-6} \times [T - 1273\ K]\right] \quad (4.44)$$

On the other hand, ferrite phase lattice parameter (nm) is calculated using

$$A_\delta(T) = 0.28863\ .\{1 + 17.55 \times 10^{-6} \times [T - 1073\ K]\} \quad (4.45)$$

The empirical relations given by Eq. 4.44 and Eq. 4.45 is adopted to estimate the temperature dependent lattice parameter of austenite, which includes carbon percentage since carbon is a good austenitic stabilizer and lattice parameter is highly influenced by carbon concentration (Onink et al., 1993). However, for 9Cr-Mo steel alloy, the volumetric strain is evaluated from dilatometric plot with varied alloying elements.

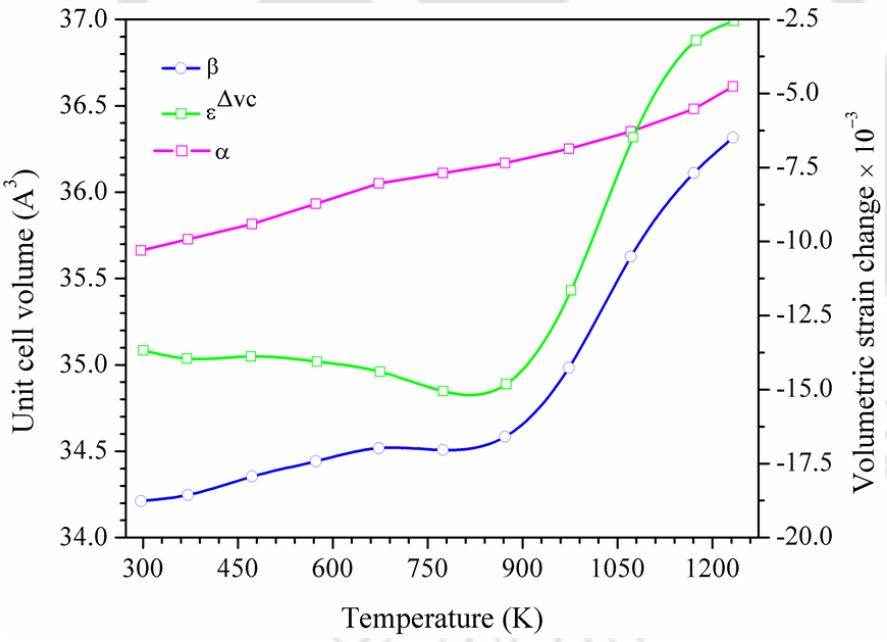

Fig.4.12 Volumetric strain with temperature during SSPT

4.8 Implementation of TMM model

Numerical simulation of thermo-metallurgical-mechanical model is performed in two different stages. In order to enable time-temperature history for the 3D solution domain, DFLUX

user subroutine is used to define the spatial and temporal movement of volumetric heat sources. An hourglass heat source for SS304 weldment and a double ellipsoidal heat source model for Ti-alloy are written using FORTRAN language. However, USDFLD and UEXPAN subroutines is developed for the execution of metallurgical modeling in the case of Ti-alloy, SS304 and 9Cr-Mo steel. The maximum nodal temperature attained during heating and cooling cycle is monitored by creating temperature flag in USDFLD user subroutine. Three range of temperature flag have been generated such as $T_{\alpha} < T < T_{\beta}$ (beta transus temperature), $T_{\beta} \leq T_{melt}$ (melting temperature) and $T > T_{melt}$ for heating stage, and another temperature flag i.e. $T_{\alpha'}(923\ K) \leq T \leq T_{\beta \rightarrow \alpha'}(1053\ K)$ is created for cooling stage. Thereafter, logical decision associated with rate of change of temperature i.e. cooling rate and attained maximum temperature (i.e. temperature flag) verified for each node. The node, which satisfies the cooling rate condition and its maximum attained temperature, belongs to the SSPT temperature range, exhibits volumetric dilation and undergoes phase transformation phenomena. Hence, those nodes and corresponding time-temperature output is initialized in different state dependent variables (SDVs). Furthermore, field variables are defined for α to β transformation (during heating cycle) and β to α′-martensitic transformation (during cooling cycle). Under, UEXPAN user subroutine, phase fraction growth of β-phase (heating stage) and α′-martensite phase (cooling stage) is estimated using modified JMAK and KM theory respectively, and corresponding decomposition α-phase and β-phase volume fraction is calculated by applying lever rule. The volumetric strain is estimated through the interpretation of lattice constant of α and β-phases. Finally, the strain induced due to SSPT for a particular phase fraction at time t and temperature T is computed by multiplying it (phase fraction) with change in volumetric strain. Similar procedure has been followed for the prediction of phase fraction growth of γ-austenite and corresponding δ-ferrite decomposition for stainless steel weldments. Moreover, the volumetric strain is extracted from dilatation plot for different alloying compositions in case of 9Cr-Mo steel weld metals. The estimated phase transformation induced strain is algebraically summed up with the thermal strain. The overall steps involve during metallurgical modeling is presented in Fig. 4.13. This final strain component is further utilized for the evaluation of thermo-mechanical model. The route followed for developing the TMM model using commercial software is illustrated in Fig. 4.14.

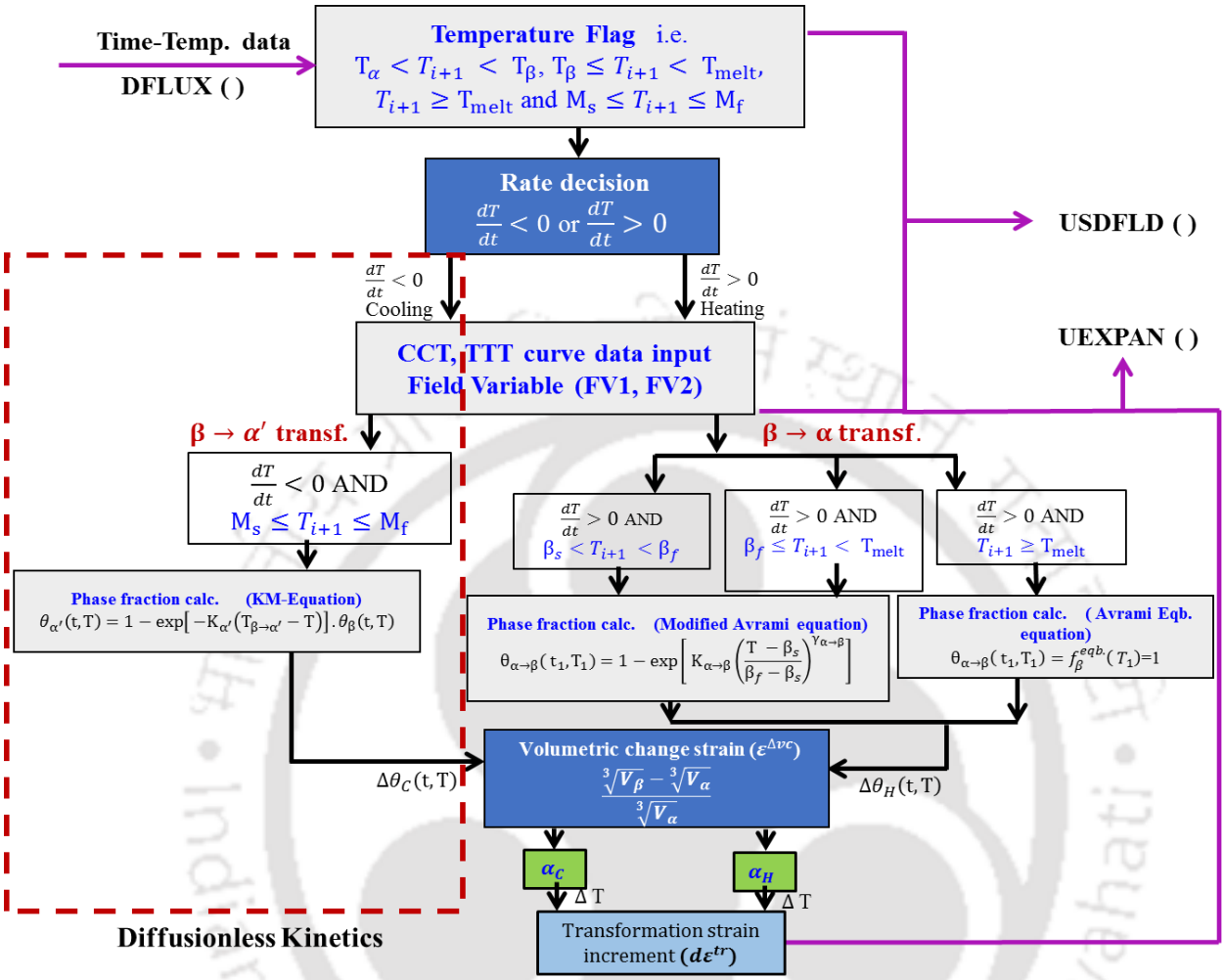

Fig. 4.13 Overall flowchart representing development of metallurgical model

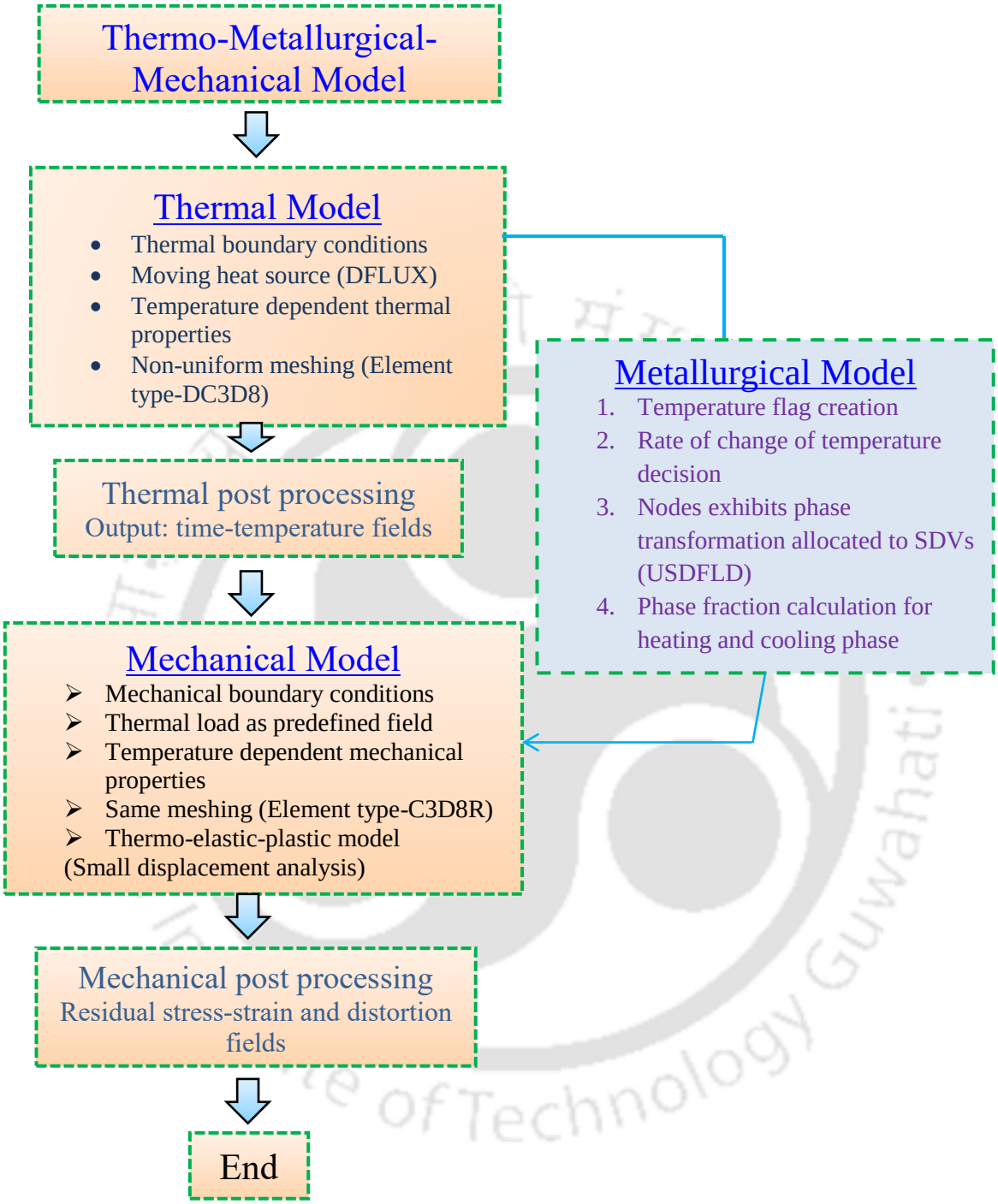

Fig. 4.14 Overall Flowchart of thermo-metallurgical-mechanical analysis

4.9 Summary

In the present chapter, the theoretical background of all the aspects of thermal, metallurgical and mechanical analysis involved in fusion welding processes is presented to incorporate all these coupled phenomena during the prediction of residual stress and distortion pattern. Accordingly, TMM model is executed in a sequentially coupled fashion. The thermal analysis is accomplished by solving the three-dimensional Fourier heat conduction equation using a moving double ellipsoidal or hourglass type heat source model and using temperature dependent thermo-physical properties. This chapter includes the mechanism as well as implementation technique of solid-state phase transformation effect to precisely estimate residual stress and distortion. Furthermore, this chapter also includes systematic strategies to incorporate thermal, elastic, plastic and phase transformation strain components by using in-house developed user subroutines for the assessment of residual stress distribution in three different types of materials. Although, it is difficult to incorporate all physical phenomena that exist during the actual welding process into the mathematical model, the author tried to incorporate the most significant practical occurrence for the improvement of the modeling approach. Nevertheless, few other factors, i.e., transformation-induced plasticity, microstructural morphology induced strain component, twinning-induced plasticity components need to be incorporated within the numerical simulation in order to enhance the robustness of the model. Due to lack of temperature dependent transformation kinetic parametric data, i.e., K and n, a constant value is implemented at some point of time for the sake of convenience, which might produce some error during phase fraction calculation. Hence, it must be taken care in the future scope of work to estimate a more reliable estimation of residual stress distribution.

Chapter 5

5.0 Results and Discussions

5.1 Introduction

Phase transformation has pronounced effect on the generation of residual stress and distortion which is often neglected in thermo-mechanical analysis. Primarily, to investigate the same for dual phase ($\alpha + \beta$) Ti-alloy, a finite element based sequentially coupled thermal-metallurgical-mechanical model is developed for pulse laser welding condition and validated with experimental results. Different phases evolved during welding are qualitatively estimated as a function of transient temperature change by allowing volumetric expansion or contraction induced by β-transformation or α'-martensitic transformation. The influence of non-isothermal diffusional transformation during heating and non-diffusional transformation in cooling cycle on residual stress and deformation pattern is evaluated. Further, an attempt is made to investigate the significance of the pulse parameter over continuous mode in Yb-fiber laser welding of 800 μm thin Ti6Al4V alloy. The intuitive objective is to furnish fundamental insight into the simultaneous interaction of thermal-metallurgical-mechanical characterization at both pulse and continuous mode of operation through temperature simulation, cooling rate estimation and targeted experimental analysis. Special attention is focused on assessment of contamination level through surface discoloration technique for the qualitative analysis of the weld Joints.

The development of compressive residual stress is substantially governed by the metallurgical transformation and associated microstructure, which in turn influences the mechanical properties of welded structure. Secondly, the microstructural interaction with the thermo-mechanical performance of Yb-Fiber laser-welded austenitic stainless steel (SS304) is evaluated at different heat inputs and varying defocus distances. The implication of dual-phase microstructure and associated morphologies on the

residual stress generation mechanism is systematically explored. High cooling rate accompanied with low heat input (45 J/mm) leads to the enriched δ-ferrite phase fraction ~12% which in turn, improves the tensile strength property by minimizing tensile residual stress. The finite element based thermo-metallurgical-mechanical model predicts the residual stress with a maximum deviation of ± 50 MPa compared to the experimental output.

In order to fulfil another objective various weld metal with different compositions are used to weld 9Cr steels. The austenite stabilizing elements present in these weld metals strongly influence the transformation kinetics and the transformation induced strain. Martensitic start, finish temperature and their difference play a key role to alter the phase fraction during cooling stage of the weld. Residual stress (RS) development in 9Cr weld metals made using fusion welding process and the influence of weld metal composition on its evolution are studied. The experimentally measured RS profile in the weldments are validated using a 3D finite element based sequentially coupled thermal-metallurgical-mechanical model developed to predict RS evolution in 9Cr steel at different compositions. The model incorporates the dilation during martensitic transformation using state dependent variables (SDVs) approach.

5.2 Thermal-metallurgical-mechanical modelling of Laser welded Ti-alloy

To overcome the detrimental effect of residual stress and distortion in a welded structure, there is a continued interest on the assessment of these stress field and deformation pattern. In general, the non-uniform heat distribution and uncontrolled heat input results in higher residual stress and associated distortion in a welded structure (Lathabai et al., 2001). Residual stress in component may not tolerate equilibrium with environment, rather the stress retains even after removal of the external load (Rodgers and Fletcher, 1938). Retained stress produces predominant effect for structural integrity and life assessment of weldment where its magnitude may arise close to yield strength. Non-uniform heating and cooling, structural deformation due to metal working, heterogeneity in crystallographic arrangement and type of mechanical constraints are some of the major factors responsible for the generation of residual stress (Ivetic et al., 2009). In fusion welding, the transient heating, melting and solidification occurs simultaneously in the FZ (fusion zone) which involves highly non-uniform temperature distribution across the weld joint. Hence, the thermal contraction and expansion during cooling and heating periods leads to non-uniform deformation pattern. Accordingly, the welded structure is subjected to residual stress and inevitable distortion from the unbalanced thermally induced strain in mechanical-restraint

condition (Long et al., 2009). Contemporary process designer is strongly assisted by numerical model which contributes to the simulation of complex phenomena like fusion welding process where thermal, mechanical and metallurgical phenomena are simultaneously involved. Accurate temperature dependent data as well as different algorithms are needed to precisely simulate the phase transformation phenomena. A large discrepancy was found when phase transformation effect was neglected (Zubairuddin et al., 2014). Volumetric changes are predominant factor for the alteration of residual stress distribution during phase transformation that may significantly reduce the accumulated longitudinal stress. The volumetric expansion in the welded zone takes place due to crystallographic transformation of the body centred cubic (BCC) to hexagonal close packed (HCP) structure (Deng and Murakawa, 2013). Beside, finite element (FE) based model has increasing demand to precisely predict the residual stress field and associated deformation in a large structure. Therefore, development of time-effective numerical modeling technique by undertaking complex material model for titanium alloy to evaluate the temperature field, stress distribution and associated deformation, and phase distribution is of primary importance in the present study. In an attempt to handle these effects, a two-step validation methodology is carried out on a new model and is estimated the residual stress and distortion in Ti6Al4V weldment. Sequentially coupled thermo-metallurgical-mechanical model is developed using in-house developed user subroutines in commercial software ABAQUS. The overall mechanism and strategy that deals with the implementation of metallurgical model and theoretical formulation associated with thermo-mechanical analysis is extensively discussed in section 4.6. The developed model also predicts how the rapid cooling rate corresponding to a faster scanning speed leads to increase in volume fraction of martensite in the welded structure. In accordance with present investigation, the important findings are demonstrated herein.

5.2.1 Temperature profile and cooling rate

Laser welding of dual phase Ti-alloy of thickness 800 μm is considered to validate the developed numerical model. The process parameters which are adapted from literature are depicted in Table 5.1. It is noteworthy that the simulation is performed by considering temporal pulse effect which is different from the continuous average power.

Table 5.1 Process parameters for laser welded sample (Gao et al., (2013))

Parameter	Peak power (P_{pk})	Pulse repetition rate (f)	Pulse energy (P_e)	Pulse duration (P_d)	Scanning speed (S_v)	Focal distance (f_d)	Heat input (H_i)
Value	1.5 kW	20 Hz	8.25 J	5.5 ms	10 mm/s	-2 mm	16.5 J/mm

The boundary condition associated with mechanical analysis is described in Fig. 5.1. The boundary conditions are imposed to simulate the actual clamping condition used during experiment. Two different cases of boundary conditions are analyzed to predict the residual stress and distortion. Although it is difficult to control distortion, the common practice to use welding fixture is to minimize it as much as possible. The amount of constrains can define the extent of distortion and the magnitude of residual stress. Table 5.2 describes three different cases of boundary constraints that are analyzed in the present investigation.

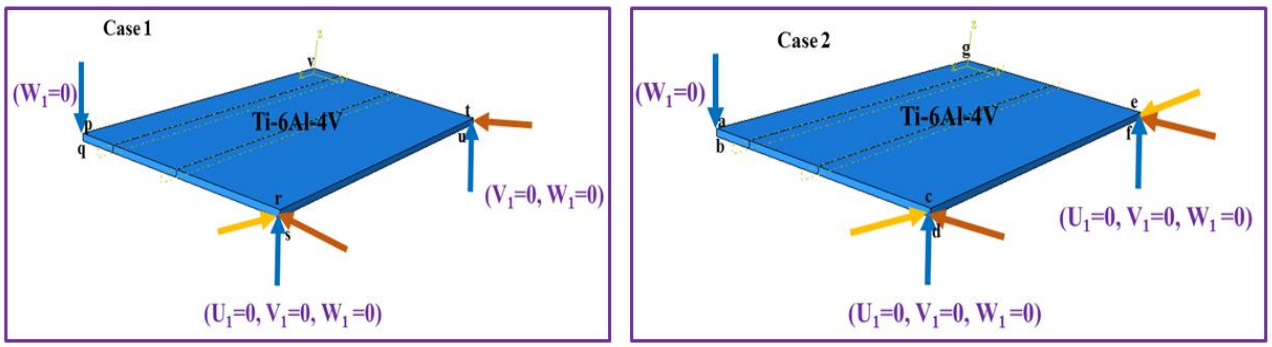

Fig. 5.1 Displacement constraint condition applied in numerical simulation of mechanical analysis

Table 5.2 Description of seized degree of freedom applied in mechanical analysis

Cases	**Position**				
1 (Without phase-transformation effect)	**p, q**	**r, s**	**t, u**	**p, q, v, w**	**q-s-u-w**
Seized degree of freedom **(translational)**	W=0	U, V, W=0	**V, W=0**	$\frac{\partial V}{\partial y} = 0$	U, V=0
	Position				
2 (Without phase-transformation effect)	**a, b**	**c, d**	**e, f**	**a, b, g, h**	**b-d-f-h**
Seized degree of freedom **(translational)**	W=0	U, V, W=0	**U, V, W=0**	$\frac{\partial V}{\partial y} = 0$	U, V=0
	Position				
3 (With phase-transformation effect)	**a, b**	**c, d**	**e, f**	**a, b, g, h**	**b-d-f-h**
Seized degree of freedom **(translational)**	W=0	U, V, W=0	**V, W=0**	$\frac{\partial V}{\partial y} = 0$	U, V=0

Thermal model predicts the nodal temperature distribution from where different quantitative measurements are performed. Fig. 5.2 shows the comparison between experimental (left) and numerically measured (right) macrograph of weld bead geometry. It is obvious that the predicted isotherm reasonably matches with the experimental result (Gao et al., 2013). Heat affected zone (HAZ) which manifests solid state phase transformation, mushy zone which is characterized by liquidus (~ 1933 K) and solidus (~ 1877 K) temperature, and fusion zone (FZ) are represented by different color isotherms. Gray color band depicts FZ, achieved maximum temperature of ~ 3100 K followed by mushy zone (red band) and HAZ (region between blue and yellow). Since the maximum temperature is well below the boiling temperature of $\alpha + \beta$ Ti-alloy (i.e., ~ 3563 K), the conduction mode of laser welding is predominant for the present set of welding condition. In fusion zone, the width at three levels (i.e., top, middle and lower) is found

to be closer to the experimental value. The width of HAZ at two levels (i.e., top and lower) are found to be 0.23 and 0.43 mm (experimentally), and, 0.24 and 0.40 mm (numerically), respectively. The error in estimation at different region of the welded structure is depicted in Fig. 5.2.

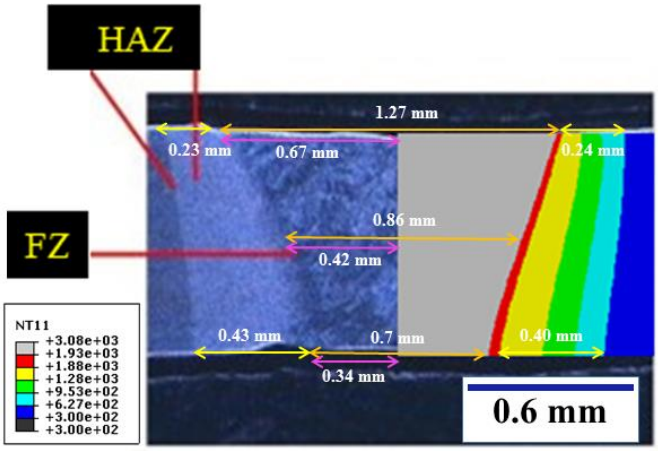

Fusion zone	Experimental (mm)	Numerical (mm)	Error (%)
Top	0.67	0.60	10
Middle	0.42	0.44	5
Lower	0.33	0.36	9

Heat affected zone	Experimental (mm)	Numerical (mm)	Error (%)
Top	0.23	0.24	4
Lower	0.43	0.40	7

Fig. 5.2 Comparative study of experimentally (left) and numerical (right) computed weld profile at heat input of 16.5 J/mm

The temperature profiles at the upper and lower surfaces and at the middle point along weld central line in different time zone is depicted in Fig. 5.3a. The variation of peak temperature between top and bottom surfaces is not significant. The thermal energy diffusion takes place throughout the thickness direction with insignificant temperature gradient. When the time elapsed between heating and cooling increases the peak temperature decreases gradually for both surfaces. The temperature profile is very stiff due highly concentrated heat flux from laser source. Fig. 5.3b shows the temperature profile across the welding line (i.e., transverse) at a distance of 0.5, 0.75 and 1.25 mm, respectively away from the weld center line. Due to localization of concentrated heat source, the maximum temperature is restricted to the domain nearest to the heat source while low temperature zone is fanning out. The maximum temperature attained at a distance of 0.5, 0.75 and 1.25 mm is ~ 2650 K, ~ 2000 K and ~1500 K, respectively. The fluctuating temperature profile is obvious due to effect of pulse and gradually dampens out towards the edge of the solution domain. The pulsation effect is vanished at a location of 1.25 mm.

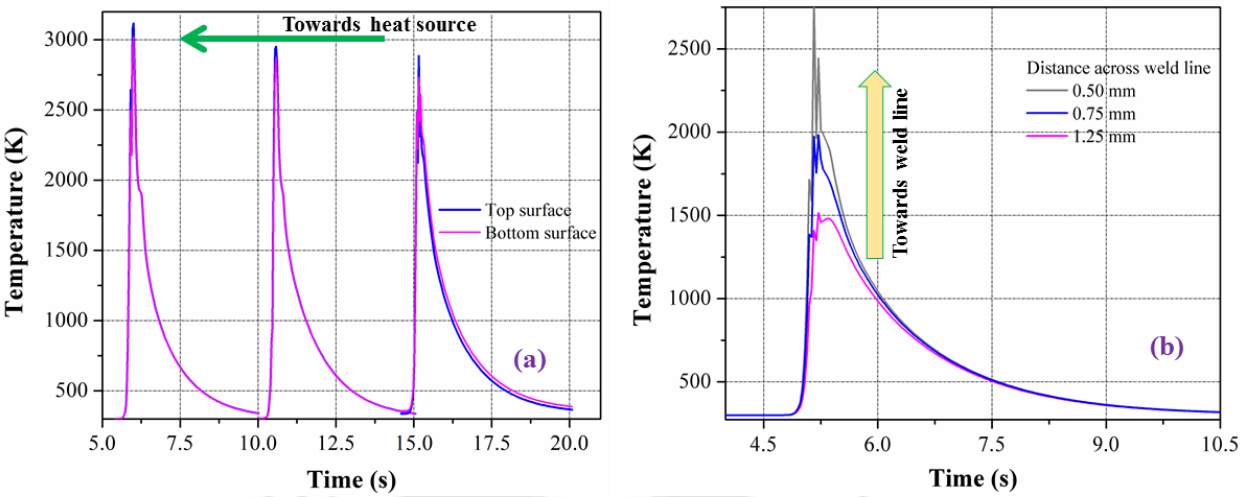

Fig. 5.3 (a) Thermal profiles at different location along weld line, (b) thermal profiles across mid of the weld central line of the plate

Fig. 5.4a signifies the transient temperature profile at the mid of weld center line. It exhibits the pulsation effect through fluctuation in temperature profile. Steep temperature profile is observed due to the consideration of very high welding velocity (~ 10 mm/s). For mechanical and metallurgical analysis, the temperature simulation is carried out by considering average laser power which is analogous to continuous mode welding. It is apparent that the maximum temperature estimated by assuming average power is ~ 2330 K which is efficiently lower than that of evaporation temperature whereas the average temperature is ~ 2650 K after consideration of the pulse effect. It seems that the calibrated temperature estimated by both the procedures is quite in similar range. Some of the literature performed the similar strategy to estimate the temperature distribution and associated residual stress (Baruah and Bag, 2017). Fig. 5.4b shows the transient change in temperature along the transverse direction with a step size 0.03 s. The utmost change of temperature is ~ 412 K whereas it is ~ 375 K, ~ 330 K, ~ 220 K at locations of 0.5, 0.75 and 1.25 mm, respectively. The change in the maximum temperature occurs at a location which is in direct contact with laser and reduces further away from the center. The heat transfer by radiation is proportional to the fourth order of temperature and hence becomes more effective at higher temperature. At the farthest location, the probability of heat transfer through radiation mode is less. The declination of temperature change is obvious away from the weld center line and hence, no significant change in properties is expected. It is reported that time-temperature profiles are comparatively steeper for laser welding as compared to GTAW.

Moreover, rapid heating and cooling stage is associated with laser welding as compared to other conventional welding processes (Yadaiah and Bag, 2014). Under steep temperature gradient, the heat transfer per unit time increases in the melt pool which leads to enhanced cooling rate locally (Fredriksson and Akerlind, 2006).

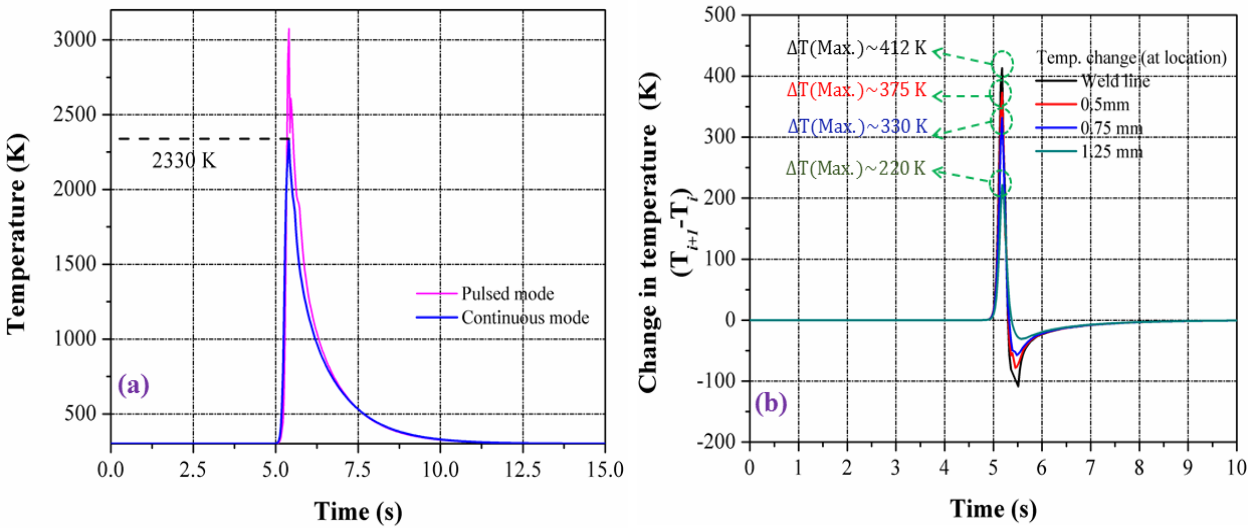

Fig. 5.4 (a) Representation of temperature profile in pulsed and continuous mode of Nd: YAG laser welding, (b) change in temperature with time across the weld line

Phase transformation and exhibited morphological changes in welded structure depends upon cooling and heating rates, which in turn is influenced by various parameters such as beam energy, scanning velocity, boundary interactions, solidification parameters, and thermal efficiency of the processes. The microstructural variation directly affects the mechanical behavior of the welded joint. Hence, it is significant to quantitatively estimate the thermal cycle and associated cooling rate for the prediction of transformed microstructure. The solidification behavior in fusion welding is associated with temperature gradient (G) and growth rate (R) (Arnberg et al., 1993). Maximum growth rate (R) along the weld velocity vector is normally equal to the magnitude of the velocity and cooling rate directly depends upon temperature gradient which in turn leads to different phases of microstructure. Depending upon attained cooling rate, two different modes, i.e., diffusional and non-diffusional solid-solid state phase transformation could be possible. If the cooling rate varies from slow to moderate value, existing prior β-phase transforms into α-phase through nucleation mechanism that leads to lamellar type microstructure, i.e., Widmänstatten microstructure. However, at very high cooling rate non-

diffusional phase transformation, i.e., martensitic transformation takes place which results in needle type α′-acicular structure. Since, the current investigation is focused on the estimation of transformed phase fraction evolved during cooling cycle, the rate of change of temperature and time-temperature data has been analyzed only for cooling phase. Fig. 5.5 depicts the correlation between the rate of change of temperature and time-temperature profile for cooling cycle at different locations across the weld velocity vector. The rate of change of temperature corresponding to the maximum cooling rate at location of 0.0 mm, 0.5 mm, 0.75 mm and 1.25 mm are found to be ~ 3550, ~ 3010, ~ 1850 and ~ 1010 K/s, respectively. Literature indicates that the cooling rate varies between 10^4 – 10^5 K/s for Nd:YAG pulse laser welding (He et al., 2006, 2003). In the present study, the predicted rate of change of temperature is quite valid and lies within the feasible range. It is found that the rate of change of temperature increases (-ve direction) at initial cooling stage due to rapid heat transfer. After reaching at optimum value, it starts to increase in +ve direction rapidly and finally (at ~ 10 s) becomes constant (when it establishes thermal equilibrium with the outer environment. Manikandan et al. (Manikandan et al., 2014) has shown similar inference as predicted in the present investigation. Radiation from the weld line by the laser beam yields a rapid increase of temperature which is attributed to high temperature gradient between weld line and farther away location.

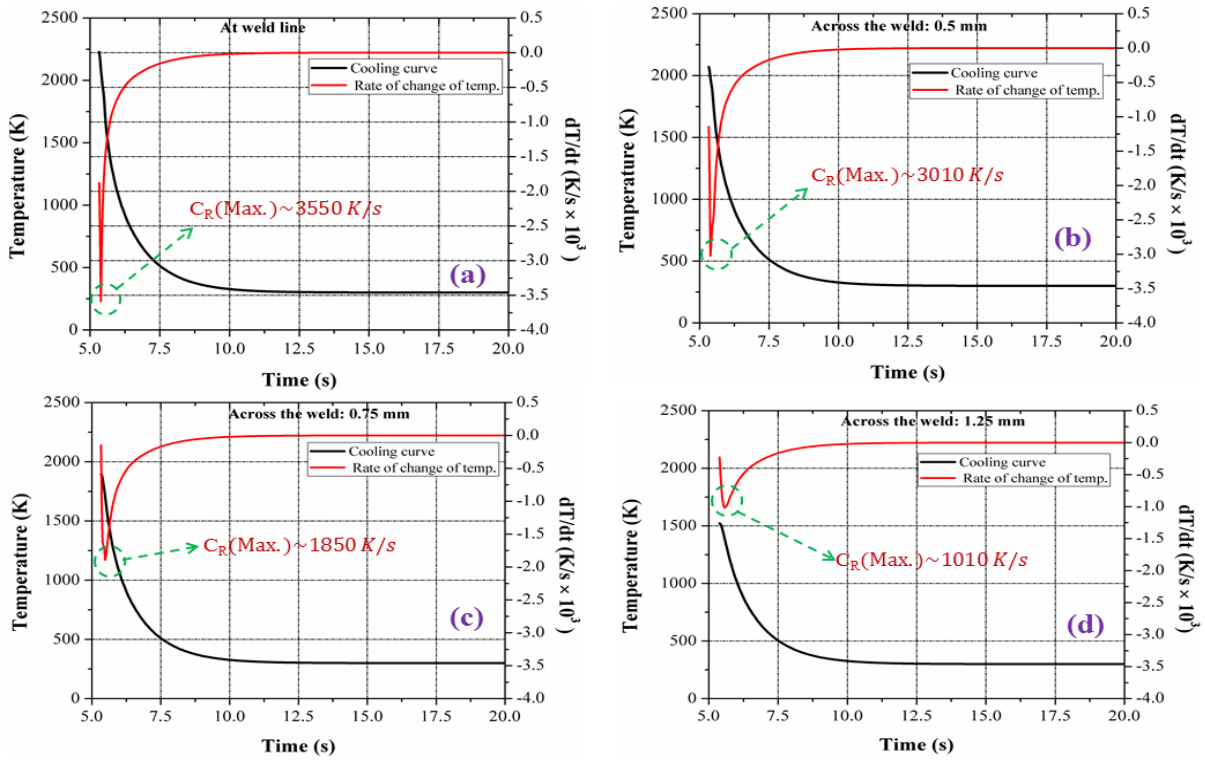

Fig. 5.5 Relation between rate of change of temperature and cooling cycle at a distance of (a) 0 mm, (b) 0.5 mm, (c) 0.75 mm and (d) 1.25 mm from weld line in transverse direction

Fig. 5.5a-c depicts that the maximum rate of change of temperature up to half-width (0.75 mm) is more than critical cooling rate (~ 410 K/s). Therefore, in these cases, predominant fully martensitic transformation is expected. However, at a farthest location (i.e., at 1.25 mm) due to attainment of low temperature phase transformation, mixed phase, i.e., composed of martensite and another prior phase is expected (Fig. 5.5d).

5.2.2 Phase distribution

Ti6Al4V alloy is considered as a dual phase alloy that consists of Aluminium (Al) as α-stabiliser and Vanadium (V) as β-stabiliser. In the present work, contribution of retained β-phase in Ti-alloy at room temperature is suspended and it is assumed that Ti-alloy is fully composed of α-phase initially such that transformation of $\alpha \rightarrow \beta$ can easily be distinguished. The thermal cycle experienced at a particular location substantially drives the phase transformation. Fig. 5.6a-b depicts contour plot of β-phase distribution at time interval of 1.7 s and 6 s, respectively. Fig.

5.6a'-b' represents the cross-sectional view of Fig. 5.6a-b. Red band represents the β transformed region at FZ and HAZ which exhibits T_β. However, the strip between base plate (black band) and red band emerge due to the involvement of mixed phase since the peak temperature attained in this area is between α-dissolution temperature and T_β.

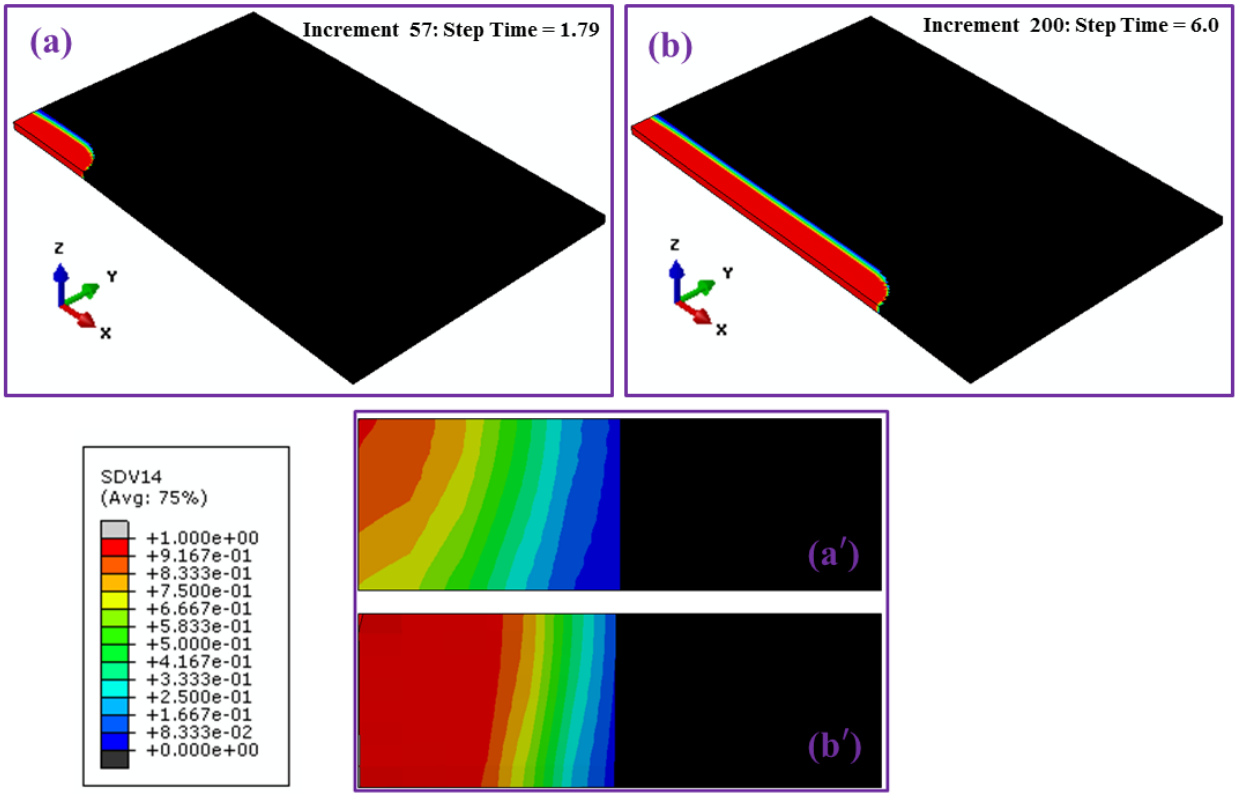

Fig. 5.6 (a-b) The growth of β-phase distribution at different time interval during heating cycle, (a'-b') cross-sectional view of 5.6a-b, respectively

Fig. 5.7a depicts the growth of transformed β-phase fraction with temperature during heating cycle. In primary stage, transformed β–phase fraction grows by diffusional migration of dual phase α/β interface. When temperature is high enough, i.e., within the range of α-dissolution and T_β, α-phase starts to transform into β-phase (Fig. 5.7a). When the temperature reaches α-dissolution limit, α → β transformation begins. Thereafter, β-transus limit is achieved when approximately 95 % of α transforms into β-phase. At temperature of 1350 K, α-phase is fully (100 %) transformed into β-phase. Due to extremely rapid heating, dissolution of α-phase shifts

towards higher temperature and fully β-phase fraction is attained slightly after T_β [Murgau, (2016)].

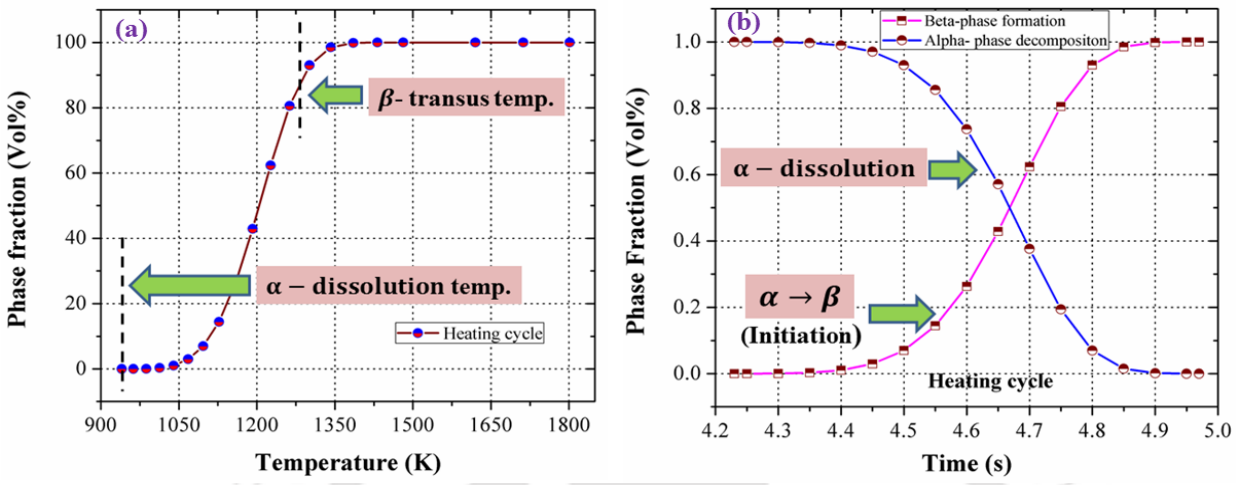

Fig. 5.7 (a) Variation of β-phase fraction with respect to temperature, (b) growth of β-phase fraction time during α→β transformation

The β–phase is found to be fully stable at the temperature beyond T_β. Fig. 5.7b represents the degree of transformation, i.e., α → β as a function of time during heating cycle. It is observed that the progression of transformed β–phase and decomposition of α-phase take place simultaneously. The volume fraction of α and β-phase remains unchanged until 4.4 s (Fig. 5.7b). It is based on the fact that attained temperature is less than that of α-dissolution temperature upto that point of time. Beyond 4.4 s, it reaches to α-dissolution temperature (940 K) and results in the nucleation and growth of β-phase. It is interesting to know that at time 4.65 s during heating stage, the volume fraction of both α and β-phases are 50 %. It conveys the message that the primary α-phase transformed into β–phase until it reaches to 100 % of β at temperature above β-transus during heating cycle. If heating rate is fairly low, α → β transformation follows the thermodynamically equilibrium condition and α-phase fraction would reduce to zero at T_β.

Fig. 5.8a shows the variation of transformed martensitic fraction (in vol. %) with temperature at different locations of weld zone during a cooling cycle. Weld zone of Ti6Al4V alloy cools rapidly (i.e., cooling rate is much more than critical cooling rate ~ 410 K/s) from the β-phase field and leads to martensitic transformation. As soon as the molten zone attains

martensitic start temperature (M_{st} ~ 1090 K), the transformation begins and martensitic phase fraction grows significantly upto 98 % at martensitic finish temperature (M_{fn} ~ 910 K).

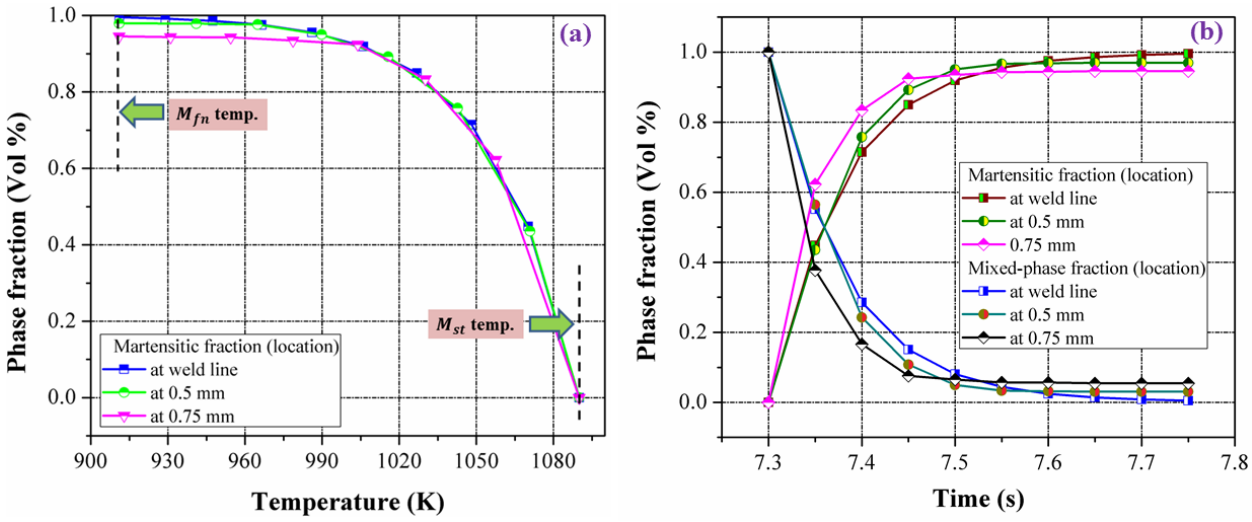

Fig. 5.8 Distribution of martensitic phase fraction (a) with respect to temperature, (b) with respect to time at different locations

Nevertheless, the martensitic phase fraction at a distance of 0.5 mm and 0.75 mm away from the weld line is found to be 96 % and 92 %, respectively. Heat input away from the weld line is comparatively low. Hence, the range of M_{st} at that location lasts for very short period that may not allow growing fully martensitic phase. Fig. 5.8b illustrates the martensitic phase fraction with time at different locations. It is observed that the martensitic transformation begins at 7.3 s and achieves 50% at 7.35 s. The transformation is completed at 7.7 s and becomes constant afterwards. In cooling phase, when substrate reaches beyond T_β, transformation starts from β-phase field to α-phase or any other secondary phase upto M_{st}. It can be concluded that at M_{st}, retained phase is a mixture of β-phase, α-phase and other secondary phases. As martensitic phase progresses, the dissolution of mixed phase can also be seen from Fig. 5.8b with respect to time at different locations. It is reported that martensitic phase has hexagonal α′-acicular appearance with small needle type structure. The product of β-phase decomposition can be hexagonal α′-martensite, primary α-phase and diffusional controlled secondary lamellae phase depending upon cooling rate followed.

Fig. 5.9 represents the contour plot of martensitic phase distribution during cooling cycle. Since, the composition of the transformed part (i.e., martensite) is same as that of parent phase (i.e., β-phase) it infers that no atomic diffusion takes place during the transformation and in this perspective martensitic transformation is diffusionless. Growth of fully martensitic phase fraction at three different time interval during cooling cycle is represented as red band in Fig. 5.9. However, mixed phase fraction composed of martensite and β-phase is depicted by other color bands. As time progresses during cooling cycle, weld area which experiences martensitic transformation temperature transformed into α′-martensite.

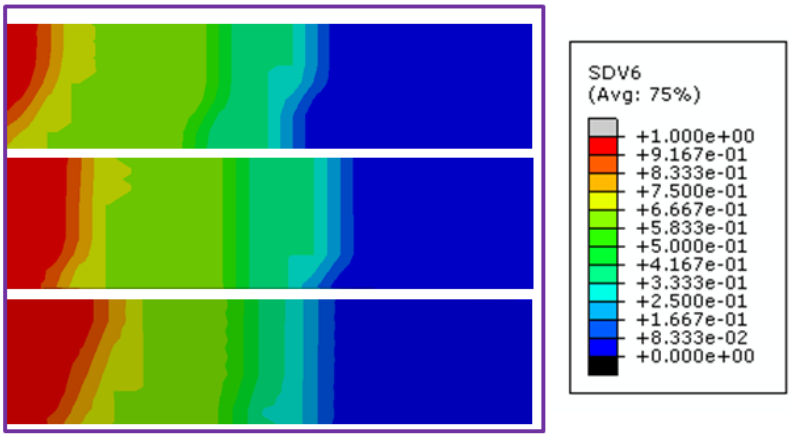

Fig. 5.9 Distribution of martensitic and mixed phase (β-phase+ α-phase) during cooling phase w.r.t time

Fig. 5.10 describes the distribution of martensite phase and mixed phase (i.e., β-phase + martensitic phase) at different weld time. Martensitic fraction growth can easily be recognized as red band whereas mixed phase fraction is defined by green and yellow band. The unaffected region by phase transformation is illustrated by blue colour. When the temperature away from the weld zone decreases, the material diffusion in this region is limited which leads to a combined diffusional-displacive mode of phase growth. Fig. 5.11 depicts the single phase contour plot of martensitic transformation at different time interval. Fully martensitic phase fraction is depicted by red strip and the region which does not undergo non-diffusional transformation is represented by blue color. Blue banded region does not withstand any martensitic transformation temperature at respective span of time. It is noteworthy that during martensitic transformation, generated lattice strains almost fulfill the invariant plane strain condition due to which magnitude of lattice invariant shear is relatively small, which provides flexibility in the characterization of the substructure of martensite (Banerjee and Mukhopadhyay, 2010).

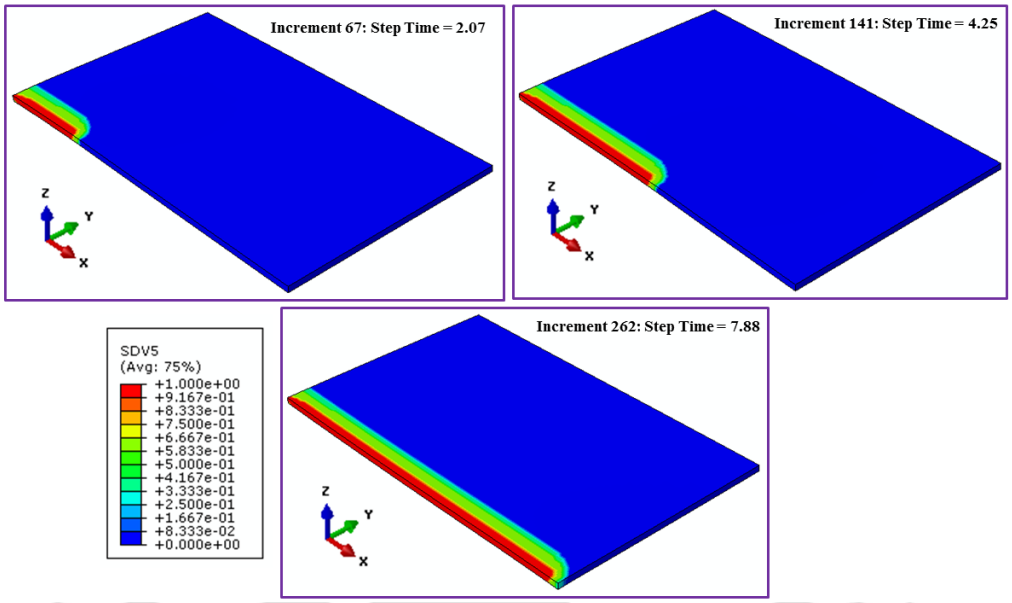

Fig. 5.10 3D plot of martensitic and mixed phase distribution at different time interval during cooling cycle

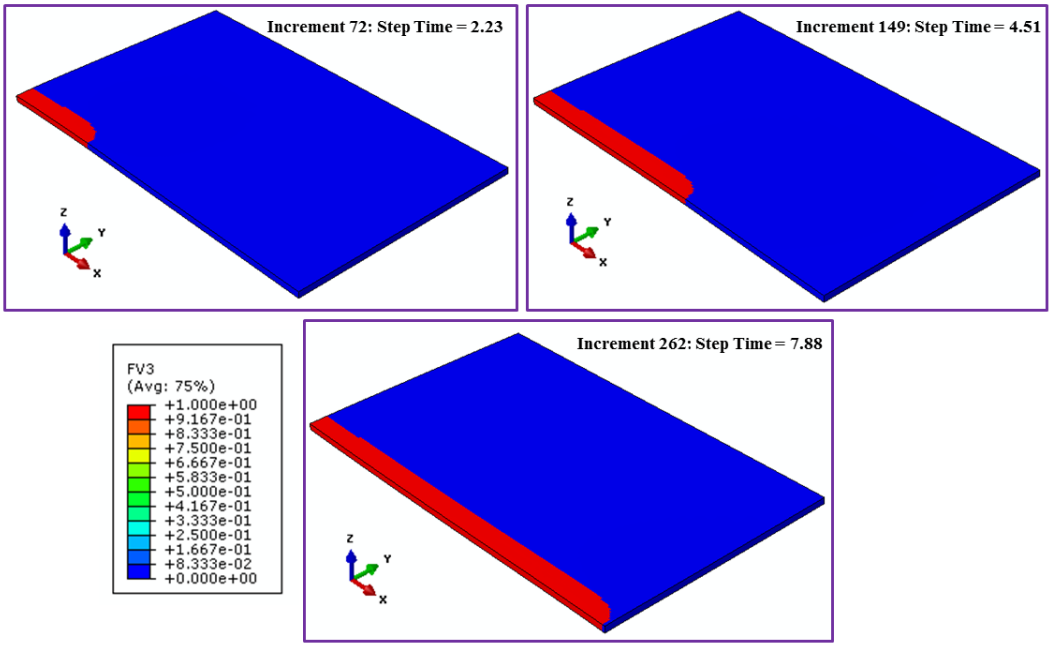

Fig. 5.11 Growth of martensitic phase distribution at different time interval

5.2.3 Residual stress distribution

Generally, residual stress evolved during welding has undesirable effect on the mechanical response of welded structure. High temperature gradients and corresponding dynamic microstructural evolution generate residual stress during welding of Titanium alloy. It is quite difficult to predict distribution of residual stress specially, in thin plate due to complex coupling of thermal, metallurgical and mechanical phenomena simultaneously. Several phase transformation in FZ and HAZ leads to residual stress in welded joints. These phase transformation characterized by specific volume expansion (martensitic phase) at microscopic level. The strain induced due to liquid-solid and solid-solid phase transformation alters the residual stress state. It is noteworthy that relative stability of phase transformation during heating cycle, i.e., $\alpha \rightarrow \beta$ phase change, favours significant martensitic transformation. Hence, it can be inferred that ultimately martensitic transformation contributes alteration of state of residual strain or stress. Some of the authors made similar conclusion that phase transformation during heating stage is insignificant for the residual stress generation (Lee and Chang, 2011). In the present investigation, the numerical simulation indicates that (Fig. 5.12a-b) almost stable β- transformed volume fraction has been achieved in the weld zone and HAZ. So, martensitic transformation is obvious. Depending upon the expansion attended by $\beta \rightarrow \alpha'$ martensitic transformation and thermal shrinkage during cooling stage, it can be predicted whether residual stress state accompanied by martensitic transformation is compressive or tensile. If it is tensile in nature, then it intensifies the applied tensile stress and if generated residual stress state is compressive in nature it can minimize the overall net stress attained by welding (Payares-Asprino et al., (2008)).

The welding stresses are characterized by three components, i.e., longitudinal (along welding direction, i.e., S11), transverse (perpendicular to welding direction, i.e., S22) and thickness (along thickness direction, i.e., S33). In the present study only longitudinal (S11) and transverse (S22) stresses along X-axis and Y-axis, respectively, on the top surface of material have been taken into account. Fig. 5.12a represents the estimated value of longitudinal residual stress (S11) perpendicular to the weld direction (i.e., towards Y-direction) by assuming phase transformation effect, i.e., for case 3 and, case 1 and case 2 by neglecting the phase transformation effect. It is clearly observed that the longitudinal residual stress (S11) is tensile and gradually changes to compressive in nature when moving away from the weld line (i.e.,

towards base metal edge). The pattern of distribution of longitudinal residual stress is quite similar for all assumed condition even in phase transformed condition. However, the magnitudes are significantly different. The maximum magnitudes of residual stress are ~ 707 MPa, ~ 605 MPa, and ~ 505 MPa for different cases, i.e., 1, 2 and 3, respectively. Although the maximum magnitude of longitudinal residual stress for case 1 is fairly more than case 2, but the average value of S11(~ 577 MPa) for case 2 is notably more than that of S11 (~ 532 MPa) for case 1 in FZ as well as in HAZ when phase transformation effect is neglected. Similar trend of results have been observed by other researchers (Deng and Murakawa, 2008). Due to reversal of constraint condition, a remarkable difference of longitudinal residual stress in the Y-direction is observed corresponding to case 1 and case 2, respectively.

It is obvious from the Fig. 5.12a that overall magnitude of longitudinal residual stress in HAZ and BM zone increases with increase in the number of constraints. Kohandehghan and Serajzadeh (Kohandehghan and Serajzadeh, 2011) observed that higher constraint can cause 7 % increase in maximum value of longitudinal residual stress. Restricting the movement of the weldment in different direction acts as constraint and prevents the deformation of the plate after welding which leads to additional plastic strain in the substrate. Moreover, the strain induced in the weldment due to expansion and contraction of different zones could not be released hence, they retained inside and lead to relatively higher residual stress generation. Abid and Siddique and Zeng et al. (Abid and Siddique, 2005; Zeng et al., 2009) have reported similar effect of constraints on longitudinal residual stresses in their study. However, comparatively large difference in stress value is observed in transverse direction between case 3 (i.e., with phase transformation effect) and case 1 (i.e., without of phase transformation effect). This is due to the fact that the volumetric dilation due to $\beta \rightarrow \alpha'$ martensitic transformation is much more significant during phase transformation. When the temperature at FZ and HAZ attained martensitic start temperature during cooling cycle, the acquired tensile stress (i.e., in case 1 and 2) begins to decrease (as depicted in case 3 in Fig. 5.12a) because volumetric expansion takes place due to $\beta \rightarrow \alpha'$ martensitic transformation (as shown in Fig. 5.11). Additionally, temperature suppression continues upto martensitic finish temperature and martensitic volume fraction increases. It promotes the decrement of longitudinal stress more and even changes its sign from positive (tensile) to negative (compressive). It is interesting to note that longitudinal

residual stress found to be more compressive for case 3 as compared to case 2 at a distance 4 mm away from the weld centre line.

Fig. 5.12b depicts the transverse residual stress (i.e., S22) across the welding direction for different conditions. The transverse residual stress is compressive in nature immediately after the weld central line for all the cases upto a distance of 5 mm. Beyond 5 mm, it gradually transformed into tensile stress. It is obvious that the magnitude of transverse stress for case 3 is much different from other cases. The maximum magnitude of transverse stress (S22) is found to be ~200 MPa for case 2, whereas ~210 MPa and ~105 MPa for case 1 and case 3 respectively**.** It is obvious that utilizing more constraint decreases transverse residual stress insignificantly, but inclusion of phase transformation effect alters both distribution and magnitude of S22 significantly. It is also noteworthy that the maximum value of transverse residual stress in FZ and HAZ predicted by case 1 and case 2 is larger than case 3 in which solid state (i.e., martensitic) transformation is considered. The maximum value of residual stress (S22) is decreased by ~ 50% when phase transformation effect is considered. Distribution of transverse stress is in contrary to longitudinal stress. Existence of higher temperature gradient in transverse direction might be responsible factor for lowering the residual stress in transverse direction. Furthermore, unlike other cases (i.e., case 1 or case 2), generation of tensile transverse residual stress due to martensitic transformation may be the possible reason due to which overall net magnitude of compressive transverse stress decreases in case 3 (Fig. 5.12b). It is also observed that increasing the number of constraint can increase the residual stress at some extent. The similar trends of transverse residual stress across the weld line are observed by another researcher (Chuan et al., 2009).

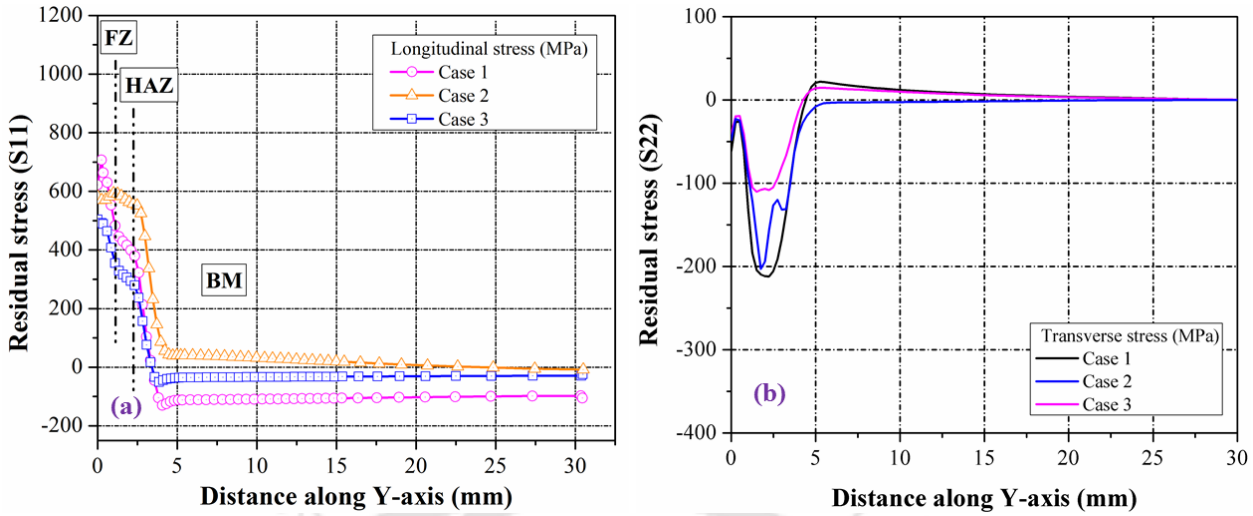

Fig. 5.12 (a) In plane longitudinal residual stress distribution, (b) transverse residual stress distribution

Fig. 5.13 depicts the influence of phase transformation on longitudinal residual stress (S11) along welding direction. It is obvious that the values of longitudinal residual stress within the range approximately from X = 10 mm to X = 50 mm is almost uniformly distributed for case 1 and case 3. Moreover, the variation in the value of residual stress (S11) is of about 200 MPa. Nearest to weld start and end location, the magnitude is of compressive nature. The fusion zone (FZ) undergoes significant longitudinal stress of tensile in nature. When the weld zone experiences contraction during cooling stage, the holding of the base plate to maintain the initial length leads to the weld to get plastically deformed (Long et al., 2009). Author (Guo et al., 2003) revealed that the residual stress increases with the volume fraction of lamellar grains and residual stress decreases as volume fraction of acicular (martensite) structure increases. It should be noted that diffusion controlled lamellar structured morphology is predominant in moderate cooling rate (i.e., 20 K/s to 410 K/s) and acicular type morphology exist within higher range of rate of change of temperature i.e., cooling rate (> 410 K/s). In the present work, it is observed that the attained rate of change of temperature in FZ and HAZ in significantly higher than critical cooling rate which resembles predominant martensitic transformation. This is the fact by virtue of which residual stress decreases for case 3 in which phase transformation effect is taken into account.

Fig. 5.14 illustrates the distribution of effective von-Mises stress exhibited by welded plate for different cases. It indicates that the effective stress get released at some extent if phase transformation effect is undertaken during mechanical analysis. The magnitude of maximum von-Mises stress is found to be ~ 823 MPa for case 1, ~ 987 MPa for case 2 and ~ 735 MPa for case 3. It is noteworthy that the effective stress at

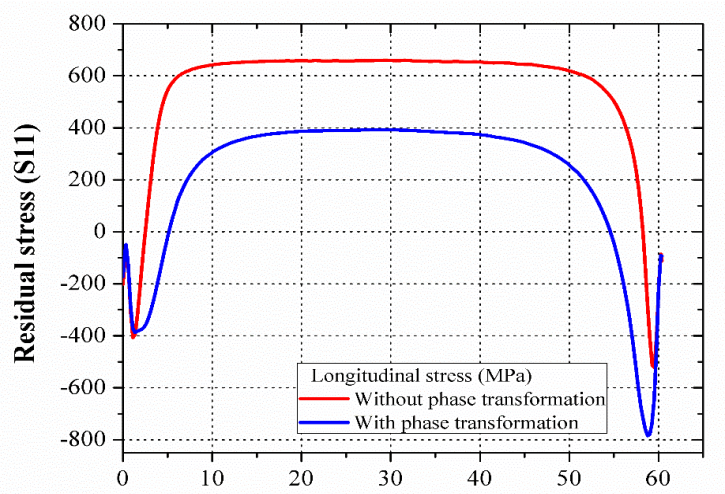

Fig. 5.13 Distribution of longitudinal residual stress along welding direction by considering phase transformation effect (Case 3) and by the neglecting phase transformation effect (Case 1)

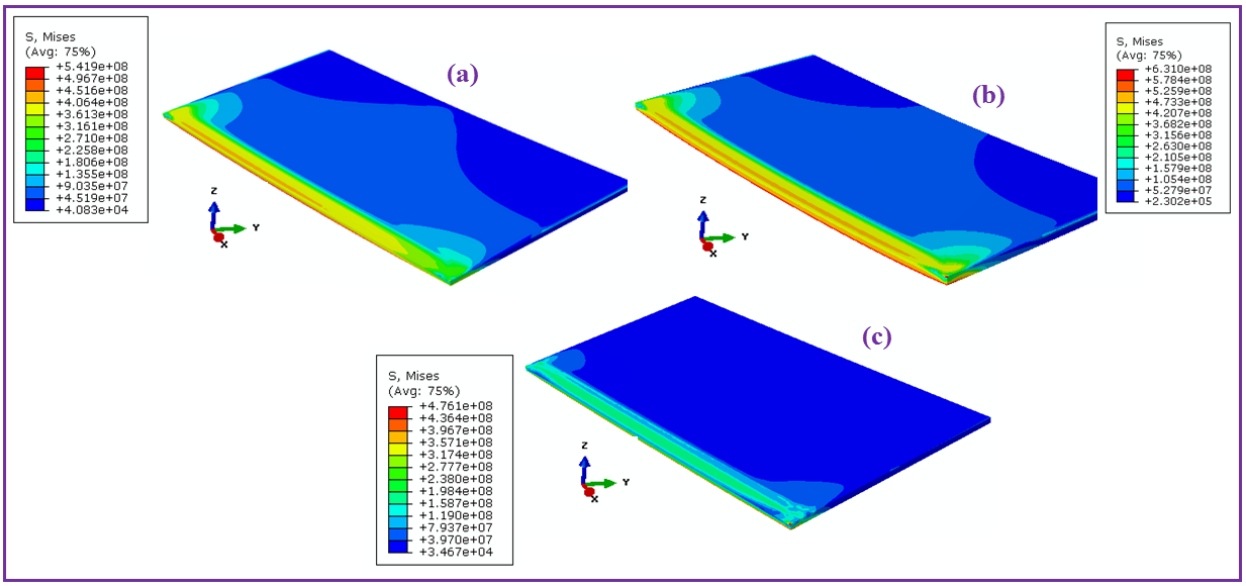

Fig. 5.14 Contour plot of von-Mises stress distribution in (a) Case 1, (b) Case 2, and (c) Case 3

top surface of the weld zone is less than the bottom surface. Furthermore, the von-Mises stress is distributed in relatively large volume of the welded zone corresponding to cases 1 and 2. However, it is localized into a small weld area with low magnitude in case 3. It seems that the effective stress is well below the yield strength (~ 1240 MPa) of Ti6Al4V alloy (Murr et al., 2009). It is obvious from Fig. 5.14 that the equivalent stress (i.e., Von-Mises) increases upon

increasing the number of constraints. In presence of constraints, it is difficult to release strain which evolves from the heating of the workpiece at elevated temperature and remains in the workpiece even after cooling and transform into effective stress. The magnitudes of longitudinal residual stress significantly more than that of transverse stress. It is to be noted that the Von-Mises stress is mainly attributed to the longitudinal residual stress.

5.2.4 Distortion in welded structure

Fig. 5.15a depicts the equivalent plastic strain (i.e., PEEQ) along transverse direction with respect to weld center line of the substrate. There is no significant difference in the magnitude and pattern of equivalent plastic strain distribution for case 1 and case 2. However, significant variation has been observed when phase transformation effect is considered. The magnitudes of PEEQ are found to be 0.15 and 0.155 for case 1 and case 2, respectively. Whereas, its value gradually dampens to 0.124 when phase transformation effect is taken into account. It is also observed that the maximum tensile plastic strain appears instantly after the weld central line. When phase transformation effect is neglected, higher equivalent plastic strain value is distributed in wider area, i.e., upto 2 mm whereas it is confined to 0.75 mm when phase transformation effect is considered. Plastic strain is that strain which could not release even after cooling phase and remained inside substrate which in turns transforms into residual stress. Hence, it is advantageous if its magnitude is kept low as observed in phase transformation condition (Fig. 5.15a-b) and restricted to closer distance. Fig. 5.15b shows the calculated value of magnitude of plastic strain component (PEMAG) for case 1, case 2 and case 3. The magnitude of plastic strain component are found to be 0.06 and 0.065 for case 2 and case 1 respectively but its value is 0.041 for case 3. Other researchers revealed similar type of inferences and trends of plastic strain distribution for butt joint component (Kohandehghan and Serajzadeh, 2011; Yadaiah and Bag, 2012).

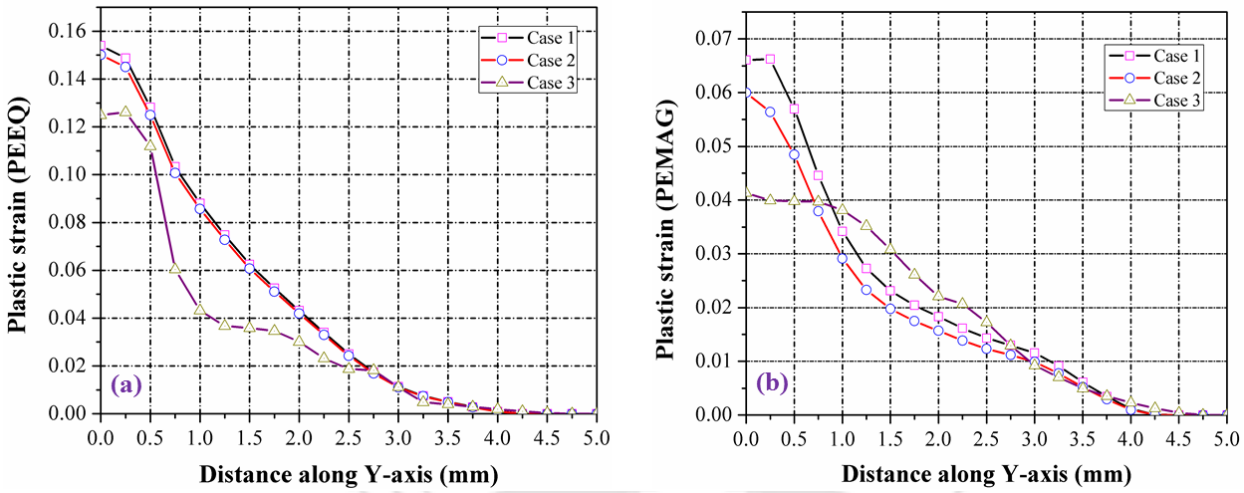

Fig. 5.15 (a) Variation of equivalent plastic strain (PEEQ), (b) magnitude of plastic strain (PEMAG) along transverse direction

It is observed from literature that the phase transformation effect does not directly impact remarkably on welding distortion for the case of low carbon steel (Deng et al., 2009). This fact is not true for welding of Ti6Al4V alloy. Distortion evolved after welding can be correlated with residual stress accompanied by phase transformation to some extent. Fig. 5.16 renders the effective deflection of symmetrical part of weld joint with and without phase transformation condition. Saddle type buckling structure is observed for all three conditions with different deformation magnitude. In all three conditions, (i.e., case 1 with less constraint condition and case 2 with more constrain condition) at the end of the weld line (i.e., blue color band) translation is restricted in z-axis where the magnitude of deflection is almost zero. Therefore, it is inferred that enforcement of constrain can restrict the deformation. Red color band designate magnitude of maximum deflection. The maximum deflection is observed at the center of the plate. The maximum magnitudes of effective deflection are found to be 1.26 mm, 1.15 mm and 1.22 mm for case 1, case 2 and case 3 respectively as depicted in Fig. 5.16a-c. It is obvious that the magnitude of effective deflection is not significantly affected by the phase transformation affect. The number of constraint plays predominant role for the amplification and reduction of effective deflection.

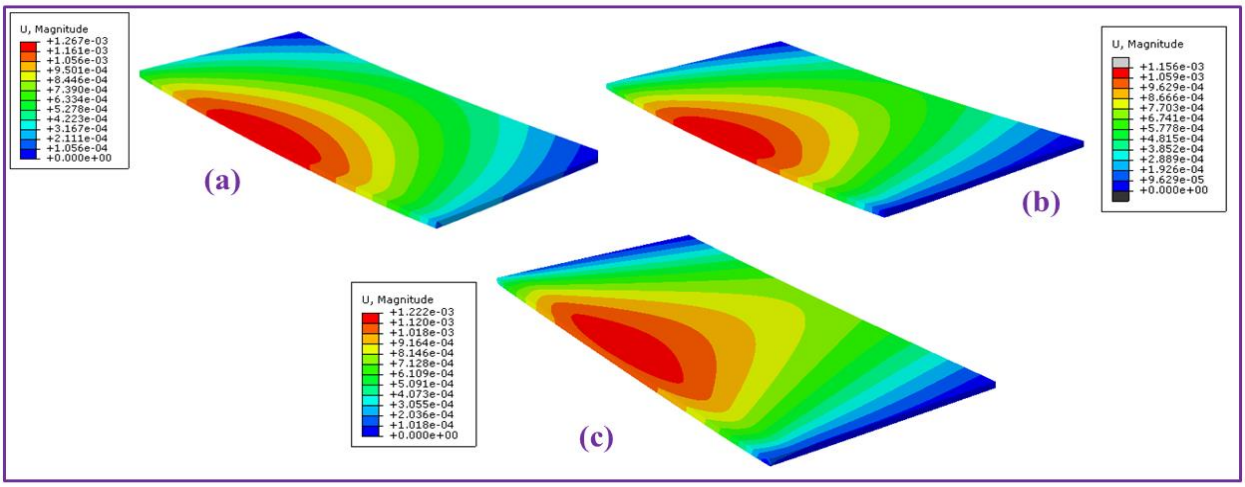

Fig. 5.16 Distribution of effective deformation for (a) Case 1, (b) Case 2, and (c) Case 3

Fig. 5.17 describes the comparison between computed and experimental data for out of the plane deflection or longitudinal deflection (U1) along transverse direction [Gao et al., (2013)]. The highest longitudinal deformation (U1) arises at section of central axis (i.e., at Y = 0) in welded plate, while least longitudinal deformation is noticed at the farthest edges of the laser welded plate. The maximum longitudinal bending is observed at 2 mm away from the weld central line in each case and somewhat less magnitude of deformation is noticed at Y = 0 mm. Even though uniform pattern of longitudinal deflection have been observed for all simulated conditions, similar pattern of longitudinal deflection distribution, as expressed in experimental result, is predicted by considering phase transformation effect. Some discrepancy is observed in the magnitude of deflection in case 3

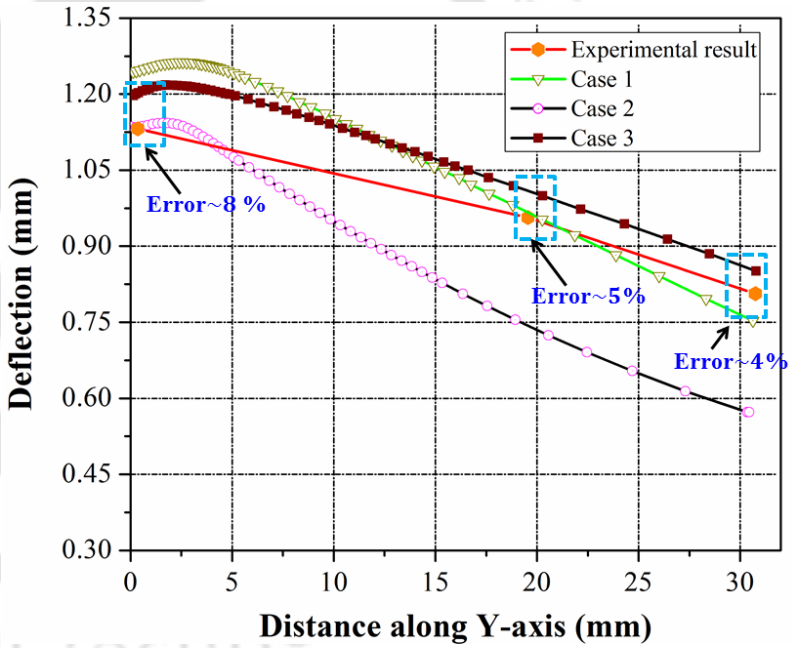

Fig. 5.17 Comparison of the out of the plane deflection (i.e., longitudinal deflection) along transverse direction

with respect to experimental data. The deflections are found to be 1.13, 0.97 and 0.82 mm in experimental condition while the numerically estimated deflections observed in case 3 are 1.2, 1.01 and 0.86 mm, at the location of Y = 0 mm, Y = 20 mm and Y = 30 mm, respectively across the weld line. It is also observed that the maximum difference between experimental and numerically calculated deflection is 0.07 mm whereas minimum difference is 0.04 mm. The average error percentage between experimental and numerical result is calculated as ~ 6 % which indicates the robustness of the developed numerical model including the phase transformation effect. Furthermore, the magnitude of deflection is same as experimental condition at Y = 0 for case 2, despite distribution of deflection in farther away locations are significantly deviated from the experimental result. This is based on the fact that more constrains are provided as a boundary condition in the case 2. Overall, the predicted longitudinal deflection is well agreed with experimentally measured value when phase transformation effect is considered.

As depicted in Fig. 5.18a, the dimensional shift (ΔY) in the Y-direction for total width of the welded plate is expressed as transverse shringkage in the present study. This type of dimensional change can be evaluated in longitudinal (i.e., along the welding direction) and transverse (i.e., across the welding direction) direction. Fig. 5.18b depicts the transverse shrinkage at the top surface of the weldment in welding direction for different cases. The magnitudes of transverse shrinkage near weld line are found to be 0.12, 0.20 mm and 0.25 mm for case 1, case 2 and case 3 respectively. Moreover, deflection for all conditions are observed in negative Z-direction. The magnitudes of deflection are negligible at the edge of the base plate. It is noteworthy that the first end of the weldment is having more deflection as compared to other edge and non-symmetric deformation pattern are obtained in both the cases. This is attributed to the fact that dispalcement along z-axis is restricted at the edge of the plate (Fig. 5.1) with the application of clamp or fixture whereas start

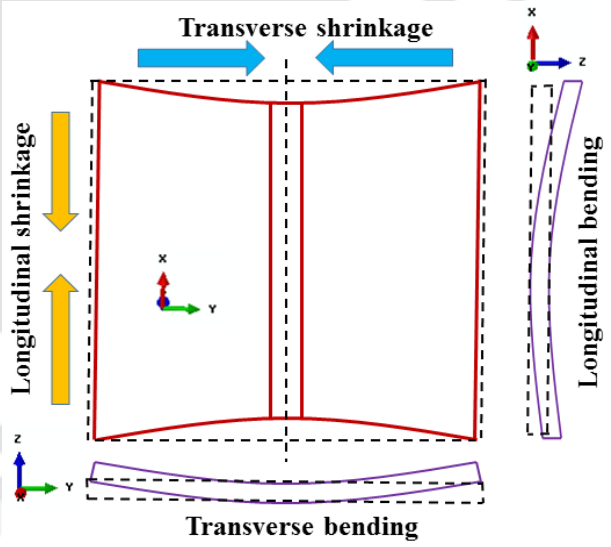

Fig. 5.18 (a) Schematic of different types of distortion exhibited in thin plate welded structure

edge is remained free which in turn allow it to deform freely for the relaxation of residual stress during cooling phase. It is also observed that the overall transverse deformation of the plate is found to be comparitively very less by considering phase transformation effect. It means that this effect plays an important role to reduce transverse deflection in welding direction. Volumetric dilation takes place due to solid state phase transformation in the weld zone which is attributed to the relaxation of residual stress. Since, less amount of residual stress is persisted in longitudinal direction, very less amount of distortion is expected in this region. The maximum transverse shrinkage is observed in the middle portion of the welding direction and gradually diminishes towards the end of the plate. The highest thermal expansion occurs at the middle section of the plate. As the maximum heat transfer is predominant at start and end edge of weldment, it signifies that subtantial portion of tranverse deformation is due to thermal contraction of the parent metal. However, the weld only contribute approximately ~10% of equivalent transverse shrinkage (Masubuchi, 2013).

Fig. 5.18c illustrates the transverse shrinkage evolved in the plate across the welding direction for case 1 and case 2. It is noticed that transverse shrinkage increases in negative z-direction (i.e., in the weld zone) and after reaching a peak value upto distance of 4 mm, it gradually moves towards positive z-direction. The maximum tranverse shrinkage across the weld line are found to be 0.020 and 0.006 mm for case 1 and case 3 respectively, and 0.017 mm for case 2. It is obvious that there in no significant difference has been observed between case 1 and case 2, however, relatively large difference is found when phase transformation effect is

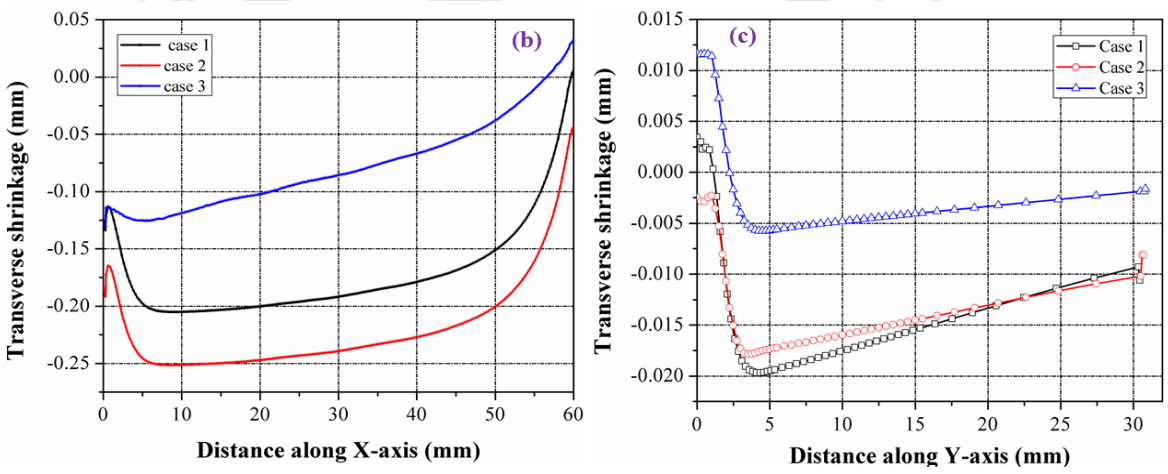

Fig. 5.18 (b) Distribution of transverse shrinkage along longitudinal direction, (c) distribution of transverse shrinkage along transverse direction

considered. The present study reveals that both transverse and longitudinal bending is generated in the weldments. The distortion mode or patterns are approximately comparable for case 3 and case 1, however, the magnitudes of deformation are different. Moreover, the simulated deformation pattern with phase transformation effect is quite similar to the literature reported results but the magnitudes are somewhat different.

5.3 Microstructural morphology and mechanical properties of Laser welded Ti6Al4V alloy

The transients and gradients generated due to localized heating and cooling by a laser source governs the thermal-metallurgical-mechanical performance of the welded structure. Ti6Al4V alloy is highly susceptible to the nitrogen and oxygen affinity at an elevated temperature that primarily deteriorates mechanical property of welded joints (Baruah and Bag, 2017). Thus, it is of critical importance to pay special attention towards the monitoring of contamination level in the weld pool by proper shielding system. Rapid solidification accompanied by low peak power offers crack initiation in weld seam and transition zone (Gursel, 2017). Porosity formation is often in laser welded Ti-alloy structure, where the amount of hydrogen and other gases entrapped within a molten pool and solubility of a gas in the molten pool decides the nature of pore (Matsunawa et al., 1998). Hence, pulse laser is well suited for a microwelding application because of controlled heat input and capability to join highly heat-sensitive components (Tzeng, 2000). An attempt is made to investigate the significance of the pulse parameter over continuous mode in Yb-fiber laser welding of 800 μm thin Ti6Al4V alloy. The tensile strength, fatigue strength, and corrosion-resistance of fusion zone and heat affected zone (HAZ) of Ti-alloy weldments are highly influenced by microstructural morphology (Poorhaydari et al., 2005). The behavior pattern of the thermal history is critically assessed with the aid of FE based heat transfer model and corresponding relation with evolved microstructural morphologies are systematically investigated. Several stages of transformation occurred in the weld zone such as α-phase dissolution, β-transus in the heating cycle, and diffusionless $\beta \rightarrow \alpha'/\alpha$ martensitic transformation during the cooling cycle are well explained by thermal history. Not only morphologies, even variation in geometrical dimensions of α-lamellae also affects

mechanical properties significantly (Cheng et al., 2009). Specific morphology can be achieved by controlled thermal cycle, which is primarily determined by the mode of thermo-mechanical processing. Therefore, morphological characterization is performed to correlate its geometrical dimensions with evolved mechanical properties. Furthermore, the Finite Element (FE) based numerical tool facilitates the adequate measure of temperature in difficult-to-reach location and to capture other intricate physical phenomena, which are otherwise difficult to achieve by simple experimental set-up (Bag and De, 2008; Trivedi et al., 2006). The estimation of temperature field in conduction based heat transfer model with enhanced accuracy depends on the choice of appropriate heat source model. Thus, in order to capture the thermal behavior and to estimate cooling rate, FE based thermal model is developed. In order to fulfil the present objective, both pulse laser system (TRUMPF 556, 10 kW) and Yb-Fiber laser set-up (YLS 2000, 2 kW) for the continuous mode of welding is adopted here (Fig. 3.1). The experimental conditions used for both the laser systems are presented in Table 3.1 of Chapter 3. The set of optimized process parameters is demonstrated in Table 3.2. Furthermore, the phases attributed at FZ of welded samples are investigated by X-ray diffractometer (XRD) with Cu K_{α} radiation. The high-resolution microstructure is obtained using a field emission scanning electron microscope (FESEM) to investigate the variation of α'-martensite lath at different welding conditions. Topographic measurements are carried out over the welded samples using surface profilometer as shown in Fig. 3.4 of Chapter 3. The tensile properties of the welded joints are examined with a universal testing machine (capacity 250 kN) at a crosshead speed of 1 mm/s. The results obtained in accordance with experimental and numerical investigation is presented here.

5.3.1 Weld bead appearance and topography

Fig. 5.19 describes the bead appearance (top view) of the welded joints at different heat inputs. The performance of shielding, contamination level as well as surface imperfection present over the weld surface, can be visually inspected by its appearance or surface discoloration. It is emphasized that the color changes from Silver → Dark straw + Brown → Light straw + Blue for continuous mode, whereas Silver → Brown → Straw + Dark blue for current pulsation, upon gradual increment of heat input from C1→ C4 or P1→ P4. The color transition implies an increasing level of contamination due to the progressive reduction of the shielding effect at the

weld zone. Since Ti-alloy is prone to severe oxidation, the chances of contamination are high at elevated temperatures. The appearance of silver color bead for the weld metal C1 and P1, fabricated at low heat input, indicates least contamination (Hong and Shin, 2016). It can be inferred that the applied shielding environment may not worked properly at elevated temperature, especially for continuous mode weld. Therefore, suitable approach such as purging technique, mixture of shielding gases or vacuum chamber should be adopted to exhibit better shielding effect (Reed et al., 2000).

Mode	Increasing contamination level →		
Continuous	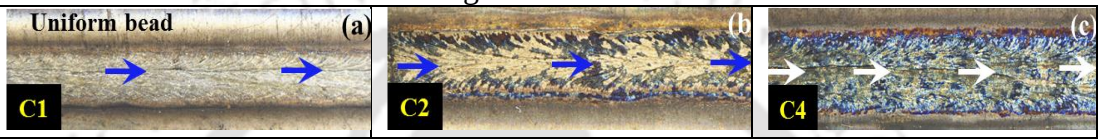		
Color	**Bright silver**	**Dark straw + Brown**	**Light straw + Blue**
Pulse	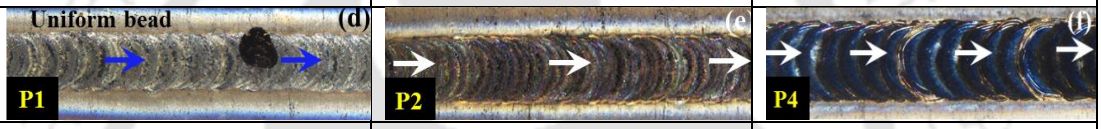		
Color	**Silver**	**Brown**	**Straw + Dark blue**

Fig. 5.19 Weld bead appearance of continuous mode (a) C1, (b) C2, (c) C4, and pulse mode (d) P1, (e) P2, (f) P4

Fig. 5.20 represents the 3D topographical image of welded specimens fabricated at maximum and minimum heat input by using surface profilometer (TALYSURF). It shows the scars or uneven surface finish at the weld region (top) that arises due to thermal agitation. A welded joint that exhibits sufficient depth of penetration is not recognized as good weld; nevertheless, other condition such as acceptable surface finish has to be fulfilled as well (Torkamany et al., 2006). The poor surface finish gives rise to the peak-valley ratio is a good indication of the existence of high surface roughness. It is

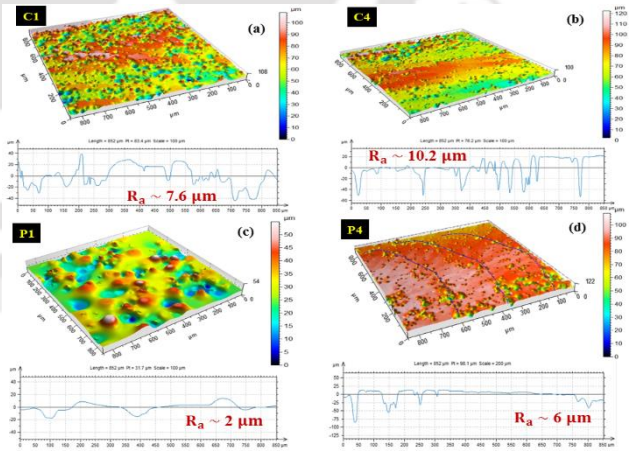

Fig. 5.20 The topology of weld surface for welding conditions of (a) C1, (b) C4, (c) P1 and (d) P4

evident that minimum surface irregularity ($R_a \sim 2$ μm) is observed for the case P1, fabricated at the lowest heat input (12 J/mm). In addition, relatively poor surface finish ($R_a \sim 6$ μm) is witnessed by the weld joint P4. Re-melting and re-solidification in pulse mode at high heat input attribute higher surface roughness. Accordingly, the average roughness value is found to be maximum ($R_a \sim 10.2$ μm) for weld metal C4 that implies the inferior surface finish. In contrast, a layer of TiO_2 and Al_2O_3 provides improved wear-resistant property to the weld surface, get spall off automatically upon the continuous rising of oxidation temperature due to prolonged exposure of molten zone at elevated temperature (Wang et al., 2016). Thus, upon rising heat input from P1 → P4 → C1 → C4, peak-to-valley ratio gradually increase, which results in significant surface roughness of 2 μm → 6 μm → 7.6 μm → 10.2 μm, respectively.

5.3.2 Weld bead profile

The weld bead profile of Ti-alloy under various process conditions are illustrated in Fig. 5.21 and 5.22. The fusion width at the top (F_{TW}), penetration depth (P_d), fusion area (F_A), and root width (F_{RW}) are plotted against heat input in Fig. 5.23. It confirms that the heat input significantly affects the overall weld bead characteristics. Nearly half penetration is apparent at the lowest heat input of 45 J/mm for continuous mode. In addition, full penetration is accomplished by increasing heat input to 64.6 J/mm. The rise in heat input causes additional heat generation in the localized area, which provides more time to permeate throughout the thickness, hence the depth of penetration increases for weld metal C2, C3, and C4. Particularly, the top to root fusion width ratio is approximated as ~ 1.5 for C3 and C4 indicates that the conduction mode is adopted in the continuous weld. Apart from that, aspect ratio (depth/width) of the fusion zone is used to distinguish between conduction and keyhole mode as well (Weckman et al., 1997). Conduction mode is predominant if aspect ratio is less than 0.4, whereas keyhole mode comes into existence beyond 0.4 if welding power is an order of 1 kW. In the present investigation, the aspect ratio is estimated as < 0.4 for the cases C1, C2, C3, and C4; thereby, it confirms that conduction mode is prevalent for continuous current welding. For pulse current, full penetration is achieved for the lower heat input of 12 J/mm and 19.65 J/mm at a pulse frequency of 8 Hz. However, partial penetration is observed for higher heat input of 26.4 J/mm and 35.7 J/mm at a pulse frequency of 10 Hz. Wider F_{TW} and narrow F_{RW} demonstrated by P1,

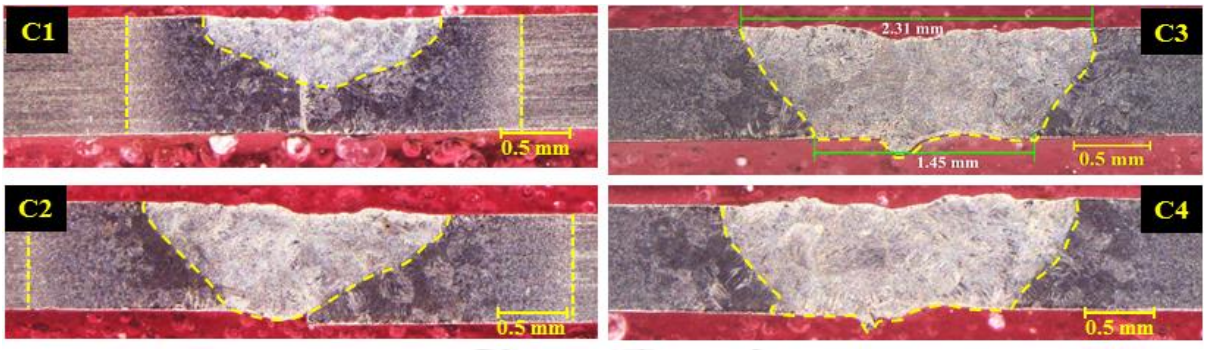

Fig. 5.21 Weld profile at continuous mode of laser welding.

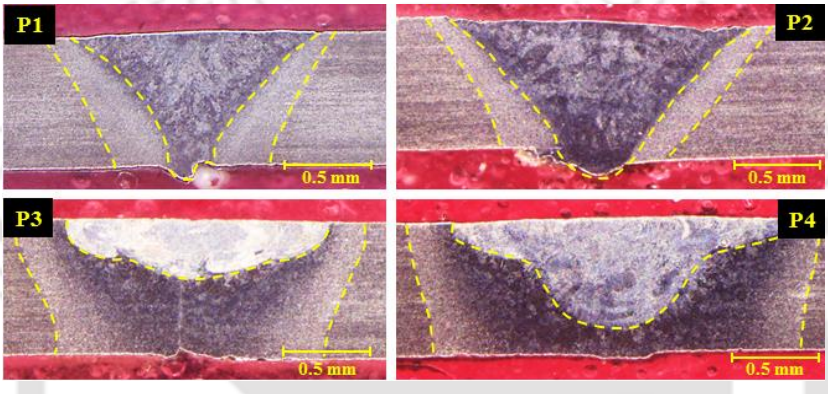

Fig. 5.22 Weld pool shape at pulse welding conditions.

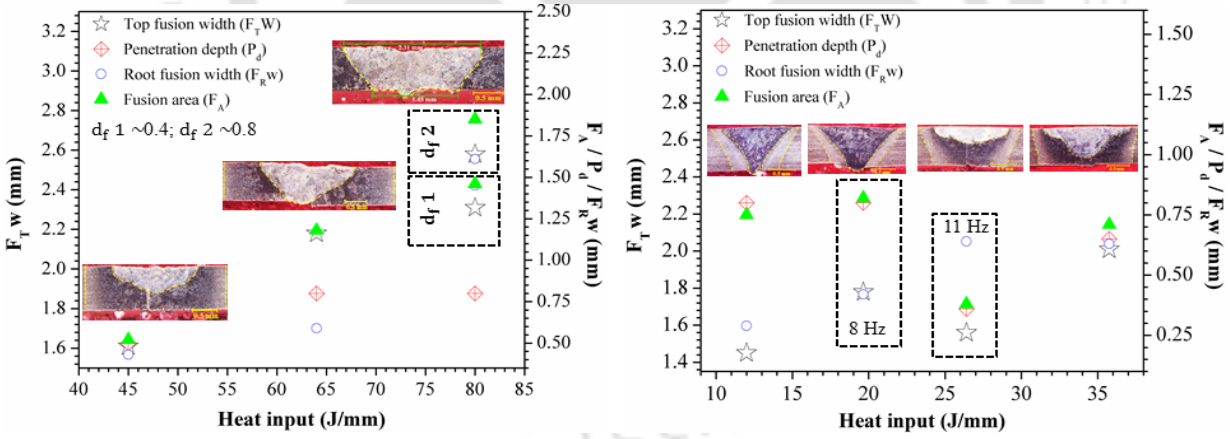

Fig. 5.23 Characteristics of weld geometries under different heat inputs

P2, and P4 indicate that keyhole mode prevails over conduction mode for pulse welding (Ventrella et al., 2010). V-shaped keyhole is exhibited by P1, P2, whereas P4 illustrates a T-shaped keyhole. Surface tension variation between the upper and lower half of weld bead, recoil pressure, and the gravity force are the physical properties that trigger the flow pattern of the molten pool and helps in the formation of a keyhole (Kim and Ahn, 2012). It can be concluded

that a pulse frequency of 8 Hz is found to be threshold frequency beyond which significant deviation in F_{RW} is observed, and partial penetration is achieved even after increasing laser power as well.

The variation of weld bead parameters at different heat input is depicted in Fig. 5.23. It is obvious that weld characteristics for all the specimens (except P3 and P4) exhibit linear relation with heat input. Although, the C3 and C4 are welded at the same heat input of 80 J/mm, the fusion area of weld metal C4 is relatively higher due to the deviation in defocusing distance. With increasing defocused distance (from -0.4 mm for C3) to -0.8 mm (for C4), the area of interaction between laser beam and substrate increases because of the divergence of the laser beam to a greater extent. It is noteworthy that despite heat input increases for the case P2 → P3, F_A decreases owing to reduced depth of penetration.

5.3.3 Phase constituents in weld material

Fig. 5.24 shows the X-ray diffraction spectrum obtained from weld metals fabricated in pulse and continuous modes. The center of the weld zone reveals hcp-α′ martensite, hcp prior-α phase, and a small amount of retained β-phase. The sharp peak of hcp-α solid solution and the weak peak of β(211) are observed in the base metal. The lattice parameter of α and α′ martensite is nearly same. Hence, these peaks correspond to dominant α′ is seen in the spectrum. It is observed that the peak corresponding to plane (20$\bar{2}$0), (11$\bar{2}$2) and (20$\bar{2}$1) seen in base metal, converted into the single peak of plane α(11$\bar{2}$2) after welding. In addition, the intensity of these

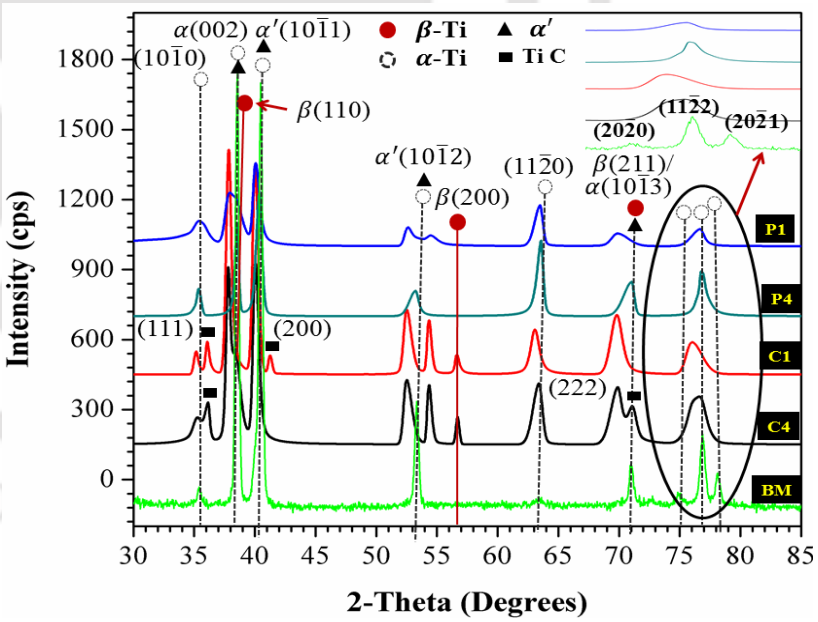

Fig. 5.24 X-ray spectrum of weld zone at different heat inputs

peaks decreases upon changing the weld mode from continuous to pulse, which indicates significant changes in texture associated with elongated grain transformed into equiaxed grain. However, relatively higher intensity of $\alpha'(10\bar{1}1)$, $\alpha'(11\bar{2}0)$ and $\alpha'(002)$ signifies the existence of the large amount of α'-martensite for pulse condition of low heat input (~12 and 35 J/mm). The solid-state phase transformation from $\beta \rightarrow \alpha$ follows diffusionless transformation that exhibits a higher amount of α'-martensite at low heat input. It is evident that the peak associated with retained β-phase, i.e., β(211) and β(200), is intensified at higher heat input (~ 45 and ~ 80 J/mm) of continuous mode. This is attributed to the fact that $\beta \rightarrow \alpha$ phase transformation is diffusional at high heat input, resulting less amount of metastable β-phase fraction ready to be transformed into α'/ α-phase, and hence, retained β-phase fraction is higher. It is inferred that weld metal C4 and C1 resemble reduced phase fraction of α' martensite, and the remaining phase contributes retained β-phase and α-phases. Moreover, P4 and P1 exhibits enriched α'-martensite and lean out retained β-phase and α-phase. In addition, the diffraction peaks corresponding to the plane (111), (200) and (222) confirms the presence of carbide compound (TiC) for continuous current weldments since Ti is highly susceptible towards carbide formation if it is subjected to significantly higher heat input (Buffa et al., 2013). Therefore, the risk of carbide formation is higher in continuous mode welding. Furthermore, peak broadening and peak shift phenomena are also notified for welded joints.

The microstructure of Ti6Al4V alloy is much sensitive to thermal cycle followed during thermo-mechanical processing. The cooling rate adopted during solidification of the weld pool beyond β-transus temperature (1275 K) plays a decisive role in the determination of final material properties. Therefore, in order to track temperature distribution and to estimate the cooling rate, thermal simulation is performed, and the results are depicted in Fig. 5.25. The experimentally measured bead profiles are in good correspondence with a numerically calculated peak temperature of 2680 K and 2519 K for weld metal P1 and C4, respectively as demonstrated in Fig. 6.7a. Although heat input is less for pulse condition relative to continuous mode, the temperature is significantly higher owing to the augmented peak power (i.e., 1000 W) experienced by the substrate during pulse on time. Fig. 5.25b elucidates the schematic representation of the molten zone and nearby region (top view). Gray color region attains temperature beyond melting (1933 K) and bounded by a narrow saffron band that exhibits

temperature between solidus (1877 K) and liquids. Fully transformed HAZ (FT-HAZ) is defined by β-transus and solidus temperature whereas partially transformed HAZ (PT-HAZ) is subjected to less than β-transus temperature, separated by the green dashed line. The temperature profile and associated cooling rate (dT/dt) for specimen P1 and C4 are indicated in Fig. 5.25c. The maximum cooling rate (K/s) during the cooling phase is assumed for further analysis. Crest and trough characteristics caused by pulse on and off utility render a very high-temperature gradient that results in an extremely high cooling rate in pulse condition. Fig. 5.25d demonstrates the non-linear variation of estimated cooling rate and maximum temperature against overall heat input under various parameters. Accordingly, the cooling rate decreases with increase in heat input for both pulse and continuous mode of welding. It is thus apparent that the cooling rate achieved is the highest for minimum heat input. Since the molten pool lasts for the shortest time for the lowest heat input; hence, it exhibits low solidification time or high cooling rate.

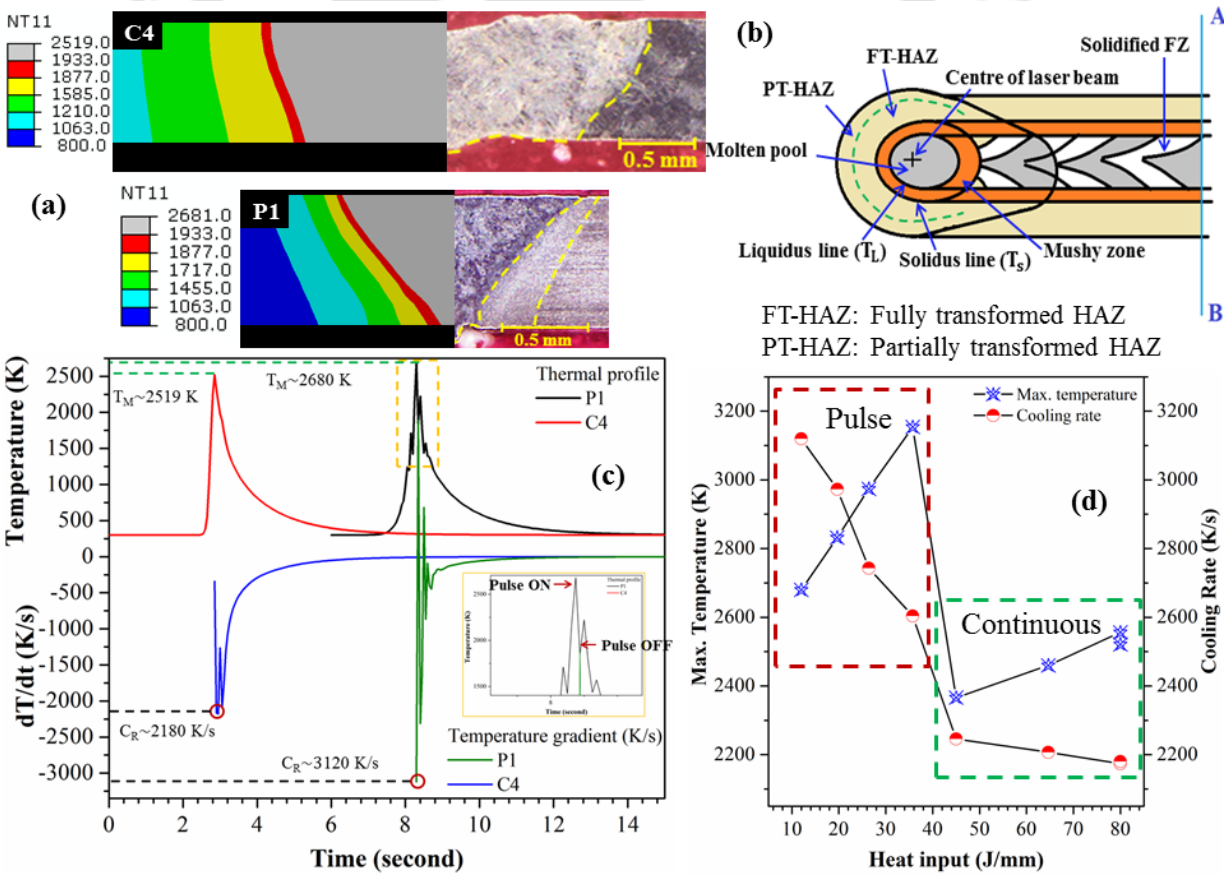

Fig. 5.25 Temperature profile of laser welding: (a) comparison between experimental (right) and numerically calculated (left) weld profile in continuous (top) and pulse (bottom) mode, (b)

schematic of the different zones in linear laser welding, (c) temperature profile and cooling rate with time, and (d) variation of cooling rate and maximum temperature at different heat inputs

5.3.4 Microstructural evolution at non-diffusional transformation

The microstructure evolved at the weld zone for heat input of 80 J / mm (case C3) is shown in Fig. 5.26. The solidification of dual-phase Ti-alloy occur as an epitaxial growth of β-crystal, and upon further cooling, it decomposes into α-phase through diffusional transformation or into α′-martensite by diffusionless transformation or a mixture of both. Fig. 5.26 signifies that the temperature gradient arises due to non-uniform thermal agitation that emerges at four different zones (FZ, FT-HAZ, PT-HAZ, and base material). It is emphasized that the entire weld zone consists of α′-martensite within large columnar β-grain and retained α-phase. Continuous cooling transformation (CCT) diagram explains that 410 K/s as a critical cooling rate (Ahmed and Rack, 1998; Sieniawski et al., 2013) beyond which molten pool manifests displacive mechanism of solidification, which results in diffusionless transformation and exhibits α′-martensite within β-matrix sufficiently. The estimated cooling rate for all the specimens is remarkably higher than that of critical limits. Hence, predominant α′-martensitic type microstructure is noticed for both continuous and pulse mode. However, variation in distribution and the geometrical dimension of α′ and β-phase is observed under different weld conditions. It is worth mentioning that fusion zone renders columnar grain growth along with coarse prior β-grain boundary (yellow dashed line), as demonstrated in Fig. 5.26b. Gray blocky plate α′-martensite in FZ and fine acicular α′-martensite in FT-HAZ is obtained (Ahmed and Rack, 1998). The accomplishment of a low heat

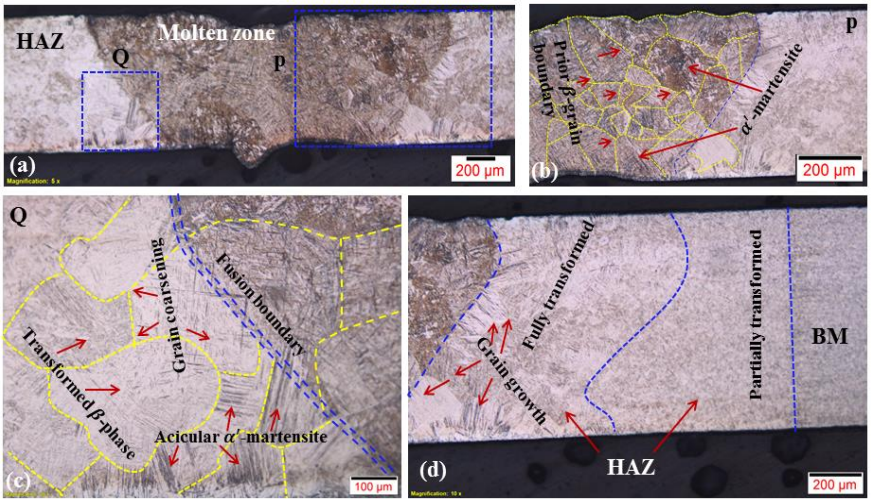

Fig. 5.26 Microstructure at different zones for (a) C3, (b) scanned area 'P', (c) scanned area Q and (d) at FT-HAZ & PT-HAZ

input at farther away region inhibits the grain growth and coarsening of the prior β-grain boundary. Therefore, partial grain growth, as well as indistinguishable β-grain boundaries, prevails in HAZ, as shown in Fig. 5.26c, d. Aditionally, Fig. 5.26d indicates that the α′-martensite phase fraction diminishes at a location away from the weld region i.e., FZ → FT-HAZ → PT-HAZ due to the reduction in local cooling rate. Likewise, other weld metals prepared in continuous mode exhibits similar type of microstructure at FZ and HAZ with varied average grain sizes in increasing order of C1→ C2 → C4.

Fig. 5.27 illustrates the microstructure of P1 prepared using lowest heat input of 12 J/mm in pulse mode. Tiny columnar grain with partially transformed prior β-grain boundary is observed in the weld zone as depicted in a magnified view corresponding to the scanned area "R" (Fig. 5.27b). This could be due to extremely high power subjected to the weldment for a millisecond (pulse duration) during pulsation, which in turn increases the nucleation rate. Moreover, a higher nucleation rate leads to retardation of the grain growth and favours the fine grain structure (Conrad, 2000). It is noteworthy that only PT-HAZ is significant for the cases P1 and P2, whereas P3 and P4 exhibit both FT-HAZ and PT-HAZ. The high cooling rate accomplished by reduced heat input for the former cases is responsible for the insignificant FT-HAZ. Needle shape acicular α′-martensite is observed within the pre-matured β-grain boundary in FZ, as depicted in Fig. 5.27c. For low heat input of 12 J/mm (P1) and 19.65 J/mm (P2), life span of molten pool at elevated temperature decreases, which results in substantially higher cooling rate (i.e., 3120 K/s and 2973 K/s respectively) over solidification range of temperature. This helps in the formation of acicular α′ martensite and fine prior β-grain. Moreover, upon

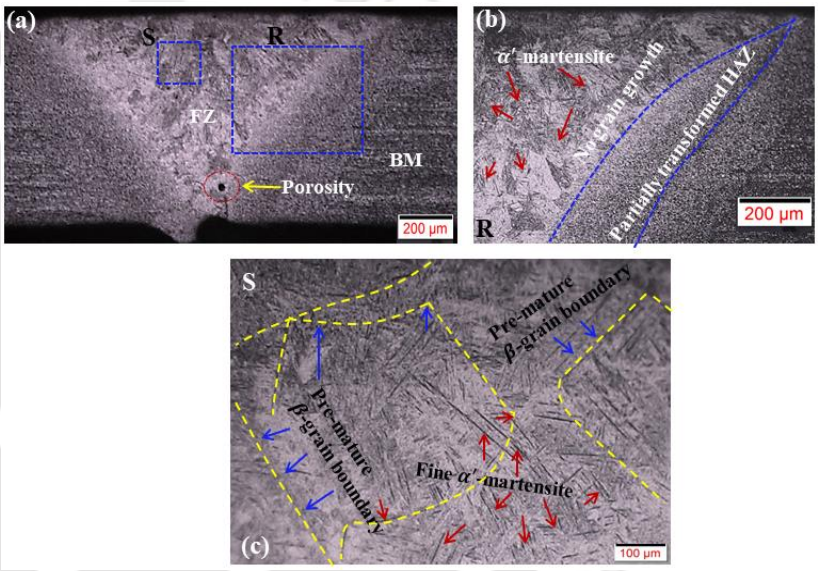

Fig. 5.27 Microstructure evolution at pulse mode (a) P1, (b) scanned area 'R' and (c) scanned area 'S'

increasing heat input up to 26.4 J mm (P3) and 35.75 J/mm (P4), the time spent at higher temperatures widens, which leads to a decrease in cooling rate and increasing growth rate. As a result, the morphology transforms from finer α′martensite to plate structured α′-martensite and promotes prior β-grain coarsening. Besides, porosity arises during the welding of Ti-alloy at the lowest heat input of 12 J/mm (P1). Fig. 5.27a indicates that the entrapment of some gases within the molten pool during solidification might be the consequence of porosity formation in this weldment. However, porosity is not observed in other weldments.

5.3.5 Thermal cycles and microstructural morphologies

In order to establish the relation between the thermal cycle and microstructure of α + β Ti-alloy, a schematic for possible microstructural evolutions is demonstrated in Fig. 5.28. Ti-alloy weldments gradually heated from point 'l' (~ 300 K) to the liquid phase. Upon cooling liquid begins to solidify as it crosses point "n," which lies on the solidus line. Within the range of solidus and β-transus temperature, β-grain nucleates. Subsequently, the coarsening of the β-grain occurs due to prolonged exposure of the weld region at this temperature range. Eventually, nucleation of α-lath starts at the β-grain boundary as the temperature reaches well below of β-transus value and continues to form up to martensitic start temperature (1053 K) i.e., at point "o". Cooling rate for weld metal C4 is estimated as 2180 K/s, which is far beyond the critical cooling rate but significantly lesser than pulse condition. Therefore, weld metal C4 exhibits a relatively higher amount of transformed α-phase rather than in P1. Finally, after the attainment of martensitic transformation temperature, i.e., lowers than point "p", hexagonal plate structured α′martensite nucleates and grows within the prior β-grain boundary. Heat input for continuous weld, i.e., C4, is sufficiently higher, which allows more growth of α′-martensite and transforms into blocky plate α′martensite, and coarsening of the prior β-grain boundary as well. SEM image of weld metal C4 illustrated in Fig 5.28c reveals similar microstructure and its morphology as predicted by schematic one. It can be deduced that the FZ exhibits mixed-mode transformation represented by $\alpha' + \alpha$ phases (Yang et al., 2019).

The correlation between temperature and microstructural evolution for specimen P1 is demonstrated in Fig. 5.28b. The pulse mode P1 achieves relatively high temperature than the

continuous one, and the nature of the thermal profile is significantly different as well. Point “s” signifies the maximum temperature where the material exists as a liquid phase. The sudden fall of the temperature indicates that the residence time of the weld pool at elevated temperatures is too short. Due to subsequent heating and cooling by pulse frequency, the stirring force comes into existence towards the molten pool and plays a crucial role in grain refinement. Because of the extremely high cooling rate (3120 K/s), the molten pool is solidified into smaller columnar β-grain below the solidus line and continues to form up to β-transus temperature. Point "t" lies in between of this stage. Grain growth is insignificant due to the very high cooling rate and exhibits a partially transformed fine β-grain boundary. The present case (P1) also exhibits mixed-mode transformation. Nevertheless, the transformed α-phase is sufficiently lower than the C4. Beyond martensitic start temperature, it evolves finer acicular α′-martensite along with very less transformed α-phase within the fine prior β-grain boundary. Rapid solidification inhibits the growth of α′-martensite lath and helps to transform into a fine needle shape acicular structure that is signified by the FESEM image in Fig. 5.28d. The average length and thickness of α′-martensite lath is found to be 11.5 μm and 415 nm for the sample fabricated at the lowest heat input (P1), whereas 20 μm and 320 nm for highest heat input (C4) as depicted by the scanned area C and D.

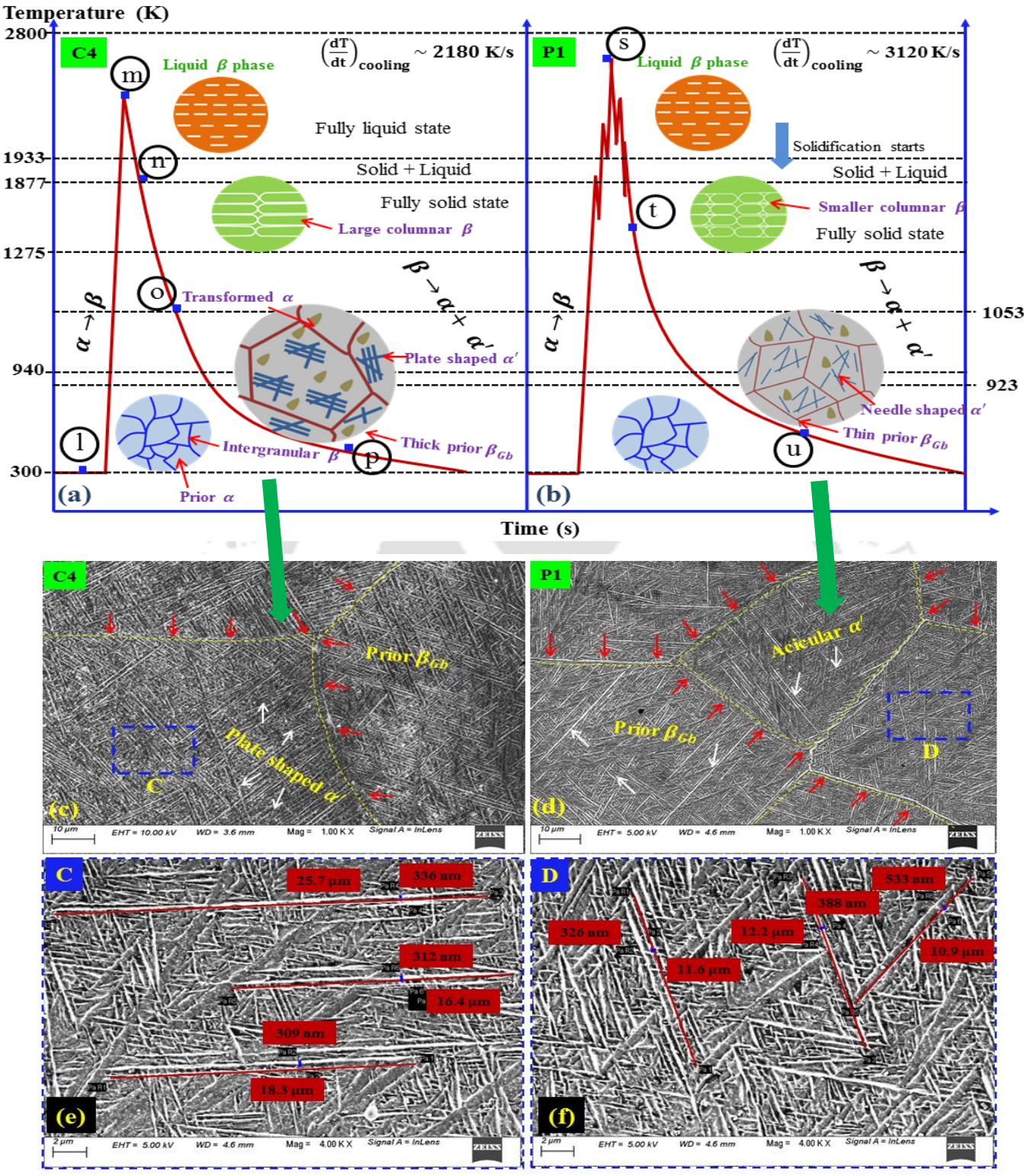

Fig. 5.28 Evolution of different phases with thermal cycles: (a)-(c) C4, (b)-(d) P1, measurement of α′-lath dimension of (e) scanned area 'C' and (f) scanned area 'D'

Fig. 5.29 describes the microstructural morphologies attributed to the weldments P4 and C1. The average length and thickness of α′-martensite lath for P4 is observed as 13 µm and 572 nm, respectively, whereas for C1, it is found to be 14 µm and 458 nm, respectively. It infers that upon increasing the heat input, the length of α-lath increases irrespective of pulse or continuous mode of welding. Besides, α′-lath thickness increases with heat input for pulse mode, where the reverse trend is observed for continuous mode.

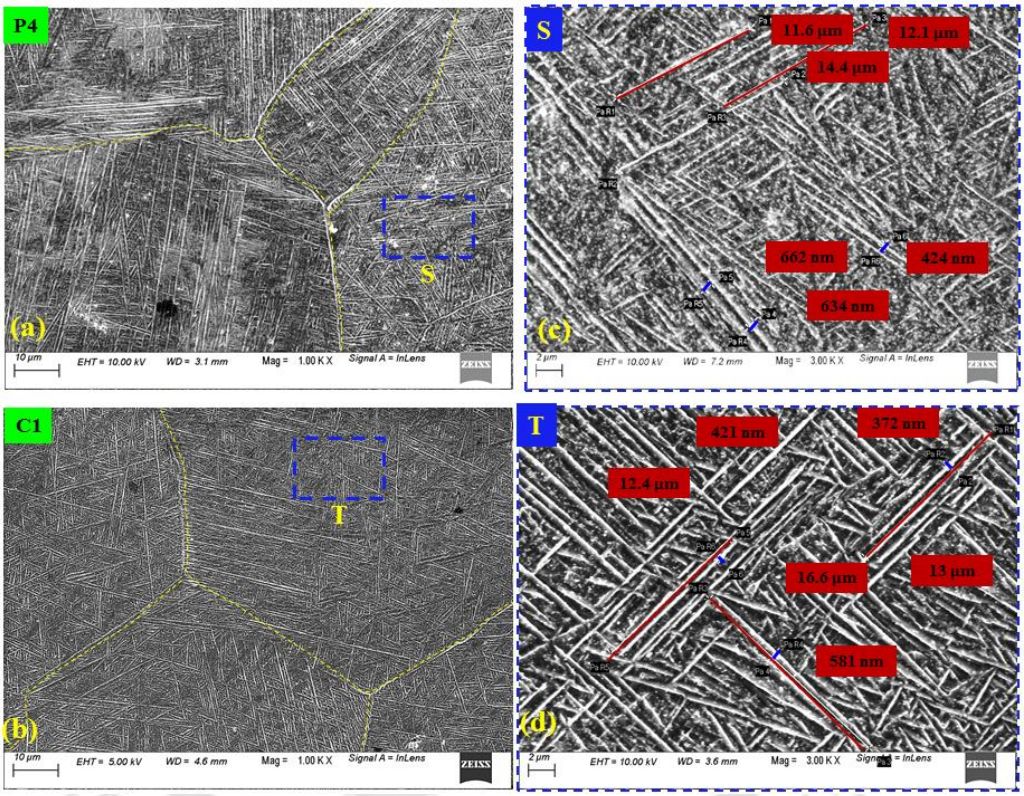

Fig. 5.29 Microstructural development for (a) P4 and (b) C1, measurement of α'-lath at the scanned area (c) 'S' and (d) 'T'

Fig. 5.30 illustrates the correlation between the time-temperature profile and evolved morphology in the HAZ for specimen C4. The heat input is too low to attain solidus temperature hence reaches up to ~ β-transus temperature in fully transformed HAZ represented by the point "x". Moreover, the attained temperature is higher than α-dissolution temperature (940 K) at FT-HAZ, thereby transformed into β-phase during the heating cycle. Chances of α-dissolution diminish gradually at farther away location from FT-HAZ → PT-HAZ. Very less amount of β-phase undergoes β → α′ transformation through the non-diffusional process during the cooling

stage, and the remaining phase exists as transformed β- and α-phase as signified by point "y". Besides, the temperature attained at PT-HAZ is well below of β-transus value thus possesses prior α+ β-phase, transformed β-phase as well as few α′-martensite in this region.

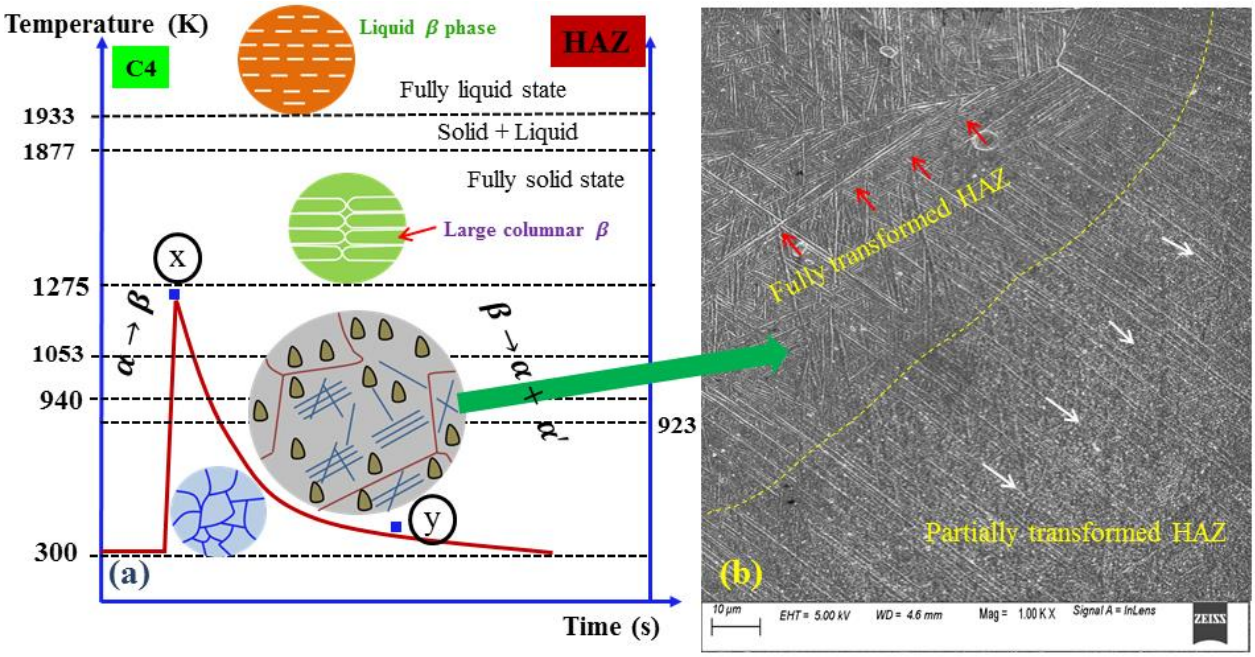

Fig. 5.30 (a) Thermal cycles, (b) microstructural evolution at HAZ

5.3.6 Evaluation of mechanical properties

The consistent variation in morphology of microstructure in a welded structure indicates that the mechanical properties are primarily controlled by variations in $\alpha + \beta$ fraction in the alloy. The ultimate tensile strength and elongation estimated for welded samples are presented in Table 5.3. Fig. 5.31a represents the engineering stress-strain diagram and fracture location of welded samples. It is observed that the sample P1 and P2 fractured at the base metal region, whereas other specimens (welded at more substantial heat input) manifested relatively wider FZ and HAZ, fractured at FZ only. The maximum tensile strength and resulting percentage elongation for P1 and P2 are marginally higher than the base material. This is attributed to the variation in morphology of α′-phase in an α/β alloy weld metal.

Pulse specimens P1 and P2 (low heat input) exhibits very fine acicular α′-martensite within the β matrix. Very fine acicular α′-martensite in α/β Ti-alloy is relatively much harder than that of retained β and transformed α-phase. Therefore, these precipitate (α′-martensite) scarcely deform and generate a large number of α/β interface that acts as resistance to dislocation movement (Qin et al., 2013). On the contrary, other specimens P4, C1, and C4 welded at a heat input of 35.75, 45, and 80 J/mm attributes relatively thicker α′-martensite within coarsened β-grain. Thicker lamellae α′-martensite are softer and fairly large to deform by slipping, and shearing mechanism, which in turn efficiently produces dislocation site and joints failure occur before its actual tensile strength (Qin et al., 2013). On the other hand, presence of impurities or contamination and lack of penetration triggers the mechanical performance of welded structure as well. Enrichment of contamination facilitates the formation of oxide or carbide-based brittle compounds during joining of Ti-alloy. In the present study, surface discoloration technique reveals that the welded sample fabricated through continuous mode of operation, exhibits higher level of contamination. In addition, some peaks corresponding to carbide formation i.e. TiC (Titanium carbide) is observed in XRD analysis as well. Furthermore, the mechanical properties for continuous mode weld are found to be much more inferior than pulse one. Besides, partial penetration is observed for the weld metal C1, P3 and P4 cause instantaneous failure before yield point. Therefore, it can be concluded that enrichment of contamination and lack of penetration depth might be the other possible reasons for the deterioration of engineering properties.

Fractography analysis shows that the fracture surface of P1 has composed of small and large dimples as well as breakage of the α-grain boundary, which is clearly visible in the investigated region as demonstrated in Fig. 5.31b, c, d. A large number of dimples are observed in the fracture surface of base metal, and samples P1 and P2 imply that prior to fracture, the welded joint is subjected to large deformation; hence fracture mode is confirmed as ductile mode (Gao et al., 2013). On the other hand, micropores of different sizes are observed in the fracture surface of weldment C1. The presence of micropores might be the center of localization of stress concentration, which promotes crack initiation and failure of the joint before actual strength value. Very less amount of elongation is noticed for continuous weld C1, C4 and pulse sample P4 caused by the fact that parallel thicker α′-lath growing with prior-β-grain boundary at relatively higher heat input due to which elongated dimples or tear ridges occurs on the fracture

surface (Lin et al., 2016). Hence it can be concluded that the morphology of α′-precipitate has a strong influence on the strength rather than its volume fraction.

Table 5.3 Mechanical properties of the tensile specimens

Specimens	UTS (MPa)	Elongation	Fracture location
Base metal	**1113**	15	BM
P1	**1138**	15.5	BM
P2	**1144**	15.8	BM
P3	218	0.8	FZ
P4	937	2.6	FZ
C1	264	0.8	FZ
C2	836	2.1	FZ
C3	723	2.0	FZ
C4	698	2.2	FZ

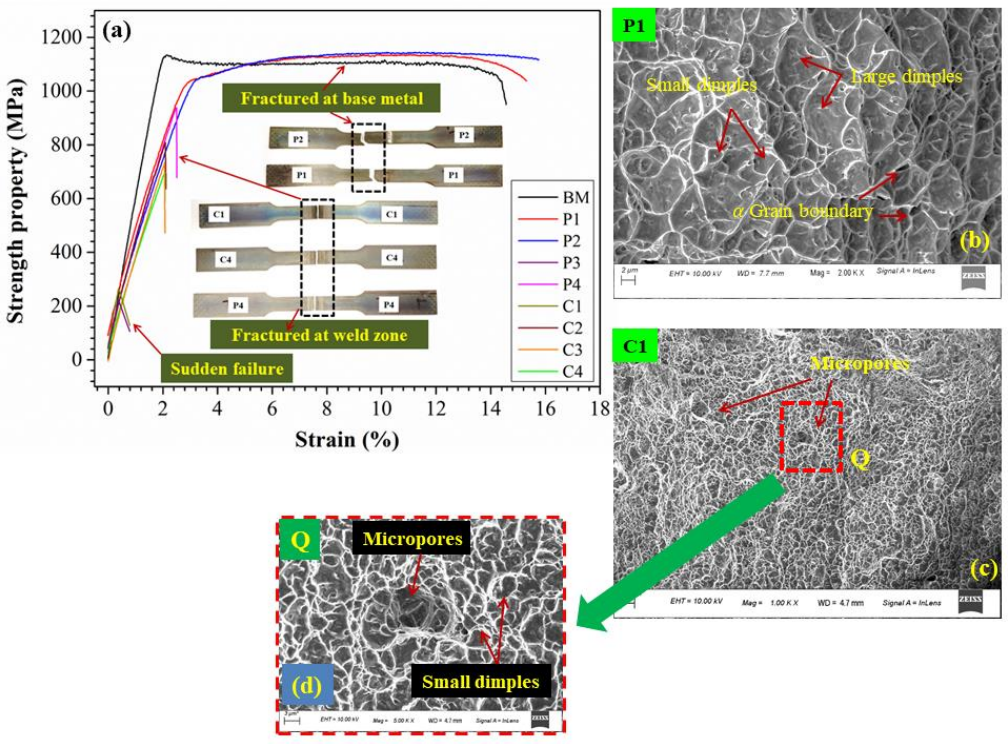

Fig. 5.31 (a) Stress-strain profile of tensile test; Fractured surface of the weld joint for (b) P1, (c) C1, and (d) magnified image of scanned area 'Q'

5.4 Role of diffusionless transformation on residual stress distribution

Residual stress is critical for the life assessment of weldments, which may rise close to the yield strength. The welding of Ti-alloy is a challenging task owing to inherent influence of phase transformation and resulting microstructure on residual stress generation (Dovzhenko et al., 2018). Any micro- or macro- mechanism that exhibits misfit between different parts, different phases and different zones within same structure results in the development of residual stresses (De and DebRoy, 2011; Dong, 2005). Type II is of significant interest in present study since it deals with strain induced due to phase change, inter- and intra-granular interaction, and microstructural morphologies. Generally, metal is subjected to thermal or thermo-mechanical loading to acquire favourable microstructure and associated mechanical properties, nevertheless fairly controlled residual stress must be accounted in order to ensure optimum performance (Rae, 2019). Hence, precise quantification of life-limiting residual stress is vital to find a way of mitigation that helps to improve the fatigue life of a welded structure. Volumetric dilation during thermal cycle give rise to transformation strain that alters the residual stress and, its consolidation is crucial to precisely predict the state and magnitude residual stress. Phase change is accompanied by transformation strain owing to variation in crystal structure (Withers and Bhadeshia, 2001). Volumetric expansion during martensitic transformation is beneficial in minimizing the effect of constrained thermal contraction during cooling stage, hence reduces residual stress (Dai et al., 2008). FE (finite element) based numerical tool renders flexibility to track the non-uniform thermal cycle, mechanical and phase transformation kinetics occurs simultaneously. Microstructural characteristics and morphological distribution by varying the dimension of α and β phases exceptionally correlated with cooling rate, induces microscopic strain at grain level (Azarniya et al., 2019; Xu et al., 2016). Solid-state diffusionless transformation is predominant, especially during rapid cooling assisted welding process. One of realistic approach is pulsation effect that permits the refinement of grain size and reduction of heat affected zone (HAZ) by controlling transformation kinetics and chemical segregation (Junaid et al., 2017; Mehdi et al., 2016). Current pulsation also affects the solidification behavior of the weld pool which diverse the temperature distribution within the weld pool (Grill, 1981). The tensile residual stress is reduced by using pulse laser energy and even it changes the nature

to compressive by increasing pulse frequency. However, little effort is put to investigate the effect of phase transformation kinetics on the estimation of residual stress and the influence of pulsation on martensitic transformation of Ti6Al4V weldment. Therefore, possible distinctive features of intermediate phenomena, i.e., metallurgical transformation and assisted morphological evolution, and its role on alteration in residual stress behavior under various mode of operation are accounted in the present study. With the aim of current objective, surface residual stress measurement is performed using non-destructive XRD technique. The process parameters are depicted in Table 3.9 of Chapter 3. The details of thermo-metallurgical-mechanical model are also illustrated in Section 4.6 of Chapter 4.

5.4.1 Temperature field and cooling rate

Dynamic temperature distribution and, high heating and cooling rate experienced by the substrate cause residual stress generation. In order to assess thermal behavior of welded specimens, bead geometry is analyzed in Fig. 5.32a, whereas evolved temperature and associated temperature gradient (dT/dt) are evaluated through thermal modeling, depicted in Fig. 7.1b. It confirms localized melting with Y-shaped bead profile for pulse mode (i.e., PW1, PW2) however; relatively wide fusion area is accomplished for continuous mode (i.e., CW2, CW3). Continuous weld samples possess both fully (FT) and partially (PT)-transformed heat affected zone (HAZ) owing to augmented heat input which allows grain to grow more whereas only PT-HAZ is perceived at pulse mode. The maximum temperature of 2366 K, 2460 K, and 2556 K is attained at heat input of 45 J/mm, 65 J/mm and 80 J/mm for weld metal CW1, CW2 and CW3 respectively. Aditionally, 2680 K, 2832 K and 3154 K is achieved at 12 J/mm, 20 J/mm and 35 J/mm for PW1, PW2 and PW3 respectively. Despite of being welded at low heat input (~12 J/mm, ~20 J/mm), Fig. 5.32b illustrates higher temperature for pulse welded samples by virtue of high peak power during pulse ON time. Estimated thermal gradient profile affirms rapid cooling in a range of 10^3 K/s for all weld metals, which is quite higher for diffusionless transformation. On the contrary, the time elapsed to achieve phase transformation from β- to α-phase is found to be 100 msec which confirms the average cooling rate lies in the range of $\sim 10^3$ K/s as well. Thus, in the present study maximum magnitude of temperature gradient (dT/dt) is introduced as cooling rate for pulse as well as continuous condition (Manikandan et al., 2014).

Nevertheless, continuous weld attained relatively lower cooling rate (CW1~2246 K/s, CW2~2207 K/s, CW3~2174 K/s) which may attribute diversification in microstructure owing to variation in distribution of α and β-phase. Fig. 5.32c represents temperature distribution during welding by considering pulsation effect. Maximum temperature of 3124 K is achieved at pulse on time while it reduced to 2176 K at pulse off time for weld metal PW3. Fig. 5.32d demonstrates satisfactory resemblance between experimental and numerical weld bead profile where most sensitive zone i.e., mushy zone (red) is separated by solidus and liquidus temperature.

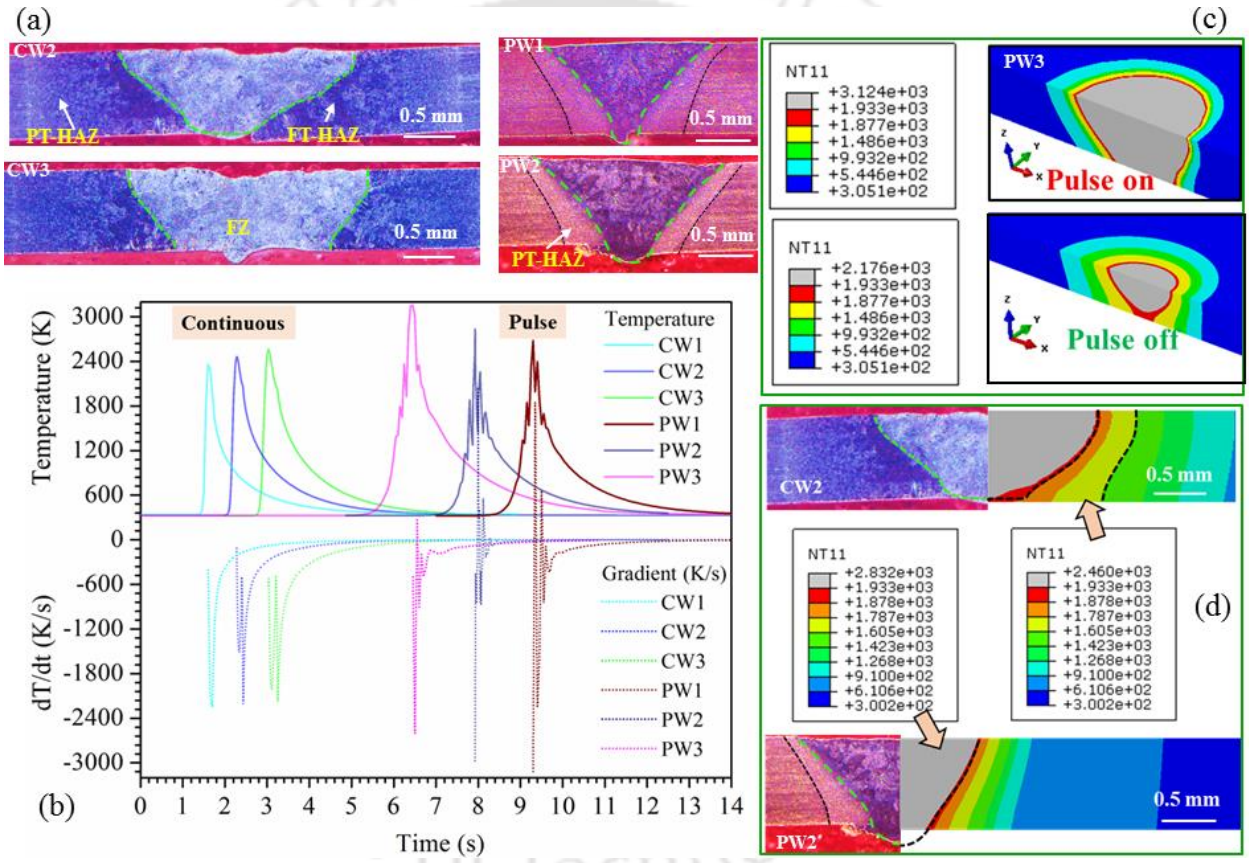

Fig. 5.32 Depiction of thermal behavior of welded samples (a) bead macrograph, (b) temperature profile and temperature gradient (K/s), (c) pulse ON-OFF and (d) comparison of weld geometry at pulsed and continuous condition

5.4.2 Peak-shifting and peak broadening

Fig. 5.33 exemplifies the characteristic behavior of diffraction pattern that exhibits peak-shifting and peak-broadening phenomena with reference to a base metal. Bragg's peak shifted insignificantly (~ 0.45°) for α/α′ in case of PW3 whereas notably shifted (~1.2°) for CW3 with respect to the base metal. Low cooling rate ~2174 K/s promotes heterogeneous thermal gradient which results in dramatic diversification in lattice parameter change during crystallographic transformation from bcc (β-phase) → hcp (α′-phase). These severe aberrations are also responsible for higher strain field generation at microscale which promoted much peak broadening in continuous mode of operation, i.e., for weld metal CW3. Low and localized heat input ~12 J/mm and, consequent higher cooling rate ~3120 K/s leads to relatively less microstrain generation for pulsed sample, i.e., PW3. Hence, comparatively lesser broadening is observed in Bragg's peak (2.2°). In particular, the peak of plane α (002)/α′ is broadened to (3.02°) for CW3 from 1.08° of base metal. On the contrary, intensity of plane $(10\bar{1}2)$, $(10\bar{1}1)$ and (002) corresponds to α/α′-phase dampens during transition of welding mode from continuous to pulse, which implies remarkable variation in texture as a result of transformed grain from elongated to equiaxed type. Besides, relatively intense diffraction peak corresponding

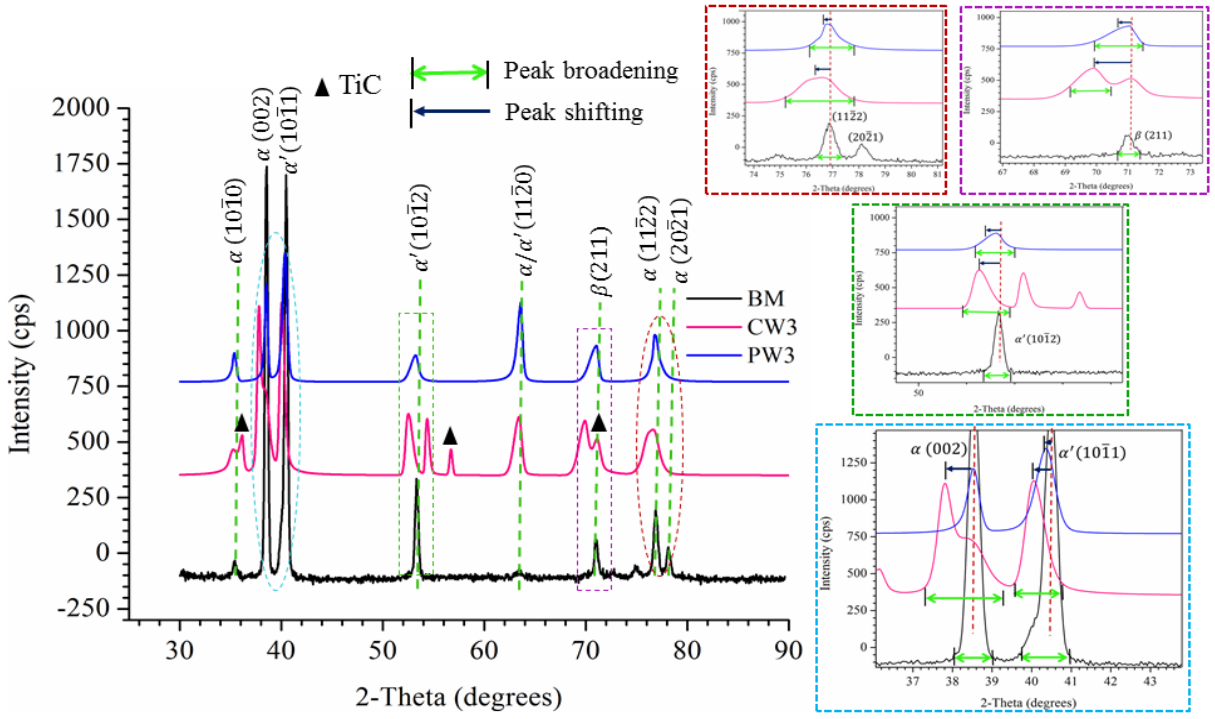

Fig. 5.33 Depiction of peak broadening and peak shifting during solid state phase

to β(211) for CW3 signifies enriched volume phase fraction of β phase. Presence of diffraction peaks associated with TiC (titanium carbide) indicates the inclusion of contamination especially for weldment CW3 since Ti-alloy is highly susceptible towards carbide formation at elevated heat input (Buffa et al., 2013).

5.4.3 Volumetric dilation in laser welding

α + β-phase alloy undergoes solid state phase transformation during heating and cooling stage of thermal cycle. Fig. 5.34 signifies the schematic representation of volumetric transformation and associated crystallographic change during SSPT. Initially metal temperature rises from ambient to α-dissolution or β-start temperature is illustrated by positive slope $\left(\frac{\Delta v}{\Delta T}\right)$ of the curve where metal is composed of HCP+BCC crystal structure. Further, as the metal reaches α-dissolution temperature (~ 940 K), volumetric contraction begins due to crystallographic transformation from HCP+BCC → BCC leads to diffusional transformation, represented by negative slope. In contrast, volumetric expansion takes place by virtue of crystallographic change into HCP structure results in diffusional α-phase transformation (CR <410 K/s) or diffusionless α′-martensitic transformation (CR ≥ 410 K/s) depending upon the path followed during cooling stage beyond β-transus temperature. The solid state phase transformation that occurs during cooling cycle is depicted by slope change from negative to positive.

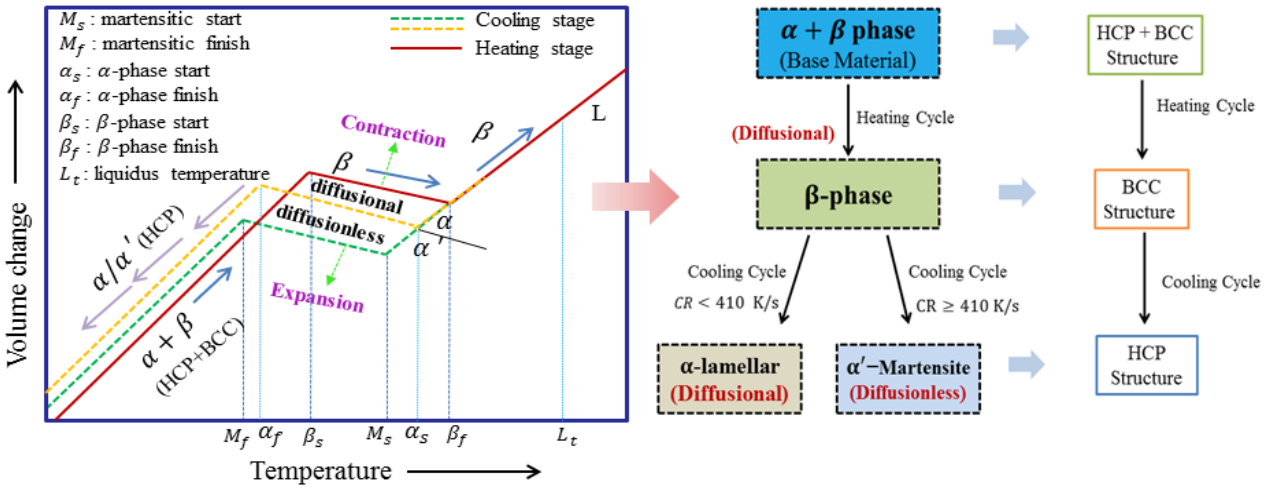

Fig. 5.34 Relation between volumetric dilation and crystallographic change during SSPT

Crystallographic transformation from HCP + BCC ($\alpha + \beta$ phase) $\rightarrow$ BCC (β phase) $\rightarrow$ HCP (α'/α phase) during thermal cycle exhibits volumetric dilation at FZ (fusion zone) and HAZ (heat affected zone), give rise to transformation strain. The transformation strain is deciding factor for the final interpretation of residual stress, i.e., whether it would be of tensile or compressive nature.

5.4.4 Phase fraction in SSPT

Fig. 5.35 depicts graphical representation of variation in phase fraction of different phasesα, β, α'-martensite corresponds to thermal cycle during full SSPT. Primarily, Ti6Al4V alloy consists of α-phase $\geq$90% and β-phase $\leq$10% which are identical to equilibrium phase fraction. However, it is assumed that weld metal contains fully α-phase fraction ($\theta_\alpha \sim 1$) at pre-weld condition during metallurgical modeling. Figure shows that as the temperature rises rapidly beyond α-dissolution to β-transus or β-finish temperature, β-phase fraction quickly ascends from 0 to 1, by the time being α-phase fraction decreases to zero. Further, as the temperature exceeds melting temperature, entire molten zone assumed to be exhibits β-phase ($\theta_\beta \sim 1$) in liquid state and maintains equilibrium volume fraction upto peak temperature viz. different under varied weld conditions CW2, CW3, PW1 and PW3 depicted in Fig. 5.35. Besides, as soon as molten metal begins to cool beneath β-transus temperature, different microstructure can be produced either diffusionally or non-diffusionally depending upon cooling rate attained. Nevertheless, it is observed that each weld metal either fabricated at pulse or continuous mode possesses sufficiently higher cooling rate than its critical value, hence follows non-diffusional mechanism of transformation. It is obvious from the figure that martensitic phase fraction increases when the weld metal acquires M_s and attains its highest magnitude at M_f, consequently β-phase fraction decreases upto minimum value. Welded joints attained martensitic phase fraction of 0.925, 0.92 and 0.90 for CW1, CW2 and CW3 respectively, while martensitic phase fraction of 0.96, 0.94 and 0.93 is achieved by weld metal PW1, PW2 and PW3 respectively. Relatively higher cooling rate accomplished at low heat input might be the possible reason for the enrichment of martensitic phase fraction. Since rapid cooling exhibits immediate crystallographic change without rearranging the atoms or short-range atomic rearrangement which accelerates shear-type

diffusionless transformation leads to martensite formation. It is to be noted that generated lattice strains almost fulfil the invariant plane strain condition due to which magnitude of lattice invariant shear is relatively small during martensitic transformation, which provides flexibility in the characterization of the substructure of martensite (Banerjee and Mukhopadhyay, 2010).

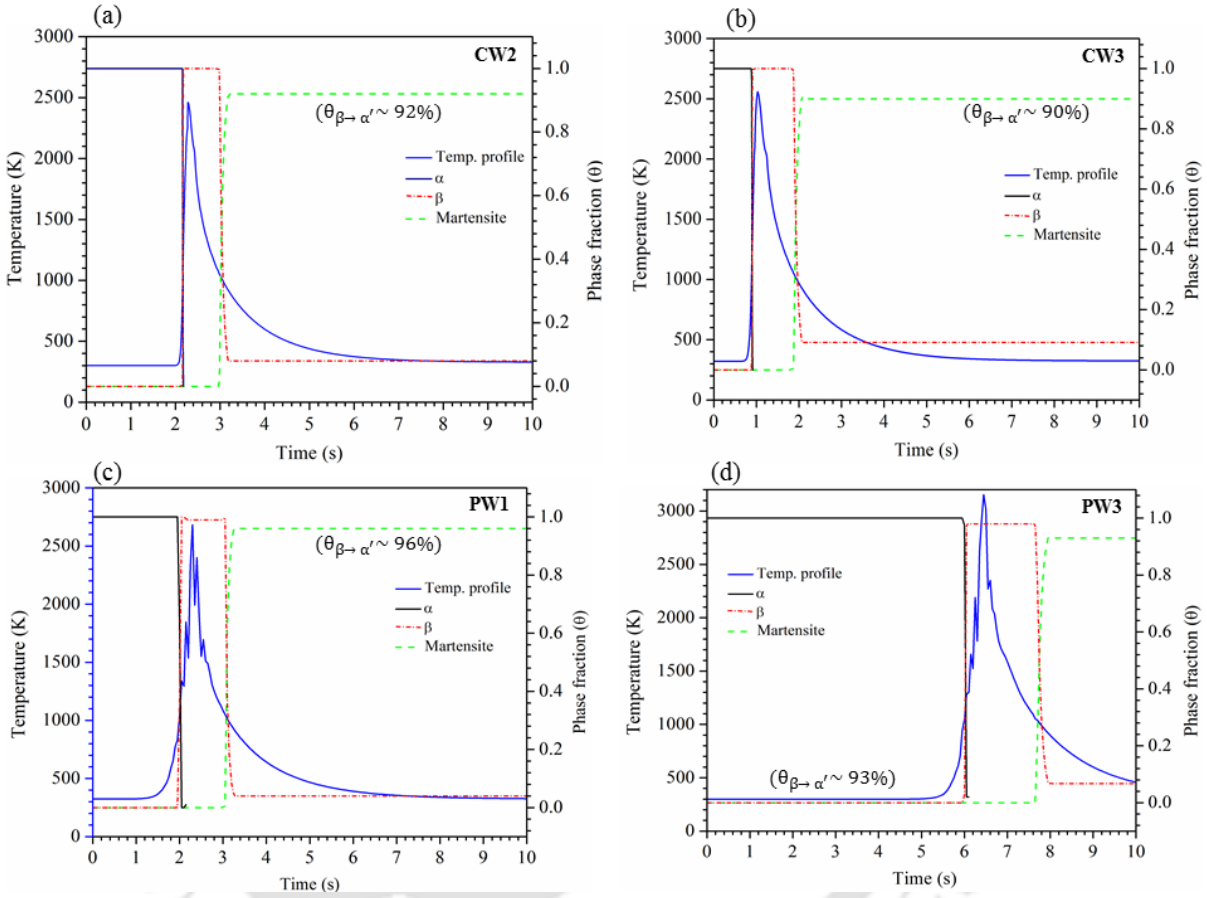

Fig. 5.35 Depiction of α, β, α′-martensite phase growth during weld thermal cycle: (a) CW2, (b) CW3, (c) PW1 and (d) PW3

Fig. 5.36 illustrates 2D & 3D contour based diffusional and non-diffusional phase distribution in solution domain during SSPT for weld metal PW3 and CW3. The output field, i.e., state dependent variable (SDV4) represents the growth of β phase fraction during heating stage in Fig. 5.36a, b while SDV6 manifests the progress of martensite phase fraction in Fig. 5.36c, d. Development of β phase fraction beyond β start temperature is captured at two different time scale: (i) intermediate stage (increment 205) and (ii) on the verge of completion (increment 293). It shows fully transformed β phase at FZ and HAZ where metal experienced β start and

finish temperature however, phase fraction declined towards thermally unaffected region. On the other hand, red band signifies highest martensitic phase fraction of 93% and 90%, attained during diffusionless transformation for sample PW3 and CW3 respectively in Fig. 5.36c, d. At a higher cooling rate, the prior β-phase transformed into α′-martensitic structure through a displacive mechanism (Azarniya et al., 2019). Therefore, the entire microstructure comprised of metastable HCP (hexagonal) α′-martensite (α = 0.293 nm, c = 0.467 nm) upon rapid cooling (> 410℃/s). Moreover, prominent mixed volume fraction of α′ + β is portrayed by other color components at far away location from fusion boundary. Owing to insufficient heat experienced at distant location, lower amount of metastable β-phase available to get transformed into α/ α′phase. This could be probable reason due to which α′-phase fraction decreases and subsequently β-phase fraction increases at further away location.

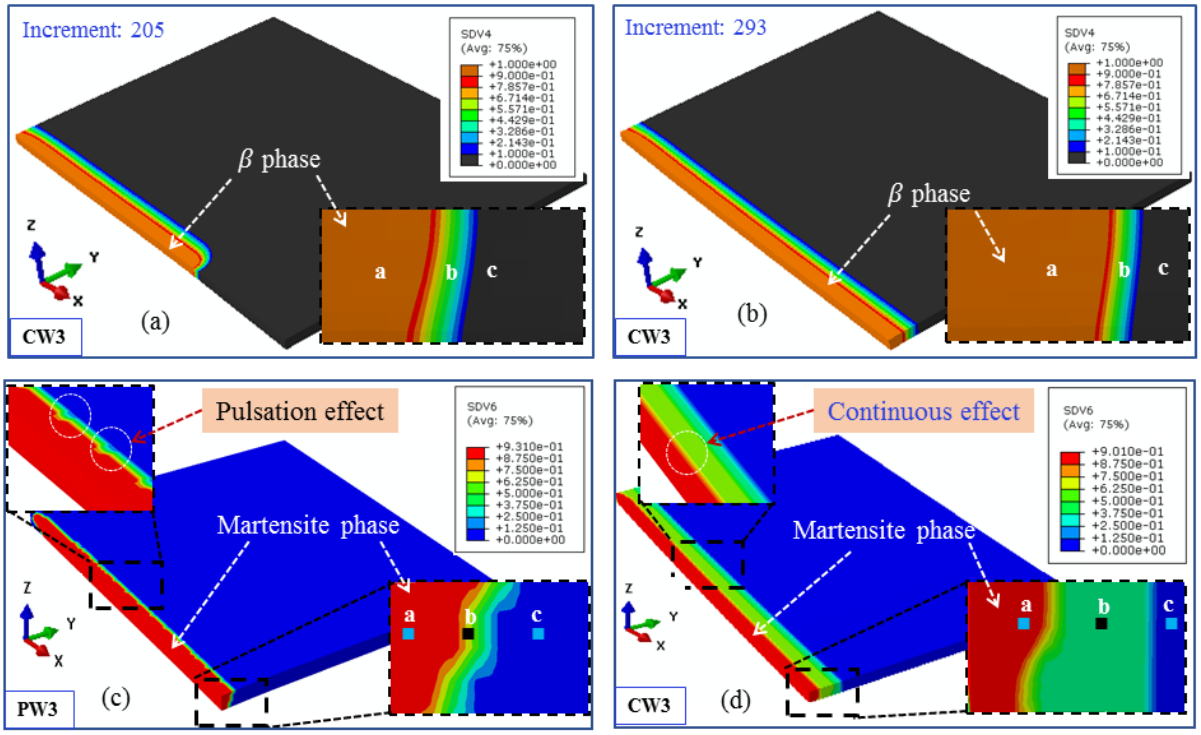

a: Fully transformed zone; b: Partially transformed zone; c: Untransformed zone

Fig. 5.36 Contour plot of phase change (a) α → β (intermediate stage) (b) α → β (verge of completion stage), martensitic transformation (c) PW3, (d) CW3

5.4.5 Effect of diffusionless transformation on residual stress

Nature and magnitude of residual stress depend upon the volumetric expansion accompanied by diffusionless transformation and thermal contraction of molten metal during cooling cycle. Fig. 5.37 describes uniaxial residual stress pattern assessed from the XRD and extracted from FE modeling by incorporating phase transformation kinetics for pulsed and continuous samples. Tensile residual stress of ~43±11 MPa, ~40±21 MPa and ~116±19 MPa is observed at weld central line while FE model predicted 39 MPa, 71 MPa and 118 MPa for the weld metal CW1, CW2 and CW3 respectively. On the contrary, shifting of weld mode from continuous → pulse fully transformed the state of stress from tensile to compressive. Compressive residual stress of ~158 MPa, ~127 MPa and ~145 MPa is anticipated by FE modeling for specimen PW1, PW2 and PW3 as shown in Fig. 5.37b. Diffusionless or martensitic transformation renders the surface under compression by virtue of the volumetric expansion accompanied by crystallographic change from BCC → HCP due to the formation of martensite. Therefore, enriched phase fraction of martensite from 90% → 92.5% reduces the overall tensile magnitude of residual stress from 118 MPa → 39 MPa by owning more volumetric expansion as perceived in case CW3 → CW1, not only this, even changes the nature of stress state from tensile (+ 43±11 MPa) → compressive (-158 MPa) for the case CW1 (45 J/mm) → PW1 (12 J/mm). On the other hand, distinguishable fluctuation in stress magnitude is obtained between experimental and numerical result, at a distance of 5 mm for continuous mode whereas at farther location for pulse mode, as a consequence of negligence of microstructural model and strain induced due to transformation plasticity (TRIP). Dramatic change in stress distribution pattern across the molten pool comes into existence due to non-uniform expansion as a result of local heating. Figure 5.37c, d shows two- and three-dimensional color contour of residual stress distribution pattern over the solution domain respectively. Grey color band characterizes maximum magnitude of tensile residual stress for weldment CW3 whereas most compressive stress state is reflected at FZ for case PW1 and labelled by blue band. It must be noted that tensile stress state at weld zone and its vicinity is counter balanced by compressive stress at farther away region. Therefore, it can be concluded that martensitic transformation contributes the diversification of residual strain

or stress distribution. Some of the authors made similar conclusion that phase transformation during heating stage is insignificant for the residual stress generation (Lee and Chang, 2011).

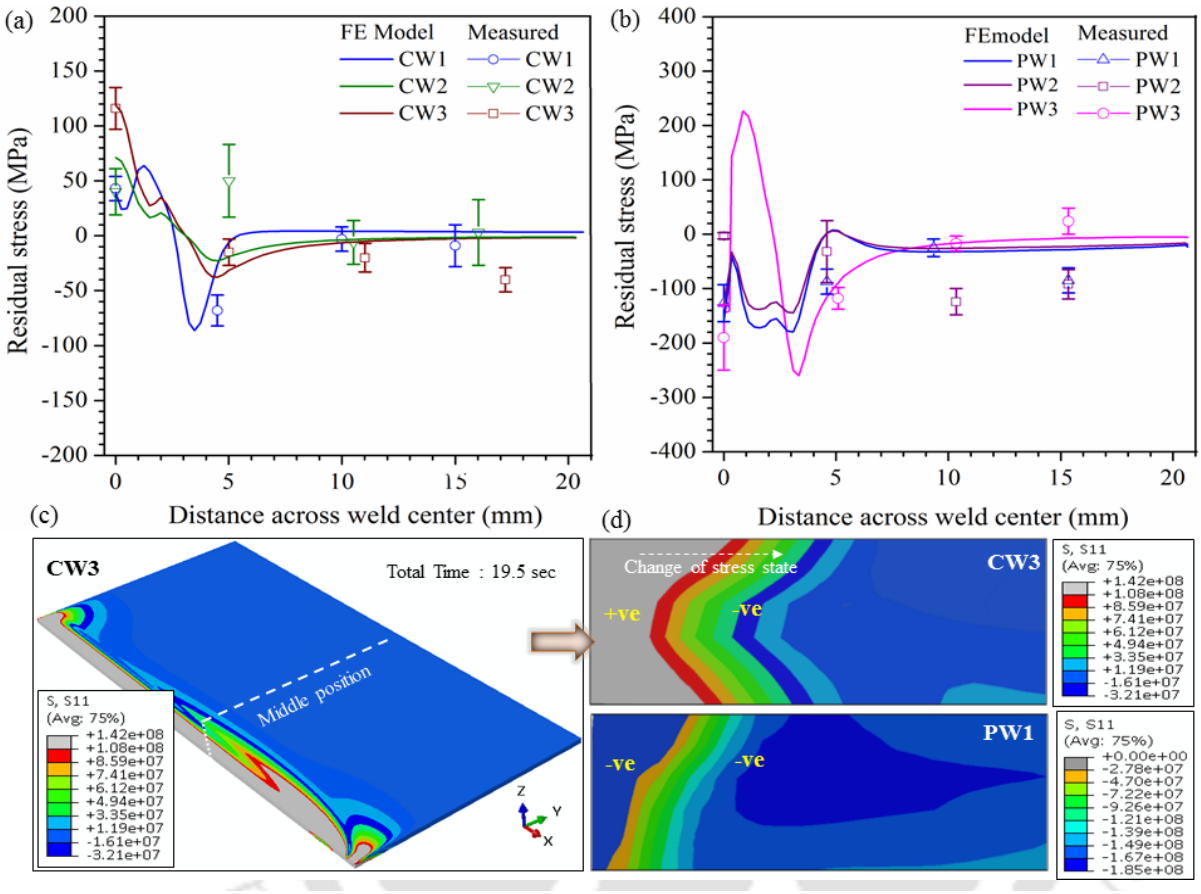

Fig. 5.37 Depiction of uniaxial surface residual stress distribution across the weld interface by considering SSPT: (a) continuous, (b) pulsed, color contour distribution of longitudinal residual stress: (c) volumetric domain, (d) cross-sectional domain

5.4.6 Interrelation between evolved microstructure and residual stress

Fig. 5.38 illustrates the microstructural development mechanism in FZ at different stages of thermal cycle. Microstructural evolution in FZ and HAZ is associated with variant selection mechanism, i.e., variation in orientation and distribution of α′/ α lath within prior β-grain as a result of inter- and intra-granular stress occurs during β → α′ transformation. Figure shows that Ti6Al4V alloy composed of equiaxed-α phase and intergranular-β phase within α/β matrix at room temperature. It attains fully β phase at temperature of 1273 K during thermal cycle as

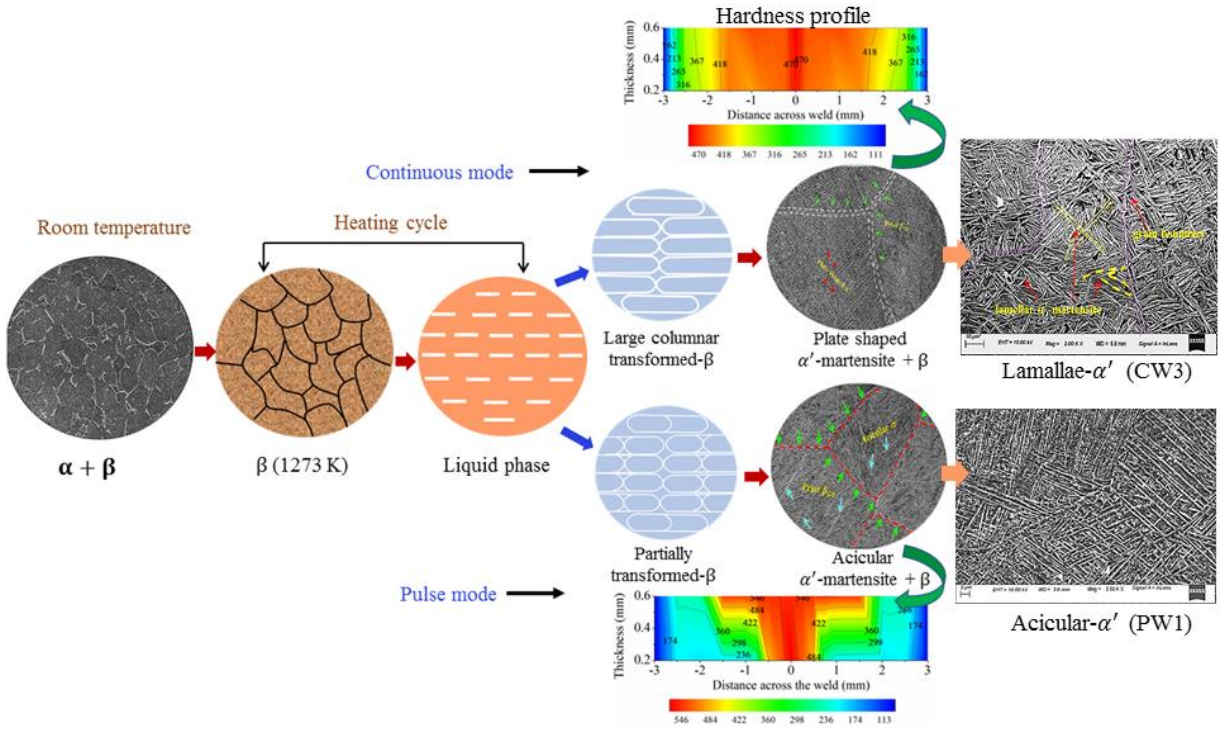

Fig. 5.38 Mechanism of microstructural evolution during continuous and pulse mode of welding

depicted in second stage. Eventually, liquid phase exists beyond liquidus temperature (1933 K). During cooling, solidification happens through epitaxial growth of prior-β grain at the interface of FZ and HAZ. Moreover, nucleation of α′-martensite occurs within prior-β grain boundary below β-finish temperature. Solidification of continuous weld metal that exhibit relatively low cooling rate allows coarsening of prior-β grain boundary and growth of α′-martensite into plate or lamellae structure within prior-β grain boundary, as revealed in final microstructure of sample CW3. Nevertheless, during pulsation, sharp decline of temperature renders short life span of weld pool at elevated temperature by virtue of which only fine or acicular α′-martensite within partially transformed prior-β grain boundary is indicated for weld metal PW1. Since, the stirring force emerges towards the molten pool due to successive heating and cooling by pulse frequency, plays a key role in grain refinement. Interestingly, it is already well explained that tensile residual stress increases with volume fraction of lamellar or coarse structured grain (Guo et al., 2003). This might be caused by deformation incompatibility around the lamellae interface or grain boundary, or due to higher localized stress field as a result of heterogeneous

microstructure. This is the fact that leads to higher residual stress generation for weld metal CW3 which possesses enriched phase fraction of prior-β phase and lamellae structured α′-martensite.

Reversible crystallographic change from HCP↔BCC accompanied with solid state phase transformation during thermal cycle is advantageous feature of Ti-alloy. Orientation and dimension of evolved morphology attributes significant impact on engineering properties and thermo-mechanical behavior of Ti-alloy weldments. As the weldment attains α-dissolution temperature at heating stage of thermal cycle, $\alpha + \beta \rightarrow \beta$ transformation occurs which leads to deviation in slope of $\Delta l/l_0$ and temperature as depicted by dotted green line in Fig. 5.39a. Furthermore, as the metal attains temperature beyond martensitic start (Ms), $\beta \rightarrow \alpha'$-martensitic transformation takes place at cooling stage, due to which again diversion in linear slope of $\Delta l/l_0$ and temperature is observed as depicted by brown dotted line. During current pulsation stirring drag force come into existence towards molten pool which plays a role in grain refinement and directional solidification. Cyclic variation of pulse frequency attributes rapid cooling rate in pulsed wave condition or low heat input condition favours very fine α′-martensite formation due to unavailability of sufficient time for grain growth where directional solidification allow α′-lath to grow in lateral direction. Hence, fine α′lath is obtained for P (pulse)-wave as revealed in Fig. 5.39b whereas relatively coarse α′lath is formed in continuous weld indicated in Fig. 5.39c.

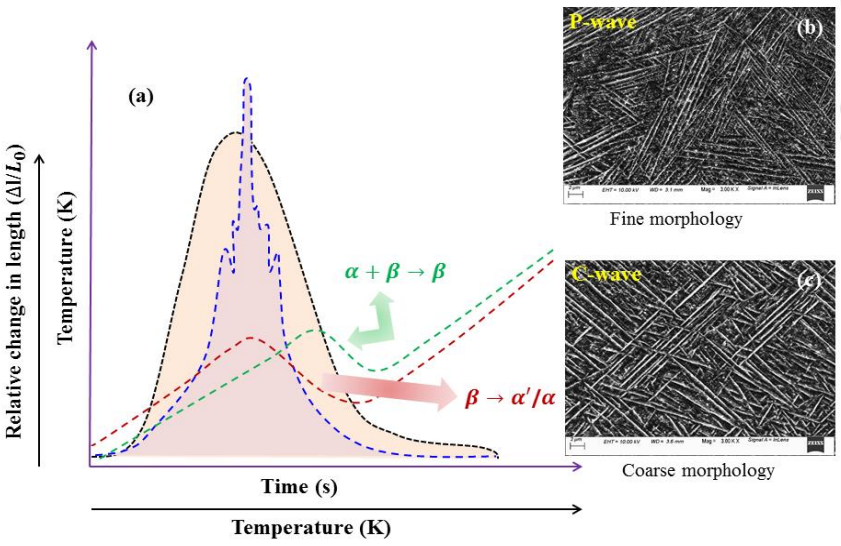

Fig. 5.39 Interplay of solid state phase transformation and associated morphology for Ti-alloy weldments

5.4.7 Hardness distribution and microstructural morphology

Hardness distribution over the Ti6Al4V alloy welded joints greatly influenced by the martensitic transformation at FZ and nearby region. Since, laser welding process is rapid cooling assisted process exhibits sufficiently high cooling rate than that of critical cooling rate (410 K/s) beyond which martensitic transformation is predominant. The entire set of specimens fabricated at pulsed and continuous mode in the present study possessed martensitic transformation as revealed in microstructural analysis in previous section. Moreover, in accordance with varied heat input, alteration in microstructural morphologies distribution comes into existence. 3D contour plot of hardness distribution is presented for weld metal CW3 and PW1 in Fig. 5.40, the hardness value (HV) is found to be 546 and 470 for PW1 and CW3 respectively. Additionally, Fig. 5.40 signifies the 2D contour-based hardness distribution across the weld interface for sample CW1, CW2, PW2 and PW3. It shows that as the heat input increases for both the mode, bead width widened due to increasing volume of molten metal. On the contrary, highly localized hardness distribution is observed for pulsed sample, i.e., PW1 and PW2. Maximum hardness of 487 Hv is observed for case CW1 whereas it is 479 for CW2. In contrast, remarkably enhanced magnitude of hardness, i.e., 532 Hv for PW2 and 507 Hv for PW3 is perceived for pulsed specimen. Maximum magnitude of hardness is obtained at fusion line for each specimen. This is based on the fact that increasing heat input favours low cooling rate that renders diffusional growth of α-phase due to which shifting of diffusionless, i.e., martensitic transformation towards diffusional transformation might be possible. Hence, coarse martensite forms at weld and nearby zone, which is relatively softer in nature as compared with low heat input, assisted specimen. It indicates that lamellae structured α′-martensite accomplished at cooling rate 2174 K/s is relatively softer than acicular structured α′-martensite. This could be another factor due to which lamellae structured martensitic transformation puts the weld surface under less compression stress state comparative to acicular structured martensite. Thus, residual stress is found to be higher for weld metal CW3 rather than PW1, despite of being transformed into martensite for both the cases.

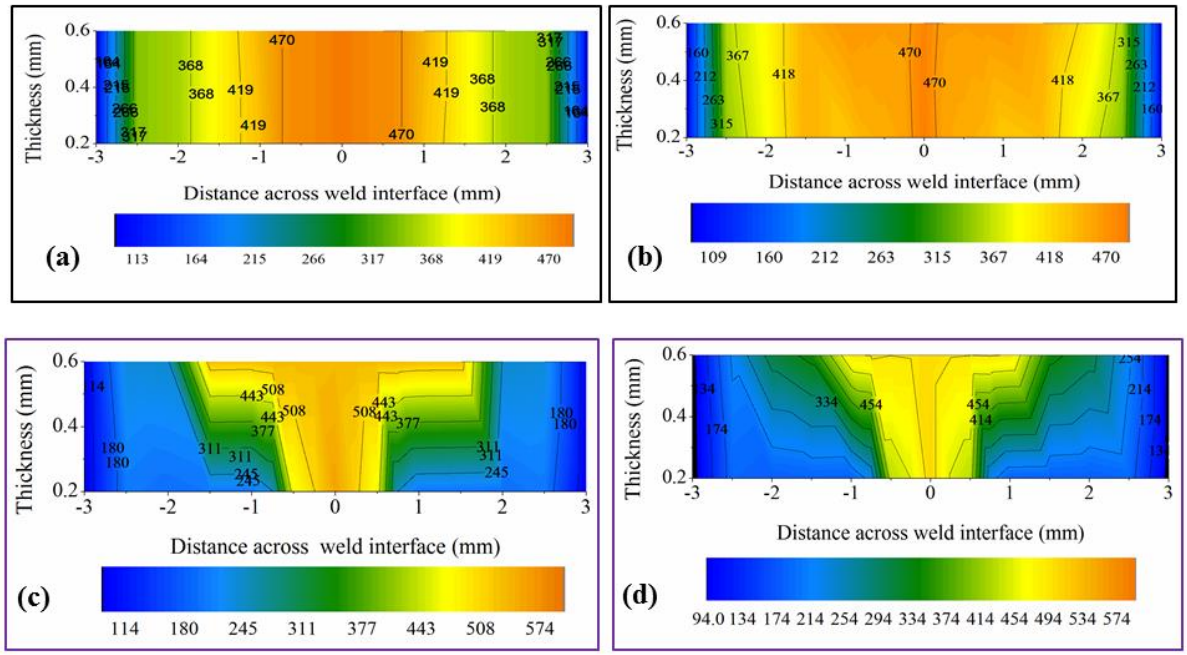

Fig. 5.40 2D contour based hardness distribution across the weld interface at (a-b) continuous mode, (c-d) pulse mode

5.5 Interaction of microstructure with residual stress in Laser welded SS304 Steel

Austenitic stainless steel (SS304) is mainly known for its strength at elevated temperature, fracture toughness at low temperature, and corrosion-resistant properties. However, relatively high thermal expansion coefficient, low specific heat capacity, and low thermal conductivity facilitate higher distortion, shrinkage, and residual stress generation in a welded structure (Lin and Chou, 1995). The fusion welding of SS304 is a typical process in the fabrication of bellow and other applications. Nevertheless, the mechanical performance of a welded joint is often inferior to the parent material due to the lack of knowledge about the metallurgical changes. The attributes such as (a) primary mode of solidification, (b) cooling rate and corresponding solute distribution, (c) nucleation mechanism, and growth performance of $\delta \rightarrow \gamma$ transformation during solidification, decides the microstructural morphologies (Hsieh et al., 2014). It is opined that the distribution and amount of δ-ferrite in stainless steel weldment are of utmost importance since they control the properties and on-site behavior of weld joint in terms

of thermal stability, mechanical performance, and residual stress generation (Unnikrishnan et al., 2014). The growth of δ-ferrite which is a function of chromium [$Cr_{eq.}$] and nickel equivalent [$Ni_{eq.}$], primarily depends on the chemical composition, cooling rate, and primary mode of solidification manifested during welding (Padilha and Rios, 2002). Hence, it is tried to explore these aspects in present study. Apart, the progress of residual stress during welding is associated with the metallurgical changes and assisted microstructural morphology. Tensile residual stress adversely affects the structural integrity. However, its compressive nature usually produces a beneficial effect on fatigue strength (Khurshid et al., 2017). The evaluation of residual stress in austenitic steel is relatively complex, where solidified morphology may play an important role. The lattice parameter, which is the function of interstitial atom content, is crucial for the interpretation of desired residual stress in expanded austenite (Hummelshøj et al., 2010). In ferrite-austenite Fe-Cr-Ni alloy, the compressive elastic strain is generated in the ferrite phase. In contrast, tensile elastic strain emerges within the γ-austenite matrix due to variation in the thermal expansion coefficient of alloying elements (Harjo et al., 1998). The finite element (FE) based numerical model is one of the justifiable approaches to simulate the thermal behavior and associated mechanical response. To enhance the robustness of the thermo-mechanical model, it is essential to incorporate metallurgical behavior for the prediction of residual stress distribution. The residual stress generation and mechanical properties are predominantly associated with phase transformation and evolved microstructure for austenitic stainless steel. Therefore, the interrelation between metallurgical changes and residual stress generation is critically assessed, which can find a way to promote compressive residual stress in a welded structure in current study. A detailed description related to experimental and numerical tool that have been used for the fulfillment of present objective is presented in Section 3.2 & 3.4, and Table 3.4 & 3.9, of Chapter 3, and Section 4.4-4.6, and Table 4.2 of Chapter 4, respectively. Furthermore, the FE-based, sequentially coupled thermo-metallurgical-mechanical models are developed to predict the instantaneous phase fractions of constituent phases, i.e., δ-ferrite, γ-austenite, and corresponding residual stress distributions are validated with the experimental measurement. The crucial outcomes extracted from the current investigation are presented herewith.

5.5.1 Temperature distribution and phase constituents

Fig. 5.41 demonstrates the weld bead geometry produced at different welding conditions. Full-depth penetration is observed for all the cases at an optimized laser power of 750 W. However, the shape and size of the fusion zone (FZ) vary with laser scanning speed. The macrograph of FZ changes from wineglass at the highest scanning speed to an hourglass type and finally reaches bowl shape with a decreased scanning speed. The half-width (top) of FZ increases from 0.38 to 0.78 mm, corresponding to the reduction of speed from 1000 to 600 mm/min. Similar behavior is observed when the defocus distance is changed to 1 mm. Fig. 5.42a shows the time-temperature distribution of the weld zone as a function of scanning speed and defocus distances at a laser power of 750 W. The maximum temperature achieved at the top surface is ~ 2949 K, ~ 2862 K, and ~ 2709 K, corresponding to the scanning speed of 600, 800, and 1000 mm/min, respectively. The temperature rise in the weld pool is a function of interaction time (t_i) with the laser, which is better represented by the ratio of laser spot diameter and scanning speed (Assuncao et al., 2012). As scanning speed increases from 600 to 1000 mm/min, interaction time decreases for constant laser spot diameter, and hence the attained temperature gradually decreases. Since the minimum spot diameter is possible at the focal plane, positive or negative defocus enlarges the laser spot due to convergence or divergence of the beam. The same amount of heat energy is distributed over the large volume of a substrate through a negative defocus of 0.5 and 1 mm, which attributes less solidification time for defocused beam (lesser for - 0.5 mm; least for -1 mm). The local cooling rate is the highest for defocus of -1 mm and relatively lowers for - 0.5 mm defocus distance. Hence, the temperature decreases as negative defocus increases from $D_1 \rightarrow D_2 \rightarrow D_3$, respectively, at the same scanning speed. At scanning speed 1000 mm/min, the lowering of temperature is found to be 20 K from $S_{45}D_1 \rightarrow S_{45}D_2$ while 14 K from $S_{45}D_2 \rightarrow S_{45}D_3$, whereas 38 K from $S_{56}D_1 \rightarrow S_{56}D_2$ for 800 mm/min. The temperature difference is observed as $10 - 12$ K for the least speed. Under less speed and minimum thickness of weldments (1 mm), heat diffusion is high through the thickness direction. Therefore, the influence of weld speed is more predominant than defocus distances in the present analysis. Fig. 5.42b represents the temperature distribution for the welding condition of $S_{56}D_1$. Here, the FZ is defined by liquidus temperature (~ 1723 K), and the heat-affected zone (HAZ) is predicted by isotherm contour between 1673 K and 1041 K. The Grey color band signifies the

molten zone, which is bounded by a thin red band, referred to as the mushy zone (between solidus and liquidus temperature range). The region far away from the aqua color band depicts HAZ, followed by the base material.

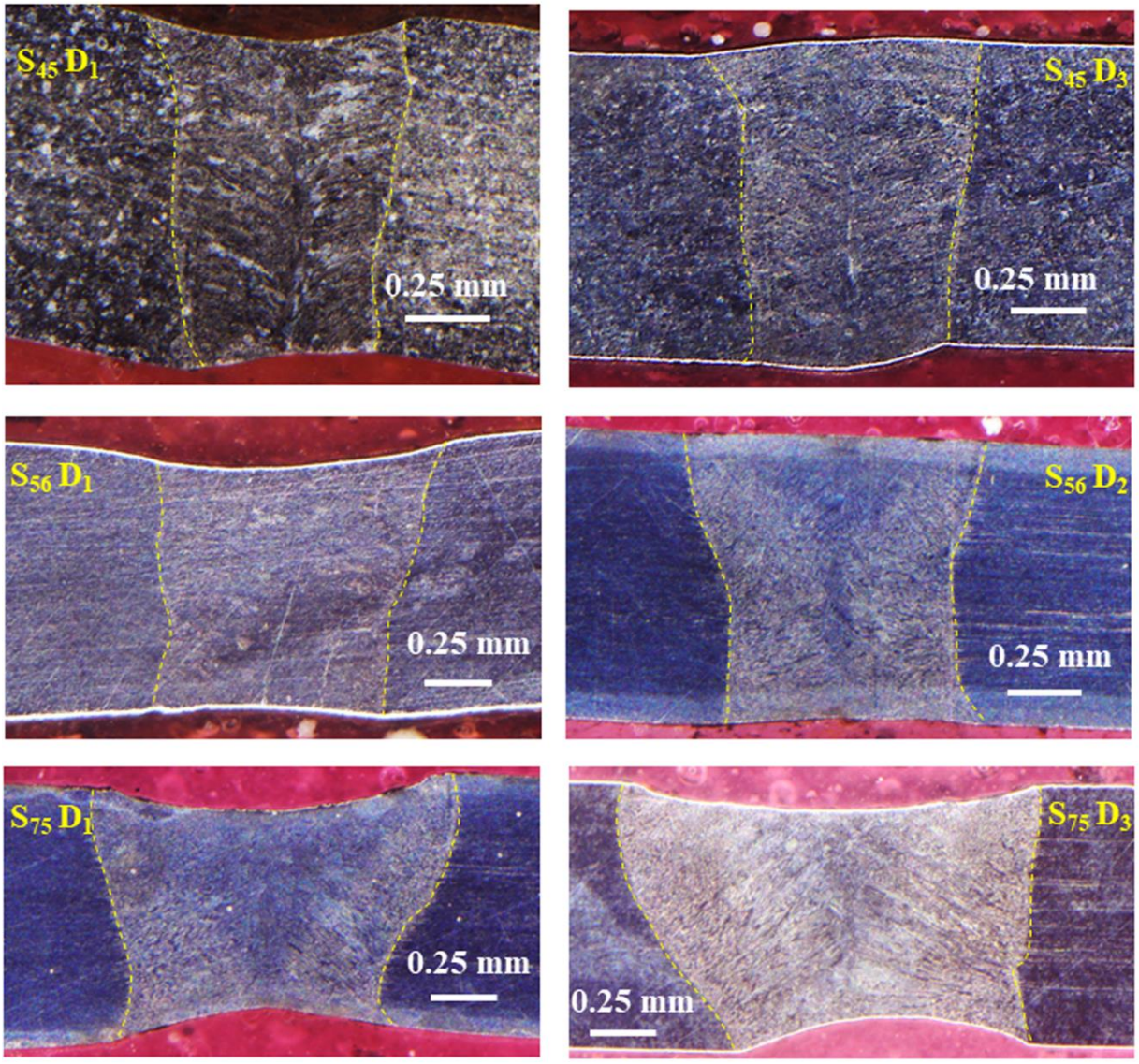

Fig. 5.41 Macrographs of fiber laser welded samples at a different heat input of 45 J/mm ($S_{45}D_1$, $S_{45}D_3$), and 56 J/mm ($S_{56}D_1$, $S_{56}D_2$)

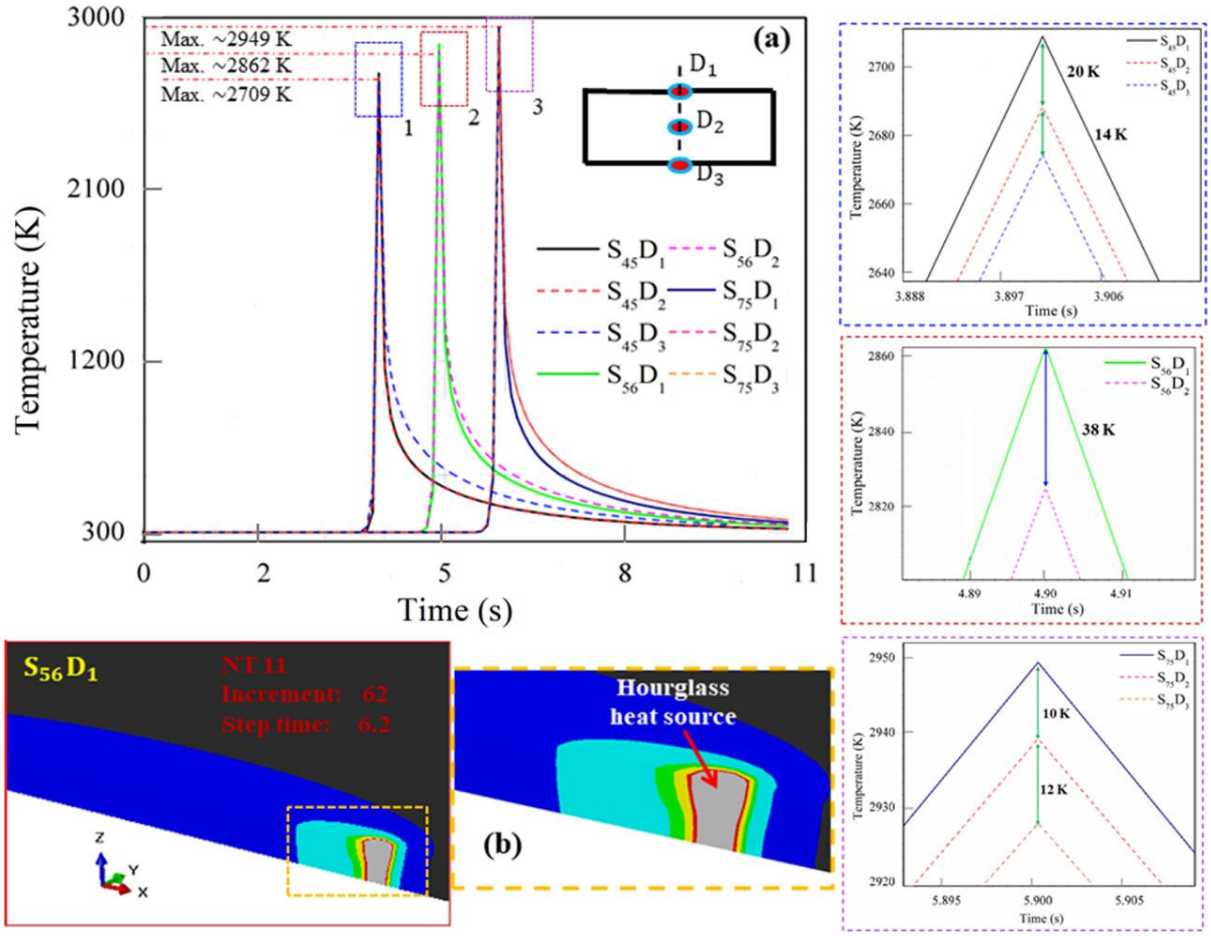

Fig. 5.42 (a) Temperature profile at different heat inputs and defocus distances, (b) 3D weld profile using hourglass heat source model

Fig. 5.43 illustrates the comparison between simulated (left) and experimentally (right) measured macrograph at different process parameters. The depth of penetration and fusion boundary well agrees with simulated results. At low speed, high heat input per unit length enhances the enlargement of melting volume. With a change in defocus distance, there is considerable variation in weld width. The width (top) of FZ increases from 0.77 to 0.96 for $S_{45}D_1 \rightarrow S_{45}D_3$ and 1.36 to 1.56 for $S_{75}D_1 \rightarrow S_{75}D_3$. The increase in defocuses gradually enhances the effective laser spot diameter, which resembles more spread out of energy distribution over the workpiece surface. Besides, the concave crater is observed at the top surface of the weld bead ($S_{45}D_1$, $S_{56}D_1$, $S_{75}D_1$, and $S_{75}D_2$) due to the vaporization of materials. However, the weldments $S_{45}D_3$ and $S_{56}D_2$ are found to be crater-free. Crater formation weakens the weld joint but may not influence the residual stress alteration. It is obvious that the relatively

good quality of the weld is obtained at a defocus distance of -1 mm with the highest welding speed (1000 mm/min). The maximum and mean error in the prediction of weld width is 14-16% and 10.6%, respectively as shown in Table 5.4. It is within the acceptable range and shows the robustness of the numerical model employed for the present study.

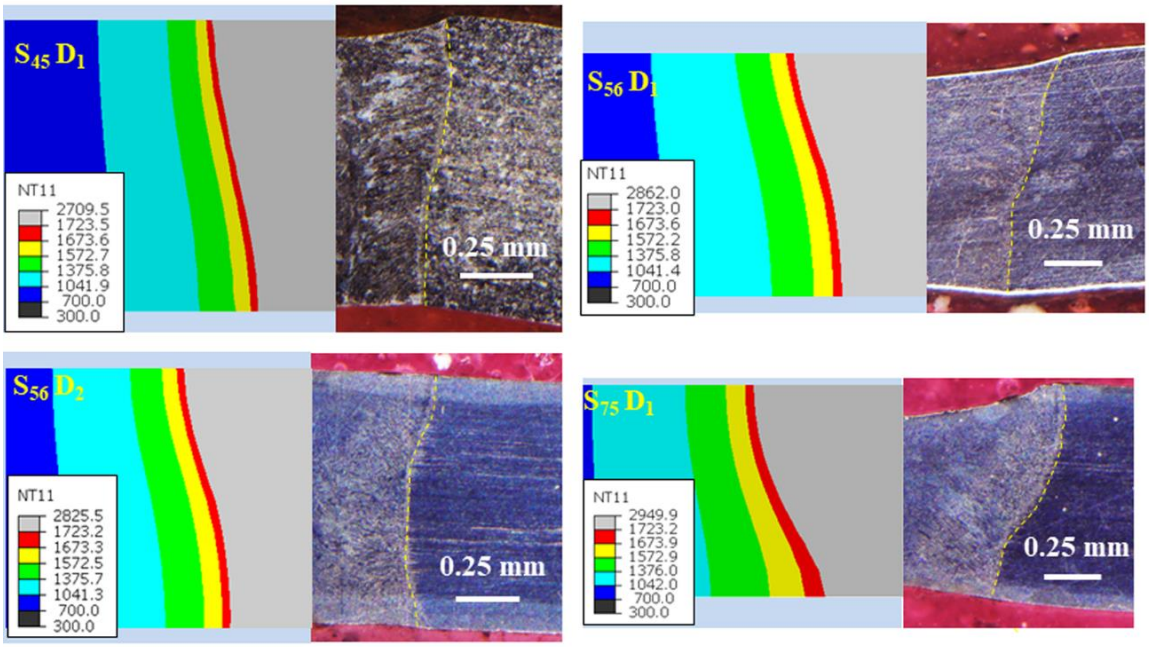

Fig. 5.43 Comparison between numerical (left) and experimental (right) weld bead geometry at different welding conditions ($S_{45}D_1$, $S_{56}D_1$, $S_{56}D_2$, and $S_{75}D_1$)

Table 5.4 Error in the estimation of weld bead profiles by numerical model.

Specimens	Fusion Zone (Error %)			Mean Error %
	Top	Mid	Root	
$S_{45}D_1$	8	6	2.5	5.5
$S_{45}D_2$	8	7	1	5.3
$S_{45}D_3$	3	2	2	2.3
$S_{56}D_1$	9	16	14	13
$S_{56}D_2$	1	3	11	5
$S_{75}D_1$	9	7	6	7
$S_{75}D_2$	14	11	7	10.6
$S_{75}D_3$	9	12	9.5	10.2

Fig. 5.44 depicts the diffraction pattern of the welds $S_{45}D_1$, $S_{56}D_1$, and $S_{75}D_1$, along with base metal (BM). The spectrum depicts the austenite (γ) peaks corresponding to (111), (200), (220), (311), and (222) planes in all the samples. However, a very weak (100) peak of the ferrite (δ) phase is also observed whose intensity changes. The amount of phase present (counts) in the investigated area is a peak intensity function (Bansal et al., 2016). The intensity counts of δ{110}, γ{111}, and γ{200} are shown in Fig. 5.44. It is obvious that the intensity of the γ phase decreases with an increase in heat input. This observation is attributed to the incomplete δ → γ transformation during solidification. Moreover, the intensity of peak related to δ-phase gradually increases. A more intense δ{110} peak is observed for weld metal $S_{45}D_1$, fabricated at low heat input viz. high cooling rate, whereas a weak peak is found for $S_{75}D_1$, fabricated at high heat input. It signifies that δ-ferrite content is more at a high cooling rate (Capello et al., 2003).

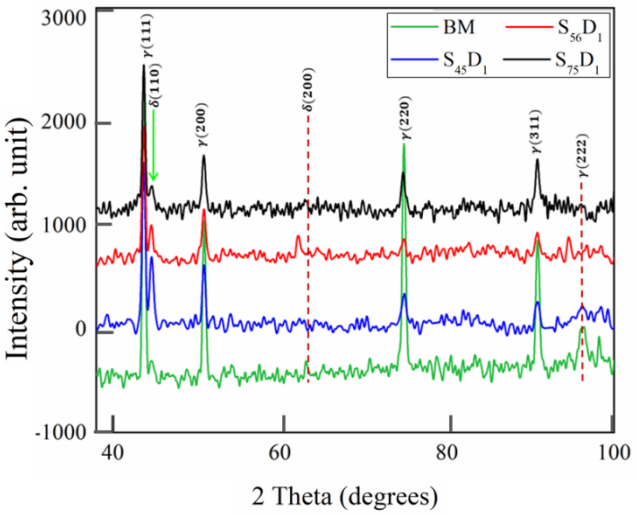

Sample	δ − ferrite (110) (Counts)	δ − ferrite (200) (Counts)	γ − phase (111) (Counts)	γ − phase (200) (Counts)
BM	200*	147*	2200	1500
$S_{45}D_1$	700	40	1600	600
$S_{56}D_1$	400	40	1400	500
$S_{75}D_1$	300	50	1300	400

decrease (δ − ferrite (110) (Counts))

decrease (γ − phase (111) (Counts))

* Residual ferrite content in as received-base metal

Fig. 5.44 The XRD peaks at different heat inputs of 45, 56, and 75 J/mm for zero defocus distance. The table presents intensity counts for δ-ferrite and γ-austenite

The diffraction peaks exhibited by weldments $S_{45}D_3$, $S_{56}D_2$, and $S_{75}D_3$ are demonstrated by Fig. 5.45. The trend of each diffraction peak corresponds to δ-ferrite, and γ-austenite is similar, while the magnitude of the count is different at different defocus distances. A very weak peak of ferrite (δ{200}) is observed for $S_{45}D_3$and $S_{75}D_3$. It confirms that ferrite content is slightly higher for the defocused specimens. The local cooling rate is comparatively higher for

the specimens having defocused distance ($S_{45}D_3$, $S_{56}D_2$, and $S_{75}D_3$), which resembles enhanced δ-ferrite content relative to specimens of zero defocus distance.

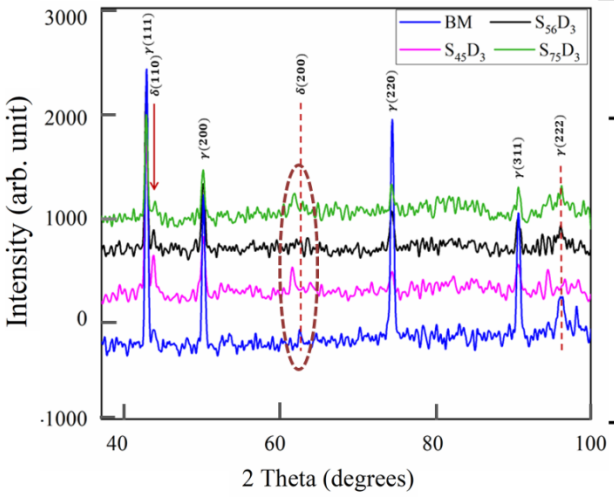

Sample	δ – ferrite (110) (Counts)	δ – ferrite (200) (Counts)	γ – phase (111) (Counts)	γ – phase (200) (Counts)
BM	200	**147**	2200	1500
$S_{45}D_3$	400	**332**	1500	500
$S_{56}D_3$	200	**100**	1200	500
$S_{75}D_3$	100	**271**	1000	500

decrease

decrease

Fig. 5.45 The XRD pattern at different heat inputs of 45, 56, and 75 J/mm for defocus distance of – 1 mm

5.5.2 Solidification morphology and microstructure

The microstructural evolution of the welded structure primarily depends on the solidification behavior of stainless steel. The Chromium equivalent [$Cr_{eq.}$] and Nickel equivalent [$Ni_{eq.}$] are the key parameters to drive the solidification kinetics (Sabooni et al., 2015). To determine the solidification mode and ferrite number of laser welding, [$Cr_{eq.}$] and [$Ni_{eq.}$] are calculated in the present study. The value of [$Cr_{eq.}$] and [$Ni_{eq.}$] is estimated as 20.9 and 12.4, respectively. The numerical values are fitted on the Schaeffler diagram (Fig. 5.46a). It indicates that the SS304 exhibits ferrite no. 14, and both austenite and ferrite phases constitute the fusion zone. The ratio of [$Cr_{eq.}$] / [$Ni_{eq.}$] is estimated as 1.69 and fitted on isopleth of the ternary Fe-Ni-Cr system (70 wt. % Fe-content) as depicted in Fig. 8.6b. It confirms that SS304 weldments manifest FA (Ferrite-Austenite) mode of solidification that would cause lathy ferrite and austenite type morphology. Therefore, weld metal would follow the different stages of solidification under FA mode (Lippold and Kotecki, 2005), which is expressed as

$$L \rightarrow (L + \delta) \rightarrow (L + \delta + \gamma) \rightarrow (\delta + \gamma) \quad (8.1)$$

where L, δ, and γ represents the liquid, ferrite, and austenite phase, respectively.

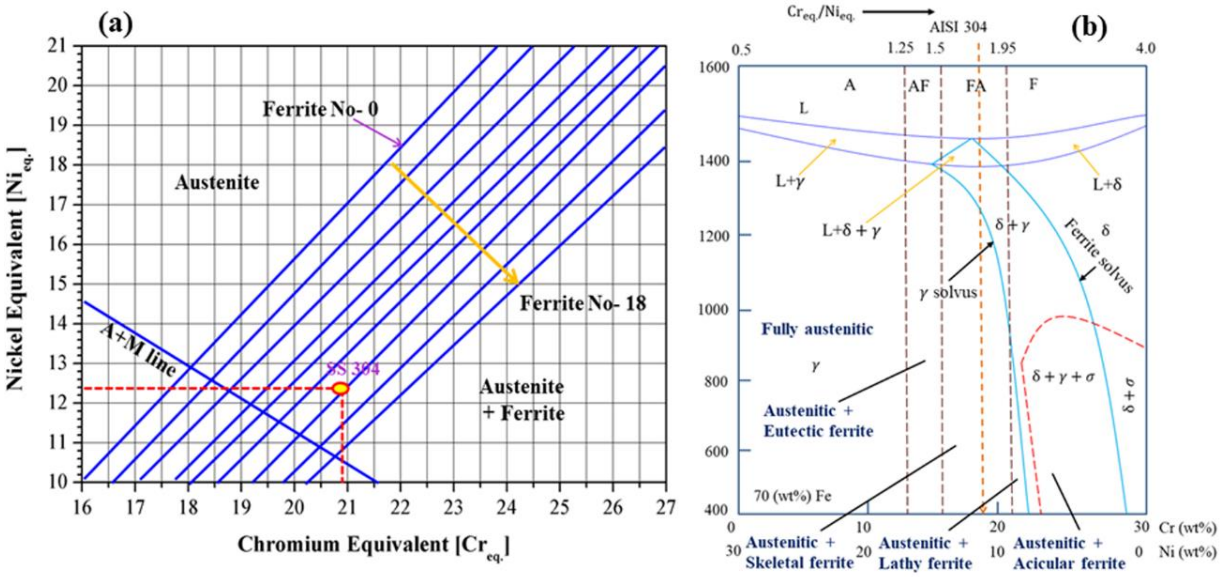

Fig. 5.46 Constitution of SS304 weld deposit on (a) Schaeffler diagram, (b) isopleth of ternary Fe-Ni-Cr system with 70 wt.% Fe-content (Lippold and Kotecki, 2005)

Fig. 5.47a depicts the microstructure of the weld zone for the specimen$S_{45}D_2$. The fusion zone is composed of δ-ferrite in the γ-austenite matrix. Figs. 5.47b-d represents the magnified image of sub-region P, Q, and R, respectively. The rapid cooling suppresses the $\delta \rightarrow \gamma$ transformation owning to retained ferrite. The base material region is comprised of equiaxed austenite grains (Fig. 5.47b), where the FZ exhibits both lathy and skeletal δ-ferrite (Fig. 5.47c). The presence of two different δ-phase morphologies is attributed to the local cooling rate variation in the FZ. High (75 J/mm) to intermediate heat input (56 J/mm) resembles predominant skeletal δ-ferrite followed by lathy δ-ferrite at low heat input (45 J/mm). Fig. 5.47d illustrates epitaxial growth at the fusion boundary, which splits the FZ from the base material. Ferrite stringers are also observed in the nearby region of the fusion boundary. At high temperature, the residual ferrite resulting from the segregation of ferritic stabilizer retains at the weld zone. The weldments joined at low heat input or high cooling rate (cases of $S_{45}D_1$, $S_{45}D_2$, and $S_{45}D_3$) exhibit a significant portion consisting of lathy δ-ferrite and less skeletal morphology. Whereas the microstructure of weld metal $S_{75}D_1$, $S_{75}D_2$, and $S_{75}D_3$ indicates the presence of a negligible

amount of lathy δ-ferrite. Carbide precipitation is notified at a localized region of spectrum 1 (Fig. 5.47c). The EDS image of the precipitated region is shown in Fig. 5.47e. It is found that the percentage of Cr (wt. % ~20) and C (wt. % ~7) content is remarkably high in this spectrum, which confirms the Cr-based carbide (i.e., $M_{23}C_6$) formation since Cr is strong carbide former.

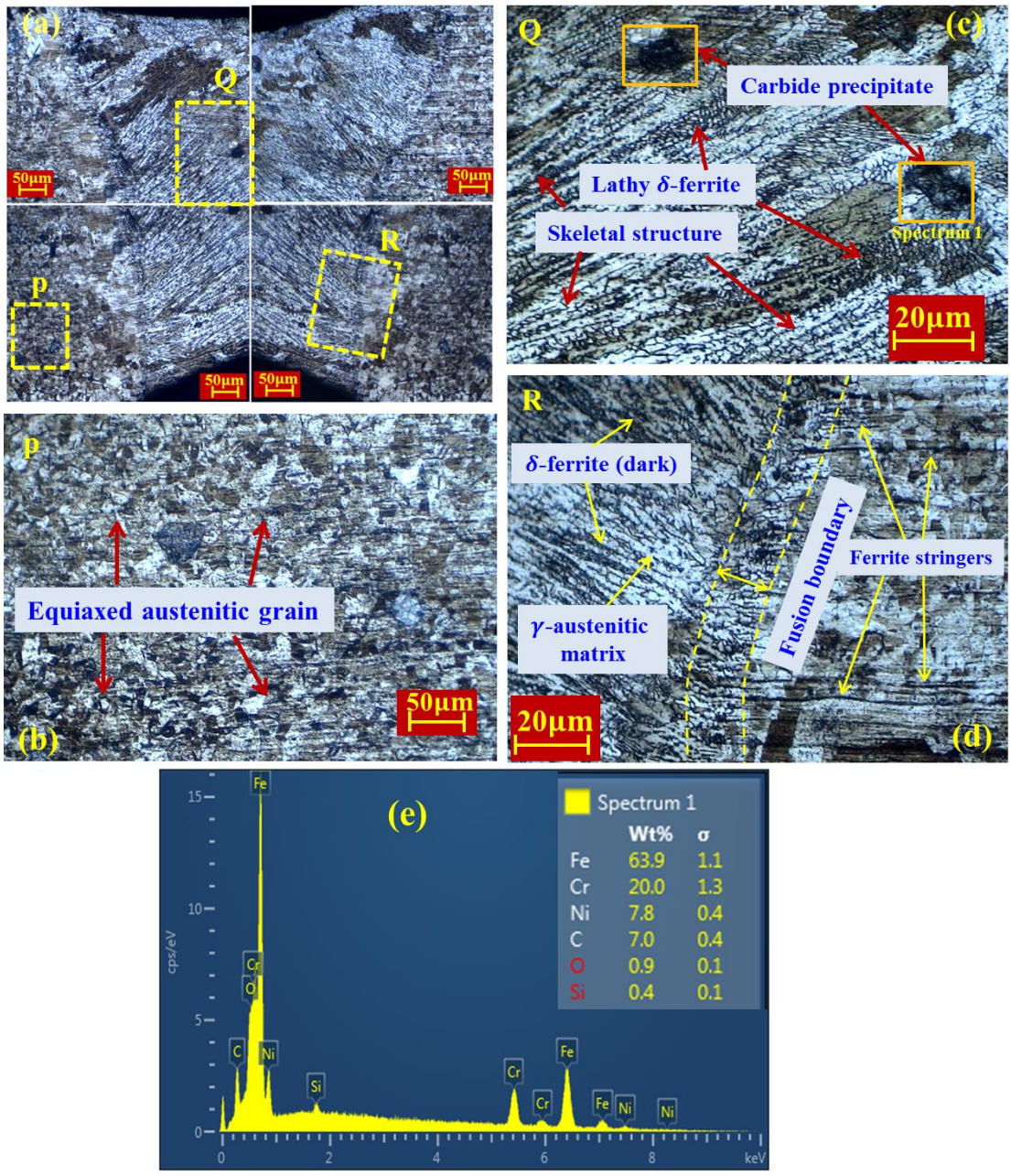

Fig. 5.47 (a) Microstructure of the weld zone for $S_{45}D_2$; Magnified images at different spectrum (b) 'P', (c) 'Q', and (d) 'R', and (e) EDS image of the spectrum 1

It is a well-known fact that chromium (Cr), silicon (Si), and molybdenum (Mo) are ferritic stabilizers, while nickel (Ni), carbon (C), manganese (Mn), and nitrogen (N) act as an austenitic stabilizer. Fig. 5.48 demonstrates the elemental distribution of Cr, Ni, and Mn in the dendritic core of skeletal δ-ferrite and the transformed austenitic matrix. Spectrum 9 and 10 renders austenitic matrix and ferritic dendrite site, respectively (Fig. 5.48b). Fig. 5.48c and d indicates that the concentration of Cr content is more at the primary dendritic core region. In contrast, the content of Ni is higher at the austenitic matrix region. It signifies that the phase transformation from δ-ferrite to γ-austenite is a diffusion-controlled process. EDS analysis confirms the increasing weight percentage of Cr (19 to 24) from austenitic to ferritic sites. The Ni percentage also increases from 3 to 9, as observed in Fig. 5.48d. It implies that the austenitic growth is accomplished by the acceptance of Ni, and the segregation of Cr from the austenite matrix leads to agglomeration or enrichment of chromium (Cr) and reduction of nickel (Ni) content in the residual ferrite. It is obvious that element diffusion plays a crucial role in controlling $\delta \rightarrow \gamma$ transformation. In solidification, the incomplete transformation occurs due to suppression of elemental diffusion by rapid cooling. By virtue of which only thin lamellae primary dendrite is transformed into γ-austenite. However, a thicker one cannot be dissolved completely. Hence, it retains as a skeletal or lathy δ-ferrite with enriched Cr and leans Ni content in the dendrite core even at room temperature.

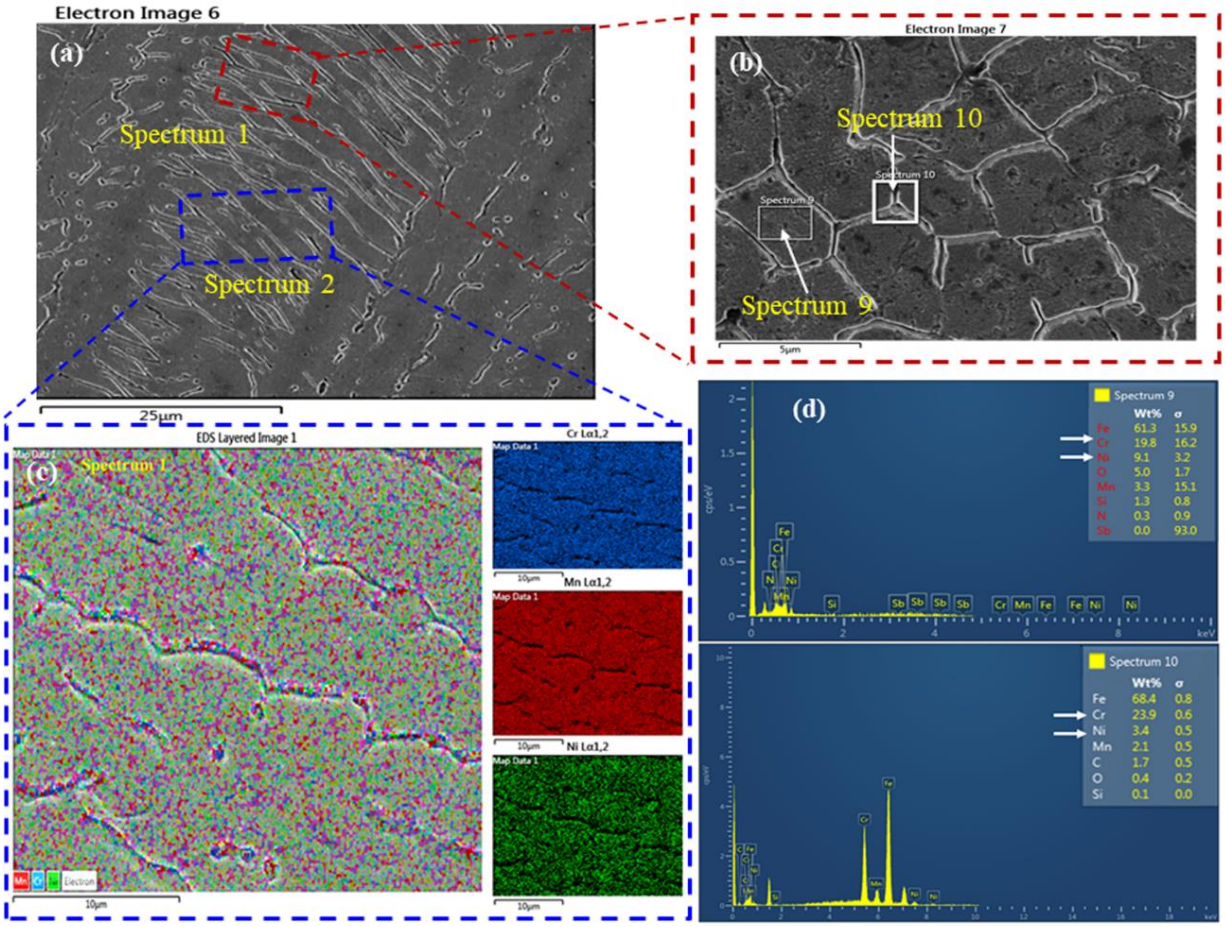

Fig. 5.48 (a) Selective area of FZ for the evaluation of elemental distribution; (b) magnified image of spectrum 1; (c) Elemental distribution of alloying elements (Cr, Mn, and Ni) due to incomplete δ → γ transformation and (d) EDS image of spectrum 9 (top) and spectrum 10 (bottom) of Fig. 5.48b

The schematic of probable solidification behavior of SS304 is illustrated in Fig. 5.49a and b. The initial phase of steel weldment consists of an equiaxed γ -austenite grain indicated by point 'p'. The material is heated gradually from ambient temperature to beyond liquidus temperature. The points 'q' and 'w' correspond to the cases $S_{45}D_1$ and $S_{75}D_1$, respectively, that exhibit a liquid phase. When the molten metal passes liquidus temperature (~1723 K) during the cooling phase, the solidification begins. Since specimen $S_{75}D_1$ corresponds to high heat input, it attains a low solidification rate, whereas specimen $S_{45}D_1$(low heat input) achieves a relatively high cooling rate. It is apparent that FA mode of solidification prevails where the molten region passes through two intermediate stages between liquidus and solidus temperatures. The first is

characterized by $(L + \delta)$ phases, while the other stage is composed of $(L + \delta + \gamma)$ phases. Point 'r' and 'x' attributes to the liquid phase and some amount of δ-ferrite due to the agglomeration of ferritic stabilizing elements (mainly Cr at the dendritic core), as demonstrated in Fig. 5.49c. Owing to rapid solidification, the formation of δ-ferrite is found higher at point 'r' than that of 'x'. Additionally, on the verge of solidus temperature, three-phase mixtures (liquid, δ-ferrite, and γ-austenite) are exhibited for a short period at points 's' and 'y'. The phase γ-austenite forms due to a complete $\delta \rightarrow \gamma$ transformation. Elemental diffusion (i.e., agglomeration of Cr at dendritic core and segregation of Ni from the austenitic matrix) is responsible for phase change from $\delta \rightarrow \gamma$ as illustrated in Fig. 5.49d. When the metal passes between solidus temperature to room temperature, a dual-phase microstructure composed of $\delta + \gamma$ is developed at points 't' and 'z'. Despite being partially transformed from the $\delta \rightarrow \gamma$ phase in both the cases, enriched lathy and skeletal structured δ-ferrite are observed due to suppression of elemental diffusion at a high cooling rate at low heat input (45 J/mm). A low amount of coarse δ-ferrite is achieved for higher heat input (75 J/mm).

Fig. 5.50 depicts the SEM images of the weld zone at different welding conditions. The microstructure exhibits a mixture of lathy and skeletal δ-ferrite, but the proportion of lathy δ-ferrite enhances with an increase in cooling rate. The magnified SEM images are analyzed herein to investigate the variation of primary dendrite lath size and associated inter-dendritic spacing of δ-ferrite. The average thickness of primary dendrite lath is found as 393 nm and 484 nm for the weldments $S_{45}D_3$ ($D_3 \sim 1$ mm) and $S_{45}D_1$ ($D_1 \sim 0$ mm), respectively, at a minimum heat input of 45 J/mm whereas 1163 nm and 927 nm for specimens $S_{75}D_1$ ($D_1 \sim 0$ mm) and $S_{75}D_2$ ($D_2 \sim 0.5$ mm), respectively at the maximum heat input of 75 J/mm. At the intermediate heat input of 56 J/mm, the lath thickness for $S_{56}D_1$ and $S_{56}D_2$ is observed as 739.8 nm and 655 nm, respectively. It is inferred that the primary dendrite arm becomes finer when the cooling rate increases. At high heat input, a relatively coarse or thick dendritic lathe is observed. The high cooling rate allows less time for the growth of dendritic lath. However, at high heat input viz. low cooling rate renders ample time to grow coarse dendrite in the fusion zone (Kumar and Shahi, 2011). Relatively more diffusion time during δ-ferrite → γ-austenite transformation leads to the generation of lathy δ-ferrite rather than skeletal morphology at a high cooling rate. Hence, the

proportion of lathy δ-ferrite increases upon decreasing heat input. The average inter-dendritic spacing increases from 3 μm to 6 μm for the rise of heat input from 45 to 75 J/mm.

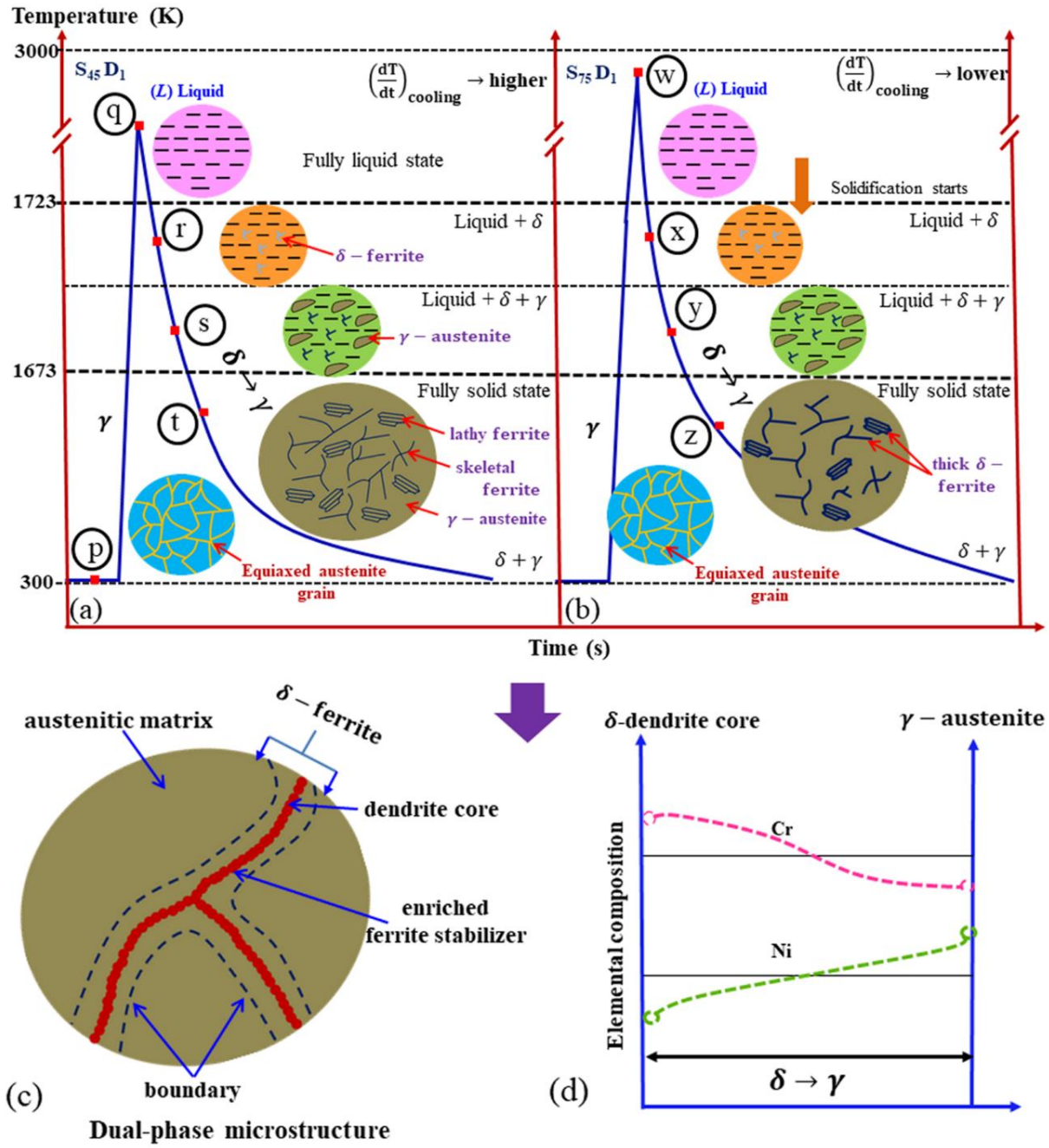

Fig. 5.49 Demonstration of thermal cycle and associated metallurgical changes at different stages of solidification for cases: (a) $S_{45}D_1$ and (b) $S_{75}D_1$, (c) Illustration of dual-phase microstructure with ferrite boundary and (d) Compositional variation of Cr and Ni during δ → γ transformation

Fig. 5.50 indicates the distribution of dendritic laths at different welding conditions. The average thickness of primary dendritic lath increases with an increase in heat input, i.e., 484 nm (45 J/mm), 739 nm (56 J/mm) and 1163 nm (75 J/mm). However, the dendrite size decreases for the defocused beam (~1 mm) relative to the focused beam, i.e., 484 nm → 393 nm for 45 J/mm, 739 nm → 655 nm for 56 J/mm and 1163 nm → 927 nm for 75 J/mm.

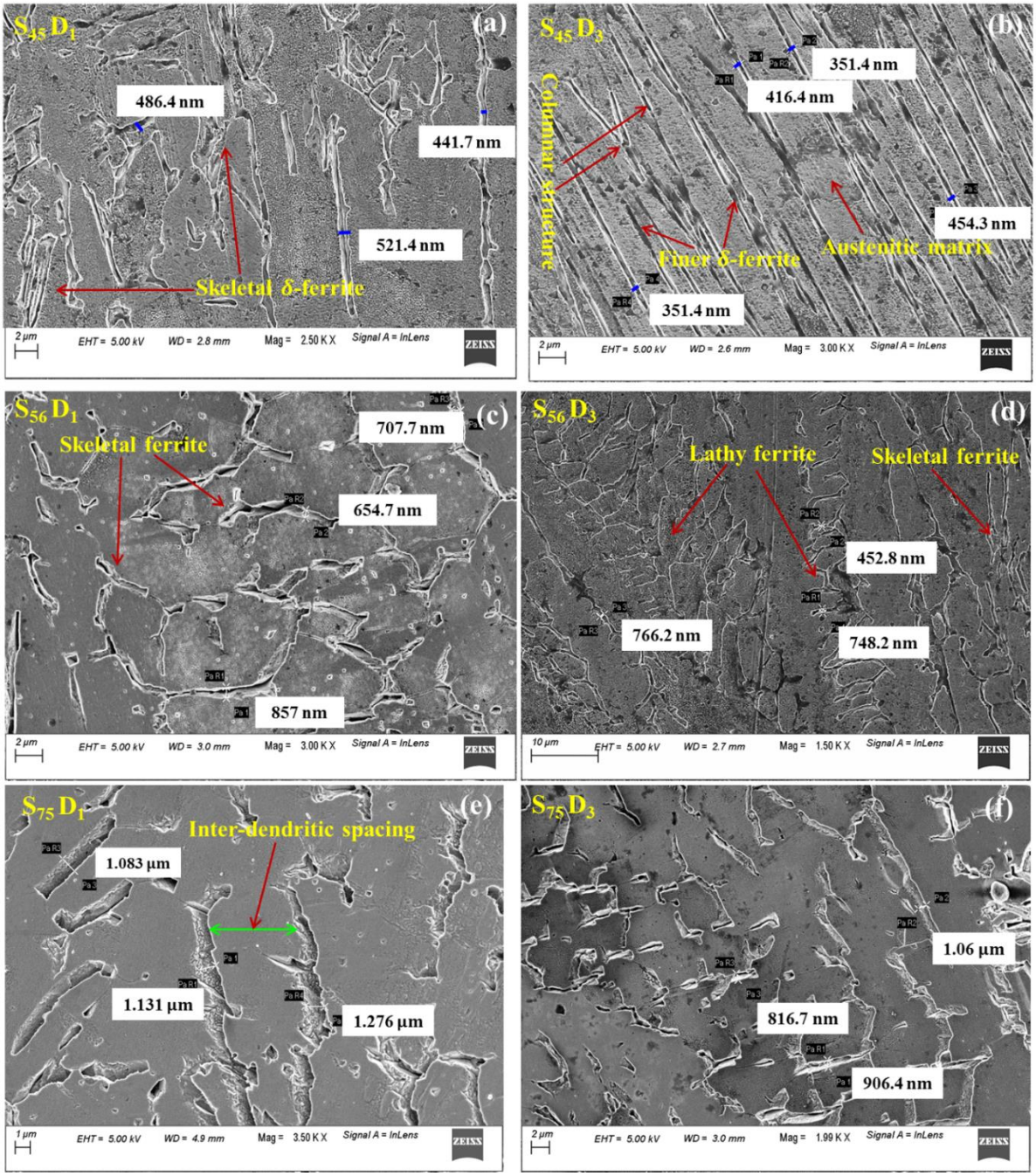

Fig. 5.50 Variation in primary dendritic lath of δ-ferrite at different welding conditions

5.5.3 Prediction of phase fraction

Fig. 5.51a, b, and c illustrate $\delta \rightarrow \gamma$ transformation at FZ with time and temperature during the cooling stage. As the weld zone begins to solidify through the formation of δ-ferrite and γ-austenite below solidus temperature, γ-austenite starts to consume unstable δ-ferrite through a diffusion-controlled mechanism such that crystallographic arrangement changes from bcc to fcc structure. This transformation produces volumetric expansion at the weld zone. As a result, the phase fraction of austenite increases due to the decomposition of ferrite into austenite, and volume fraction of ferrite phase decreases. Below austenitic finish temperature (1273 K), some fraction of retained ferrite remains within the FZ, which is unable to transform into austenite phase even at room temperature. The highest retained ferrite fraction of $\sim 12\%$ is achieved at a minimum heat input of 45 J/mm, whereas it is the lowest ($\sim 7.3\%$) at the highest heat input of 75 J/mm. The rest of the phase fraction is comprised of an austenitic matrix in the weld zone. A substantial difference is observed between the slope of the equilibrium phase diagram and the numerical results. It may be due to a drastic change in the cooling rate during solidification. Fig. 5.51d represents the overall phase fraction of austenite and ferrite in the equilibrium stage (Avrami model) and different heat inputs at room temperature. The results indicate that the equilibrium fraction attained for both phases is approximately similar to the model results at the lowest heat input. However, a significant deviation is observed by increasing heat input.

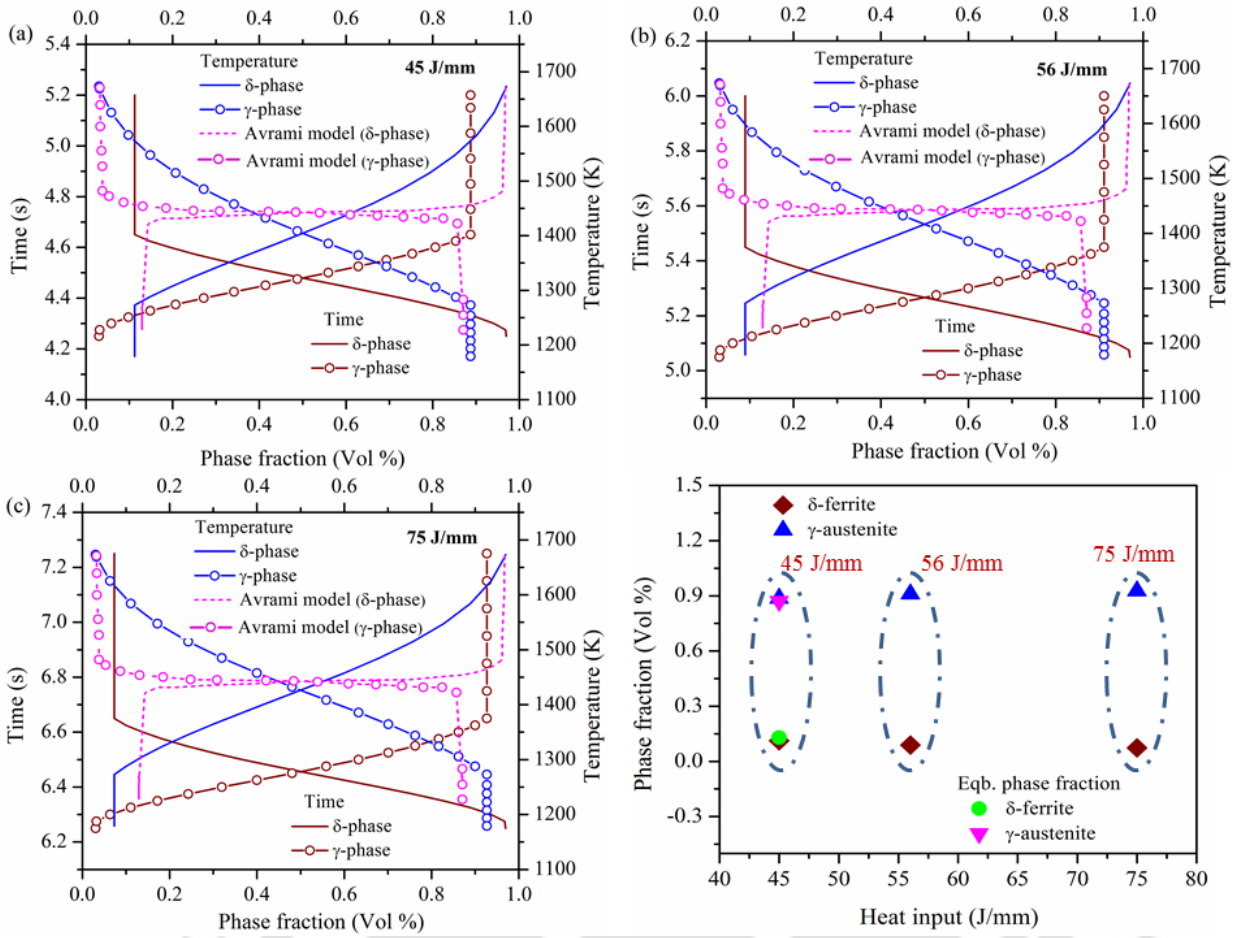

Fig. 5.51 δ → γ transformation at different heat inputs of (a) 45 J/mm, (b) 56 J/mm, and (c) 75 J/mm, and (d) ferritic and austenitic phase fraction at room temperature

Fig. 5.52 depicts the distribution of δ-ferrite at intermediate stages at a heat input of 45 J/mm. The FZ is comprised of a fully ferritic phase (~96%) at equilibrium condition. Fig. 5.52b indicates the decomposition of δ-ferrite at the intermediate stage whenever the δ-ferrite phase reaches towards equilibrium amount at 4.57 s. Fig. 5.52c represents the retained ferrite phase fraction distribution over the domain at a time interval of 4.62 s. It shows that the δ → γ transformation is about to a final state where ~12% ferrite is observed. The schaffler-Delong diagram indicates that the maximum ferrite fraction of 10-13% is possible at $Cr_{eq.}$ / $Ni_{eq.}$ ~1.69, which shows the robustness of the developed metallurgical model. Therefore, the modification in residual stress distribution is expected with significant variation of ferrite phase fraction obtained at different heat inputs.

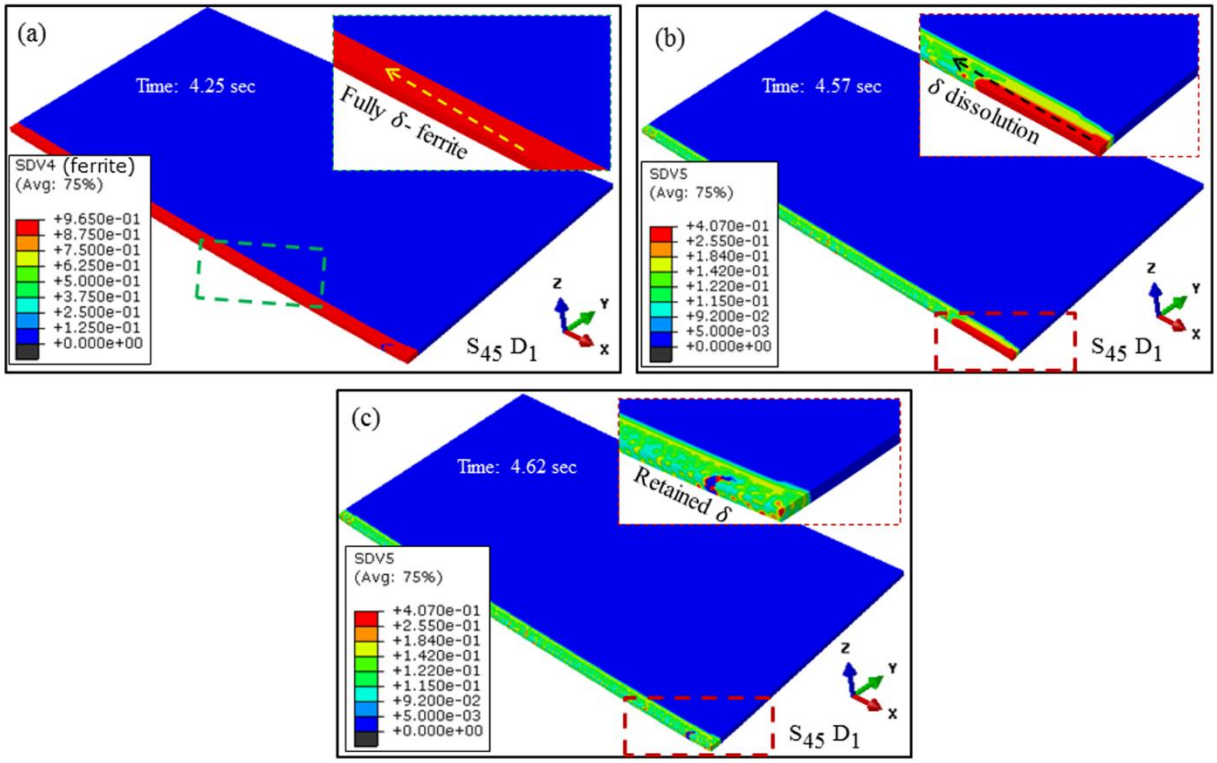

Fig. 5.52 Decomposition of δ-ferrite during SSPT for heat input of 45 J/mm at (a) 4.25 s, (b) 4.57 s and (c) 4.62 s

5.5.4 Residual stress distribution

The residual stress distribution for the cases $S_{45}D_1$, $S_{56}D_1$, and $S_{75}D_1$ is illustrated in Fig. 5.53. The maximum and the minimum magnitude of stress is characterized by red and blue band respectively. The appearance of red contour in every sample confirms the accomplishment of a tensile state of stress at a nearby region of the weld center. The longitudinal stress component extends up to a certain limit depending on the amount of heat input. The compressive state of stress is perceived at a further location for this case. Relatively high tensile residual stress at the fusion zone is observed. To maintain overall equilibrium condition of the welded structure, the nature of residual stress follows the sequence of tensile and compressive state. Fig. 5.53d indicates that a higher magnitude of stress is found to localize in a small region for the case of the lowest heat input ($S_{45}D_1$).

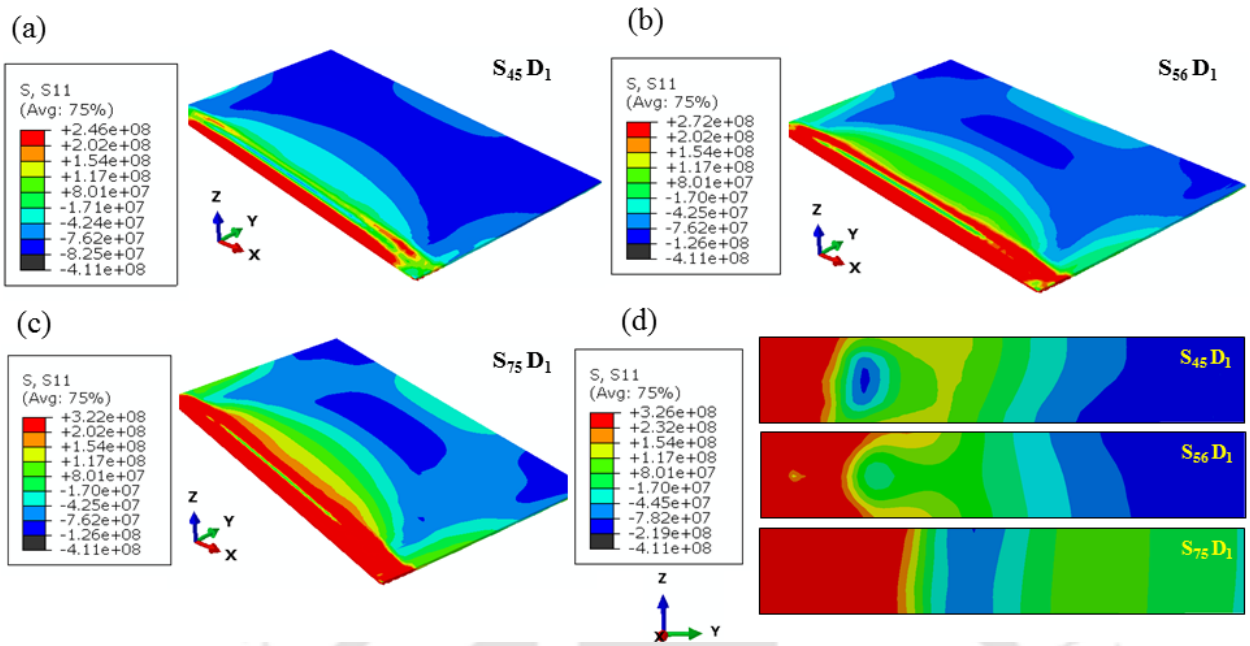

Fig. 5.53 Contour of longitudinal (S11) residual stress distribution for cases: (a) $S_{45}D_1$, (b) $S_{56}D_1$, (c) $S_{75}D_1$, and (d) transverse cross-sectional view captured at the middle section of the welded plate.

Fig. 5.54 shows the comparison between the computed and experimentally measured residual stress at a heat input of 56 J/mm and 75 J/mm, respectively. It is apparent that both the components of residual stress are high (S11~ 347 ± 47 MPa; S22~ 190 ± 24 MPa), where the FZ consists of a large amount of γ-austenite (~93 %) produced at a high heat input of 75 J/mm. Relatively low stress is accomplished for 56 J/mm heat input, which exhibits a relatively higher amount of δ-ferrite phase content (~ 90 %). A high amount of δ-ferrite allows an increased concentration of Cr and lean distribution of Ni. A typical characteristic of Ni and Cr in a phase constituent is schematically shown in Fig. 8.15a (Karunaratne et al., 2016). The thermal expansion coefficient of Ni (γ-phase) $[\alpha_T \sim (15 - 17.5) \times 10^{-6}\ K^{-1}]$ is higher than that of Cr (δ-phase) $[\alpha_T \sim (9 - 11) \times 10^{-6}\ K^{-1}]$. Under these circumstances, γ-site contract substantially than δ-ferrite in a dual-phase system and produces tensile strain in the γ-austenite region whereas compressive strain in δ-ferrite rich dendrite core (Fig. 5.55). In similar context, it is illustrated that the lattice parameter, which is the function of interstitial atom content, is crucial for the interpretation of desired residual stress in expanded austenite (Hummelshøj et al., 2010). The overall mechanism of compressive stress generation at the dendrite core and tensile residual

stress at the austenite region is illustrated in Fig. 5.55b. The enriched δ-ferrite reduces the overall tensile residual stress due to the dominant behavior of compressive strain at relatively low heat inputs (45 and 56 J/mm). Nevertheless, decreasing the amount of δ-ferrite with increasing heat input limits the compressive strain generation and enhances overall tensile stress. Similarly, it is demonstrated in literature that tensile elastic strain emerges within the γ-austenite matrix due to variation in the thermal expansion coefficient of alloying elements (Harjo et al., 1998). Additionally, the microstructural variation with residual stress distribution has a proportional relationship in dislocation density accomplished by local misorientation. Local misorientation for the constitutive austenitic phase is larger than the ferritic phase that favors the accumulation of high dislocation density driven by thermal activation and plastic misfit (Wan et al., 2019). The austenite is considered as a hard component, and plastic deformation of δ-ferrite is restrained by the hard component. It leads to retardation of the growth of back stress, which resembles lower stress level due to δ-ferrite. Therefore, a substantial amount of δ-ferrite (56 J/mm) attributes relatively lower residual stress as compared to the sample with low δ-ferrite content (75 J/mm). It is also perceived that the coarsening of primary dendritic lath ($739\ \text{nm} \rightarrow 927\ \text{nm}$) and increasing inter-dendritic spacing from $4\ \mu\text{m}$ to $6\ \mu\text{m}$ enhances the residual stress components. Hence, increasing heat input from 56 J/mm to 75 J/mm may deteriorate the overall mechanical performance of the weldment. It can be concluded that at relatively low heat input, enhanced δ-ferrite content with finer dendritic lath and lower interdendritic spacing promotes the significant reduction of longitudinal (S11) and transverse (S22) residual stresses.

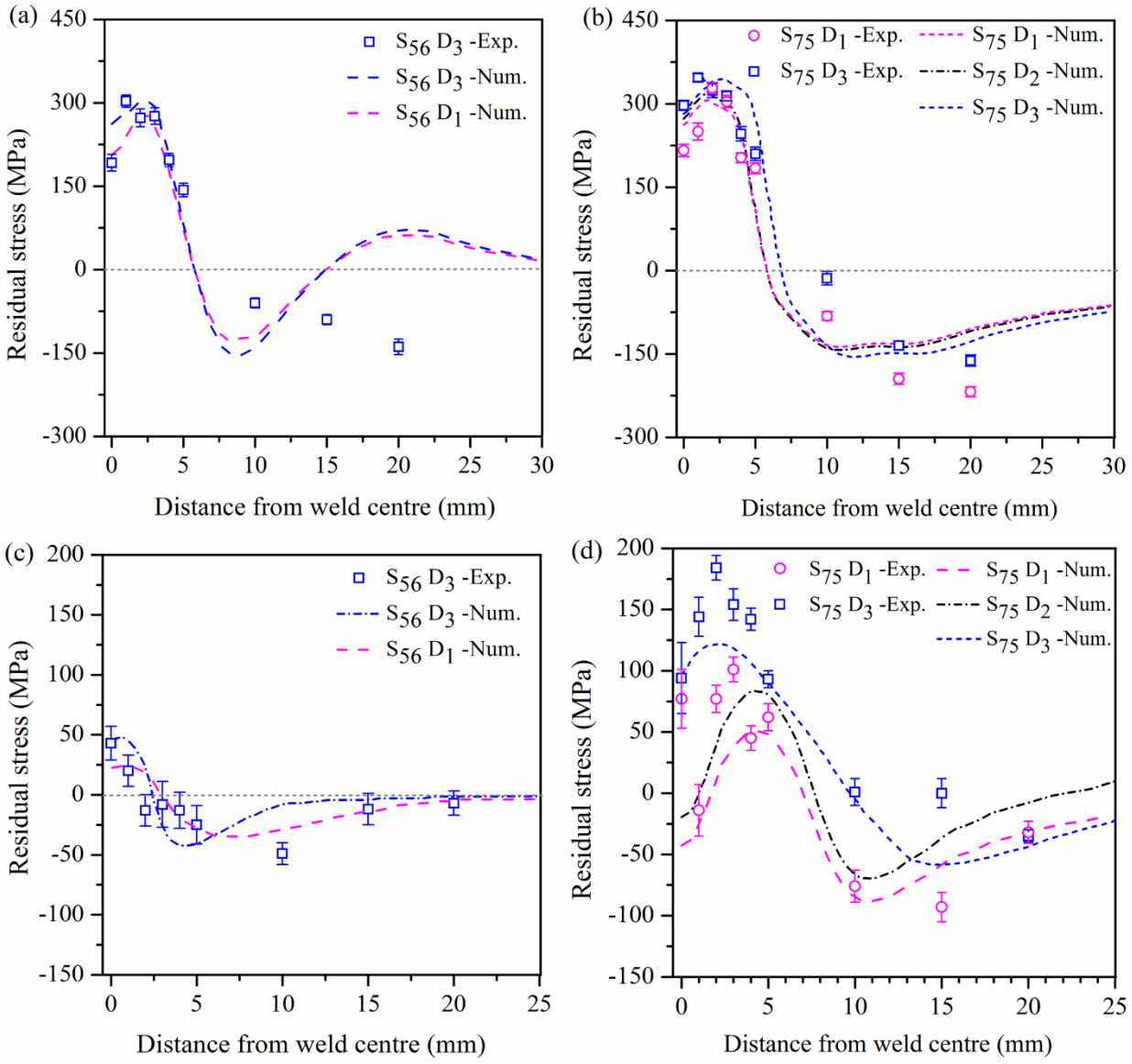

Fig. 5.54 Comparison between experimentally measured and numerically computed residual stress distribution: (a-b) longitudinal residual stress, (c-d) transverse residual stress distribution

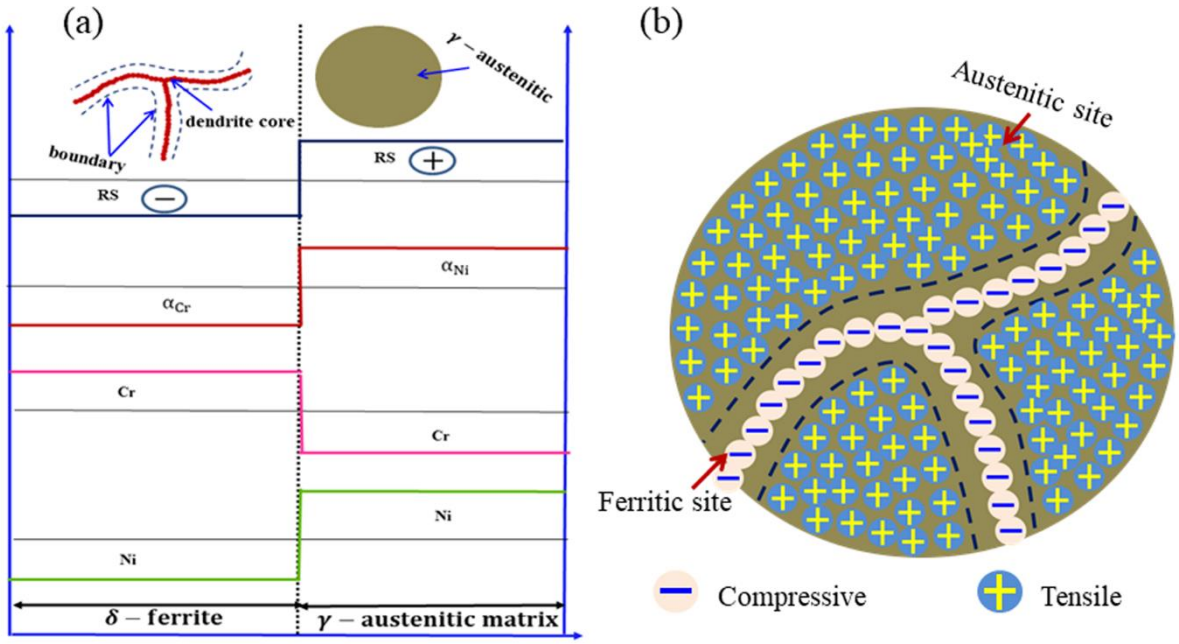

Fig. 5.55 (a) Interrelation between microstructural evolution and associated stress generation, (b) distribution of microscopic stress generation at austenitic-ferritic site

Fig. 5.56a indicates the longitudinal (S11) and transverse (S22) residual stress distribution across the weld at the minimum heat input (~45 J/mm). It is apparent that the minimum tensile stress is achieved for $S_{45}D_1$ relative to all other conditions. Even localization of residual stress is also perceived for $S_{45}D_1$ weld metal. At a low-focused laser beam, a high cooling rate with low heat input is responsible for localizing the stress. The maximum tensile longitudinal residual stress is ~245 MPa at 0.8 mm (distance across the weld center), while ~165 MPa is observed at the weld line. It is noteworthy that the residual stress is well below the yield strength of the base metal (i.e., ~283 MPa). Weldments $S_{45}D_1$, $S_{45}D_2$, and $S_{45}D_3$ attain maximum transverse residual stress of -165 MPa, -192 MPa, and -190 MPa at 1 mm, 1.5 mm, and 1.5 mm, respectively. Reversal of residual stress from tensile to compressive occurs at a distance of ~5 mm from the weld center for the case $S_{45}D_1$, whereas at 6.5 and 7 mm for the cases $S_{45}D_2$ and $S_{45}D_3$, respectively. Stresses in the region nearest to the fusion zone are compressive because of the expansion and subsequent obstruction by surrounding low-temperature materials. It infers that δ-ferrite content and its morphological (dendrite) characteristics within the austenitic matrix play a crucial role in governing the residual stress

distribution. Low thermal expansion of δ-ferrite compared to austenite diminishes the thermal contraction phenomena through the higher expansion of retained δ-ferrite within the austenitic matrix. Hence, tensile residual stress is significantly reduced, even lower than yield value (S11), and changes its nature from tensile to compressive (S22) upon accomplishing maximum δ-ferrite at the highest cooling rate. The morphological transformation from coarse dendritic lath (927 nm) to fine δ-ferrite (484 nm) and the reduction of inter-dendritic spacing upon increasing cooling rate endorses the mitigation of tensile residual stress as depicted in Fig. 5.56b.

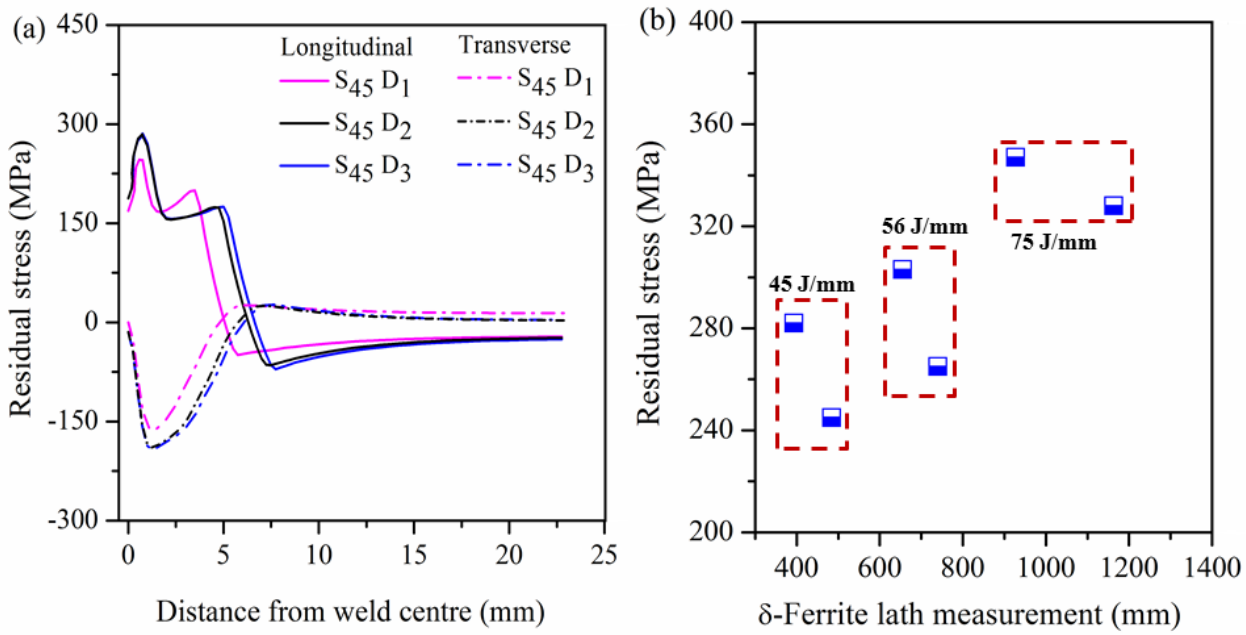

Fig. 5.56 (a) Residual stresses distribution at the lowest heat input of 45 J/mm, (b) variation of the primary dendritic size of δ-ferrite against residual stress

It is apparent that the effect of weld bead geometry less influences the pattern of residual stress distribution, and hence the negligible effect of material loss prevails in the residual stress distribution of the laser welding process. However, material depletion severely alters the strength properties. Heat input and associated changes in expansion and contraction for a particular material, type of the welding process, and nature of mechanical constraints can trigger the residual stress behavior. In the present study, the simulated result assumed a flat surface with identical mechanical constraints of the experiments. Hence, it does not alter the residual stress distribution even there is a crater in the experimentally measured weld macrograph.

5.5.5 Prediction of tensile properties

The tensile behavior of all the samples is investigated. The weld metal $S_{45}D_2$ directly fractures at the FZ and exhibits minimum ultimate tensile strength (UTS) (~ 426 Pa) and elongation ($\sim 2\%$) as illustrated in Fig. 5.57a. The samples $S_{45}D_1$, $S_{56}D_1$, $S_{75}D_2$, and $S_{75}D_3$ fail at the fusion boundary, whereas $S_{45}D_3$, $S_{56}D_2$, and $S_{75}D_1$ fail at the base metal region. The maximum tensile strength of 760 MPa is achieved by weld joint fabricated at low heat input ($S_{45}D_3$). The next joint strength of 747 MPa is achieved at high heat input ($S_{75}D_1$). The maximum elongation of 40 % is reached for the specimen $S_{75}D_3$ welded at a heat input of 75 J/mm. However, minimal elongation of 8 % is observed for weld metal $S_{45}D_1$ fabricated at a heat input of 45 J/mm. High heat input or low cooling rate renders coarsening of δ-ferrite dendritic core and widening of inter-dendritic spacing, which results in the development of low tensile strength. Low heat input or high cooling rate restricts the coarsening of δ-ferrite and yields less interdendritic space. Hence, UTS is found to be higher for weld metal $S_{45}D_3$ and low for weld metal $S_{75}D_3$. It is observed that UTS and elongation are inversely related to each other. An increase in chemical heterogeneity is related to a decrease in ferrite percentage in the weldment (Zumelzu et al., 1999). Low heat input diminishes chemical heterogeneity in the molten zone and causes an increase in δ-ferrite content. It results in higher tensile strength of the welded joints. Specimens $S_{45}D_3$, $S_{56}D_2$, and $S_{75}D_1$ fractured at the base metal indicate that the tensile strength is more than that of base metal, i.e., joint efficiency is more than 100 %. Weld metals $S_{45}D_1$, $S_{56}D_1$, $S_{45}D_2$, and $S_{75}D_2$ own concave-type crater or reduced molten zone (in Fig. 5.41). The local stress concentration is sufficiently high and might be the reason for achieving the low UTS as compared to other samples.

Figs. 5.57b-d demonstrates the fractography images of the samples $S_{45}D_2$ and $S_{75}D_2$. A large number of dimples with varied shape and size is observed at the fractured surface. It indicates large energy absorption prior to failure and leads to a ductile mode of fracture. The presence of a higher population of large and shallow dimples at low heat input ($S_{45}D_2$) is evidence for achieving relatively high tensile strength. However, elongated dimples and the appearance of micropores (in Fig. 5.57d) on the fractured surface of the weld metal $S_{75}D_2$ might be the factor responsible for the degradation of mechanical properties.

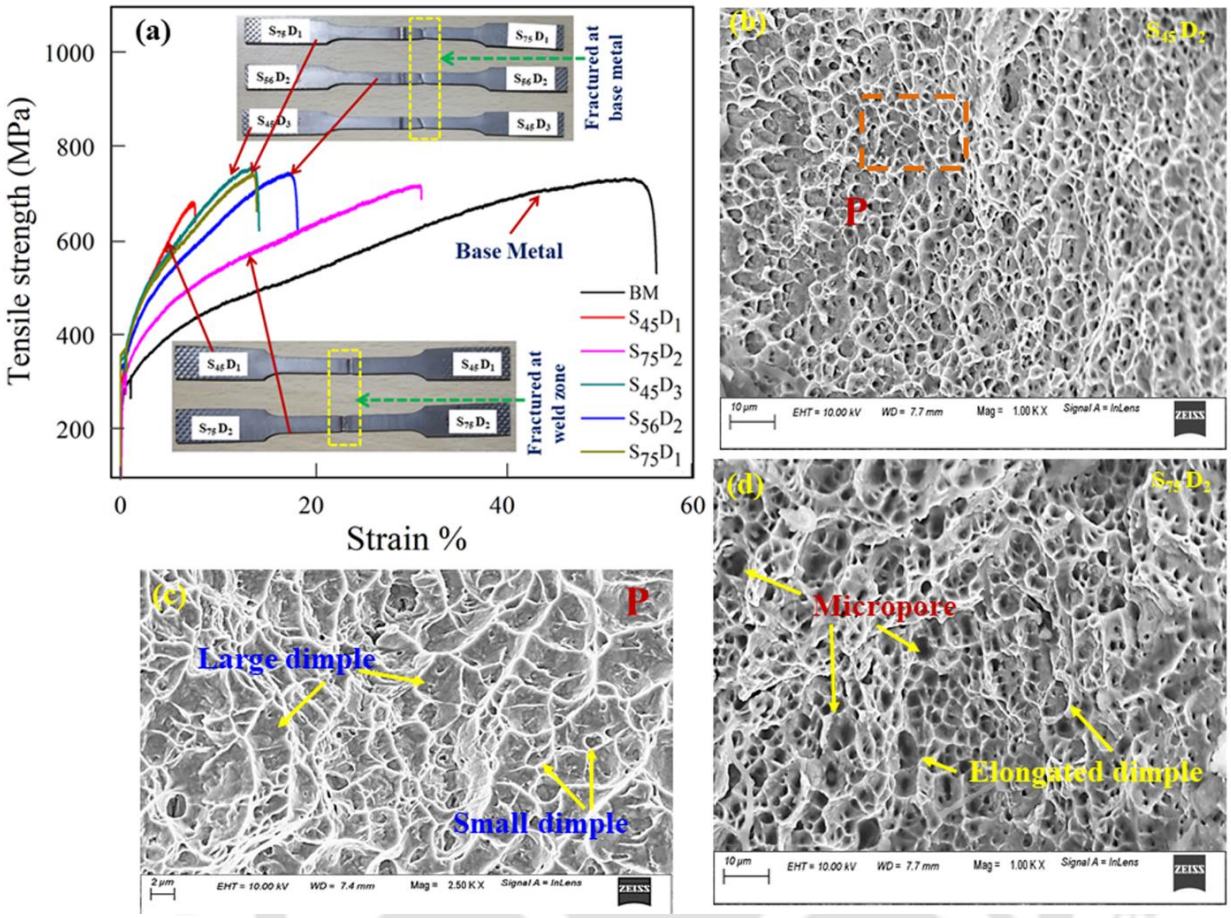

Fig. 5.57 (a) Stress-strain diagram of all welded samples; fractographic images of (b) specimen $S_{45}D_2$, (c) magnified image of scanned area 'P' and (d) specimen $S_{75}D_2$

5.6 Influence of weld metal composition on residual stress in 9Cr-1Mo Steel weldments.

Owing to the superior thermal conductivity, lower thermal expansion, and better oxidation resistance property of 9Cr based ferritic-martensitic steels relative to austenitic stainless steel, these steels are favoured for high temperature (~580 °C) applications. Nevertheless, these steels experience hydrogen-assisted cracking and type-IV cracking immediately after fabrication or before erection due to improper pre-heating and post-weld heating. In Easter coil fire power plant, 2000 cracks are reported in butt welds of evaporator tubes made up of T24 steel within three weeks of operation, and stress corrosion cracking is exposed as a cause for this damage. Undesirable residual stresses (RS) in welded structures often

results in stress corrosion cracking, brittle fracture and low fatigue life (Maddox, 1991; Taljat et al., 1998). A considerable amount of residual stress, either compressive or tensile, is produced in the HAZ whenever 9Cr steel structures are welded using conventional processes (Kundu et al., 2013). Martensitic transformation temperature is critically important in structural steel since it controls the overall stress distribution within the welded structure (Payares-Asprino et al., 2008). Hence, monitoring the martensitic start and finish temperature by controlling weld metal compositions can be an effective tool to regulate solid state phase transformation during cooling stage in the welding of ferritic-martensitic steel. The transformation induced strain compensates the thermal contraction strain that generates during the cooling of the weld metal. Welded structure with compressive residual stress improves several characteristics such as cold crack resistance, stress corrosion crack (SCC) resistance, fatigue life, brittle fracture resistance, and service life of structural steel (Dong, 2005). Residual stress development in 9Cr based steel weld joints is altered by liquid to solid, solid to solid phase transformations, and corresponding contraction strain (Yaghi et al., 2008). Though, studies on 9Cr based weld consumables are limited, the influence of austenite stabilizing elements (i.e., mainly Ni and Mn) on evolved residual stress is highlighted. The alloying element in metal substantially contributes to diversification in transformation temperature and leads to the alteration of residual stress behavior. For instance, Al, Ti, and Co increases the martensitic transformation temperature. However, Cr, Ni, Mn, and C diminish the transformation temperature (Payares-Asprino et al., 2008). The emergence of relatively high expansion strain at lowered martensitic start temperature can transform the state of stress from tensile to compressive. On the contrary, the establishment of contractive strain generates a tensile state of stress (Hamelin et al., 2014). Therefore, it is essential to pay attention towards the assessment of residual stress distribution across the weld and change its state by controlling the Ms temperature through suitably varying the alloy compositions in order to improve the safety of the fabricated components immediately after welding. Finite element (FE) based numerical simulation provides the flexibility to explore the complex phenomena of metallurgical-mechanical characteristics during the fusion welding process. Four weldments, i.e., W1, W2, W3 and W4 with varying alloying compositions are taken into account to fulfill the present objective. Detailed descriptions associated with the experimental tool are well explained in Section 3.3 of Chapter 3. In contrast, the theoretical model to incorporate alloying compositions is presented in Section 4.4 and 4.5 of Chapter 4.

5.6.1 Impact of composition on transformation temperatures

The Ac1 and Ac3 temperatures extracted from dilatation plots and calculated using Thermocalc^{TM} software is presented in Table 5.5. It is evident that the transformation temperature decreases upon increasing the content of austenite stabilizing elements. The critical temperatures are found to be highest for W1 whereas lowest for the case W4 with 2.49 wt.% of Ni+Mn+C+N. Besides, Ac1 and Ac3 temperatures are almost similar for the case W2 and W3 due to insignificant difference in the weight percentage of Ni+Mn+C+N content, i.e., 1.43 and 1.52 wt. % respectively. The transformation temperatures obtained from dilation plots are significantly higher rather than equilibrium values, which could be due to the difference in heating rates. It should be noted that the transformation temperature obtained from dilatometric and equilibrium calculation matches closely for weld metal W1, in which the austenite stabilizing elements are lowest. However, the deviation for other weld metals is more with increasing austenite stabilizing elements. Since, it is not the main objective of the present work, hence not detailed herein. Alloy composition and equilibrium phase diagram-based Thermocalc^{TM} data are applied quantitatively to calculate the austenite phase fraction during numerical modeling.

Table 5.5 Austenitic transformation temperature (TT) based on Thermocalc^{TM} (T) software and Dilation curve (D)

	Weld metal							
	W1		**W2**		**W3**		**W4**	
TT	T	D	T	D	T	D	T	D
Ac1	882 ℃	885 ℃	765 ℃	843 ℃	765 ℃	835 ℃	661 ℃	820 ℃
Ac3	915 ℃	916℃	829 ℃	902℃	822 ℃	905℃	786 ℃	880 ℃

The heating rate critically influences the austenite transformation temperature (Piekarska et al., 2017; Santella et al., 2001). Variation in temperature as a function of (Ni+Mn + C) Wt.% for

different heating rates is shown in Fig. 5.58. It signifies that austenitic transformation (i.e., $\alpha \rightarrow \gamma$) temperature (Ac1) of different weld metal increases significantly in the case of rapid heating. Rapid heating minimizes the time of elemental diffusion during austenitization, due to which transformation shifts towards a relatively higher temperature than its equilibrium stage. The drastic variation in critical temperature estimated through different means is obvious for the lower austenitic stabilizing composition (i.e., Mn+Ni). However, at an alloying concentration of 1.2-1.5%, Ac1 converged towards the same value. Furthermore, again a significant difference is observed at a higher percentage of alloying elements. The phase transformation at a high heating rate occurs through the displacive mechanism, i.e., known as austenite reversion. This type of austenite evolves lath-shaped grain with a high density of dislocations, which results in increased hardness (Spezzapria et al., 2017).

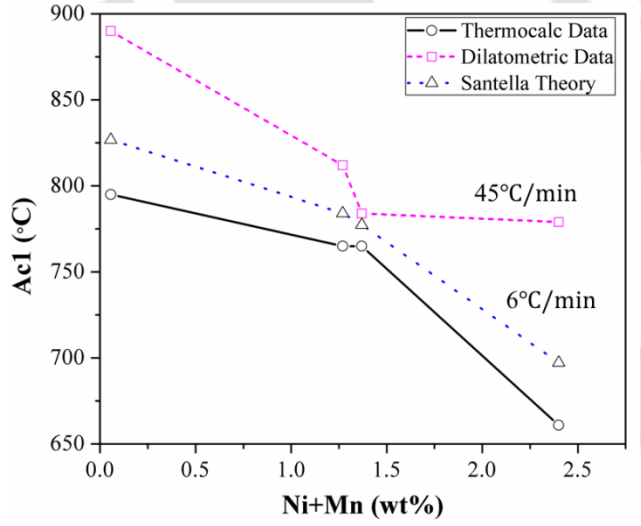

Fig. 5.58 Variation of Ac1 with (Ni+Mn) compositions at different heating rate

Furthermore, the martensitic transformation temperatures, i.e., Ms and Mf are extracted from the dilatation curve, are given in Table 5.6. It signifies that Mf temperature lowers even up to preheat temperature (i.e., ~200 ℃) beyond 1.4% (Ni+Mn) (Pandey et al., 2018). Gradual increase of austenite stabilizing elements from W1 → W4 lowers the transformation temperature. This is based on the fact that a progressive proliferation of austenitic stabilizing elements from W1 → W4 renders reduced AC1 temperature (as depicted in Table 5.5) resulting highly stable γ-austenite phase that can scarcely transform into martensite. To make it happen, a considerable

amount of driving force is required, which can only be attained at a significantly lower temperature. Hence, martensitic transformation temperature decreases.

Table 5.6 Martensitic transformation temperature (TT) based on Dilation curve (D)

	Weld metal			
TT	**W1**	**W2**	**W3**	**W4**
	D	D	D	D
Ms	408 ℃	360 ℃	351 ℃	350 ℃
Mf	330 ℃	255 ℃	259 ℃	204 ℃

5.6.2 Residual stress analysis

The distribution of residual stress across the weld center up to a distance of 20 mm from the weld line on either side of the weld metal is shown in Fig. 5.59a. It is evident that the nature of stress distribution changes from highly compressive to tensile at the weld line with reduced austenite stabilizing elements. However, its magnitude within the HAZ varies widely between W2, W3 and W4, while it is entirely different from W1. Highly tensile residual stress of magnitude 360 MPa is obtained for W1 (0.68 wt. %), while compressive residual stress value of 158, 104, and 208 MPa is obtained in case W2 (1.43 wt. %), W3 (1.52 wt. %) and W4 (2.49 wt. %), respectively at weld line. Variations in the magnitude of RS are attributed to the combined effect of the constraint-induced strain, lattice strain due to the martensitic transformation, and the volumetric strain to accommodate the austenite stabilizing elements. The induced strain is an invariant-plane strain that prevents the development of tensile residual stress that emerges from the weld's contraction as it cools, results in the generation of compressive stress (Francis et al., 2009).

The austenite to martensitic transformation puts the surface under a compression state owing to the expansion accompanied by martensite formation. It can be assumed that a change in

length during cooling below Mf to room temperature should coincide with the increase in length during heating. However, the dilation curve (Fig. 3.10 of Chapter 3) clearly shows that the final strain on reaching room temperature changes systematically with transformation induced strain. Accordingly, a variation of residual stress against relative change in length at room temperature is plotted in Fig. 5.59b, respectively. The relative change in length at room temperature is estimated as -0.13, -0.11, -0.09, and 0.02 for W1, W2, W3, and W4 weld metal. Even though a change in length accompanied by volumetric expansion is higher for W3 weld metal, compressive RS is found to be lower than W2 weld metal. By comparing the dilatometric data, it is confirmed that Mf temperature is relatively higher for W3 weld metal. The residual stress at ambient temperature will be smaller if the transformation temperatures are low (Hamelin et al., 2014). Therefore, it suggests that the onset and finish of martensitic transformation is as critical as expansion in governing the final residual stress state (Payares-Asprino et al., 2008).

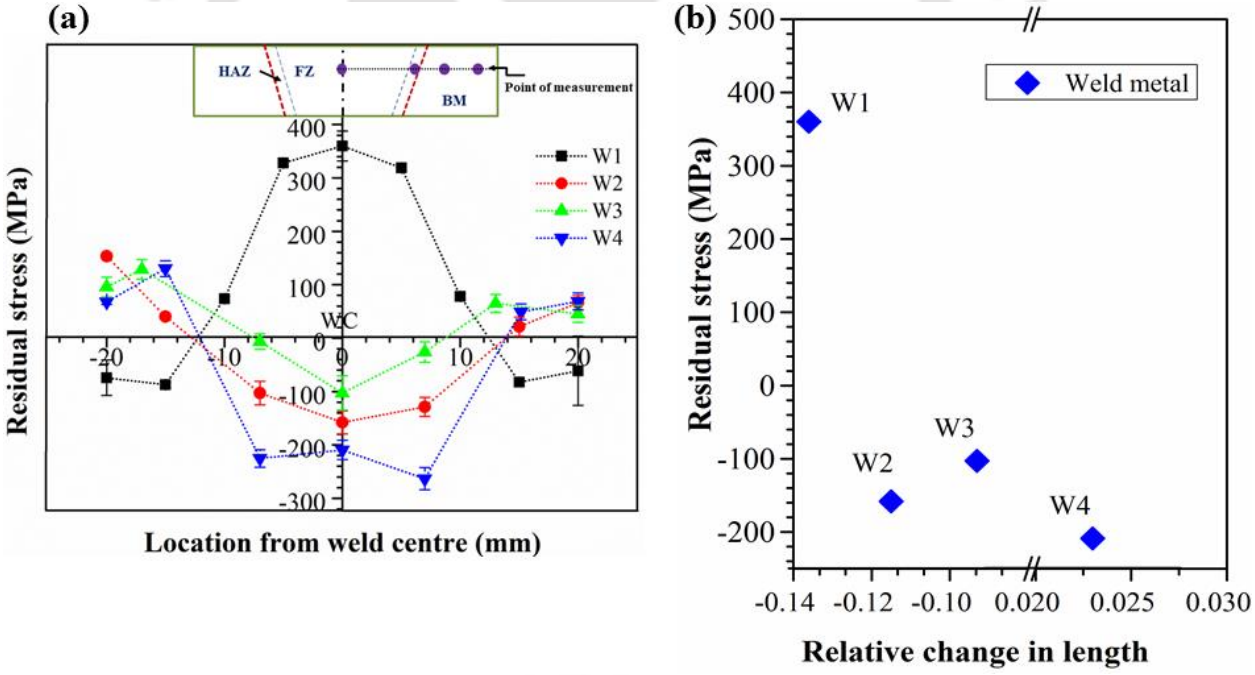

Fig. 5.59 (a) Longitudinal residual stress distribution (S11) across the weld interface, (b) demonstration of strain attained at Ms to Mf

5.6.3 TEM analysis

Effect of weld metal compositions on transformation temperature is evident from Fig. 5.58 and Table 5.6. Bright-field TEM images of weld metals W2, W3, and W4 at the molten zone are shown in Figs. 5.60a-c. Martensitic laths of various dimensions are clearly visible in the samples. From the figures, it is apparent that lath size decreases with increasing austenite stabilizing elements. Martensitic lath of a combination of coarse and intermediate thickness is observed for W3 weld metal might be due to less volume expansion. However, owing to relatively high volumetric dilation, martensite lath of uniform and intermediate thickness is obtained for weldment W2. It might be the prevailing factor due to which more compressive stress is generated at the FZ region. On the contrary, martensite lath of finer and smaller size, and in highly elongated shape are formed in W4 weld metal. It confirms a substantial volumetric dilation in this case. Since, this volume expansion accomplished at lowest martensitic transformation enhances lattice strain favours smaller lath adjustment within a given volume. This severe modification in volumetric change accompanied with martensitic transformation for enriched austenitic composition plays key role in the evolution of compressive stress generation in weld metal W4.

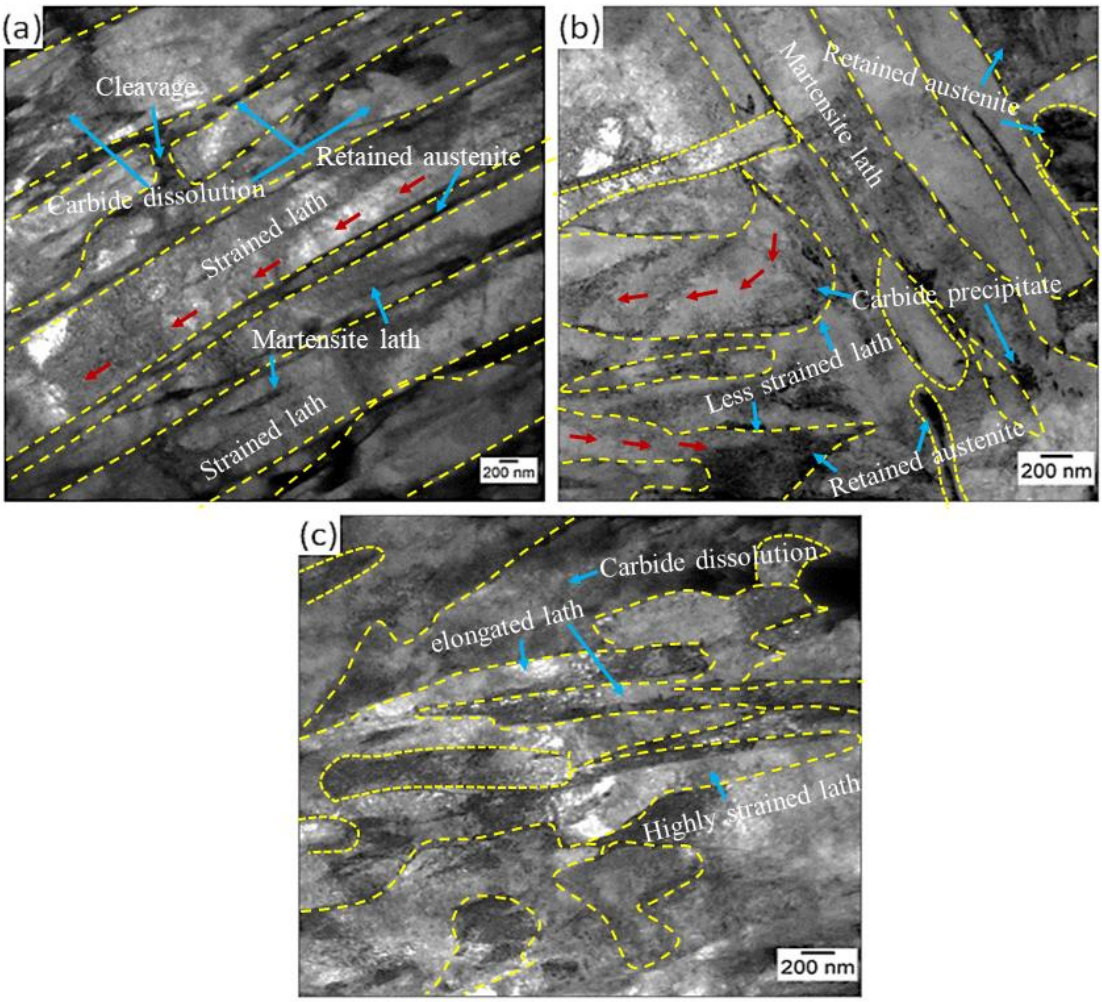

Fig. 5.60 Bright field TEM image of (a) W2, (b) W3 and (c) W4 as-welded weld metal

5.6.4 Thermal analysis

Fig. 5.61a and b illustrates the comparison between numerically predicated (left) and experimentally obtained (right) size of different regions in W1and W4 weld joints. Various zones of the weldment are characterized by isotherm contours in the simulated result, as shown in Fig. 5.61a and b. The golden-red band represents FZ, followed by HAZ as a green band on the outer side of the FZ. The small strip of the red band that separates FZ and HAZ is the mushy zone bounded by the solidus and liquidus temperature. Moreover, the blue color depicts base metal (BM). The maximum temperature of ~ 2250 K and ~ 2457 K is estimated at the weld centreline of weld metal W1 and W4, respectively, whereas a temperature range of 1073-1693 K is

estimated within the HAZ of W1 and W4 weld joint. The quantitative measurements of FZ and HAZ width and corresponding error percentage relative to the experimental data are presented in the corresponding Table in Fig. 5.61 as well. Therefore, it can be inferred that the predicted numerical weld profiles are in good agreement with the experimental result and exhibited a maximum error % of < 20% within FZ and HAZ.

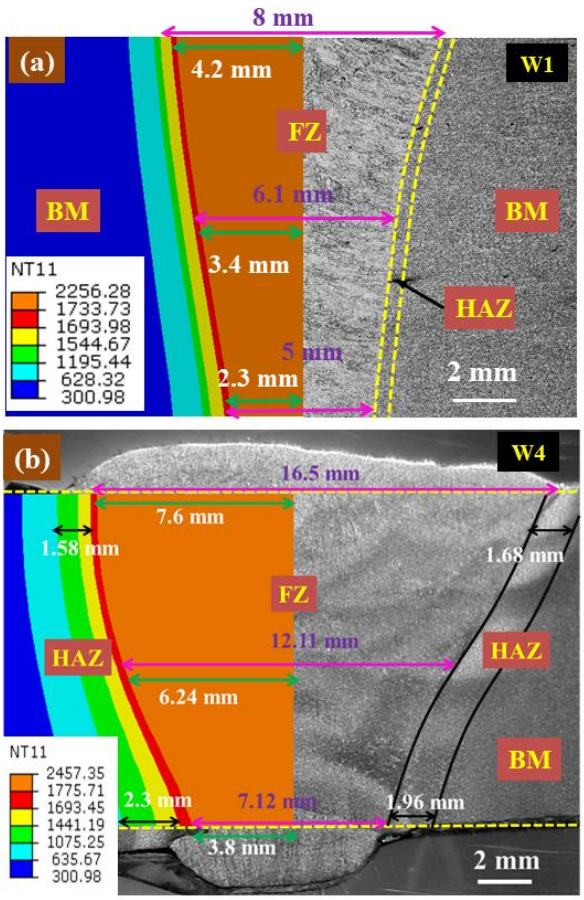

W1	Fusion zone (FZ)	Simulated (mm)	Experimental (mm)	Error %
	Top	4.2	3.8	10
	Root	2.35	2.65	11
	Heat affected zone (HAZ)	**Simulated (mm)**	**Experimental (mm)**	**Error %**
	Top	0.65	0.6	11
	Root	0.65	0.6	8

W4	Fusion zone (FZ)	Simulated (mm)	Experimental (mm)	Error %
	Top	7.6	8.9	13
	Middle	6.24	5.87	6
	Root	3.8	3.32	15
	Heat affected zone (HAZ)	**Simulated (mm)**	**Experimental (mm)**	**Error %**
	Top	1.58	1.68	6
	Root	2.3	1.96	17

Fig. 5.61 Comparison between experimental (right) and numerical (left) different regions of weldment of (a) W1, (b) W4 weld metal

Fig. 5.62a shows the temperature distribution over the W4 weld pad at two different time intervals during the SMA welding process. Initially, the molten pool acts as a transient and afterward reaches to quasi-steady state. Fig. 5.62b and c illustrate the thermal profile distribution across the weld cross-section and along with the thickness respectively in weldment W4 during welding. The legends in each of the figures identify the location. The temperature increases progressively and then decreases gradually with time. It is evident that the maximum temperature

of ~ 2460 K is achieved at the fusion line, whereas it is ~ 1000 K at 10.5 mm from the fusion line. Localization of the heat source restricts the maximum temperature in the confined region, whereas a relatively lower temperature zone is fanning out. Accordingly, a gradual reduction in peak temperature is observed away from the weld zone. The thermal profile along the thickness direction is shown in Fig. 5.62c. The peak temperature is lower, i.e., ~1950 K at the bottom surface of the geometrical domain. It could be because the applied heat flux is implemented in such a fashion that flux density decreases in a thickness direction. Furthermore, to validate the predicted width of HAZ, hardness measurement and associated temperature distribution, are performed between weld interface and BM region as depicted in Fig. 5.62d. Phenomenal change in hardness value at 0.5 mm and 2 mm distance from the weld interface for weldment W1 and W4 respectively manifests transition from HAZ to BM zone. Therefore, 0.5 and 2.0 mm is approximated as HAZ width, which is in good agreement with the obtained result from thermal modeling. This difference in HAZ width between W1 and W4 weld joints is attributed to the employment of electron beam welding process and shielded metal arc welding process for respective weld joint preparation. The heat source is highly localized in electron beam welding compared to the SMAW process. Temperature distribution across the weld interface indicates a sharp temperature gradient for the EBW weld joint (W1), whereas gradual temperature decay is observed at faraway location for W4 weld joint.

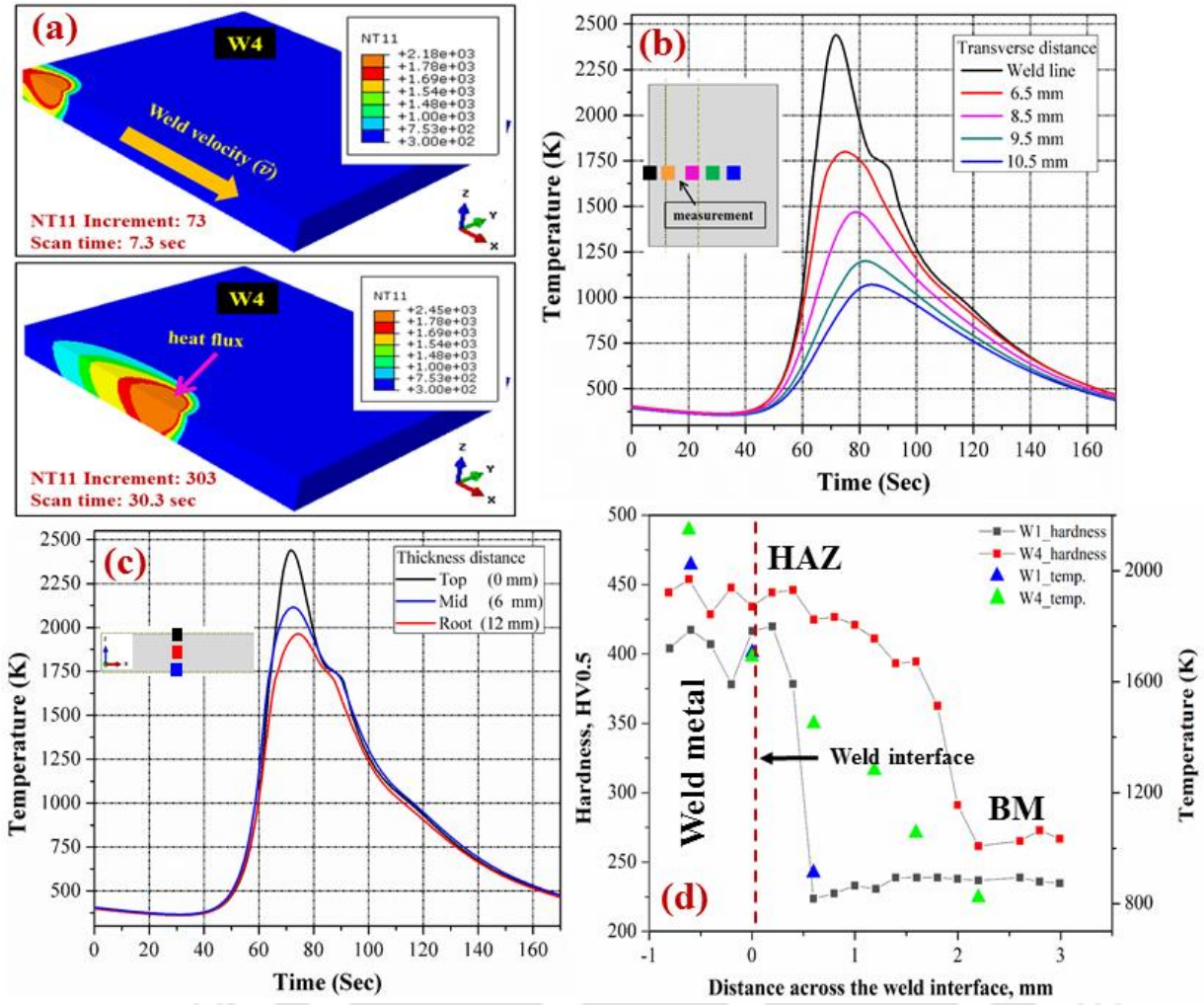

Fig. 5.62 (a) Temperature distribution during welding at different time span, (b-c) temperature profile along transverse and thickness direction, respectively, and (d) hardness distributions across the weld cross-section

5.6.5 Solid state phase transformation (SSPT)

Solid state phase transformation occurs during both heating, and cooling cycles of welding govern residual stress distribution during welding. The final content of austenite stabilizing elements influences Ac1, Ms and Mf temperature (Santella et al., 2001). Although there is no straight relation revealed between austenitic transformation and final residual stress distribution nevertheless, austenite grain size exhibited during austenitization greatly influences

the martensitic transformation, which in turn triggers residual stress evolution (Celada-Casero et al., 2019; Guimarães and Gomes, 1978). Apart, austenitic transformation influences martensitic transformation in various means such as by diversifying dissolution of carbide content through solid solution precipitation and austenitic grain growth. All these phenomena alter chemical drag force during martensitic transformation. The local strength of austenite adjudicates resistance against plastic deformation and hence, the strain energy anticipated during the growth of martensitic lath or plate (Van Bohemen and Sietsma, 2014). It is a well-known fact that the variation in austenite stabilizing elements attributes the dramatic difference in grain refinement under austenitic transformation. This microstructural variation shifts the Ms to the less value and hastens the transformation rate at the initial stage (Celada-Casero et al., 2019). It causes potentially less detrimental stress distribution in and nearby region of FZ. Therefore, it can conclude that the relative stability of austenitic transformation at several austenitic compositions indirectly influences the residual stress significantly. Although the present study is not dealing with microstructural aspects but focused on solid state transformation during the thermal cycle and its influence on stress distribution.

In order to understand $\alpha \rightarrow \gamma$ transformation during the heating stage, the evolution of γ-phase fraction with temperature is plotted in Fig. 5.63. It is already discussed that weld metal W4 possesses the lowest Ac1. As metal attains Ac1 (~ 661 °C) in heating stage, α-ferrite begins to transform into γ-phase and attains fully stable austenitic fraction prior to Ac3, i.e., at ~725 °C. At the same time, other specimens attended 100% austenite at Ac3 temperature. The $\alpha \rightarrow \gamma$ transformation can be achieved through very slow equilibration of austenite and prior ferrite by controlling austenitic stabilizer diffusion in austenite (Speich et al., 1981). In the present case, the non-uniform distribution of alloying elements, i.e., Ni and Mn, renders inhomogeneous $\alpha \rightarrow \gamma$ transformation since the part that acquires high Mn and Ni content begins to transform first. Accordingly, specimen W4 possessed fully transformed austenite far before Ac3.

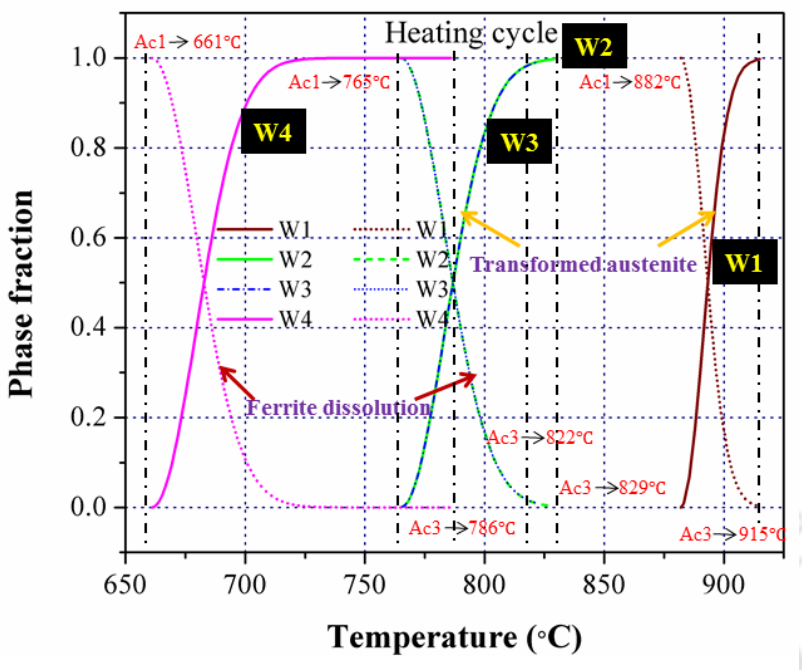

Fig. 5.63 Depiction of development of austenite phase fraction during α → γ transformation

Fig. 5.64 depicts the 2D contour of martensitic transformation for different weld pads. Contour plot of martensitic phase fraction distribution is captured at the cross-sectional (transverse) interface of all weld metals at two different time span, i.e., at an intermediate temperature between Ms and Mf, and at martensitic finish temperature. The γ → α′ martensitic transformation is displacive in nature, where the FCC structure (austenite) transforms into a BCT structure (α′-martensite) during the cooling phase cause an increase in volume, as shown in deformed shape (Fig. 5.64) (Moyer and Ansell, 1975). The red color zone signifies a fully martensitic phase, whereas the light green band exhibits a partially transformed region followed by a blue non-transformed region. Since the scanned contour (left) is captured at a temperature between Ms and Mf temperature (i.e., ~350 °C (W1); ~280 °C (W2, W3, and W4)), a partially transformed zone appears. It is presumed that the partially transformed zone is composed of α′-martensite and γ-phase. Mixed phase fraction transforms into fully martensitic phase, as the temperature reaches Mf as shown in in the right side (2nd column) of Fig. 5.64.

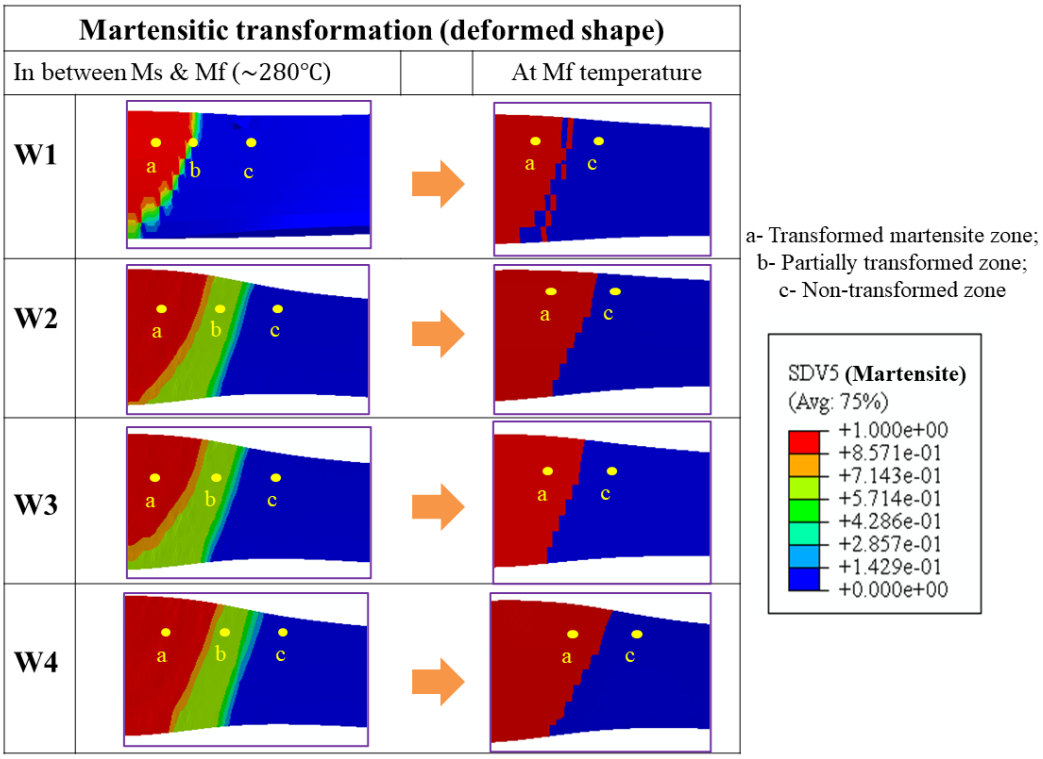

Fig. 5.64 2D distribution of martensitic phase fraction accomplished during cooling cycle

Fig. 5.65 demonstrates the graphical development of $\gamma \rightarrow \alpha'$ martensitic transformation with temperature during cooling stage. As the molten metal attains Ms temperature, i.e., 350 ℃ (case W4) during solidification, decomposition of austenite and subsequent development of martensite takes place. As the weld pad cools beyond the Ms temperature, martensitic phase fraction increases significantly and achieves fully martensitic fraction near the weld center line. It is noteworthy that every weld pad attains 100% martensite at nearby location of weld line. However, phase fraction decreases gradually beyond a distance; of 3.5 mm for W1 and of 6 mm for W2, W3 and W4 from weld center line as indicated in Fig. 5.65. As presented in Table 5.6, weld metal W4 possesses the lowest Ms temperature. It is evident that ~ 98 % martensite up to temperature of 204 ℃ and remaining 2 % as retained austenite phases is observed for weld metal W4. However, for case W1 where martensitic transformation takes place at relatively higher temperature, martensitic fraction is found to be 90 %. Weld metal W3 and W2 shows higher Ms as compared to W4, achieved 50 % of martensitic phase fraction at the temperature 330 ℃ and 335 ℃ whereas W1 and W4 at 380 ℃ and 320 ℃ respectively. It is reported that 100 % martensite can be possible by air cooling in P91 steel (Pandey et al., 2018; Santella et al., 2001).

However, the maximum martensitic phase fraction attained by W3 and W2 are 94 % and 96 % respectively, while corresponding retained austenitic fraction is 6 % and 4 %, respectively at room temperature. Therefore, it emphasizes that the martensitic phase fraction increases from 94 % → 98 % for specimen W3 → W4 and 96 % → 98 % for specimen W2 → W4 upon decreasing martensitic transformation temperature accompanied by proliferation of austenitic stabilizing. In order to inhibit exhaustion of transformation prior to ambient temperature, the Ms temperature should be maintained low. Therefore, through the progressive growth of austenitic stabilizer for samples W1 to W4, it is affirmed that Ms temperature extensively decreases. Low temperature martensitic transformation renders great change in chemical driving force for transition from austenite to martensite which results in larger volumetric dilation (i.e., higher magnitude of relative change of length) within FZ and HAZ caused generation of higher martensitic phase fraction. Hence, martensitic phase fraction is found to be highest for Case W4. Otherwise, at high temperature martensitic transformation, thermal contraction exhibits agglomeration of tensile stress as the weld continues to cool after transformation is exhausted. Hence, low martensitic phase fraction with tensile residual stress pattern is observed for weldment W1. Similarly, some other authors also stated that increasing volume fraction of martensite favours the reduction of tensile residual stress owing to volumetric expansion and promotes compressive residual stress generation in their study (Cottam et al., 2014; Pandey et al., 2018). However, this approach is found to be extensively invalid for the case W2 and W3. Although transformation temperature decreases for W2 → W3, phase fraction decreases as well. There might be dominance of other factor which is being dealt in further section.

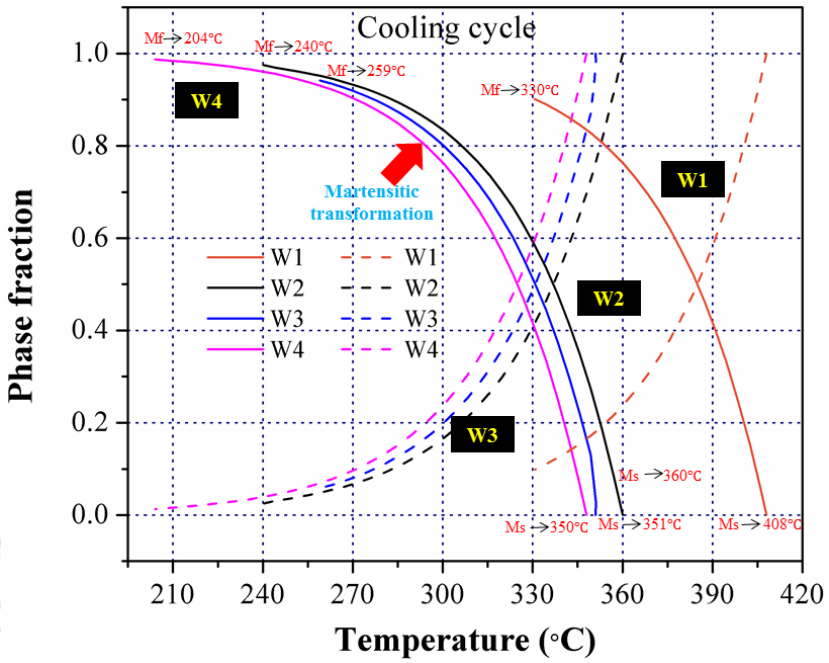

Fig. 5.65 Growth of α′-martensitic phase fraction with temperature at far away location (W1 ~3.5 mm and W2=W3=W4= 6 mm) from weld line

5.6.6 Residual stress with weld compositions

Comparison of FE based residual stress distribution and experimental results are shown in Fig.5.66a. The magnitude of predicted residual stress value appears to be marginally higher, i.e., variation of 55 MPa for W1, 15 MPa for W2 and W3, and 40 MPa for W4 is observed. Negligence of microstructural model, TRIP effect, transformation effect on yield strength might be the probable reasons for this discrepancy. Even though significant expansion is observed during martensitic transformation for weld metal W1, tensile stress is obtained unlike W4. Lattice parameter of martensite in W4 weld metal is higher compared to W1 weld metal. This suggested that W4 weld metal expands and it would get resisted by the base metal resulting compressive residual stress in this weld metal. Jiang et al. (Jiang et al., 2018) reported that residual stress state progressively move into tensile with increasing martensitic transformation temperature. In addition, Payares-Asprino et al. (Payares-Asprino et al., 2008) indicated that high martensitic transformation temperature reduces the influence of transformation induced compressive stress development. The 2D contour plot of residual stress distribution in the cross

section of W4 (top) and W1 (bottom) are shown in Fig. 5.66b. Compressive residual stress is rendered by blue band while red band signifies tensile stress. In order to clarify the influence of welding process for a given composition, residual stress evolution in W4 weld metal where austenite stabilising elements are highest, modeling is performed incorporating EBW process parameters, whereas for weld metal W1 where the austenitic stabilizing composition is low, modeling is carried out considering SMAW process parameters. Obtained result is presented in Fig. 5.66c. Despite change in welding technique, the state of stress remains as compressive. This suggest that the variation in residual stress for different weldments occurs owing to variations in transformation temperature caused by change in composition and transformation induced strain, irrespective of change in cooling rate or welding process. Furthermore, it is notified that the difference between Ms and Mf temperature is highly related to the evolution of residual stress as revealed in Fig. 5.66d. It signifies that, the magnitude of compressive residual stress progressively increases, i.e., W3<W2<W4 with the difference between Ms and Mf temperature, i.e., 92 ℃<105 ℃<146 ℃. It manifests wider range of martensitic transformation (Santella et al., 2001). This could be another factor by which weld metal W2 renders more compressive stress than W3. Carbon is a strong austenite stabilizing element as well has significantly influence on BCT lattice strain (Bhadeshia, 2013). However, Fig. 5.66d confirms that it does not have any significant influence in residual stress evolution. Presence of carbon content in similar range (Table 3.8) for different weld metals may be the probable explanation for insignificant variation of residual stress with or without carbon containing weld metal.

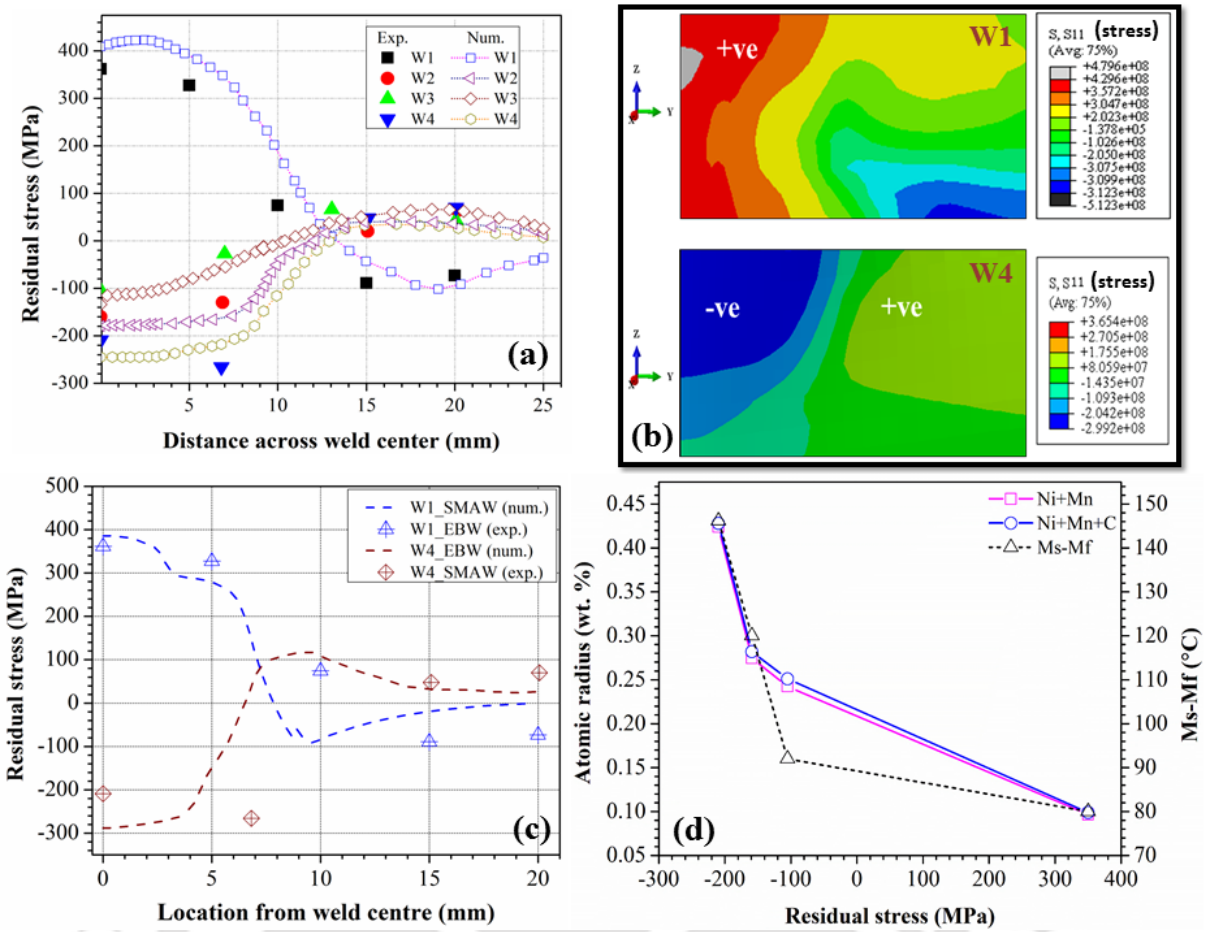

Fig. 5.66 (a) Comparison of experimental and numerical distribution of residual stress, (b) contour plot of longitudinal (S11) residual stress distribution, (c) depiction of residual stress distribution in weld metal W4 for SMAW and EBW, and (d) illustration of residual stress as a function of Ms-Mf and alloying elements

5.7 Summary

Nd:YAG pulse laser welding of dual phase Ti-alloy in butt joint configuration is studied with regard to the macroscopic residual stress distribution and associated deformation patterns at two different boundary conditions in which phase transformation effect is incorporated. The conclusions for the present investigation are summarized as follows: Satisfactory agreement has been found out on weld pool size and shape between numerically predicted and experimentally measured results. Robustness of the established model is confirmed by estimating average error

of ~ 12 % in FZ and ~ 10 % in HAZ profile. The apex temperature reached to ~ 3100 K which is quite lower than the boiling temperature and pulsation effect is progressively diminishes farther away from the weld center line. The maximum rate of change of temperature in transverse direction is found as ~ 3550 K/s. The relative stability of $\alpha \rightarrow \beta$ transformation during heating cycle favors significant martensitic transformation. Hence, it can be concluded that ultimately martensitic transformation contributes alteration of the state of residual strain or stress. Martensitic phase fraction at 0.75 mm across the weld line is found as ~ 92 %. Content of martensitic morphology decreases further away from the weld line significantly. The material diffusion in this region is limited which favors combined diffusional-displacive (i.e., β-phase + martensitic) mode of phase transformation. The residual stress during martensitic transformation could be tensile or compressive depending upon expansion accompanied by $\beta \rightarrow \alpha'$ transformation. Generation of compressive longitudinal residual stress due to phase transformation effect can minimize the overall acquired tensile stress in welded structure as observed in case 3. However, the distribution of transverse residual stress is contrary to longitudinal stress. When martensitic start temperature attains during cooling cycle, the acquired tensile stress (in case 1) starts to decrease because volumetric expansion takes place due to $\beta \rightarrow \alpha'$ martensitic transformation. If martensitic volume fraction further increases, the longitudinal stress decreases more and even change its nature from tensile to compressive. As the number of mechanical constraint increases, the probability of getting higher magnitude of residual stress is more whereas the effective distortion may decrease. The mechanical constraint obstructs the deformation of weldment during expansion and contraction of weld zone, due to which plastic strain induced in the structure. This induced strain retains within the material and plays significant role in the generation of relatively higher residual stress.

Continuous and pulse mode of laser welding of 800 μm thin sheet Ti6Al4V alloy are performed under various welding conditions. The interrelation between the thermal history and metallurgical findings is demonstrated at FZ and HAZ with the aid of finite element based heat transfer model. Based on the present study, the following conclusions are inferred. The level of shielding during welding is estimated through surface discoloration technique. Silver color bead appearance indicates the lowest contamination for the specimen fabricated at a minimum heat input of 12 J/mm in pulse mode, whereas, blue bead appearance implies higher contamination for 80 J/mm. Welded joint fabricated at the highest heat input characterized by low cooling rate

shows the maximum average roughness of 10.2 μm, whereas minimum average roughness ~2 μm is obtained at the lowest heat input. Full-depth of penetration with minimum bead dimension is obtained at a lower heat input of 12, and 19.6 J mm, and pulse frequency of 8 Hz. Conduction mode of heat transfer prevails in continuous laser welding whereas keyhole mode prevails for pulse laser welding. Both pulse and continuous mode laser welding reveal the mixed mode of transformation, which comprises of $\alpha' + \alpha$ phases. However, α'-martensite is found to be high in pulse condition, whereas α-phase contributes a significant fraction in continuous mode. Peak shift and peak broadening indicate a considerable change in lattice constant, i.e., bcc ↔ hcp in FZ. Microstructure of FZ consists of plate α'-martensite within the coarse β-grain for all conditions except the weldments performed at a heat input of 12 and 19.6 J / mm in pulse mode. However, needle-shape acicular α' martensite within the fine β-grain is observed for these two specimens. Tensile strength of 1138 MPa with elongation of 15.5% is achieved for the weld metal that possesses very fine α'-lath of length and thickness, 11.5 μm, and 415 nm, respectively by incorporating pulsation effect. Presence of contamination and lack of penetration, are other decisive considerations that affect thermo-mechanical performance of coalesced joints as well. The influence of diffusionless martensitic transformation on the development of residual stress and microstructural evolution in the course of pulse and continuous mode of welding is studied, for thin sheets (~800 μm) of Ti6Al4V alloy. It can be concluded that the pulsation effect drastically triggered the metallurgical behavior which reduces residual stress magnitude and distribution. Non-uniform thermal gradients modify the lattice parameter which results in peak shift and lattice parameter change induces microstrain within the substrate that promotes peak broadening. Volumetric expansion accompanied with solid state phase change from $\beta \rightarrow \alpha'$, exhibits diffusionless transformation. Lowest heat input 12 J/mm and assisted significant diffusionless transformation during cooling stage favours minimization of tensile residual stress and even changes its nature to compressive by achieving 96% of martensite phase. Despite of being transformed into martensite, pulse weld metal acquired very fine acicular structure martensite whereas continuous weld exhibited lamellar structured α'-martensite by virtue of variation in heat input. Lamellar structured α'-martensite within coarsened prior-β grain boundary is relatively softer and its increasing phase fraction promotes tensile residual stress generation whereas increasing acicular α'-martensite at significant high cooling rate favours the reduction of residual stress.

Fiber laser welding of SS304 is investigated by finite element-based thermo-mechanical model, including the effect of solid-state phase transformation. The influence of the microstructure on the residual stress development and corresponding mechanical properties are studied. The major conclusions are derived from the present investigation are detailed as follows: The estimated value of $[Cr_{eq.}]$ / $[Ni_{eq.}]$ as 1.69 confirms the FA mode of solidification where the dual-phase microstructure is composed of skeletal and lathy δ-ferrite with an austenitic matrix. The maximum δ-ferrite of 12% is found at the lowest heat input of 45 J/mm, whereas 7-8% is observed at the maximum heat input of 75 J/mm. These predictions are well agreed with the Schaffler-Delong equilibrium diagram and show the robustness of the developed metallurgical model. When the content of skeletal δ-ferrite increases, lathy δ-ferrite decreases with an increase in heat input from 45 to 75 J/mm. The average dendrite thickness changes from 484 nm to 927 nm, and inter-dendritic spacing increases from 3 μm to 6 μm. The maximum joint efficiency of 103% is apparent for the minimum heat input of 45 J/mm attributed to the very fine dendritic size and minimum inter-dendritic spacing. The high thermal expansion coefficient of Ni relative to Cr promotes tensile strain in the γ-austenitic phase and results in the compressive strain at the δ-ferrite rich dendritic core. The propagation of δ-ferrite accomplished by low heat input with enriched Cr and lean Ni content causes compressive strain. With a reduction in heat input from 75 to 45 J/mm, overall tensile longitudinal stress reduces to 245 MPa (less than yield stress), and the transverse residual stress changes from tensile to compressive. Fine δ-ferrite morphology with minimum inter-` dendritic spacing possessed at minimum heat input aids in mitigating the residual stress.

Residual stress evolutions in the 9Cr steel weld metals with varied austenitic stabilizing compositions are discussed. A thermo-metallurgical-mechanical model is developed to incorporate the phase transformation effect. Influence of several metallurgical factors such as volumetric changes, amount of austenitic stabilizer, Ms and Mf, temperature and phase fraction, on residual stress is systematically studied. The conclusions drawn on the basis of present investigation are discussed here: the developed thermo-mechanical model including metallurgical characteristics for different austenitic stabilizing compositions using SDV approach predicted residual stress pattern, is in good correspondence with experimental outcome. Relative stability of austenitic transformation can trigger martensitic transformation at a

particular temperature field. Weld metal with an enriched austenitic stabilizing composition renders minimal AC1 temperature, highly stable γ-austenite phase and higher martensitic phase fraction. Reduced austenitic stabilizing elements increases Ms and Mf transformation temperature. Higher martensitic transformation temperature favours tensile driven residual stress despite attending sufficient lattice expansion. Ms-Mf, recognized as another important factor for the alteration of residual stress as well. At its minimum value, higher magnitude of tensile residual stress is produced low Ni+Mn+C containing weld metal whereas compressive residual stress is attained weld metal containing higher austenite stabilizing elements. Higher lattice stain gives higher resistance force during martensitic transformation resulting reduced lath size in weld metal containing highest austenite stabilising elements. Enrichment of austenitic stabilizing element (Ni+Mn+C+N) plays deterministic role for the accomplishment of martensitic transformation. Increased lattice strain with increasing austenite stabilizing element and, lower Ms and Mf temperature introduces compressive residual stress in the weld metal.

Chapter 6

6.0 Conclusions and Scope of Future Work

6.1 Introduction

The important conclusions that are drawn from the present studies executed using different experimental set-up and numerical tools as a part of the thesis work are summarized in this chapter. The application domain and possible expansion of the present work is exclusively discussed herein. The principal deed of the present study relies on the development of a sequential coupled thermal-metallurgical-mechanical (TMM) model using finite element based commercial software, which is capable of undertaking the effect of current pulsation, diffusional or non-diffusional phase transformation kinetics, volumetric dilation, and cooling rate during linear welding process for the adequate prediction of temperature, residual stress and distortion pattern. The undesirable tensile residual stress that inevitably induces within welded structure facilitates failure of structure prior to its service life. Therefore, the nature of residual stress and the influence of metallurgical attributes on residual stress distribution and mechanical properties for Ti6Al4V, austenitic stainless steel, ferritic-martensitic steel are investigated here. However, the thermo-chemical reactions that emerge between the weld pool and working atmosphere essentially affect the weld metal properties and weld joint quality. Therefore, the surface quality in a laser-welded structure is also assessed in the present study. In the current work, Nd:YAG laser is used in pulse mode, and Yb-fiber laser is used in continuous mode to weld thin sheet Ti6Al4V and SS304 stainless steel. In addition, the shielded metal arc welding (SMAW) process and electron beam welding (EBW) technique are implemented to weld thick 9Cr-Mo steel alloy.

6.2 Conclusions

The following conclusions are drawn in the course of surveying literatures, performing the experiments, and developing the computational model on fusion welding processes. The special emphasis is vested on to the development of phase transformation kinetics model from experiments and implementation of the same in a FE based thermo-mechanical model for better prediction of residual stress distribution.

- It is understood that a rigorous thermal, metallurgical, and mechanical analysis is of significant help in understanding the solid-state phase transformation and associated microstructural evolution, which leads to alteration of residual stress distribution. Preliminary attempt made by researchers were empirical and analytical, which had considerable limitations from the context of general use and reliability. The present numerical model for the estimation of welding induced residual stress and distortion have demonstrated a promising outcome by undertaking most of the realistic phenomena that arise in real-time weld design.
- The most practical approach is adopted for the evaluation of residual stress distribution under various parametric conditions by establishing a TMM model with a phase transformation effect. The quantitative estimation of time-temperature history, cooling rate, residual stress, and associated distortion is indispensable to estimate the final weld bead geometries, resulting microstructure, solidification morphology, phase fraction estimation, and mechanical behaviour of the welded joints.
- The investigation is carried out on laser welding of Ti6Al4V alloy, austenitic stainless steel. Besides, SMA welding and EBW of ferritic-martensitic steel are also performed. The formation of oxides and other contamination is prevalent at the weld zone that deteriorates weld joint quality. Thus, the surface discoloration technique is found to be an effective tool, especially for Ti6Al4V alloy by which contamination level is analysed through visual inspection. It is obvious that achievement of better surface finish is one of the primitive conditions, specifically for Ti-alloy, to accomplish quality weld.
- Heat input is the most influential parameter to obtain stable welding. If welding velocity increases, power shifts towards low heat input and facilitates high cooling rate condition. The

weld dimension increases with heat input resulting from the increasing volume of molten metal.

- In laser welding of Ti-alloy, the fusion zone is mainly composed of α'-martensite with prior β-phase because the cooling rate is greater than the critical value, i.e., 400 K/s. The presence of martensitic structure greatly contributes to the mechanical properties of the weld joint. With further increases in heat input, lamellar α growth takes place, which lowers the strength. Overall, the heat input must be kept optimum for better mechanical properties. The microhardness of the molten zone is higher than that of base metal as a result of α' martensitic formation.
- The microstructure and its morphology of Ti6Al4V alloy is very much sensitive to cooling rate. In case of austenitic stainless steel, microstructural evolution is substantially controlled by the ferrite stabilizer (Cr) and austenitic stabilizer (Ni) and their equivalent ratio decides the morphology at the weld zone. On the contrary, critical temperature, i.e., Ac1, Ac3, Ms and Mf, depending upon austenitic stabilizing elements, primarily determines the transformation kinetics for 9Cr-Mo steel. In the present work, either diffusional or non-diffusional transformation kinetics is considered for accurate prediction of the residual stress distribution in three different alloy systems.
- The diffusional transformation of Ti-alloy weldment is characterized by nucleation and growth mechanism, and non-diffusional phase transformation depends on cooling rate followed below β-transus temperature. The weldment of stainless steel is assumed only diffusional growth of γ-austenite against δ-ferrite decomposition below solidus temperature. Besides, P91 steel alloy possessed diffusionless transformation accompanied by martensite formation during the cooling stage.
- SSPT during a heating cycle has an insignificant role in the alteration of residual stress. When the phase change during heating stage triggers the martensitic transformation, it predominantly affects the stress pattern. In Ti-alloy, $\alpha \rightarrow \beta$ transformation during the heating cycle allows β-phase growth by diffusional migration in dual phase, i.e., α/β matrix and attained equilibrium state beyond β-transus temperature. On the other hand, increasing austenitic stabilizing elements offer relatively more stable austenite leads to high lattice expansion caused by lowering of martensitic transformation temperature. Hence, highly

strained martensite lath or enriched martensitic phase in P91 steel weldment is observed. However, there is insignificant SSPT is noticed for stainless steel at the heating stage.

- Volumetric expansion accompanied with solid-state phase change from $\beta \rightarrow \alpha'$ (Ti-6Al-4V alloy) or $\gamma \rightarrow \alpha'$ (P91 steel) exhibits diffusionless transformation that change the crystallographic structure to HCP (Ti-alloy) and BCT (P91 steel). The change is associated with an expansion state, leading to compressive stress generation and mitigate overall tensile residual state.
- The austenitic stainless exhibits only diffusional transformation below solidus temperature. The retained δ-ferrite due to incomplete $\delta \rightarrow \gamma$ transformation induced compressive microstrain within the molten zone can effectively release overall tensile stress to some extent. However, the austenitic phase primarily contributes a tensile residual stress at fusion zone.
- Coarse grain morphology, i.e., thick α'-lath within coarse prior β-grain boundary (Ti-alloy) or lathy δ-ferrite (stainless steel), promotes tensile residual stress state caused by deformation incompatibility around the lamellae interface or grain boundary or due to higher localized stress field as a result of heterogeneous microstructure. While fine δ-ferrite lath or acicular α'-martensite lath attributes less heterogeneity within weld zone microstructure.
- It is experienced that modification in lattice parameters owing to non-uniform temperature gradient during welding phenomena can be analyzed as peak shifting characteristics in the X-ray diffraction pattern. Additionally, this aberration results in strain induction within the welded structure causes peak broadening.
- It is evident that small grain size as well as fine morphology improves the overall mechanical performance of welded joint that can be attained by keeping heat input as minimal as possible. Current pulsation is an effective way of grain refinement associated with a reduction in HAZ and high cooling rate. It also changes the state of stress from tensile to compressive as for Ti6Al4V weldment in the present work.
- In welding of P91steel, enrichment of austenitic stabilizer possesses highly stable austenite that imparts very high lattice strain or volumetric expansion within the molten zone. Therefore, the weld surface experiences sufficiently high compressive strain as a result compressive residual stress evolves. A range of martensitic transformation temperature, i.e., Ms-Mf, could be another influencing parameter that contributes to residual stress alteration.

- Finally, the calculation technique and quantitative knowledge extracted from this research work in the fusion welding process will be expected to serve as a basis for the regulation of residual stress with more reliability in a laser welding system.

6.3 Application potential and scope of future work

Some of the essential attributes are worthwhile to investigate further and expected to be the future scope of work for the expansion of its application potential.

- An investigation related to the influence of major alloying elements on the transformation temperature and phase change effect can be a future scope of work specifically for Ti6Al4V alloy. This can be achieved through experimental and numerical investigation in such a way that it can be answered how it acts on residual stress distribution and mechanical performance of the components.
- It is obvious that the microstructural development and its morphological features significantly triggers the residual stress and mechanical performance of the welded structure. The implication of microstructural model in structural analysis is not yet examined extensively; hence, it needs to be explored especially for Ti-alloy.
- Appropriate prediction of residual stress within the structure is still a challenging task. Few crucial strain components have not been included in modelling approaches. The material model can be improved by creep strain, visco-elasto-plastic strain, transformation induced plasticity (TRIP) strain, etc. Especially, the TRIP strain that comes into existence due to the appearance of varied phases during phase transformation extensively influences the residual stress pattern. Therefore, the mechanism of its origination and influence on structural integrity is the area of interest for Ti-alloy.
- It is obvious that predominant dislocation densities and stacking fault favour relaxation of invariant strain, which in turns influences the morphology and induced stress in components. The investigation of the status of dislocation density in a localized space and the correlation between dislocation density and stacking fault energy can be explored experimentally to capture Type III residual stress components.

- In the current research work, TMM model is developed for fusion welding process using numerical modelling technique via mathematical tool ABAQUS. However, in order to determine the robustness of developed model and appropriateness of applied methodologies, it is essential to develop TMM model using analytical approach and comparative study between them is need be explored.

Appendix A: Heat source models

Double Ellipsoidal heat source model

Goldak (1984) proposed a double-ellipsoidal heat source model to account linear fusion welding process. The volumetric heat flux density distribution in the front ellipsoid is expressed as

$$q_f(x,y,z) = \frac{6\sqrt{3}(f_f Q)}{cba_f\pi\sqrt{\pi}} \exp\left(\frac{-3x^2}{a_f{}^2} - \frac{3y^2}{b^2} - \frac{3z^2}{c^2}\right), \qquad y \geq 0 \tag{A1}$$

where f_f is weighting fraction of heat deposition in front ellipse.

Total heat energy is expressed as

$$2\iiint_0^\infty q_f(x,y,z)\,dx\,dy\,dz = \frac{6\sqrt{3}(f_f Q)}{cba_f\pi\sqrt{\pi}} \int_0^\infty \exp\left(-\frac{3x^2}{a_f{}^2}\right) dx \int_0^\infty \exp\left(-\frac{3y^2}{b^2}\right) dy \int_0^\infty \exp\left(-\frac{3y^2}{c^2}\right) dz$$

$$= 2\,\frac{6\sqrt{3}(f_f Q)}{cba_f\pi\sqrt{\pi}}\,\frac{a_f}{\sqrt{3}}\,\frac{\sqrt{\pi}}{2}\,\frac{b}{\sqrt{3}}\,\frac{\sqrt{\pi}}{2}\,\frac{c}{\sqrt{3}}\,\frac{\sqrt{\pi}}{2} = \frac{1}{2}\,(f_f Q) \tag{A2}$$

Similarly, for the rear ellipse, the heat flux intensity is expressed as

$$q_r(x,y,z) = \frac{6\sqrt{3}(f_r Q)}{cba_r\pi\sqrt{\pi}} \exp\left(\frac{-3x^2}{a_r{}^2} - \frac{3y^2}{b^2} - \frac{3z^2}{c^2}\right), \qquad y < 0 \tag{A3}$$

where f_r is weighting fraction of heat distribution in rear ellipse.

$$2\iiint_0^\infty q_f(x,y,z)\,dx\,dy\,dz = \frac{1}{2}\,(f_r Q) \qquad y < 0 \tag{A4}$$

$$Q = \frac{1}{2}\,(f_f Q) + \frac{1}{2}\,(f_r Q) = \frac{1}{2} Q((f_f + f_r) \tag{A5}$$

Therefore, the fractional heat maintains the relation

$$f_f + f_r = 2 \tag{A6}$$

Hourglass heat source model

The heat intensity distribution for a laser heat source at any plane of Cartesian coordinate system perpendicular to the Z-axis is expressed as:

$$\dot{Q}(Z, r) = q_* \exp\left[-d\frac{r^2}{r_{eff}{}^2}\right] \quad \text{(A7)}$$

where q_* is maximum heat flux in the center of laser heat source, r_{eff} is effective radius of laser beam, d denotes power density distribution factor, and r is radial co-ordinate.

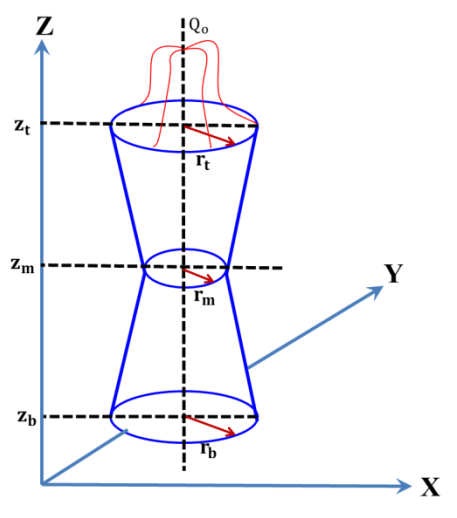

Fig. A1 Schematic representation of Hourglass heat source model.

For the Upper truncated cone,

$$\frac{r_{eff}-r_m}{r_t-r_m} = \frac{Z_o-Z_m}{Z_t-Z_m} \quad \text{(A8)}$$

$$r_{eff} = \frac{Z_o-Z_m}{Z_t-Z_m}(r_t - r_m) + r_m \quad \text{(A9)}$$

While, for the Lower truncated cone,

$$r_{eff} = \frac{Z_o-Z_b}{Z_m-Z_b}(r_b - r_m) + r_m \quad \text{(A10)}$$

Now, from energy conservation theory,

$$\eta P_{laser} = \int_0^H \int_0^{2\pi} \int_0^{r_{eff}} \dot{Q}(Z,r)\, r\, dr\, d\theta\, dh = \int_0^H \int_0^{2\pi} \int_0^{r_{eff}} \frac{\alpha dP}{\pi {r_{eff}}^2} \exp\left[-d\frac{r^2}{{r_{eff}}^2}\right] r\, dr\, d\theta\, dh$$

$$= \int_0^H \int_0^{2\pi} \int_0^{r_o} q_o \exp\left[-d\frac{r^2}{{r_{eff}}^2}\right] r\, dr\, d\theta\, dh \quad \text{(A11)}$$

where, P_{laser} is laser power and η represents the efficiency of laser source.

Applying 1st integration in Eq. A11

$$\int_0^{r_{eff}} q_o \exp\left[-d\frac{r^2}{{r_{eff}}^2}\right] r\, dr = \frac{-q_o {r_{eff}}^2}{2d}[\exp(-d) - 1] = \frac{q_o {r_{eff}}^2}{2d}[1 - \exp(-d)] \quad \text{(A12)}$$

Therefore, Eq. A11 is substituted as

$$\int_0^H \int_0^{2\pi} \frac{q_o {r_{eff}}^2}{2d}[1 - \exp(-d)]\, d\theta\, dh = \frac{q_o \pi}{d}[1 - \exp(-d)] \int_0^H {r_{eff}}^2 dh \quad \text{(A13)}$$

For the Upper truncated cone,

$${r_{eff}}^2 = \left[\frac{Z_o - Z_m}{Z_t - Z_m}(r_t - r_m) + r_m\right]^2 \quad \text{(A14)}$$

For simplification, we put: $h = Z_o - Z_m$ and $H = Z_t - Z_m$, then Eq. (A14) becomes

$${r_{eff}}^2 = \left[\frac{h}{H}(r_t - r_m) + r_m\right]^2 = \frac{[H.r_m + h.r_t - h.r_m]^2}{H^2}$$

$$= \frac{[H^2.{r_m}^2 + h^2.{r_t}^2 + h^2.{r_m}^2 + 2.H.h.r_m.r_t - 2.h^2.r_m.r_t - 2.H.h.{r_m}^2]}{H^2} \quad \text{(A15)}$$

Thus, for the upper truncated cone,

$$\int_0^H {r_{eff}}^2 dh = \int_0^H \frac{[H^2.{r_m}^2 + h^2.{r_t}^2 + h^2.{r_m}^2 + 2.H.h.r_m.r_t - 2.h^2.r_m.r_t - 2.H.h.{r_m}^2]}{H^2} dh = \frac{H[{r_m}^2 + r_m.r_t + {r_t}^2]}{3} \quad \text{(A16)}$$

Therefore, we rewrite eq. (A11) as

$$\eta P_{laser} = \frac{q_o \pi}{d}[1 - \exp(-d)]\frac{H[r_m{}^2 + r_m.r_t + r_t{}^2]}{3} \quad \text{(A17)}$$

Thus,

$$q_* = \frac{3d\eta P_{laser}}{\pi.[1-\exp(-d)].H[r_m{}^2 + r_m.r_t + r_t{}^2]} \quad \text{(A18)}$$

Now overall, Eq. A7 is rewritten as:

$$\dot{Q}(Z, r) = \frac{3d\eta P}{\pi.[1-\exp(-d)].(Z_t - Z_m)[r_m{}^2 + r_m.r_t + r_t{}^2]} \exp\left[-d\frac{r^2}{r_{eff}{}^2}\right]; \quad \text{if } (Zo \geq Zm) \quad \text{(A19)}$$

$$\dot{Q}(Z, r) = \frac{3d\eta P}{\pi.[1-\exp(-d)].(Z_m - Z_b)[r_m{}^2 + r_m.r_t + r_t{}^2]} \exp\left[-d\frac{r^2}{r_{eff}{}^2}\right]; \quad \text{if } (Zo < Zm) \quad \text{(A20)}$$

References

Abe, F., 2001. Creep rates and strengthening mechanisms in tungsten-strengthened 9Cr steels. Materials Science and Engineering: A 319, 770–773.

Abid, M., Siddique, M., 2005. Numerical simulation of the effect of constraints on welding deformations and residual stresses in a pipe–flange joint. Modelling and Simulation in Materials Science and Engineering 13, 919–933.

AF, Pordilha, PR, Rios, 2002. Decomposition of austenite in austenitic stainless steels. ISIJ international 42, 325–327.

Ahmed, T., Rack, H.J., 1998. Phase transformations during cooling in α+ β titanium alloys. Materials Science and Engineering: A 243, 206–211.

Ahn, J., He, E., Chen, L., Wimpory, R.C., Dear, J.P., Davies, C.M., 2017. Prediction and measurement of residual stresses and distortions in fibre laser welded Ti-6Al-4V considering phase transformation. Materials & Design 115, 441–457.

Albert, S.K., Laha, K., Bhaduri, A.K., Jayakumar, T., Rajendrakumar, E., 2016. Development of IN-RAFM steel and fabrication technologies for Indian TBM. Fusion Engineering and Design 109, 1422–1431.

Alipooramirabad, H., Ghomashchi, R., Paradowska, A., Reid, M., 2016. Residual stress-microstructure-mechanical property interrelationships in multipass HSLA steel welds. Journal of Materials Processing Technology 231, 456–467.

Argyris, J.H., Szimmat, J., Willam, K.J., 1982. Computational aspects of welding stress analysis. Computer Methods in Applied Mechanics and Engineering 33, 635–665.

Arnberg, L., Chai, G., Backerud, L., 1993. Determination of dendritic coherency in solidifying melts by rheological measurements. Materials Science and Engineering: A 173, 101–103.

Asoka-Kumar, P., Lynn, K.G., Welch, D.O., 1994. Characterization of defects in Si and SiO2- Si using positrons. Journal of Applied Physics 76, 4935–4982.

Assuncao, E., Williams, S., Yapp, D., 2012. Interaction time and beam diameter effects on the conduction mode limit. Optics and Lasers in Engineering 50, 823–828.

ASTM Int, ASTM E384, Standard Test Method for Knoop and Vickers Hardness of Materials. ASTM Stand, 2012, p 1–43.

ASTM Standard E8/E8m, Standard Test Methods for Tension Testing of Metallic Materials. ASTM International, 2008, p 743–746.

ASTM Int, ASTM A1033, Practice for quantitative measurement and reporting of hypoeutectoid carbon and low-alloy steel phase transformations', ASTM International, Philadelphia, PA, USA, 2010.

ASTM Int, ASTM E2142-01, Standard test methods for rating and classifying inclusions in steel using the scanning electron microscope, in Annual book of ASTM standards, Vol. 03.01, West Conshohocken, PA, 2008.

ASTM International, ASTM E407-07, Standard Practice for Microetching Metals and Alloys (ASTM International, West Conshohocken, PA), 2015.

ASTM International, ASTM B946, Standard Test Method for Surface Finish of Powder Metallurgy (PM) Products (ASTM International, West Conshohocken, PA), 2011.

ASTM International, ASTM E975, Standard Practice for X-Ray Determination of Retained Austenite in Steel with Near Random Crystallographic Orientation (ASTM International, West Conshohocken, PA), 2013.

Avrami, M., 1940. Kinetics of phase change. II transformation-time relations for random distribution of nuclei. The Journal of chemical physics 8, 212–224.

Azarniya, A., Colera, X.G., Mirzaali, M.J., Sovizi, S., Bartolomeu, F., Wits, W.W., Yap, C.Y., Ahn, J., Miranda, G., Silva, F.S., 2019. Additive manufacturing of Ti–6Al–4V parts through laser metal deposition (LMD): Process, microstructure, and mechanical properties. Journal of Alloys and Compounds 804, 163–191.

Bag, S., De, A., 2008. Development of a three-dimensional heat-transfer model for the gas tungsten arc welding process using the finite element method coupled with a genetic algorithm–based identification of uncertain input parameters. Metallurgical and Materials Transactions A 39, 2698–2710.

Bag, S., Kiran, D.V., Syed, A.A., De, A., 2012. Efficient estimation of volumetric heat source in fusion welding process simulation. Welding in the World 56, 88–97.

Bag, S., Trivedi, A., De, A., 2008. Use of a multivariate optimization algorithm to develop a self-consistent numerical heat transfer model for laser spot welding. The International Journal of Advanced Manufacturing Technology 38, 575.

Bajpei, T., Chelladurai, H., Ansari, M.Z., 2017. Experimental investigation and numerical analyses of residual stresses and distortions in GMA welding of thin dissimilar AA5052-AA6061 plates. Journal of Manufacturing Processes 25, 340–350.

Balasubramanian, T.S., Balakrishnan, M., Balasubramanian, V., Manickam, M.A.M., 2011. Influence of welding processes on microstructure, tensile and impact properties of Ti-6Al-4V alloy joints. Transactions of Nonferrous Metals Society of China 21, 1253–1262.

Balmforth, M.C., Lippold, J.C., 2000. A new ferritic-martensitic stainless steel constitution diagram. Welding Journal 79, 339s–345s.

Banerjee, S., Mukhopadhyay, P., 2010. Phase Transformations: Examples from Titanium and Zirconium Alloys. Elsevier.

Bansal, A., Sharma, A.K., Das, S., Kumar, P., 2016. On microstructure and strength properties of microwave welded Inconel 718/stainless steel (SS-316L). Proceedings of the Institution of Mechanical Engineers, Part L: Journal of Materials: Design and Applications 230, 939–948.

Barriobero-Vila, P., Requena, G., Buslaps, T., Alfeld, M., Boesenberg, U., 2015. Role of element partitioning on the α–β phase transformation kinetics of a bi-modal Ti–6Al–6V–2Sn alloy during continuous heating. Journal of Alloys and Compounds 626, 330–339.

Baruah, M., Bag, S., 2016. Influence of heat input in microwelding of titanium alloy by micro plasma arc. Journal of Materials Processing Technology 231, 100–112.

Baruah, M., Bag, S., 2017. Characteristic difference of thermo-mechanical behavior in plasma microwelding of steels. Welding in the World 61, 857–871.

Baruah, M., Bag, S., 2017. Influence of pulsation in thermo-mechanical analysis on laser micro-welding of Ti6Al4V alloy. Optics & Laser Technology 90, 40–51.

Becker, D.W., Adams, C.M., 1979. The role of pulsed GTA welding variables in solidification and grain refinement. Weld. J 58.

Belahcene, F., Lu, J., 1999. Study of residual stress induced in welded steel by surface longitudinal ultrasonic method, in: Society for Experimental Mechanics, Inc, Proceedings of the SEM Annual Conference on Theoretical, Experimental and Computational Mechanics(USA),. pp. 331–334.

Bennett, C.J., Attallah, M.M., Preuss, M., Shipway, P.H., Hyde, T.H., Bray, S., 2013. Finite element modeling of the inertia friction welding of dissimilar high-strength steels. Metallurgical and Materials Transactions A 44, 5054–5064.

Bhadeshia, H., 2013. Carbon in cubic and tetragonal ferrite. Philosophical Magazine 93, 3714–3725.

Bhatti, A.A., Barsoum, Z., Murakawa, H., Barsoum, I., 2015. Influence of thermo-mechanical material properties of different steel grades on welding residual stresses and angular distortion. Materials & Design (1980-2015) 65, 878–889.

Blackburn, J., 2012. Laser welding of metals for aerospace and other applications, in: Welding and Joining of Aerospace Materials. Elsevier, pp. 75–108.

Broderick, T.F., Jackson, A.G., Jones, H., Froes, F.H., 1985. The effect of cooling conditions on the microstructure of rapidly solidified Ti-6Al-4V. Metallurgical Transactions: A 16, 1951–1959.

Brown, S.B., Song, H., 1992. Implications of three-dimensional numerical simulations of welding of large structures. Welding Journal 71, 55–62.

Bru, D., 1997. Influence of material properties at high temperatures on the modelling of welding residual stress and deformation state. Mathematical Modelling of Weld Phenomena 3, 456–463.

Buffa, G., Ducato, A., Fratini, L., 2013. FEM based prediction of phase transformations during friction stir welding of Ti6Al4V titanium alloy. Materials Science and Engineering: A 581, 56–65.

Buffa, G., Ducato, A., Fratini, L., Micari, F., 2012. Numerical prediction of Biphasic Titanium Alloys Microstructure in Hot Forging Operations., in: Metal Forming. Verlag Stahleisen GmbH, pp. 135–138.

Burak, Y., YA, B., 1979. Selection of the optimum fields for preheating plates before welding.

Canas, J., Picon, R., Pariis, F., Blazquez, A., Marin, J.C., 1996. A simplified numerical analysis of residual stresses in aluminum welded plates. Computers & Structures 58, 59–69.

Cao, X., Jahazi, M., Immarigeon, J.P., Wallace, W., 2006. A review of laser welding techniques for magnesium alloys. Journal of Materials Processing Technology 171, 188–204.

Cao, X., Jahazi, M., 2009. Effect of welding speed on butt joint quality of Ti–6Al–4V alloy welded using a high-power Nd:YAG laser. Optics and Lasers in Engineering 47, 1231–1241.

Capello, E., Chiarello, P., Previtali, B., Vedani, M., 2003. Laser welding and surface treatment of a 22Cr–5Ni–3Mo duplex stainless steel. Materials Science and Engineering: A 351, 334–343.

Carmignani, C., Mares, R., Toselli, G., 1999. Transient finite element analysis of deep penetration laser welding process in a singlepass butt-welded thick steel plate. Computer Methods in Applied Mechanics and Engineering 179, 197–214.

Celada-Casero, C., Sietsma, J., Santofimia, M.J., 2019. The role of the austenite grain size in the martensitic transformation in low carbon steels. Materials & Design 167, 107625.

Chande, T., Mazumder, J., 1984. Estimating effects of processing conditions and variable properties upon pool shape, cooling rates, and absorption coefficient in laser welding. Journal of applied physics 56, 1981–1986.

Chang, W.S., Na, S.-J., 2002. A study on the prediction of the laser weld shape with varying heat source equations and the thermal distortion of a small structure in micro-joining. Journal of materials processing technology 120, 208–214.

Charles, C., 2016. Microstructure model for Ti-6Al-4V used in simulation of additive manufacturing (PhD Thesis). Lulea tekniska universitet.

Chen, L., Mi, G., Zhang, X., Wang, C., 2019. Numerical and experimental investigation on microstructure and residual stress of multi-pass hybrid laser-arc welded 316L steel. Materials & Design 168, 107653.

Chen, S.J., Jiang, F., Lu, Y.S., Zhang, Y.M., 2014. Separation of arc plasma and current in electrical arc—An initial study. Welding journal 93, 253–261.

Cheng, D.H., Huang, J., Lin, H., Zhang, H., 2009. Microstructure and mechanical analysis of Ti-6Al-4V laser butt weld joint [J]. Transactions of the China Welding Institution 30, 103–106.

Cho, S.-H., Kim, J.-W., 2002. Analysis of residual stress in carbon steel weldment incorporating phase transformations. Science and Technology of Welding and Joining 7, 212–216.

Chou, C.P., Lin, Y.C., 1992. Reduction of residual stress by parallel heat welding in small specimens of Type 304 stainless steel. Materials Science and Technology 8, 179–183.

Chuan, L., Jianxun, Z., Jing, N., 2009. Numerical and Experimental Analysis of Residual Stresses in Full-Penetration Laser Beam Welding of Ti6Al4V Alloy. Rare Metal Materials and Engineering 38, 1317–1320.

Churiaque, C., Amaya-Vazquez, M.R., Botana, F.J., Sánchez-Amaya, J.M., 2016. FEM simulation and experimental validation of LBW under conduction regime of Ti6Al4V alloy. Journal of Materials Engineering and Performance 25, 3260–3269.

Colegrove, P., Ikeagu, C., Thistlethwaite, A., Williams, S., Nagy, T., Suder, W., Steuwer, A., Pirling, T., 2009. Welding process impact on residual stress and distortion. Science and Technology of Welding and Joining 14, 717–725.

Conrad, H., 2000. Influence of an electric or magnetic field on the liquid–solid transformation in materials and on the microstructure of the solid. Materials Science and Engineering: A 287, 205–212.

Cottam, R., Luzin, V., Thorogood, K., Wong, Y.C., Brandt, M., 2014. The role of metallurgical solid state phase transformations on the formation of residual stress in laser cladding and heating, in: Materials Science Forum. Trans Tech Publ, pp. 19–24.

Criales, L.E., Özel, T., 2017. Temperature profile and melt depth in laser powder bed fusion of Ti-6Al-4V titanium alloy. Progress in Additive Manufacturing 2, 169–177.

Dai, H., Francis, J.A., Stone, H.J., Bhadeshia, H., Withers, P.J., 2008. Characterizing phase transformations and their effects on ferritic weld residual stresses with X-rays and neutrons. Metallurgical and Materials Transactions: A 39, 3070.

Dar, N.U., Qureshi, E.M., Hammouda, M.M.I., 2009. Analysis of weld-induced residual stresses and distortions in thin-walled cylinders. Journal of Mechanical Science and Technology 23, 1118–1131.

Das, C.R., Albert, S.K., Bhaduri, A.K., Srinivasan, G., Murty, B.S., 2008. Effect of prior microstructure on microstructure and mechanical properties of modified 9Cr–1Mo steel weld joints. Materials Science and Engineering: A 477, 185–192.

Das, C.R., Albert, S.K., Bhaduri, A.K., Raj, B., Swaminathan, J., Murty, B.S., 2012. Improvement in creep resistance of modified 9Cr-1Mo steel weldment by boron addition. Welding in the World 56, 10–17.

De, A., DebRoy, T., 2011. A perspective on residual stresses in welding. Science and Technology of Welding and Joining 16, 204–208.

De, A., Walsh, C.A., Maiti, S.K., Bhadeshia, H., 2003. Prediction of cooling rate and microstructure in laser spot welds. Science and technology of welding and joining 8, 391–399.

Deng, D., 2009. FEM prediction of welding residual stress and distortion in carbon steel considering phase transformation effects. Materials & Design 30, 359–366.

Deng, D., Liang, W., Murakawa, H., 2007. Determination of welding deformation in fillet-welded joint by means of numerical simulation and comparison with experimental measurements. Journal of Materials Processing Technology 183, 219–225.

Deng, D., Murakawa, H., 2006. Prediction of welding residual stress in multi-pass butt-welded modified 9Cr–1Mo steel pipe considering phase transformation effects. Computational Materials Science 37, 209–219.

Deng, D., Murakawa, H., 2008. Prediction of welding distortion and residual stress in a thin plate butt-welded joint. Computational Materials Science 43, 353–365.

Deng, D., Murakawa, H., 2013. Influence of transformation induced plasticity on simulated results of welding residual stress in low temperature transformation steel. Computational Materials Science 78, 55–62.

Deng, D., Murakawa, H., Ueda, Y., 2002. Theoretical prediction of welding distortion considering positioning and the gap between parts, in: The Twelfth International Offshore and Polar Engineering Conference. International Society of Offshore and Polar Engineers.

Deng, D., Ogawa, K., Kiyoshima, S., Yanagida, N., Saito, K., 2009. Prediction of residual stresses in a dissimilar metal welded pipe with considering cladding, buttering and post weld heat treatment. Computational Materials Science 47, 398–408.

Deo, Mv., Michaleris, P., 2003. Mitigation of welding induced buckling distortion using transient thermal tensioning. Science and technology of Welding and Joining 8, 49–54.

Depradeux, L., Jullien, J.-F., 2004. Experimental and numerical simulation of thermomechanical phenomena during a TIG welding process, in: Journal de Physique IV (Proceedings). EDP sciences, 697–704.

Desai, R.S., Bag, S., 2014. Influence of displacement constraints in thermomechanical analysis of laser micro-spot welding process. Journal of Manufacturing Processes 16, 264–275.

DeWald, A.T., Hill, M.R., 2003. Improved data reduction for the deep-hole method of residual stress measurement. The Journal of Strain Analysis for Engineering Design 38, 65–77.

Dong, P., 2005. Residual stresses and distortions in welded structures: a perspective for engineering applications. Science and Technology of Welding and Joining 10, 389–398.

Dovzhenko, G., Hanke, S., Staron, P., Maawad, E., Schreyer, A., Horstmann, M., 2018. Residual stresses and fatigue crack growth in friction surfacing coated Ti-6Al-4V sheets. Journal of Materials Processing Technology 262, 104–110.

Eagar, T.W., Tsai, N.S., 1983. Temperature fields produced by traveling distributed heat sources. Welding Journal 62, 346–355.

El-Batahgy, A.-M., DebRoy, T., 2014. Nd-YAG Laser Beam and GTA Welding of Ti-6Al-4V Alloy 2, 8.

Elmer, J.W., Palmer, T.A., Babu, S.S., Zhang, W., DebRoy, T., 2004. Phase transformation dynamics during welding of Ti–6Al–4V. Journal of applied physics 95, 8327–8339.

Elmer, J.W., Palmer, T.A., Zhang, W., Wood, B., DebRoy, T., 2003. Kinetic modeling of phase transformations occurring in the HAZ of C-Mn steel welds based on direct observations. Acta Materialia 51, 3333–3349.

Fachinotti, V.D., Cardona, A., Baufeld, B., Van der Biest, O., 2012. Finite-element modelling of heat transfer in shaped metal deposition and experimental validation. Acta Materialia 60, 6621–6630.

Fan, Y., Cheng, P., Yao, Y.L., Yang, Z., Egland, K., 2005. Effect of phase transformations on laser forming of Ti–6Al–4V alloy. Journal of Applied Physics 98, 013518.

Farjas, J., Roura, P., 2006. Modification of the Kolmogorov–Johnson–Mehl–Avrami rate equation for non-isothermal experiments and its analytical solution. Acta Materialia 54, 5573–5579.

Francis, J.A., Stone, H.J., Kundu, S., Bhadeshia, H.K.D.H., Rogge, R.B., Withers, P.J., Karlsson, L., 2009. The Effects of Filler Metal Transformation Temperature on Residual Stresses in a High Strength Steel Welding Journal of Pressure Vessel Technology 131.

Friedman, E., 1975. Thermomechanical analysis of the welding process using the finite element method. Journal of Pressure Vessel Technology 97, 206–213.

Fukumoto, S., Fujiwara, K., Toji, S., Yamamoto, A., 2008. Small-scale resistance spot welding of austenitic stainless steels. Materials Science and Engineering: A 492, 243–249.

Fukumoto, Y., Hiro, T., Fujii, T., Hashimoto, G., Fujimura, T., Yamada, J., Okamura, T., Matsuzaki, M., 2008. Localized elevation of shear stress is related to coronary plaque rupture: a 3-dimensional intravascular ultrasound study with in-vivo color mapping of shear stress distribution. Journal of the American College of Cardiology 51, 645–650.

Gao, X.-L., Zhang, L.-J., Liu, J., Zhang, J.-X., 2013. A comparative study of pulsed Nd:YAG laser welding and TIG welding of thin Ti6Al4V titanium alloy plate. Materials Science and Engineering: A 559, 14–21.

Geetha, M., Singh, A.K., Muraleedharan, K., Gogia, A.K., Asokamani, R., 2001. Effect of thermomechanical processing on microstructure of a Ti–13Nb–13Zr alloy. Journal of Alloys and Compounds 329, 264–271.

Getto, E., Jiao, Z., Monterrosa, A.M., Sun, K., Was, G.S., 2015. Effect of irradiation mode on the microstructure of self-ion irradiated ferritic-martensitic alloys. Journal of Nuclear Materials 465, 116–126.

Ghafouri, M., 2018. Solid-state phase transformation incorporated welding simulation and prediction of residual stresses and deformations of ultra-high strength steel Strenx® 960 MC.

Glavicic, M.G., Furrer, D.U., Shen, G., 2010. A Rolls-Royce Corporation industrial perspective of titanium process modelling and optimization: current capabilities and future needs. The Journal of Strain Analysis for Engineering Design 45, 329–336.

Glavicic, M.G., Miller, J.D., Semiatin, S.L., 2006. A method to measure the texture of secondary alpha in bimodal titanium-alloy microstructures. Scripta materialia 54, 281–286.

Goldak, J., 1985. A double ellipsoid finite element model for welding heat sources. IIW Doc. No. 212.

Goldak, J., Chakravarti, A., Bibby, M., 1984. A new finite element model for welding heat sources. Metallurgical transactions B 15, 299–305.

Greene, T.W., 1946. Controlled low-temperature stress relieving. Welding journal 1946, 171s–185s.

Grill, A., 1981. Effect of current pulses on the temperature distribution and microstructure in TIG tantalum welds. Metallurgical Transactions: B 12, 187–192.

Grong, Ø., Shercliff, H.R., 2002. Microstructural modelling in metals processing. Progress in materials science 47, 163–282.

Guan, Q., 1994. Dynamic control of welding distortion by moving spot heat sink. Welding In The World 33, 308–312.

Guimarães, J.R.C., Gomes, J.C., 1978. A metallographic study of the influence of the austenite grain size on martensite kinetics. Acta Metallurgica 26, 1591–1596.

Guo, F.A., Ji, V., Francois, M., Zhang, Y.G., 2003. X-ray elastic constant determination and microstresses of α2 phase of a two-phase TiAl-based intermetallic alloy. Materials Science and Engineering: A 341, 182–188.

Gursel, A., 2017. Crack risk in Nd: YAG laser welding of Ti-6Al-4V alloy. Materials Letters 197, 233–235.

Ha, Y.-S., Jang, C.-D., Kim, J.-T., Mun, H.-S., 2007. Analysis of post-weld deformation at the heat-affected zone using external forces based on the inherent strain. International Journal of Precision Engineering and Manufacturing 8, 56–62.

Haferkamp, H., Burmester, I., Niemeyer, M., Dilthey, U., TraÈger, G., 1998. Beam welding of magnesium alloys.

Hallum, D.L., Baeslack, W.A., 1990. Nature of grain refinement in titanium alloy welds by microcooler inoculation. Welding journal 69, 326s–336s.

Hamelin, C.J., Muránsky, O., Smith, M.C., Holden, T.M., Luzin, V., Bendeich, P.J., Edwards, L., 2014. Validation of a numerical model used to predict phase distribution and residual stress in ferritic steel weldments. Acta Materialia 75, 1–19.

Hansen, J.L., 2003. Numerical modelling of welding induced stresses. Department of Manufacturing Engineering and Management, Technical University of Denmark.

Harjo, S., Tomota, Y., Ono, M., 1998. Measurements of thermal residual elastic strains in ferrite–austenite Fe–Cr–Ni alloys by neutron and X-ray diffractions. Acta materialia 47, 353–362.

He, X., Fuerschbach, P.W., DebRoy, T., 2003. Heat transfer and fluid flow during laser spot welding of 304 stainless steel. Journal of Physics D: Applied Physics 36, 1388–1398.

He, X., Norris, J.T., Fuerschbach, P.W., DebRoy, T., 2006. Liquid metal expulsion during laser spot welding of 304 stainless steel. J. Journal of Physics D: Applied Physics 39, 525–534.

Heinze, C., Pittner, A., Rethmeier, M., Babu, S.S., 2013. Dependency of martensite start temperature on prior austenite grain size and its influence on welding-induced residual stresses. Computational Materials Science 69, 251–260.

Holzapfel, H., Schulze, V., Vöhringer, O., Macherauch, E., 1998. Residual stress relaxation in an AISI 4140 steel due to quasistatic and cyclic loading at higher temperatures. Materials Science and Engineering: A 248, 9–18.

Homporova, P., Poletti, C., Stockinger, M., Warchomicka, F., 2011. Dynamic phase evolution in titanium alloy Ti-6Al-4V, in: Proc. 12th World Conference on Titanium. pp. 19–42.

Hong, K.-M., Shin, Y.C., 2016. Analysis of microstructure and mechanical properties change in laser welding of Ti6Al4V with a multiphysics prediction model. Journal of Materials Processing Technology 237, 420–429.

Howard, K., Lawson, S., Zhou, Y., 2006. Welding aluminum sheet using a high-power diode laser. Welding Journal-New York- 85, 101.

Hsieh, C.-C., Lai, C.-H., Wu, W., 2013. Effect of vibration on microstructures and mechanical properties of 304 stainless steel GTA welds. Metals and Materials International 19, 835–844.

Hsieh, C.-C., Wang, P.-S., Wang, J.-S., Wu, W., 2014. Evolution of microstructure and residual stress under various vibration modes in 304 stainless steel welds. The Scientific World Journal 2014.

Hughes, T.J., 1977. Unconditionally stable algorithms for nonlinear heat conduction. Computer Methods in Applied Mechanics and Engineering 10, 135–139.

Hummelshøj, T.S., Christiansen, T.L., Somers, M.A., 2010. Lattice expansion of carbon-stabilized expanded austenite. Scripta Materialia 63, 761–763.

Hurrell, P.R., Everett, D., Gregg, A., Bate, S., 2006. Review of residual stress mitigation methods for application in nuclear power plant, in: ASME Pressure Vessels and Piping Conference. pp. 801–812.

Iracheta, O., Bennett, C.J., Sun, W., 2015. A sensitivity study of parameters affecting residual stress predictions in finite element modelling of the inertia friction welding process. International Journal of Solids and Structures 71, 180–193.

Ishigami, A., Roy, M.J., Walsh, J.N., Withers, P.J., 2017. The effect of the weld fusion zone shape on residual stress in submerged arc welding. The International Journal of Advanced Manufacturing Technology 90, 3451–3464.

Ivetic, G., Lanciotti, A., Polese, C., 2009. Electric strain gauge measurement of residual stress in welded panels. The Journal of Strain Analysis for Engineering Design 44, 117–126.

James, D.W., Moon, D.M., 1970. The martensitic transformation in titanium binary alloys and its effect on mechanical properties, in: The Science, Technology and Application of Titanium. Elsevier, pp. 767–778.

Jepson, K.S., Brown, A.R., Gray, J.A., 1970. Effect of cooling rate on the beta transformation in titanium–niobium and titanium–aluminium alloys. Royal Aircraft Establishment, Farnborough, Eng.

Jiang, W., Chen, W., Woo, W., Tu, S.-T., Zhang, X.-C., Em, V., 2018. Effects of low-temperature transformation and transformation-induced plasticity on weld residual stresses: numerical study and neutron diffraction measurement. Materials & Design 147, 65–79.

Junaid, M., Khan, F.N., Rahman, K., Baig, M.N., 2017. Effect of laser welding process on the microstructure, mechanical properties and residual stresses in Ti-5Al-2.5 Sn alloy. Optics & Laser Technology 97, 405–419.

Jung, G.H., Tsai, C.L., 2004. Fundamental studies on the effect of distortion control plans on angular distortion in fillet welded T-joints. Welding Journal-New York-. 83, 213-S.

Karunaratne, M.S.A., Kyaw, S., Jones, A., Morrell, R., Thomson, R.C., 2016. Modelling the coefficient of thermal expansion in Ni-based superalloys and bond coatings. Journal of Materials Science 51, 4213–4226.

Katzarov, I., Malinov, S., Sha, W., n.d. Finite Element Modeling of the Morphology of β to α Phase Transformation in Ti-6Al-4V Alloy. Metallurgical and Materials Transactions: A 14.

Kawahito, Y., Matsumoto, N., Mizutani, M., Katayama, S., 2008. Characterisation of plasma induced during high power fibre laser welding of stainless steel. Science and Technology of Welding and Joining 13, 744–748.

Keil, S., 1992. Experimental determination of residual stresses with the ring-core method and an on-line measuring system. Experimental Techniques 16, 17–24.

Kelly, S.M., Babu, S.S., David, S.A., Zacharia, T., Kampe, S.L., 2005. A microstructure model for laser processing of Ti-6Al-4V, in: International Congress on Applications of Lasers & Electro-Optics. Laser Institute of America, p. 1005.

Kemda, B.F., Barka, N., Jahazi, M., Osmani, D., 2019. Modeling of phase transformation kinetics in resistance spot welding and investigation of effect of post weld heat treatment on weld microstructure. Metals and Materials International 1–19.

Kempen, A.T.W., Sommer, F., Mittemeijer, E.J., 2002. Determination and interpretation of isothermal and non-isothermal transformation kinetics; the effective activation energies in terms of nucleation and growth. Journal of materials science 37, 1321–1332.

Kherrouba, N., Bouabdallah, M., Badji, R., Carron, D., Amir, M., 2016. Beta to alpha transformation kinetics and microstructure of Ti-6Al-4V alloy during continuous cooling. Materials Chemistry and Physics 181, 462–469.

Khurshid, M., Leitner, M., Barsoum, Z., Schneider, C., 2017. Residual stress state induced by high frequency mechanical impact treatment in different steel grades–Numerical and experimental study. International Journal of Mechanical Sciences 123, 34–42.

Kihara, H., Masubuchi, K., 1954. Studies on the Shrinkage and Residual Welding Stress of Constrained Fundamental Joint Part I Effects of Rod Diameter, Welding Direction, Weaving Motion, Peening and Type of Electrode on the Transverse Shrinkage. Journal of Zosen Kiokai 1954, 181–195.

Kim, C.-H., Ahn, D.-C., 2012. Coaxial monitoring of keyhole during Yb: YAG laser welding. Optics & Laser Technology 44, 1874–1880.

Klueh, R.L., 2005. Elevated temperature ferritic and martensitic steels and their application to future nuclear reactors. International Materials Reviews 50, 287–310.

Kohandehghan, A.R., Serajzadeh, S., 2011. Arc welding induced residual stress in butt-joints of thin plates under constraints. Journal of Manufacturing Processes 13, 96–103.

Korinko, P.S., Malene, S.H., 2001. Considerations for the weldability of types 304L and 316L stainless steel. Practical Failure Analysis 1, 61–68.

Kumar, S., Shahi, A.S., 2011. Effect of heat input on the microstructure and mechanical properties of gas tungsten arc welded AISI 304 stainless steel joints. Materials & Design 32, 3617–3623.

Kumar, V., Dixit, U.S., 2018. A model for the estimation of hardness of laser bent strips. Optics & Laser Technology 107, 491–499.

Kundu, A., Bouchard, P.J., Kumar, S., Venkata, K.A., Francis, J.A., Paradowska, A., Dey, G.K., Truman, C.E., 2013. Residual stresses in P91 steel electron beam welds. Science and Technolonogy of Welding and Joining 18, 70–75.

Lathabai, S., Jarvis, B.L., Barton, K.J., 2001. Comparison of keyhole and conventional gas tungsten arc welds in commercially pure titanium. Materials Science and Engineering: A 299, 81–93.

Leblond, J.B., Mottet, G., Devaux, J.C., 1986. A theoretical and numerical approach to the plastic behaviour of steels during phase transformations—I. Derivation of general relations. Journal of the Mechanics and Physics of Solids 34, 395–409.

Lee, C.-H., Chang, K.-H., 2011. Prediction of residual stresses in high strength carbon steel pipe weld considering solid-state phase transformation effects. Computers & Structures 89, 256–265.

Lee, C.K., Chiew, S.P., Jiang, J., 2012. Residual stress study of welded high strength steel thin-walled plate-to-plate joints, Part 1: Experimental study. Thin-Walled Structures 56, 103–112.

Lei, X., Huang, J., Jin, X., Chen, S., Zhao, X., 2016. Application of Johnson-Mehl-Avrami-Kolmogorov type equation in non-isothermal phase process: Re-discussion. Materials Letters 181, 240–243.

Li, J., Guan, Q., Shi, Y.W., Guo, D.L., 2004. Stress and distortion mitigation technique for welding titanium alloy thin sheet. Science and technology of welding and joining 9, 451–458.

Li, J., Shi, Q.-Y., 2011. Minimizing buckling distortion in welding by weld cooling, in: Minimization of Welding Distortion and Buckling. Elsevier, pp. 214–240.

Lin, J.J., Lv, Y.H., Liu, Y.X., Xu, B.S., Sun, Z., Li, Z.G., Wu, Y.X., 2016. Microstructural evolution and mechanical properties of Ti-6Al-4V wall deposited by pulsed plasma arc additive manufacturing. Materials & Design 102, 30–40.

Lindgren, L.-E., 2001. Finite element modeling and simulation of welding. Part 2: improved material modeling. Journal of thermal stresses 24, 195–231.

Lin, Y.-C., Chou, C.P., 1995. A new technique for reducing the residual stress induced by welding in type 304 stainless steel. Journal of Materials Processing Technology 48, 693–698.

Liu, S., Kouadri-Henni, A., Gavrus, A., 2017. Numerical simulation and experimental investigation on the residual stresses in a laser beam welded dual phase DP600 steel plate: Thermo-mechanical material plasticity model. International Journal of Mechanical Sciences 122, 235–243.

Long, H., Gery, D., Carlier, A., Maropoulos, P.G., 2009. Prediction of welding distortion in butt joint of thin plates. Materials & Design 30, 4126–4135.

Ma, J.C., Yang, Y.S., Tong, W.H., Fang, Y., Yu, Y., Hu, Z.Q., 2007. Microstructural evolution in AISI 304 stainless steel during directional solidification and subsequent solid-state transformation. Materials Science and Engineering: A 444, 64–68.

Malinov, S., Guo, Z., Sha, W., Wilson, A., 2001. Differential scanning calorimetry study and computer modeling of β⇒ α phase transformation in a Ti-6Al-4V alloy. Metallurgical and materials transactions A 32, 879–887.

Malinov, S., Markovsky, P., Sha, W., Guo, Z., 2001. Resistivity study and computer modelling of the isothermal transformation kinetics of Ti–6Al–4V and Ti–6Al–2Sn–4Zr–2Mo–0.08 Si alloys. Journal of alloys and Compounds 314, 181–192.

Malinov, S., Sha, W., 2005. Modeling thermodynamics, kinetics, and phase transformation morphology while heat treating titanium alloys. JOM 57, 42–45.

Manikandan, S.G.K., Sivakumar, D., Rao, K.P., Kamaraj, M., 2014. Effect of weld cooling rate on Laves phase formation in Inconel 718 fusion zone. Journal of Materials Processing Technology 214, 358–364.

Martin, D., 2010. Application of Kolmogorov–Johnson–Mehl–Avrami equations to non-isothermal conditions. Computational materials science 47, 796–800.

Martinson, P., Daneshpour, S., Kocak, M., Riekehr, S., Staron, P., 2009. Residual stress analysis of laser spot welding of steel sheets. Materials & Design 30, 3351–3359.

Martorano, M.A., Tavares, C.F., Padilha, A.F., 2012. Predicting Delta Ferrite Content in Stainless Steel Castings. ISIJ Int. 52, 1054–1065.

Mašek, B., Jirková, H., Hauserova, D., Kučerová, L., Klauberová, D., 2010. The effect of Mn and Si on the properties of advanced high strength steels processed by quenching and partitioning, in: Materials Science Forum. Trans Tech Publ, pp. 94–97.

Masubuchi, K., 1953. Buckling type deformation of thin plate due to welding, in: Proceedings of the 3rd Japan National Congress for Applied Mechanics. pp. 107–111.

Masubuchi, K., 2013. Analysis of Welded Structures: Residual Stresses, Distortion, and Their Consequences. Elsevier.

Matsumoto, N., Kawahito, Y., Nishimoto, K., Katayama, S., 2017. Effects of laser focusing properties on weldability in high-power fiber laser welding of thick high-strength steel plate. Journal of Laser Applications 29, 012003.

Matsunawa, A., Kim, J.-D., Seto, N., Mizutani, M., Katayama, S., 1998. Dynamics of keyhole and molten pool in laser welding. Journal of laser applications 10, 247–254.

Mazumder, J., Steen, W.M., 1980. Heat transfer model for CW laser material processing. Journal of Applied Physics 51, 941–947.

McDill, J.M.J., Oddy, A.S., Goldak, J.A., Bennison, S., 1990. Finite element analysis of weld distortion in carbon and stainless steels. The Journal of Strain Analysis for Engineering Design 25, 51–53.

Mehdi, B., Badji, R., Ji, V., Allili, B., Bradai, D., Deschaux-Beaume, F., Soulié, F., 2016. Microstructure and residual stresses in Ti-6Al-4V alloy pulsed and unpulsed TIG welds. Journal of Materials Processing Technology 231, 441–448.

Michaleris, P., Dantzig, J., Tortorelli, D., 1999. Minimization of welding residual stress and distortion in large structures. Welding Journal-New York- 78, 361-s.

Michaleris, P., DeBiccari, A., 1996. A predictive technique for buckling analysis of thin section panels due to welding. Journal of Ship Production 12, 269–275.

Mironov, S., Zhang, Y., Sato, Y.S., Kokawa, H., 2008. Development of grain structure in β-phase field during friction stir welding of Ti–6Al–4V alloy. Scripta Materialia 59, 27–30.

Moat, R.J., Stone, H.J., Shirzadi, A.A., Francis, J.A., Kundu, S., Mark, A.F., Bhadeshia, H., Karlsson, L., Withers, P.J., 2011. Design of weld fillers for mitigation of residual stresses in ferritic and austenitic steel welds. Science and Technology of Welding and Joining 16, 279–284.

Mousavi, S.A., Miresmaeili, R., 2008. Experimental and numerical analyses of residual stress distributions in TIG welding process for 304L stainless steel. Journal of materials processing technology 208, 383–394.

Moyer, J.M., Ansell, G.S., 1975. The volume expansion accompanying the martensite transformation in iron-carbon alloys. Metall. Trans. A 6, 1785.

Munsi, A., Waddell, A.J., Walker, C.A., 2001. The influence of vibratory treatment on the fatigue life of welds: a comparison with thermal stress relief. Strain 37, 141–149.

Muránsky, O., Hamelin, C.J., Smith, M.C., Bendeich, P.J., Edwards, L., 2012. The effect of plasticity theory on predicted residual stress fields in numerical weld analyses. Computational Materials Science 54, 125–134.

Murr, L.E., Quinones, S.A., Gaytan, S.M., Lopez, M.I., Rodela, A., Martinez, E.Y., Hernandez, D.H., Martinez, E., Medina, F., Wicker, R.B., 2009. Microstructure and mechanical behavior of Ti–6Al–4V produced by rapid-layer manufacturing, for biomedical applications. Journal of the Mechanical Behavior of Biomedical Materials 2, 20–32.

Nguyen, N.T., Ohta, A., Matsuoka, K., Suzuki, N., Maeda, Y., 1999. Analytical solutions for transient temperature of semi-infinite body subjected to 3-D moving heat sources. Welding Journal-New york- 78, 265-s.

Norton, J.H., Rosenthal, D., 1944. Stress measurement by x-ray diffraction. Proceedings of the society for experimental stress analysis 1, 73–76.

Noyan, I.C., Cohen, J.B., 2013. Residual stress: measurement by diffraction and interpretation. Springer.

Ohata, M., Toda, Y., Toyoda, M., Takeno, S., 1999. Control of welding distortion in fillet welds of aluminium alloy thin plates. Welding international 13, 967–976.

Olabi, A.G., Hashmi, M.S.J., 1996. Stress relief procedures for low carbon steel (1020) welded components. Journal of materials processing technology 56, 552–562.

Onink, M., Brakman, C.M., Tichelaar, F.D., Mittemeijer, E.J., Van der Zwaag, S., Root, J.H., Konyer, N.B., 1993. The lattice parameters of austenite and ferrite in Fe-C alloys as functions of carbon concentration and temperature. Scripta Metallurgica et Materialia;(United States) 29.

Pal, K., Pal, S.K., 2011. Effect of pulse parameters on weld quality in pulsed gas metal arc welding: a review. Journal of materials engineering and performance 20, 918–931.

Pandey, C., Mahapatra, M.M., Kumar, P., Saini, N., 2018. Some studies on P91 steel and their weldments. Journal of Alloys Compound 743, 332–364.

Pattee, F.M., 1975. Buckling distortion of thin aluminum plates during welding. (PhD Thesis). Massachusetts Institute of Technology.

Payares-Asprino, M.C., Katsumoto, H., Liu, S., 2008. Effect of martensite start and finish temperature on residual stress development in structural steel welds. Welding Journal, Research Supplement 87, 279s–289s.

Piekarska, W., Kubiak, M., Saternus, Z., 2012. Numerical modelling of thermal and structural strain in laser welding process. Archives of Metallurgy and Materials 57, 1220–1227.

Piekarska, W., Kubiak, M., Żmindak, M., 2017. Issues in Numerical Modeling of Phase Transformations in Welded Joint. Procedia Eng., XXI Polish-Slovak Scientific Conference Machine Modeling and Simulations MMS 2016.September 6-8, 2016, Hucisko, Poland 177, 141–148.

Pilipenko, A., 2001. Computer simulation of residual stress and distortion of thick plates in multielectrode submerged arc welding: Their mitigation techniques.

Poondla, N., Srivatsan, T.S., Patnaik, A., Petraroli, M., 2009. A study of the microstructure and hardness of two titanium alloys: Commercially pure and Ti6Al4V. Journal of Alloys and Compounds 486, 162–167.

Poorhaydari, K., Patchett, B.M., Ivey, D.G., 2005. Estimation of cooling rate in the welding of plates with intermediate thickness. Welding journal 84, 149s–155s.

Qin, L., Liu, C., Yang, K., Tang, B., 2013. Characteristics and wear performance of borided Ti6Al4V alloy prepared by double glow plasma surface alloying. Surface and Coatings Technology 225, 92–96.

Radaj, D., 2012. Heat effects of welding: temperature field, residual stress, distortion. Springer Science & Business Media.

Rae, W., 2019. Thermo-metallo-mechanical modelling of heat treatment induced residual stress in Ti6Al4V alloy. Materials Science and Technology 35, 747–766.

Ragavendran, M., Vasudevan, M., 2020. Laser and hybrid laser welding of type 316L (N) austenitic stainless steel plates. Materials and Manufacturing Processes 35, 922–934.

Rajani, H.Z., Torkamani, H., Sharbati, M., Raygan, S., 2012. Corrosion resistance improvement in Gas Tungsten Arc Welded 316L stainless steel joints through controlled preheat treatment. Materials & Design 34, 51–57.

Reddy, G.M., Murthy, C.S., Rao, K.S., Rao, K.P., 2009. Improvement of mechanical properties of Inconel 718 electron beam welds—influence of welding techniques and postweld heat treatment. The International Journal of Advanced Manufacturing Technology 43, 671–680.

Reed, C.B., Natesan, K., Xu, Z., Smith, D.L., 2000. The effect of laser welding process parameters on the mechanical and microstructural properties of V–4Cr–4Ti structural materials. Journal of Nuclear Materials 283, 1206–1209.

Ren, W., Lu, F., Yang, R., Liu, X., Li, Z., Hosseini, S.R.E., 2015. A comparative study on fiber laser and CO2 laser welding of Inconel 617. Materials & Design 76, 207–214.

Rodgers, D.E., Fletcher, P.R., 1938. The Determination of Internal Stresses from the Temperature History of a Butt Welded Pipe. Welding Journal Research Supplement 4–7.

Rogante, M., 2009. Wear characterisation and tool performance of sintered carbide inserts during automatic machining of AISI 1045 steel. Journal of Materials Processing Technology 209, 4776–4783.

Rosenthal, D., 1941. Mathematical theory of heat distribution during welding and cutting. Welding journal 20, 220–234.

Sabbaghzadeh, J., Hamedi, M.J., Ghaini, F.M., Torkamany, M.J., 2008. Effect of process parameters on the melting ratio in overlap pulsed laser welding. Metallurgical and Materials Transactions B 39, 340–347.

Sabooni, S., Karimzadeh, F., Enayati, M.H., Ngan, A.H.W., Jabbari, H., 2015. Gas tungsten arc welding and friction stir welding of ultrafine grained AISI 304L stainless steel: microstructural and mechanical behavior characterization. Materials Characterization 109, 138–151.

Sánchez-Amaya, J.M., Amaya-Vázquez, M.R., González-Rovira, L., Botana-Galvin, M., Botana, F.J., 2014. Influence of surface pre-treatments on laser welding of Ti6Al4V alloy. Journal of materials engineering and performance 23, 1568–1575.

Santella, M.L., Swindeman, R.W., Reed, R.W., Tanzosh, J.M., 2001. Martensite formation in 9 Cr-1 Mo steel weld metal and its effect on creep behavior, in: Proc. EPRI Conf. on '9Cr Materials Fabrication and Joining Technologies', Myrtle Beach, CA, USA. Citeseer.

Semiatin, S.L., Bieler, T.R., 2001. Effect of texture and slip mode on the anisotropy of plastic flow and flow softening during hot working of Ti-6Al-4V. Metallurgical and Materials Transactions A 32, 1787–1799.

Senkov, O.N., Valencia, J.J., Senkova, S.V., Cavusoglu, M., Froes, F.H., 2002. Effect of cooling rate on microstructure of Ti-6Al-4V forging. Materials science and technology 18, 1471–1478.

Serizawa, H., Nakamura, S., Tanigawa, H., Ogiwara, H., Murakawa, H., 2013. Numerical study of local PWHT condition for EB welded joint between first and side walls in ITER-TBM. Journal of Nuclear Materials 442, S535–S540.

Short, A.B., 2009. Gas tungsten arc welding of α + β titanium alloys: a review. Materials Science and Technology 25, 309–324.

Sieniawski, J., Ziaja, W., Kubiak, K., Motyka, M., 2013. Microstructure and mechanical properties of high strength two-phase titanium alloys. Titanium Alloys-Advances in Properties Control 69–80.

Sim, W.-M., 2010. Challenges of residual stress and part distortion in the civil airframe industry. International Journal of Microstructure and Materials Properties 5, 446–455.

Singh, S., Yadaiah, N., Bag, S., Pal, S., 2014. Numerical simulation of welding-induced residual stress in fusion welding process using adaptive volumetric heat source. Proceedings of the Institution of Mechanical Engineers, Part C: Journal of Mechanical Engineering Science 228, 2960–2972.

Siwek, A., Rońda, J., Banaś, K., Cybulka, P., Michalik, K., Plaszewski, P., 2013. Modeling of Inconel 625 TIG welding process. Computer Methods in Materials Science 13, 181–187.

Sluzalec, A., 2005. Theory of thermomechanical processes in welding. Springer Science & Business Media.

Soylemez, E., 2018. Modeling The Melt Pool Of The Laser Sintered Ti6al4v Layers With Goldak'S Double-Ellipsoidal Heat Source, in: Proceedings of the 29th Annual International Solid Freeform Fabrication Symposium, Austin, TX, USA. pp. 13–15.

Speich, G.R., Demarest, V.A., Miller, R.L., 1981. Formation of austenite during intercritical annealing of dual-phase steels. Metall. Mater. Trans. A 12, 1419–1428.

Spezzapria, M., Settimi, A.G., Pezzato, L., Novella, M.F., Forzan, M., Dughiero, F., Bruschi, S., Ghiotti, A., Brunelli, K., Dabalà, M., 2017. Effect of Prior Microstructure and Heating Rate on the Austenitization Kinetics of 39NiCrMo3 Steel. Steel Res. Int. 88, 1600267.

Stone, H.J., Bhadeshia, H.K., Withers, P.J., 2008. In situ monitoring of weld transformations to control weld residual stresses, in: Materials Science Forum. Trans Tech Publ, pp. 393–398.

Sundaresan, S., Ram, G.J., Reddy, G.M., 1999. Microstructural refinement of weld fusion zones in α–β titanium alloys using pulsed current welding. Materials Science and Engineering: A 262, 88–100.

Suresh, M.V., Vamsi Krishna, B., Venugopal, P., Prasad Rao, K., 2004. Effect of pulse frequency in gas tungsten arc welding of powder metallurgical preforms. Science and Technology of welding and joining 9, 362–368.

Szkliniarz, W., Grosman, F., 1988. The Estimation of Refinement Possibility of Coarse-Grained Structures of Unalloyed Titanium by the Heat Treatment, in: Sixth World Conference on Titanium. III. 1529–1534.

Taljat, B., Radhakrishnan, B., Zacharia, T., 1998. Numerical analysis of GTA welding process with emphasis on post-solidification phase transformation effects on residual stresses. Mater. Sci. Eng. A 246, 45–54.

Tan, P., Shen, F., Li, B., Zhou, K., 2019. A thermo-metallurgical-mechanical model for selective laser melting of Ti6Al4V. Materials & Design 168, 107642.

Tebedge, N., Alpsten, G., Tall, L., 1973. Residual-stress measurement by the sectioning method. Experimental Mechanics 13, 88–96.

Tekriwal, P., Mazumder, J., 1991. Transient and residual thermal strain-stress analysis of GMAW. Journal of Engineering Materials and Technology 113, 336–343.

Teng, T.-L., Lin, C.-C., 1998. Effect of welding conditions on residual stresses due to butt welds. International Journal of Pressure vessels and piping 75, 857–864.

Terai, K., Matsui, S., Kinoshita, T., Yamashita, S., Tomoto, T., Horiuchi, H., Tsujimoto, K., Nishio, K., 1978. Study on prevention of welding deformation in thin-skin plate structures. Kawasaki Technical Review 61, 61–66.

Thibault, D., Bocher, P., Thomas, M., Gharghouri, M., Côté, M., 2010. Residual stress characterization in low transformation temperature 13% Cr–4% Ni stainless steel weld by neutron diffraction and the contour method. Materials Science and Engineering: A 527, 6205–6210.

Torkamany, M.J., Hamedi, M.J., Malek, F., Sabbaghzadeh, J., 2006. The effect of process parameters on keyhole welding with a 400 W Nd: YAG pulsed laser. Journal of Physics D: Applied Physics 39, 4563.

Trivedi, A., Suman, A., De, A., 2006. Integrating finite element based heat transfer analysis with multivariate optimization for efficient weld pool modeling. ISIJ International 46, 267–275.

Tsay, L.W., Shan, Y.-P., Chao, Y.-H., Shu, W.Y., 2006. The influence of porosity on the fatigue crack growth behavior of Ti–6Al–4V laser welds. Journal of materials science 41, 7498–7505.

Tseng, K.H., Chou, C.P., 2002. The effect of pulsed GTA welding on the residual stress of a stainless steel weldment. Journal of Materials Processing Technology 123, 346–353.

Turner, R., Schroeder, F., Ward, R.M., Brooks, J.W., 2014. The importance of materials data and modelling parameters in an FE simulation of linear friction welding. Advances in Materials Science and Engineering 2014.

Tzeng, Y., 2000. Parametric analysis of the pulsed Nd: YAG laser seam-welding process. Journal of Materials Processing Technology 102, 40–47.

Ueda, Y., Fukuda, K., Tanigawa, M., 1979. New measuring method of three dimensional residual stresses based on theory of inherent strain (welding mechanics, strength & design). Transactions of JWRI 8, 249–256.

Ueda, Y., Murakawa, H., Ma, N., 2012. Welding deformation and residual stress prevention. Elsevier.

Unnikrishnan, R., Idury, K.S., Ismail, T.P., Bhadauria, A., Shekhawat, S.K., Khatirkar, R.K., Sapate, S.G., 2014. Effect of heat input on the microstructure, residual stresses and corrosion resistance of 304L austenitic stainless steel weldments. Materials Characterization 93, 10–23.

Uzun, F., Bilge, A.N., 2011. Immersion ultrasonic technique for investigation of total welding residual stress. Procedia Engineering 10, 3098–3103.

Van Bohemen, S.M.C., 2012. Bainite and martensite start temperature calculated with exponential carbon dependence. Materials Science and Technology 28, 487–495.

Van Bohemen, S.M.C., Sietsma, J., 2014. Kinetics of martensite formation in plain carbon steels: critical assessment of possible influence of austenite grain boundaries and autocatalysis. Mater. Sci. Technol. 30, 1024–1033.

Ventrella, V.A., Berretta, J.R., De Rossi, W., 2010. Pulsed Nd: YAG laser seam welding of AISI 316L stainless steel thin foils. Journal of Materials Processing Technology 210, 1838–1843.

Verdi, C., Visintin, A., 1987. A mathematical model of the austenite-pearlite transformation in plain carbon steel based on the Scheil's additivity rule. Acta Metallurgica 35, 2711–2717.

Wan, Y., Jiang, W., Song, M., Huang, Y., Li, J., Sun, G., Shi, Y., Zhai, X., Zhao, X., Ren, L., 2019. Distribution and formation mechanism of residual stress in duplex stainless steel weld joint by neutron diffraction and electron backscatter diffraction. Materials & Design 181, 108086.

Wang, J., Yuan, H., Ma, N., Murakawa, H., 2016. Recent research on welding distortion prediction in thin plate fabrication by means of elastic FE computation. Marine Structures 47, 42–59.

Wang, J., Zhang, G., Sun, J., Bao, Y., Zhuang, L., Ning, H., 2006. Low temperature nitriding of iron by alternating current pretreatment. Surface and Coatings Technology 200, 6666–6670.

Wang, S., Liao, Z., Liu, Y., Liu, W., 2014. Influence of thermal oxidation temperature on the microstructural and tribological behavior of Ti6Al4V alloy. Surface and Coatings Technology 240, 470–477.

Watanabe, M., Satoh, K., 1958. Fundamental study on buckling of thin steel plate due to bead-welding. Journal of the Japan Welding Society 27, 313–320.

Watt, D.F., Coon, L., Bibby, M., Goldak, J., Henwood, C., 1988. An algorithm for modelling microstructural development in weld heat-affected zones (part a) reaction kinetics. Acta Metallurgica 36, 3029–3035.

Weckman, D.C., Kerr, H.W., Liu, J.T., 1997. The effects of process variables on pulsed Nd: YAG laser spot welds: Part II. AA 1100 aluminum and comparison to AISI 409 stainless steel. Metallurgical and Materials Transactions: B 28, 687–700.

Withers, P.J., Bhadeshia, H.K.D.H., 2001. Residual stress. Part 1 – Measurement techniques. Materials Science and Technology 17, 355–365.

Withers, Philip J., Bhadeshia, H., 2001. Residual stress. Part 2–Nature and origins. Materials Science and Technology 17, 366–375.

Xia, J., Jin, H., 2018. Numerical modeling of coupling thermal–metallurgical transformation phenomena of structural steel in the welding process. Advances in Engineering Software 115, 66–74.

Xu, L.Y., Zhu, J., Jing, H.Y., Zhao, L., Lv, X.Q., Han, Y.D., 2016. Effects of deep cryogenic treatment on the residual stress and mechanical properties of electron-beam-welded Ti–6Al–4V joints. Materials Science and Engineering: A 673, 503–510.

Yadaiah, N., Bag, S., 2012. Effect of heat source parameters in thermal and mechanical analysis of linear GTA welding process. ISIJ international 52, 2069–2075.

Yadaiah, N., Bag, S., 2014. Development of egg-configuration heat source model in numerical simulation of autogenous fusion welding process. International Journal of Thermal Sciences 86, 125–138.

Yaghi, A.H., Hyde, T.H., Becker, A.A., Sun, W., 2008. Finite element simulation of welding and residual stresses in a P91 steel pipe incorporating solid-state phase transformation and post-weld heat treatment. The Journal of Strain Analysis for Engineering Design 43, 275–293.

Yan, J., Gao, M., Zeng, X., 2010. Study on microstructure and mechanical properties of 304 stainless steel joints by TIG, laser and laser-TIG hybrid welding. Optics and Lasers in Engineering 48, 512–517.

Yang, T., Xu, D., Chen, W., Yang, R., Lv, S., 2019. Microstructure evolution and deformation resistance of heavy-thickness Ti-6Al-4V narrow-gap welded joints. Materials Letters 250, 116–118.

Yang, Y.P., Brust, F.W., Dong, P., Zhang, J., Cao, Z., 2000. Modeling procedure development of buckling distortion in thin plate welding. ASME-Publications-PVP 410, 103–108.

Yong, T., Jianzhong, W., Daqiang, C., 1999. Electro-pluse on impriving steel ingot solidification structure. Journal of University of Science and Technology Beijing 6, 94–97.

Yunlian, Q., Ju, D., Quan, H., Liying, Z., 2000. Electron beam welding, laser beam welding and gas tungsten arc welding of titanium sheet. Materials Science and Engineering: A 280, 177–181.

Zeng, P., Gao, Y., Lei, L.P., 2009. Welding process simulation under varying temperatures and constraints. Materials Science and Engineering: A, Fifth International Conference on Physical and Numerical Simulations of Material Processing (ICPNS 2007) held at Zhengzhou, China, October 23-27, 2007 499, 287–292.

Zhan, X., Mi, G., Zhang, Q., Wei, Y., Ou, W., 2017. The hourglass-like heat source model and its application for laser beam welding of 6 mm thickness 1060 steel. The International Journal of Advanced Manufacturing Technology 88, 2537–2546.

Zhang, T., Vieh, C., Wang, K., Dai, Y., 2014. Irradiation-induced evolution of mechanical properties and microstructure of Eurofer 97. Journal of Nuclear Materials 450, 48–53.

Zhdanov, I., IM, Z., AK, G., 1978. Determining the residual welding stresses at a depth in metal. determining the residual welding stresses at a depth in metal.

Zhu, X.K., Chao, Y.J., 2002. Effects of temperature-dependent material properties on welding simulation. Computers & Structures 80, 967–976.

Zhu, X.K., Chao, Y.J., 2004. Numerical simulation of transient temperature and residual stresses in friction stir welding of 304L stainless steel. Journal of materials processing technology 146, 263–272.

Zubairuddin, M., Albert, S.K., Chaudhari, V., Suri, V.K., 2014. Influence of Phase Transformation on Thermo-mechanical Analysis of Modified 9Cr-1Mo Steel. Procedia Materials Science 5, 832–840.

Zubairuddin, M., Albert, S.K., Vasudevan, M., Mahadevan, S., Chaudhari, V., Suri, V.K., 2017. Numerical simulation of multi-pass GTA welding of grade 91 steel. Journal of Manufacturing Processes 27, 87–97.

Zumelzu, E., Sepulveda, J., Ibarra, M., 1999. Influence of microstructure on the mechanical behaviour of welded 316 L SS joints. Journal of Materials Processing Technology 94, 36–40.

Bibliography

1. Cowley, J.M., 1992. Electron diffraction techniques. Oxford University Press.
2. Donachie, M.J., 2000. Titanium: A Technical Guide, 2nd Edition. ASM International.
3. Fredriksson, H., Akerlind, U., 2006. Materials processing during casting. John Wiley & Sons Inc.
4. Goldak, J.A., Akhlaghi, M., 2005. Computational welding mechanics. Springer Science & Business Media.
5. Lippold, J.C., Kotecki, D.J., 2005. Welding metallurgy and weldability of stainless steels. Wiley-VCH.
6. Maddox, S.J., 1991. Fatigue strength of welded structures. Woodhead publishing.
7. Mills, K.C., 2002. Recommended values of thermophysical properties for selected commercial alloys. Woodhead Publishing.
8. Murgau, C.C., 2016. Microstructure model for Ti-6Al-4V used in simulation of additive manufacturing (PhD Thesis). Doctoral thesis, Lule\a a University of Technology.
9. Norrish, J., 2006. Advanced welding processes. Elsevier.
10. Radaj, D., 2003. Welding residual stresses and distortion. DVS-Verlag, Düsseldorf 332.
11. Radaj, D., 2012. Heat effects of welding: temperature field, residual stress, distortion. Springer Science & Business Media.
12. Sluzalec, A., 2005. Theory of thermomechanical processes in welding. Springer Science & Business Media.
13. Ueda, Y., Murakawa, H., Ma, N., 2012. Welding deformation and residual stress prevention. Elsevier.
14. Watkins, K.G., 2003. Laser welding of magnesium alloys. Magnesium Technology 153–156.

List of Publications

Referred Journal

1. Kumar B., Bag S., Mahadevan S., Paul C. P., Das C. R., Bindra K. S. (2021). On the interaction of microstructural morphology with residual stress in fiber laser welding of austenitic stainless steel. ***CIRP Journal of Manufacturing Science and Technology*,** 33, 158-175.

2. Kumar B., Bag S., Paul C. P., Das C. R., Ravikumar R., & Bindra K. S. (2020). Influence of the mode of laser welding parameters on microstructural morphology in thin sheet Ti6Al4V alloy. ***Optics and Laser Technology***, 131, 106456.

3. Kumar B., & Bag S. (2019). Phase transformation effect in distortion and residual stress of thin-sheet laser welded Ti-alloy. ***Optics and Lasers in Engineering***, 122, 209-224.

4. Kumar B., Bag S., Paul C. P. (2020). Influence of heat input on welding induced distortion for Yb-Fibre laser welded thin sheets. ***Materials Today: Proceedings***, 26(2), 2040-2046.

5. Kumar B., Kebede D., & Bag S. (2018). Microstructure evolution in thin sheet laser welding of titanium alloy. ***International Journal of Mechatronics and Manufacturing Systems***, 11(2-3), 203-229.

6. Mondal A. K., **Kumar B.**, Bag S., Nirsanametla Y. Y., & Biswas P. (2020). Development of a new heat source model for numerical simulation of the fusion welding process. ***International Journal of Thermal Sciences***. 166, 107005.

7. Kumar B., Bag S., Paul C. P., Ganesh P., Das C. R., Ravikumar R., Bindra K. S. (2021). Influence of diffusionless transformation on residual stress for laser-welded Ti-alloy. (**Under preparation**)

8. Kumar B., Das C. R., Mahadevan S., Bag S., Albert S. K. (2021). Comparative study on the influence of weld metal composition on residual stress evolution in fusion welded 9Cr-1Mo steels by modeling and experiments. (**Under preparation**)

9. Kumar B., & Bag S. (2021). A review on phase transformation kinetics of Ti-alloy and its influence on residual stress. **(Under preparation)**.

Book Chapter

1. Kumar B., Bag S. (2021). Critical assessment of metallurgical and mechanical characteristics

of pulse laser welded α+β phase Ti-alloy, ***Next Generation Materials and Processing Technologies***. Springer, Singapore.

2. Kumar B., Nawani R., Bag S. (2020). Effect of mechanical constraints on thermo mechanical behaviour of laser welded dissimilar Joints. ***Advances in Simulation, Product Design and development*** (pp. 107-119). Springer, Singapore.

3. Kumar B., Bag S. (2019). Effect of pulsation on temperature distribution of laser-welded dissimilar joint of thin sheet. ***Advances in Computational Methods in Manufacturing*** (pp. 165-178). Springer, Singapore.

Referred Conference

1. Kumar B., Bag S. (2021). Critical assessment of metallurgical and mechanical characteristics of pulse laser welded α+β phase Ti-alloy. ***National Conference on Research and Developments in Material Processing, Modelling and Characterization*** *(RDMPMC)*, 26-27 August 2020, National Institute of Technology, Jamshedpur.

2. Kumar B., Bag S., Paul C. P. (2020). Influence of heat input on welding induced distortion for Yb-Fibre laser welded thin sheets. ***10th International Conference of Materials Processing and Characterization (ICMPC)***, 21-23 February 2020, GLA University, Mathura.

3. Kumar B., Bag S. (2019). Effect of pulsation on temperature distribution of laser-welded dissimilar joint of thin sheet. ***2nd International Conference on Computational Methods in Manufacturing (ICCMM)***, 8-9 March, 2019, Indian Institute of Technology, Guwahati.

4. Kumar B., Nawani R., Bag S. (2018). Effect of mechanical Constraints on thermo mechanical behaviour of laser welded dissimilar Joints. ***7th International and 28th All India Manufacturing Technology Design and Research (AIMTDR) Conference***, 13−15 December, 2018, Anna University, Chennai.

5. Kumar B., Baruah M., Bag S. (2017). On the effect of heat input in cooling rate and microstructure of laser welded Ti6Al4V alloy. ***20th International conference on Advances in Materials and Processing Technologies (AMPT)***, 11-14 December, 2017, VIT University, Chennai.